Fall 2021

NOVEL SYNTHETIC METHODS AND APPLICATIONS OF POROUS MATERIALS: AEROGEL FOAMS, METALLIC AEROGELS, AMORPHOUS AND GRAPHITIC CARBON AEROGELS

Rushi Soni
Missouri University of Science and Technology

NOVEL SYNTHETIC METHODS AND APPLICATIONS

OF POROUS MATERIALS: AEROGEL FOAMS, METALLIC AEROGELS,

AMORPHOUS AND GRAPHITIC CARBON AEROGELS

by

RUSHI UMESHKUMAR SONI

A DISSERTATION

Presented to the Faculty of the Graduate School of the

MISSOURI UNIVERSITY OF SCIENCE AND TECHNOLOGY

In Partial Fulfillment of the Requirements for the Degree

DOCTOR OF PHILOSOPHY

in

CHEMISTRY

2021

Approved by:

Dr. Chariklia Sotiriou-Leventis, Advisor
Dr. Amitava Choudhury
Dr. Manashi Nath
Dr. Jeffrey G. Winiarz
Dr. K. Chandrashekhara

<u>DEDICATED TO</u>

MY PARENTS

Dr. Umeshkumar C. Soni

Mrs. Dipal U. Soni

MY SISTER

Dr. Meera U. Soni

GRANDPARENTS & LOVING FAMILY

PUBLICATION DISSERTATION OPTION

This dissertation consists of the following four manuscripts that have been published or submitted for publication:

Paper I, pages 21–42, has been published in *Polymer.*

Paper II, pages 43–76, has been published in *ACS Applied Materials & Interfaces.*

Paper III, pages 77–165, is under review in *Chemistry of Materials.*

Paper IV, pages 166–276, is under review in *Chemistry of Materials.*

ABSTRACT

We report novel methods for the synthesis of porous materials such as polymeric aerogel foams, pure metallic aerogels, amorphous and graphitic carbon aerogels, and their applications. I. Polyurethane based aerogel foams were synthesized with an aliphatic triisocyanate and ethylene glycol through a pressurized (7 bar) sol-gel method. The foam-like structure is prepared without any chemical foaming agents or templates, resulting in less expensive, more efficient, readily adaptable, and environmentally friendly process. Those materials exhibited lower thermal conductivity (by 25%) and higher oil adsorption capacity (by 36% w/w) than their corresponding aerogels. II. Monolithic, pure metallic Co(0) aerogels were synthesized from polyurea-crosslinked cobaltia xerogel powder compacts via carbothermal reduction, for application as thermites. III. Carbon aerogels were synthesized from compressed compacts of polyurea- and polyacrylonitrile-crosslinked silica xerogel powders. The process of making *aerogels-via-xerogels* allows to speed-up the solvent exchange process and bypasses supercritical fluid drying, resulting in time, energy, and materials efficient methodology. At their best, these carbon aerogels have high BET surface area (up to 1934 $m^2\,g^{-1}$), porosities (up to 83% v/v) and good CO_2 uptake (up to 9.15 mmol g^{-1}) with high selectivity toward other gases (H_2, N_2 and CH_4). IV. Sturdy, monolithic graphitic carbon aerogels with different nano-morphologies were synthesized at lower temperatures (800-1500 ºC) compared to conventional graphitization (2500-3300 ºC) from Fe- or Co-catalyzed free-radical surface-initiated polymerization of acrylonitrile monomer to polyacrylonitrile-crosslinked metal oxide xerogel powder compacts. These graphitic carbon aerogels were demonstrated as anodes for Li-ion batteries with good charge capacity.

ACKNOWLEDGEMENTS

TABLE OF CONTENTS

LIST OF FIGURES

PAPER IV

LIST OF SCHEMES

PAPER IV

LIST OF TABLES

LIST OF ABBREVIATIONS

Abbreviation	Description
SCF	supercritical fluid
RF	resorcinol-formaldehyde aerogel
PIR-PUR	poly(isocyanurate-urethane)
PBO	polybenzoxazine aerogel
PAN	polyacrylonitrile
PUA	polyurea
PU	polyurethane
PMMA	polymethyl methacrylate
NCO	isocyanate group
TIPM	triisocyanate (tris(4-isocyanatophenyl) methane)
APTES	3-aminopropyltriethoxysilane
TMOS	tetramethylorthosilicate
ABCVA	4,4'-azobis(4-cyanopentanoic acid)
DBTDL	dibutyltin dilaurate
N3300A	Desmodur N3300A, trimer of hexamethylene diisocyanate - an aliphatic triisocyanate

X-aerogel   cross-linked aerogel

MEHQ   monomethyl ether hydroquinone

Li-ion   lithium-ion

AN   acrylonitrile

TDI   toluene diisocyanate

FeOx   iron oxide

CoOx   cobaltia / cobalt oxide

PUA@silica   polyurea polymer at silica

PAN@silica   polyacrylonitrile polymer at silica

PAN@MOx   polyacrylonitrile polymer at metal oxide

PAN@FeOx   polyacrylonitrile polymer at iron oxide

PAN@CoOx   polyacrylonitrile polymer at cobalt oxide

TGA   thermogravimetric analysis

SEM   scanning electron microscopy

XRD   X-ray diffraction

XPS   X-ray photoelectron spectroscopy

FTIR   fourier transformed infrared spectroscopy

DSC	differential scanning calorimetry
MDSC	modulated differential scanning calorimetry
NMR	nuclear magnetic resonance
CP MASS ^{13}C NMR	cross-polarization magic angle spinning ^{13}C-NMR
CP TOSS ^{13}C NMR	cross-polarization total suppression of spinning sidebands ^{13}C-NMR
UV-Vis	ultraviolet-visible spectroscopy
TEM	transmission electron microscopy
EPA	environmental protection agency
TMS	tetramethylsilane
BET	Brunauer–Emmett–Teller method in the analysis of surface area from N_2-sorption porosimetry
BJH	Barret-Joyne-Halenda equation in the analysis of mesopore size distribution
DFT	density functional theory in the analysis of micropore size distribution
DR	Dubinin-Radushkevich method in the analysis of micropore volume
Q_{st}	isosteric heat of adsorption
Q_o	Q_{st} at near zero gas uptake

1. INTRODUCTION

1.1. AEROGELS

Aerogels are a class of porous materials characterized by their low bulk density (about 1000 times less dense than glass), high open porosity (up to 99% v/v air),[1–4] high pore volume (>2 cm^3 g^{-1}),[5] high specific surface area (>600 m^2 g^{-1}), low thermal conductivity, and low sound velocity. Based on these properties aerogels are excellent candidates as thermal insulators,[6,7] gas/oil adsorbents,[8–13] catalyst supports,[14–16] energy storage materials,[17–19] thermites,[17,20] ceramics,[21–23] in aerospace applications,[24–26] electrodes in batteries,[27–29] sensors,[30–32] capacitors,[33,34] etc.

According to IUPAC, aerogels are "gels comprised of microporous solids in which the dispersed phase is a gas".[35] But this definition is not correct, because there are many other microporous materials like zeolites and metal organic frameworks, which are not aerogels. A better and concise definition of aerogels was proposed by Leventis as "an open non-fluid colloidal network or polymer network that is expanded throughout its whole volume by a gas and is formed by the removal of all swelling agents from a gel without substantial volume reduction or network compaction."[21]

Aerogels are typically synthesized through a sol-gel process[36] giving a wet-gel where the pore-filling solvent is replaced by a supercritical fluid (SCF), such as SCF CO_2, which is vented off as a gas. The sol-gel process involves mixing of appropriate precursors in a non-reactive solvent, usually with a catalyst or an initiator to form a 'sol'. This sol, further 'gels' by different polymerization techniques to give a 'wet-gel'. The resulting wet-gel is a porous nanostructured solid-network with solvent filled in the pores, which is aged

and dried using appropriate drying methods. The process of SCF drying preserves the porous skeletal framework of the wet-gel with a minimum volume shrinkage.

Polymer-crosslinked Aerogels - Traditionally, aerogels were considered as silica aerogels, which were invented by S.S. Kistler.[37] These silica aerogels are extremely light-weight, highly porous, have high surface areas, low thermal conductivity, but are extremely fragile.[37,38] Generally, silica aerogels are transparent with a light blue tint because of reflected light from primary particles due to Rayleigh scattering as shown in Figure 1.1.[39] Due to their fragility issue, silica aerogels, have limited use in certain types of catalyst supports,[14–16] space exploration, for example in capturing cosmic dust in outer space (refer to NASA's Stardust program),[24–26] and thermal insulation.[6,7] Fiber reinforced aerogel composite thermal insulation blankets are commercially available from Aspen aerogels which can be bent and rolled over.[40]

The mechanical properties of these fragile silica aerogels can be enhanced by changing their nanostructure, which requires a detailed understanding of their skeletal and porous structure, which in turn requires a detailed understanding of their formation via the so-called sol-gel chemistry. Silica aerogels consist of a pearl-necklace-like skeletal framework and the interparticle neck of such structures is the weakest point, leading to their fragility.[41] While ageing of silica wet-gels, Ostwald ripening takes place, which is a dissolution and reprecipitation of silica at surfaces and the interparticle neck, which enhances the mechanical strength of the fragile silica wet-gel.[42] Longer ageing time would lead to more mechanically sturdy silica aerogels but at the expense of increasing their skeletal density.[43]
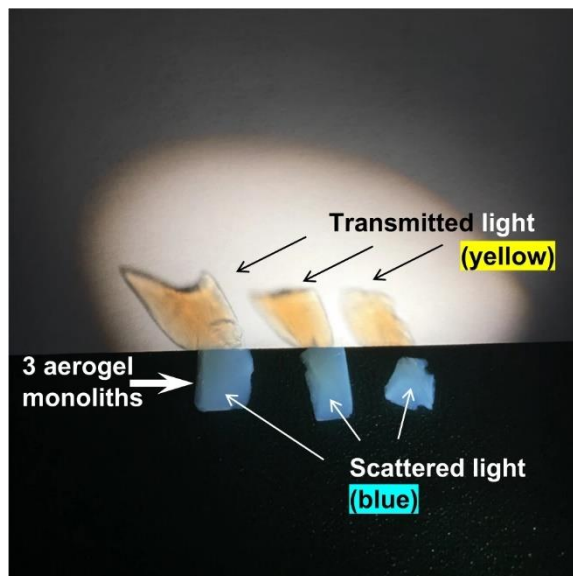
Figure 1.1. Photograph of three small silica aerogel monoliths ($\rho_b = 0.032$ g cm^{-3}) on a black surface with a white background demonstrating Rayleigh scattering by showing transmitted yellow/orange light and reflected bluish light. Samples were illuminated with a white light source from the front.

A new approach to solve the fragility issue was developed by coating the silica skeleton with an organic polymer by crosslinking different surface functional groups with an isocyanate.[44] This forms a polymer coating on the entire skeletal framework as shown in Scheme 1.1 and gives better mechanical strength without affecting much of the density. These polymer-crosslinked aerogels are referred to as *X-aerogels*. It was reported that the mechanical strength of *X-aerogels* increased by 300 times with a small increase of 3 times in density, as compared to normal silica aerogels.[43,44] Many different chemistries can be carried out to crosslink the skeletal framework with different organic polymers like polystyrene,[45] polyacrylonitrile,[22] polyurea,[21] polyurethane,[46,47] polymethylmethacrylate,[44] epoxy resins,[48] etc. There is an added advantage of these polymer-crosslinked aerogels as they can act as a source of carbon via carbothermal reduction leading initially to carbon

aerogels following by carbonization, given that the polymers are aromatic and can be carbonized in good yield.[49]
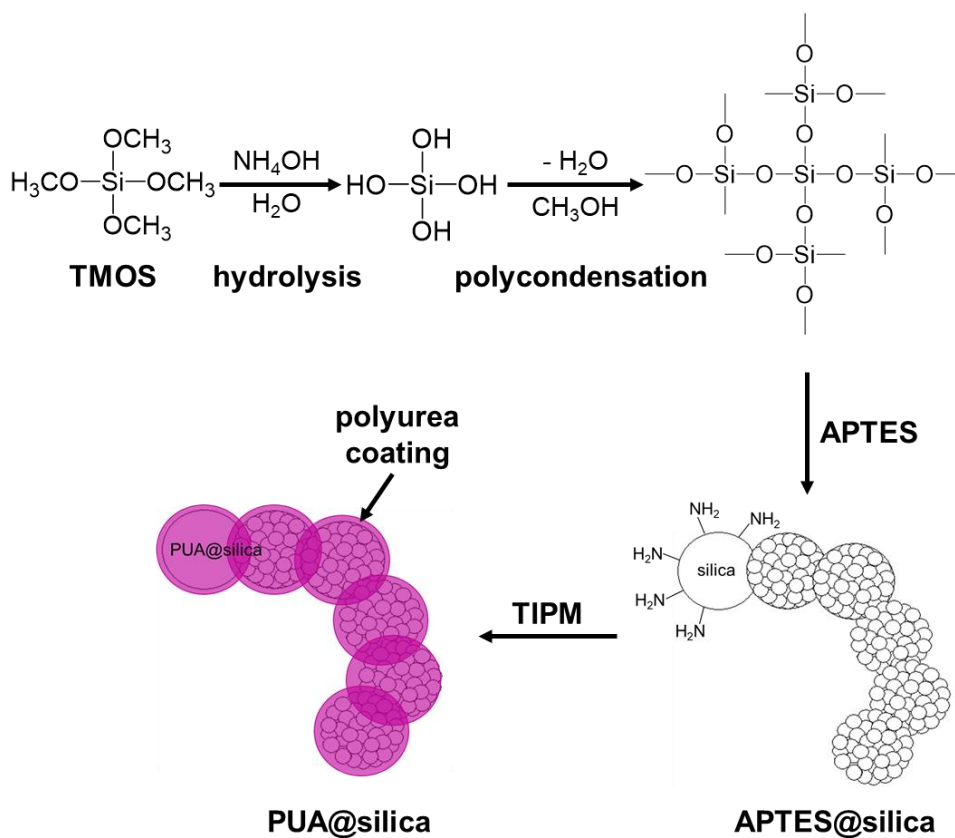
Scheme 1.1. Synthesis of polymer-crosslinked (polyurea) silica aerogels (PUA@silica).

1.2. THE ISOCYANATE CHEMISTRY

One of the most highly reactive functional groups in chemistry, is the isocyanate group (-N=C=O) due to the electron withdrawing ability of oxygen and nitrogen atoms attached to the central carbon atom, as shown in Scheme 1.2. This electron withdrawing ability induces electron deficiency on the central carbon atom, making it more prone to nucleophilic attack, as shown in Scheme 1.3.[50]
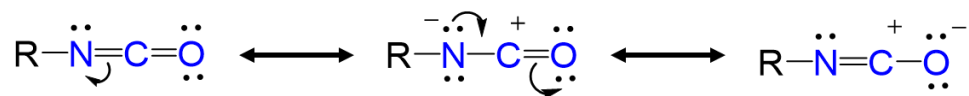
Scheme 1.2. Resonance structures of the isocyanate group.
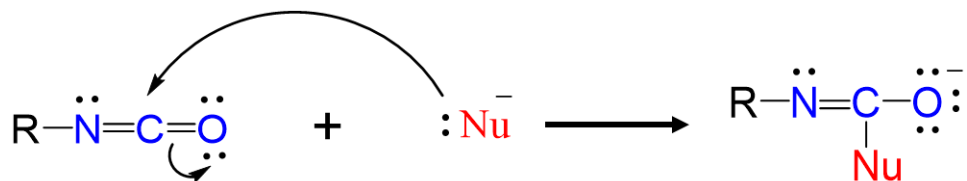
Scheme 1.3. Nucleophilic attack on the isocyanate group.

Thus, the isocyanate group can react with several functional groups like alcohols, amines, water, etc. Based on the groups attached on the nitrogen, the reactivity of the isocyanate group can be tuned. Generally, aromatic isocyanates are more reactive than aliphatic isocyanates. Several organic aerogels can be made using isocyanates. In this thesis, an aliphatic isocyanate (N3300A) has been used to synthesize polyurethane aerogel foams (Paper-I),[51] an aromatic triisocyanate (TIPM) has been used to crosslink cobaltia gel suspensions to form polyurea-crosslinked cobaltia xerogel powders, which were further processed to pure metallic Co(0) aerogels (Paper-II).[20] Finally, TIPM was used to crosslink silica gel suspension to form polyurea-crosslinked silica xerogels, which were further processed to amorphous carbon aerogels (Paper-III).

1.2.1. Reaction of Isocyanate with Amines. Formation of a urea linkage takes place if the nucleophilic nitrogen of the amino group attacks the electrophilic carbonyl

carbon of the isocyanate group, as shown in Scheme 1.4. This reaction is exothermic and occurs extremely fast.
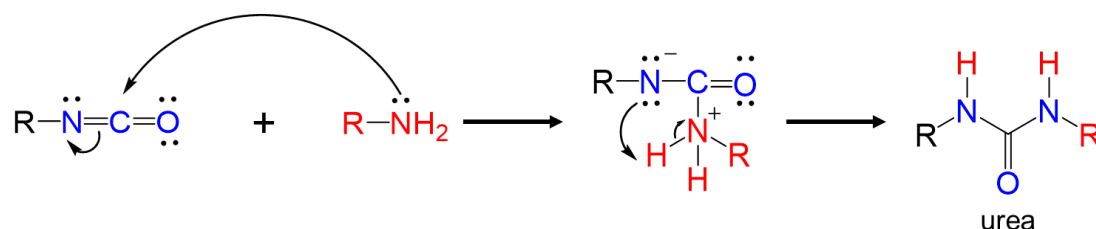
Scheme 1.4. Reaction of isocyanate with amine to form urea.

1.2.2. Reaction of Isocyanate with Water. Formation of a urea linkage can also be carried out by reaction of isocyanate with water via formation of unstable carbamic acid, which further decomposes to carbon dioxide and amine. This in-situ generated amine (Scheme 1.5) further reacts with the unreacted isocyanate to form a urea. This reaction is generally catalyzed by small quantities of amines like triethylamine.
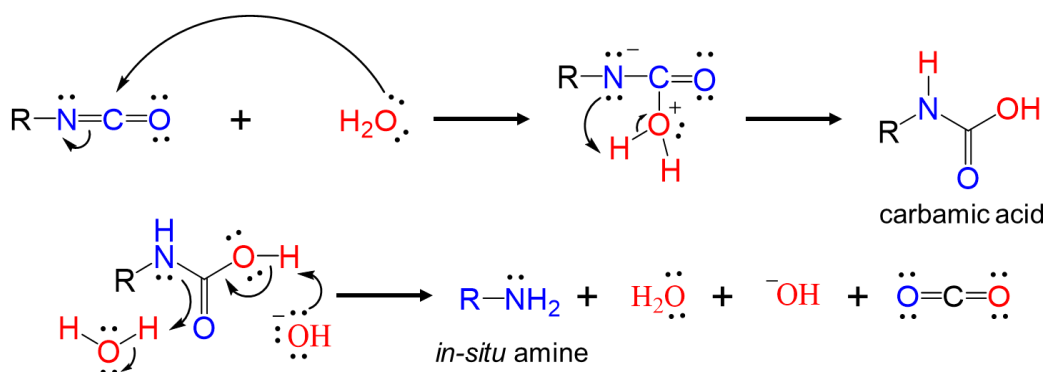
Scheme 1.5. Reaction of isocyanate with water to form amine.

1.2.3. Reaction of Isocyanate with Alcohol. Formation of a urethane linkage is usually carried out by the reaction of isocyanate and alcohol in the presence of a catalyst such as dibutyltin dilaurate (DBTDL) or metal salts like $CuCl_2$, Cu_2Cl_2, $CoCl_2$, $FeCl_3$, as shown in Scheme 1.6.
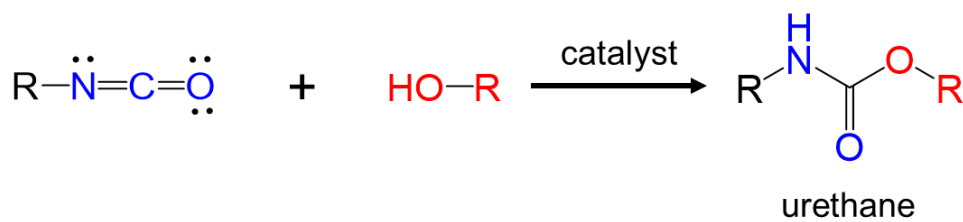
Scheme 1.6. Reaction of isocyanate with alcohol to form urethane.

1.3. AEROGELS-VIA-XEROGELS

As previously discussed, traditionally wet-gels are dried using SCF CO_2 to obtain aerogels. The SCF drying step is time-, energy-, and materials-consuming, which has hampered large scale commercialization of aerogels. However, if the wet-gels are dried by simple evaporation of solvent at room or higher temperature, under ambient pressure, the skeletal framework collapses by exerting pressure on the pore walls due to the surface tension of the liquid. This leads to an extensive shrinkage as compared to the wet-gel volume (up to 30% of initial volume) and maximum number of pores collapses, thus resulting in *Xerogels*.[36,52] According to IUPAC, a xerogel is "an open network formed by the removal of all swelling agents from a gel".[53] *Xerogels* were first introduced by Freundlich to designate shrinking or swelling of the gels.[54] Figure 1.2 shows a general schematic flow chart for preparation of a wet-gel via a sol-gel method, and further drying

of the wet-gel by two different methods to give either an *aerogel* or a *xerogel*, specifying

the important properties of these two materials. The images within show a typical silica

aerogel and a *xerogel*.
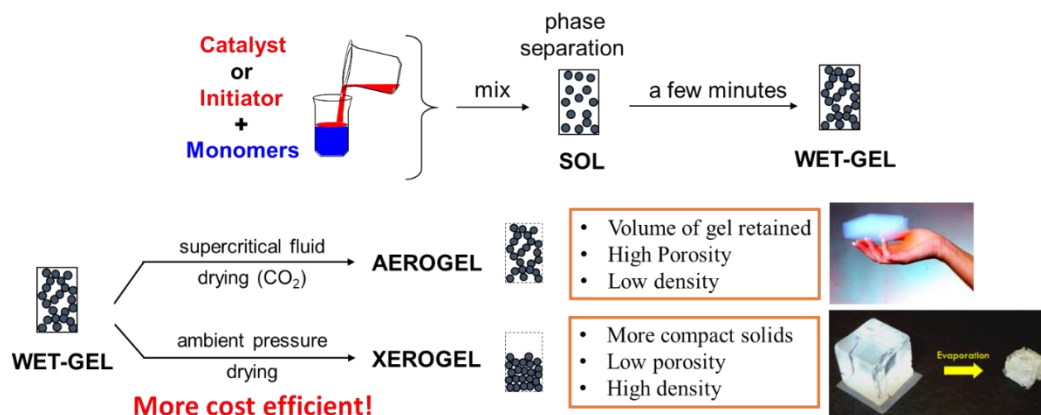
Figure 1.2. Preparation of wet-gel by sol-gel method and further drying to get a*erogel* and *xerogel*.

Making *aerogels-via-xerogels* by bypassing the SCF CO$_2$ drying offers an excellent

solution, which has been demonstrated previously in the synthesis of porous ceramic

aerogels (SiC and Si$_3$N$_4$)[21] and in this dissertation, by making porous materials like:

polyurethane aerogel foams (Paper-I),[51] monolithic pure metallic Co(0) aerogels (Paper-

II),[20] amorphous carbon aerogels (Paper-III) and graphitic carbon aerogels (Paper-IV).

For the synthesis of polyurethane aerogel foams, the gelation solvent (acetonitrile-

acetone mixture) in the final aged wet-gel was replaced with low-boiling point non-solvent

pentane (b.p. = 36 °C), thus avoiding the use of SCF CO$_2$. For the synthesis of metallic

Co(0) aerogels, polyurea-crosslinked cobaltia xerogel powders (X-CoOx) were made by

crosslinking the cobaltia (CoOx) sol-gel suspension with an aromatic triisocyanate (tris(4-

isocyanatophenyl)methane (TIPM). Since cobaltia sol resists gelation and takes very long

time (about 10 days)[55] to form a gel, long gelation times have also been observed for other

metal oxides,[56] this method of *aerogels-via-xerogels* is very advantageous to get monolithic, sturdy, pure metallic Co(0) aerogels. For polyurea-crosslinked silica xerogel powders, the gelation was disrupted by vigorous mechanical stirring, using hexane as a non-solvent. The surface of silica was modified with an amine functionality by co-gelation of tetramethoxyorthosilicate (TMOS) and 3-aminopropyltriethoxysilane (APTES) in different ratios, resulting in surface dangling -NH$_2$ and -OH groups. More -OH groups were introduced on the surface of silica suspension by washing with water saturated ethyl acetate. These surface functionalized groups were reacted with TIPM, a triisocyanate, to give polyurea-crosslinked silica xerogel powders (PUA@silica). For polyacrylonitrile-crosslinked silica (PAN@silica) or metal oxide (PAN@FeOx or PAN@CoOx), the surface dangling -NH$_2$ groups of silica suspension were modified with an azo-based free-radical initiator to induce free-radical surface-initiated polymerization of inhibitor-free acrylonitrile monomer to give polyacrylonitrile polymer. These polymer-crosslinked inorganic oxide xerogel powders were compressed and molded to different sizes and shapes to obtain the desired aerogels. Both polyurea and polyacrylonitrile are carbonizable polymers, which were further used for carbothermal reduction.

In summary, the *aerogels-via-xerogels* method has many advantages:

(a) Time-efficient: xerogel powders have faster diffusion of solvent within the grains, thus allowing faster solvent exchange.

(b) Energy-efficient: bypasses the supercritical fluid drying.

(c) Material-efficient: reduces usage of solvents for washings.

(d) Cost-efficient: reducing the time, energy, and material consumption.

(e) Robust handling and processing: bypasses handling of fragile wet-gels, gives care-free handling of xerogel powders to obtain any size and shape aerogels.

(f) Generalizable: gelation of any system can be diverted to powders by vigorous mechanical agitation and modification of the surface functional groups for desired polymerization.

This *aerogels-via-xerogel* method can be extended to any polymeric or inorganic sol-gel system to obtain their respective aerogel foams. Different polymers can be crosslinked on silica or metal oxides to get pure metallic, amorphous and graphitic carbon aerogels.

1.4. POLYURETHANES

In 1947, Otto Bayer and his coworkers discovered polyurethane (PU) as a substitute for rubber during the beginning of World War II, by reaction of polyester diols with diisocyanates.[57–59] But soon after the commercialization of PU, polyester diols were replaced by polyether polyols due to their better handling properties, low cost, and improved hydrolytic stability. The properties of polyurethanes can be modified based on the different types of alcohol and isocyanate combinations. Generally, lower molecular weight polyols form rigid and hard polyurethanes, and higher molecular weight polyols form soft elastic polyurethanes. Due to their easily modifiable mechanical and elastic properties, polyurethanes have been used as replacements for rubbers,[58] metals, and plastics.[59] Polyurethanes are used in shoes, coatings, construction, textiles, foams, adhesives, bedding, fibers, electronic appliances, medical devices, etc.[59–64] Polyurethane foams are useful in flexible thermal insulation.[65]

Based on their common applications, polyurethanes are divided into four groups:

(a) Elastomers:[66] footwear, synthetic leather, seals, O-rings, vibration damping

(b) Rigid foams:[67] thermal insulators, construction, refrigerators

(c) Flexible foams:[47,68] bedding, cushions, textile, carpet, automotive

(d) Waterborne PU:[69] protective coatings, decorative coating, adhesives

S. S. Kistler made the first nitrocellulose-based aerogel.[37] In 2013, our group has explored different types of polyurethane aerogels for controlling flexibility, nanomorphology, particle size and mechanical properties, by modifying the structure of isocyanates (aliphatic and aromatic triisocyanate) and polyols (aromatic diols and triols).[70] Subsequently, in 2017, we explored mechanical energy storage as shape-memory panels and biomimetic devices via poly(isocyanurate-urethane) aerogels.[47] In 2019, we showed the combined effect of polyurethane aerogels with cyclodextrins for high water adsorption.[46] In this thesis Paper-I, we have studied the properties of poly(isocyanurate-urethane) aerogel foams made using compressed air and dried under ambient conditions, to give better thermal conductivity and oil retention.[51]

1.5. FREE-RADICAL SURFACE-INITIATED POLYMERIZATION

Free-radical initiators are molecules which can produce radical species under mild conditions and promote radical reactions.[71] These molecules generally have weak bonds that have small bond dissociation energies. Free-radical initiators like organic or inorganic peroxides, azo compounds, nitrogen-halogen bonds, etc. are used in free-radical polymerization reactions.[72] When these free-radical initiators are modified and bounded to the surface of some suspensions, then those suspensions can participate in free-radical

surface-initiator polymerization.[22,44,73] Many literature explain the importance of free-radical initiators bounded to surfaces by a wide range of interactions such as ionic bonding, covalent bonding, etc. But the most practical examples concern asymmetric peroxides and azobisisobutyronitrile (AIBN) derived free-radical initiators.[45,74] The new generation of polymer brushes by free-radical surface-initiated polymerization has become a powerful approach to tailor the chemical and physical properties of interfaces and has given rise to great advances in surface and interface engineering.[75] Polymer brushes are defined as thin polymer films in which the individual polymer chains are tethered by one chain end to a solid interface.

In 2008, our group reported a facile synthesis of a new surface-confined bidentate free-radical initiator synthesized at 197 K using 4,4′-azobis(4-cyanovaleric acid) (ABCVA), 3-aminopropyltriethoxysilane (APTES) and tetramethoxyorthosilicate (TMOS), which was used to initiate free-radical surface-initiated polymerization to yield polymethylmethacrylate, polystyrene, and polydivinylbenzene aerogels.[44] Furthermore, in 2010, the same free-radical initiator was used to initiate polymerization of acrylonitrile monomer to obtain polyacrylonitrile-coated 3D silica aerogels, which after aromatization at 300 °C and carbonization at 1200-1600 °C gave SiC aerogels.[22]

In Paper-III, a similar bidentate azo-based free-radical silica initiator salt is synthesized at room temperature using ABCVA and APTES in anhydrous tetrahydrofuran (THF). While in Paper-IV, a different type of bidentate azo-based free-radical initiator was synthesized, but without any silica counter-part, using ABCVA, ethyl chloroformate and triethylamine in anhydrous THF.

Polymerization of Acrylonitrile to Polyacrylonitrile - Polymerization of acrylonitrile is usually carried out using a free-radical initiator in a non-interfering solvent (like toluene), as shown in Scheme 1.7.
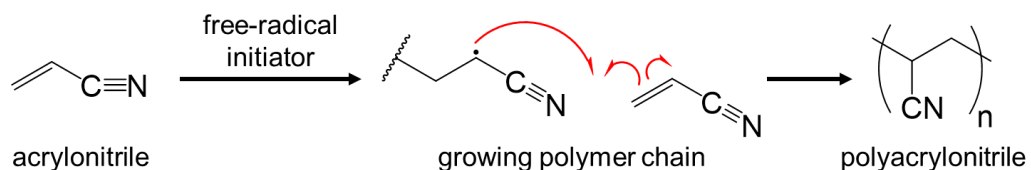
Scheme 1.7. Reaction of acrylonitrile with a free-radical initiator to form polyacrylonitrile.

1.6. CARBON AEROGELS

Carbon aerogels are well known materials for their low density, high porosity, high surface areas, and high electrical conductivity, thus becoming attractive candidates for many applications.[76] They are produced from pyrolysis of carbonizable polymeric aerogels, which in turn are prepared with typical sol-gel chemistry.[77] Carbonization is heating organic materials at temperatures between 600-1000 ℃ in an inert environment (pyrolysis).[78] Pyrolysis of an organic polymeric aerogel gives rise to monolithic porous carbon aerogels. The first carbon aerogels were reported by Pekala and were based on pyrolysis of phenolic-type of organic aerogels from condensation of resorcinol and formaldehyde.[79]

1.6.1. Amorphous Carbon Aerogels. Hard carbons, also known as non-graphitizing carbons are carbon-based materials which cannot be graphitized at any temperature.[80–82] Rosalind Franklin first identified both soft and hard carbons in 1951.[83] Polymers that can be hard carbons are sucrose, polyvinylidene chloride (PVDC), coke, etc. Applications of amorphous carbon aerogels include gas adsorption,[9] gas separation,[84] water

purification,[85] hydrogen storage,[86,87] catalyst supports,[88] electrodes for fuel cells,[89] battery electrodes,[80,90,91] and materials for supercapacitors.[33] The high porosity and surface area of carbon aerogels come from both the innate porosity of the parent polymeric aerogels, and the chemical transformation (decomposition) of the skeletal framework during pyrolysis.[92]

1.6.2. Graphitic Carbon Aerogels. Graphite, the most thermodynamically stable allotrope of carbon has attracted attention due to its excellent physicochemical properties.[93–95] Porous carbon materials with graphitic framework, easily accessible nanopores, and tunable surface areas found applications as electrode materials,[96,97] in energy storage,[98] catalysis,[99,100] super lubrication,[101,102] and water purification,[103] due to their thermal and chemical stability.[104,105] Graphite is obtained naturally from graphite mines by a multistep separation process with extensive purification.[106] The separation process of natural graphite to produce battery-grade graphite is time-consuming and environmentally unfriendly with high mass loss.[93] Since natural graphite is a non-renewable resource, different synthetic methodologies are used to produce high-quality graphite for desired applications. Soft carbons, also known as graphitizing carbons, are carbon-based materials which can be graphitized at high temperatures (2500-3300 $^{\circ}$C). Polymers that can be soft carbons are petroleum coke, polyvinylchloride (PVC), polyacrylonitrile, aromatic polyurea, etc. In this regard, three main strategies are used for obtaining porous graphitic carbons, which include: (a) high temperature chemical vapor deposition (CVD),[107] (b) high temperature and/or high-pressure treatment of carbon precursors,[108–110] and (c) catalytic graphitization.[111] However, it is very challenging to retain porous structure of final graphitic carbons due to the extremely high graphitization temperature.

Resorcinol formaldehyde (RF) aerogels are most commonly transformed into carbon aerogels, and subsequently into graphitic carbon aerogels at high temperatures.[112] Although the "gel" is no longer apparent in the carbon material, the resulting monolithic materials are still considered gels.

1.7. GAS ADSORPTION AND CO_2 CAPTURE

Greenhouse gases such as carbon dioxide (CO_2), methane (CH_4), nitrogen oxides (NO_x), carbon monoxide (CO), hydrocarbons, sulfur dioxide (SO_2), etc., are constantly being emitted every day from industries, factories, vehicles and have endangered human's survival, food sources, and nature by introducing them freely in the atmosphere, resulting in a global climate change.[113–115] Currently, fossil fuels supply more than 86% of energy for industry, and their use has led to the increase in the concentration of greenhouse gases. According to the EPA report on 2021, the total greenhouse gas emissions were 80% CO_2, 10% CH_4, 7% nitrous oxide, and 3% fluorinated gases.[116] The atmospheric CO_2 concentration has increased from the pre-industrial value of 280 ppm to nearly 410 ppm in 2021, and CH_4 has also doubled in value.[117,118] Thus, development of renewable and clean energy sources has sky-rocketed across the world in 2021. Alternatively, CO_2 capture has been considered as a great solution to this issue. Generally, there are three viable techniques currently used at large-scale:[119–121]

(a) pre-combustion capture: CO_2 is captured from CH_4 or H_2 at 40 ^{o}C and high pressure (40 bar).

(b) post-combustion capture: CO_2 is captured from flue gas with excess N_2 at 40-80 ^{o}C and ambient pressure.

(c) oxyfuel combustion: fuel is burnt in the absence of N_2 to give only CO_2 and water.

1.8. MOTIVATION AND SCOPE OF THE PRESENT WORK

From many decades mankind has been trying to understand nature and develop different materials for the betterment of civilization and personal growth. Now-a-days, a wide variety of materials are being researched, developed, and applied in commercial applications. Amongst them aerogels are extensively developed and being used commercially in a variety of applications as thermal insulating blankets, battery materials, supercapacitors, greenhouse gas absorbers, radiation detectors, purification systems, specialty chemicals, etc. The unique properties of aerogels would broaden their applications even more in the coming years and increase the market demand for more developed and streamlined manufacturing processes. In this thesis, efficient syntheses of aerogels have been accomplished and specific applications of these materials have been demonstrated.

1.8.1. Polyurethane Aerogel Foams. Solid foams are an important class of porous materials formed by pockets of gas trapped in a solid matrix, often again characterized by low bulk densities and high macroporosity. Foaming is an important industrial process, which typically provides lighter and more cost-effective materials than in their nonfoam state.[122] Existing manufacturing techniques utilize chemical foaming agents and methods involving aerogel synthesis within the macropores of prefabricated polymer templates, resulting in procedures not suitable for industrial scale. These procedures can involve large

amounts of sacrificial chemicals and therefore are expensive.[123–125] Thus, an efficient method for polymeric aerogel foams synthesis was much needed as shown in Paper-I.

Our approach of an aerogel foaming process merges the "open" porosity of an aerogel with the "closed" porosity of foams creating a novel multiscale, random, yet hierarchical open-pore structure, in which larger voids (pores) are interconnected in all directions (3D) by the innate aerogel pores. Our method for the synthesis of aerogel foams without the use of chemical agents or templates, involves gelation under pressurized air (7 bar) injection into a specially designed mold. High pressure induces air dissolution into the sol, which generates bubbles and creates a foam-like structure during depressurization. Our procedure does not alter the chemical composition of the aerogel, so it could potentially be used for a variety of different aerogel types and formulations. Therefore, without loss of generality, the method is demonstrated here with a special type of a poly(isocyanurate-urethane) aerogel (PIR-PUR). The newly synthesized aerogel foams were characterized and gave better properties than their regular aerogel counterparts in terms of bulk density, porosity, thermal conductivity, and oil absorption.

1.8.2. Pure Metallic Aerogels. Noble metal (Au, Pd, Pt) aerogels via a direct solution-based reduction have been reported in 2018 by Burpo *et. al.*[126] Fast reduction of these noble metal salts was carried out using dimethylamine borane (DMAB) and sodium borohydride, resulting in a gel above a critical concentration. These gels were freeze-dried to aerogels, have high surface area, conductivity and capacitance, and are useful for energy storage, catalysis and sensors applications. In 2014, our group demonstrated the synthesis of pure metallic iron aerogels via carbothermal reduction of polymer-crosslinked iron oxide aerogels.[17] Different types of polymers like resorcinol-formaldehyde and polybenzoxazine

were used for crosslinking, and further pyrolysis under inert atmosphere gave porous iron monoliths. These iron aerogels were further demonstrated as thermites.[18] However, these aerogels were dried using SCF CO_2 and are extremely fragile.

An efficient *aerogels-via-xerogels* method for pure metallic aerogels is shown in Paper-II. As mentioned in Section 1.1.2., our approach for the synthesis of pure metallic cobalt aerogels was carried out via carbothermal reduction of polyurea-crosslinked cobaltia xerogel powder compacts under inert atmosphere. The cobalt sol-gel system was specifically chosen because it resists or takes very long time to form a gel and thus a route via xerogel powders is beneficial for such a system. Final pure metallic Co(0) aerogels were about 70% v/v porous. Further application of these Co(0) aerogels as thermites was demonstrated by filling the aerogels' pores with lithium perchlorate ($LiClO_4$) and igniting them with the help of a nichrome wire. Temperatures above 1500 ºC were reached by the thermite reaction.

1.8.3. Porous Amorphous Carbon Aerogels. As mentioned in Section 1.5.1., amorphous carbon aerogels are excellent materials for many applications. On the downside, the use of SCF CO_2 drying during the synthesis of carbon aerogels is a high-pressure, and energy-intensive process. When it comes to preparation of monolithic carbon aerogels with a pre-determined form factor, molding and handling of potentially fragile polymeric wet-gels and aerogel precursors might lower the yield. Furthermore, the size of the monoliths is limited by the size of the pressure vessel. Thus, exploring an efficient method for the synthesis of amorphous carbon aerogels was much needed, and it is shown in Paper-III.

Our approach for the synthesis of amorphous carbon aerogels avoids supercritical fluid drying and is capable of furnishing monoliths in various sizes and shapes from compressing compacts of polymer-crosslinked silica xerogel powders. Furthermore, pyrolytic carbonization of these polymeric xerogel compacts was carried out. Overall, the porosity of these carbon aerogels was created by (a) decomposition of the carbonizable polymer to carbon; and (b) reactive removal of the silica network using hydrofluoric acid (HF). Using silica as a removable template, we proposed an etching model to achieve desired BET surface area and control the micro- and meso-porosities in the final aerogels. Additional porosity was created by using reactive etching (with CO_2) of the resulting carbon aerogels.

1.8.4. Porous Graphitic Carbon Aerogels. As mentioned in Section 1.5.2., graphitic carbon aerogels are attractive candidates for various applications. However, there are several synthetic challenges, as mentioned in Section 1.8.2.

In order to avoid high graphitization temperatures, the graphitization process is carried out in the presence of various catalysts such as Fe, Co, Mn, and Ni. Although the presence of a catalyst reduces graphitization temperatures, the desired porosity is difficult to obtain in the final graphitic carbons without the use of hard or soft templates. On the other hand, carbon aerogels are microporous carbons with excellent porosity and wide pore size distribution. Thus, exploring an efficient method for the synthesis of graphitic carbon aerogels was much needed.

In Paper-IV, we report *aerogels-via-xerogels* method for the synthesis of graphitic carbon aerogels derived from metal oxide xerogels crosslinked with a carbonizable polyacrylonitrile (PAN). Xerogels can be obtained in the form of powders which are easy

to handle by diverting the gelation of polymeric precursor by vigorous mechanical stirring. The drying and washing of xerogel powders is extremely quick due to easy transfer of solvent along the grains of xerogel powders making the process time efficient. In turn, the metal oxide (MOx) network was obtained by gelation of metal chloride hydrates ($FeCl_3.6H_2O$ and $CoCl_2.6H_2O$) and subsequent modification with a free-radical initiator. These xerogel powders were compressed into compacts with a hydraulic press, aromatized at 300 ℃ under O_2 and were pyrolytically graphitized at different temperatures from 800 ℃ to 1500 ℃ under ultrahigh purity argon into graphitic compacts. These compacts were further etched with aqua-regia at room temperature to produce porous graphitic carbon aerogels. High quality graphitic carbon aerogels with porosities in the range of 63-78% and 99.8% w/w graphitic carbon were obtained with this method.

PAPER

I. SYNTHESIS OF AEROGEL FOAMS THROUGH A PRESSURIZED SOL-GEL METHOD

Sadeq Malakooti[a], Ethan Zhao[a,b,1], Nicholas Tsao[a,c,1], Ning Bian[a], Rushi U. Soni[d], ABM Shaheen ud Doulah[d], Chariklia Sotiriou-Leventis[d,*], Nicholas Leventis[e,*] and Hongbing Lu[a,*]

[a] Department of Mechanical Engineering, The University of Texas at Dallas, Richardson, TX 75080, U.S.A. [b] Allen High School, Allen, TX 75002, U.S.A. [c] St. Mark's School of Texas, Dallas, TX 75230, U.S.A. [d] Department of Chemistry, Missouri University of Science and Technology, Rolla, MO 65409, U.S.A. [e] Aspen Aerogels, Inc., 30 Forbes Road , Bldg B, Northborough, MA 01532, U.S.A. [1] High school summer researcher.

[*]Corresponding authors: E-mail: hongbing.lu@utdallas.edu; leventis@mst.edu; cslevent@mst.edu

ABSTRACT

We report monolithic aerogel foams as solid materials with hierarchical porosity created by a foam-like structure embedded in the skeletal framework of a regular aerogel. The foam-like structure is prepared without chemical foaming agents or templates, resulting in a less expensive, more efficient, and more readily adaptable process. Specifically, pressurized air (7 bar) is injected into a suitable sol, which is allowed to gel under pressure, followed by slow depressurization. Voids are created from the air bubbles formed during depressurization. The model material used for validation of the technique is based on poly(isocyanurate-urethane) aerogels (PIR-PUR) and selected material properties of the resulted aerogel foams are compared with those of their pristine aerogel counterparts. With an eye on scalability, all wet-gels were dried under ambient conditions.

Aerogel foams exhibit lower bulk densities by about 25%, and higher porosities by about 10% in comparison with their pristine PIR- PUR aerogel counterparts. Interestingly, the thermal conductivities of aerogel foams were found reduced significantly (by 25%) from 0.104 to 0.077 $Wm^{-1}K^{-1}$ compared to the corresponding pristine aerogels. In addition, aerogel foams absorb 36% w/w more oil and show better oil retention in comparison with regular PIR- PUR aerogel samples made from the same sols. As this technique does not alter the chemical composition of the aerogel, it is anticipated that it can be used for a variety of different types of aerogels and formulations in order to lower their bulk density and improve desired physical properties such as thermal conductivity.

Keywords: aerogels, foams, porous materials, pressurized sol-gel, polyurethane

TOC Graphic
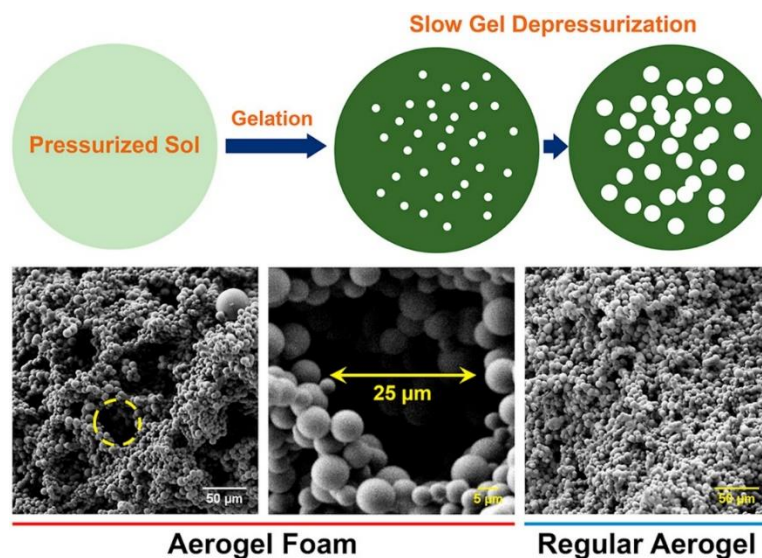
1. INTRODUCTION

Aerogels are a class of porous materials characterized by their low bulk density, high open porosity and high specific surface area [1]. They are typically synthesized through a sol-gel process at atmospheric pressure followed by drying of the resulting wet-gels with a supercritical fluid (SCF), most commonly CO_2 [1,2]. On the other hand, solid foams are a different class of porous materials formed by pockets of gas trapped in a solid matrix, often again characterized by low bulk densities and high macroporosity [3]. Foaming is an important industrial process, which typically provides lighter and more cost-effective materials than in their nonfoam state [4]. The result of an aerogel foaming process, which we refer to as an "aerogel foam," merges the open porosity of an aerogel with the "closed" porosity of foams creating a novel multiscale, random, yet hierarchical open-pore structure, in which larger voids (pores) are interconnected in all directions (3D) by the innate aerogel pores. Existing manufacturing techniques utilize chemical foaming agents and methods involving aerogel synthesis within the macropores of prefabricated polymer templates, resulting in extremely specific procedures not suitable for the industrial scale [5–7]. These procedures can involve large amounts of sacrificial chemicals and therefore are expensive [6,8].

Our approach for the synthesis of aerogel foams without the use of chemical agents or templates involves gelation under high pressure through air injection into a specially designed mold. High pressure in-duces air dissolution into the sol, which generates bubbles and creates a foam-like structure during depressurization. Our procedure does not alter the chemical composition of the aerogel, so it could potentially be used for a variety of different

aerogel types and formulations. Therefore, without loss of generality, the method is demonstrated here with a special type of a poly(isocyanurate-urethane) aerogel (PIR-PUR) [9,10]. The newly synthesized aerogel foams were characterized in terms of bulk density, porosity, thermal conductivity and oil absorption capabilities in comparison with their regular aerogel counterparts prepared from the same sol under atmospheric pressure.

Our approach for the synthesis of aerogel foams without the use of chemical agents or templates involves gelation under high pressure through air injection into a specially designed mold. High pressure induces air dissolution into the sol, which generates bubbles and creates a foam-like structure during depressurization. Our procedure does not alter the chemical composition of the aerogel, so it could potentially be used for a variety of different aerogel types and formulations. Therefore, without loss of generality, the method is demonstrated here with a special type of a poly(isocyanurate-urethane) aerogel (PIR-PUR) [9,10]. The newly synthesized aerogel foams were characterized in terms of bulk density, porosity, thermal conductivity and oil absorption capabilities in comparison with their regular aerogel counterparts prepared from the same sol under atmospheric pressure.

2. RESULTS AND DISCUSSION

2.1. PRESSURIZED SOL-GEL SYNTHESIS OF PIR-PUR AEROGEL FOAMS

The sol formulation (Figure 1a) was adopted from Donthula et al. [10]. An aliphatic triisocyanate (Desmodur N3300A) and ethylene glycol (EG) were separately dissolved in anhydrous acetone and acetonitrile (the exact ratios are listed in Table S1 of the Supporting Information). A schematic of the pressure vessel and the synthetic protocol are shown in

Figure 1b and c, respectively. A photograph of the pressure mold is shown in Figure S2 of the Supporting Information. The two solutions were combined and stirred for 5 min at room temperature. Next, the correct amount of catalyst (dibutyltin dilaurate; DBTDL, see Table S1 in Supporting Information) was added, and the resulting sol was stirred for an additional 5 min. Subsequently, the sol was poured into the gelation vessel, which was then pressurized with air to 7 bar, and it was allowed to gel and age for 2 h at room temperature. A portion of the same sol (5 mL) was set aside in an unpressurized clear syringe for comparison. Both kinds of gels were post-processed in the same way. After aging, the high-pressure ball valve (see Figure 1b) was loosened and tightened repeatedly to allow the vessel to gradually depressurize in stages. The sample was allowed to equilibrate for several minutes during each depressurization step. The total depressurization process lasted for approximately 45 min, and finally the gel was removed from the mold into an acetone-acetonitrile mixture. The gelation solvent was exchanged one more time with acetone, then with acetonitrile and finally with pentane for a period of 8 h in each bath. Those wet-gels were dried directly from pentane at room temperature under ambient pressure. The drying process was completed by placing the samples in a convection oven at 50 °C for 2 h.

2.2. GENERAL MATERIAL AND MICROSTRUCTURAL PROPERTIES

The general material properties such as skeletal densities, bulk densities and porosities are listed in Table 1. The bulk densities were calculated from the sample dimensions and masses. The regular PIR-PUR aerogel sample (gelled under atmospheric pressure) had a bulk density of 0.345 g/cm^3. At the same monomer concentration, foamed samples had about 30% lower bulk densities, as low as 0.247 g/cm^3.
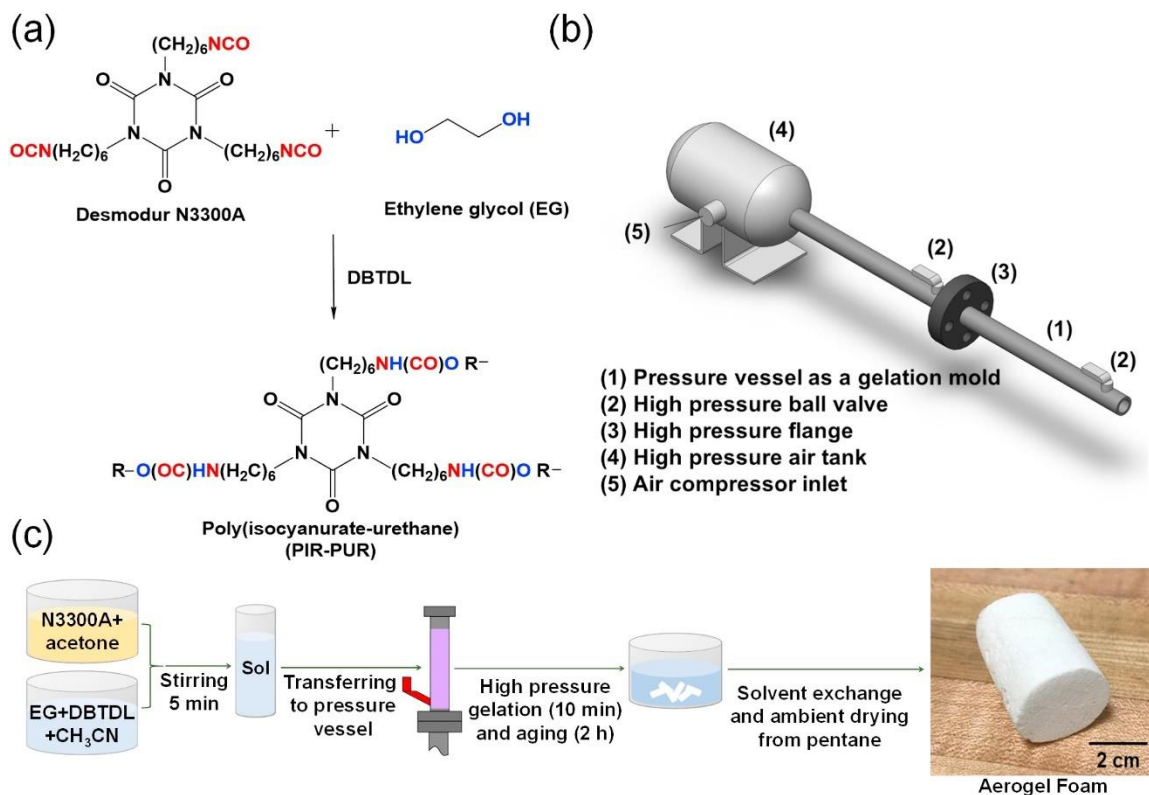
Figure 1. (a) Reaction pathway to PIR-PUR aerogels; (b) Schematic of the pressure vessel used as a mold (for a photograph see Figure S2 in Supporting Information); (c) Preparation procedure of the PIR-PUR aerogel foams.

As expected, the skeletal densities of the foamed samples were close to the skeletal density of the regular aerogel sample. Linear shrinkage was calculated by comparing the diameters of the samples with the inner diameter of the molds and it was found similar (at about 20%) between the regular and foamed samples. No significant syneresis was observed during gelation and aging. For all samples, the main shrinkage event took place during the ambient-pressure drying process. Porosities were calculated using the bulk and skeletal densities. Following the trend in bulk densities, the pressurized sol-gel approach increased the porosity by approximately 10%.

It is noted that the materials we describe fall between aerogels and xerogels: they have been prepared by ambient pressure drying, therefore they might not be considered as aerogels, but they have not been dried from the gelation solvent either, and therefore they may not be considered as xerogels. A more appropriate classification would have been as "ambigels," [11]. However, based on Leventis' previous work using supercritical drying, this particular formulation has a bulk density 0.32 g/cm^3. As the bulk density and porosity of the materials of this study are close to the values of their supercritically-dried counterpart (only about 6% higher), we have opted to refer to them as "aerogels" and "aerogel foams." It should also be noted that our aerogel foams have even lower bulk densities than their supercritical dried counterpart.

The morphology of the foamed samples was studied using scanning electron microscopy (SEM, Figure 2 and Figure S1 in the Supporting Information). It is immediately apparent that the skeletal particle size of the regular aerogel and the aerogel foam were approximately equal, and therefore it was concluded that the mechanism of particle formation (phase separation of liquid oligomers, followed by spherodization and solidification [12,13]) was not affected by the sol pressurization. Quantitatively, several random particles were selected from the SEM images and the particle diameters were used in order to construct the particle size distribution curves of Figure 3. The particle size distribution in the aerogel foam was slightly broadened compared to that of the regular aerogel samples. However, the average particle diameter of both types of aerogels was close to 8 μm.

Table 1. General material properties of regular PIR-PUR and aerogel foams [a].

Name	Bulk Density (ρ_b, g/cm³)	Skeletal Density (ρ_b, g/cm³)	Linear Shrinkage [b] (%)	Porosity [c] (%)
Regular Aerogel (PIR-PUR)	0.345 ± 0.009	1.215 ± 0.003	19	72
Aerogel Foam (PIR-PUR-P-1)	0.250 ± 0.007	1.244 ± 0.003	20	80
Aerogel Foam (PIR-PUR-P-2)	0.263 ± 0.014	1.240 ± 0.003	21	79
Aerogel Foam (PIR-PUR-P-3)	0.247 ± 0.002	1.236 ± 0.002	21	80

[a] Average of three measurements.
[b] Linear Shrinkage = 100 × [(Mold diameter – Sample diameter)/Mold diameter].
[c] Porosity = 100 × [(ρ_s – ρ_b)/ρ_s].
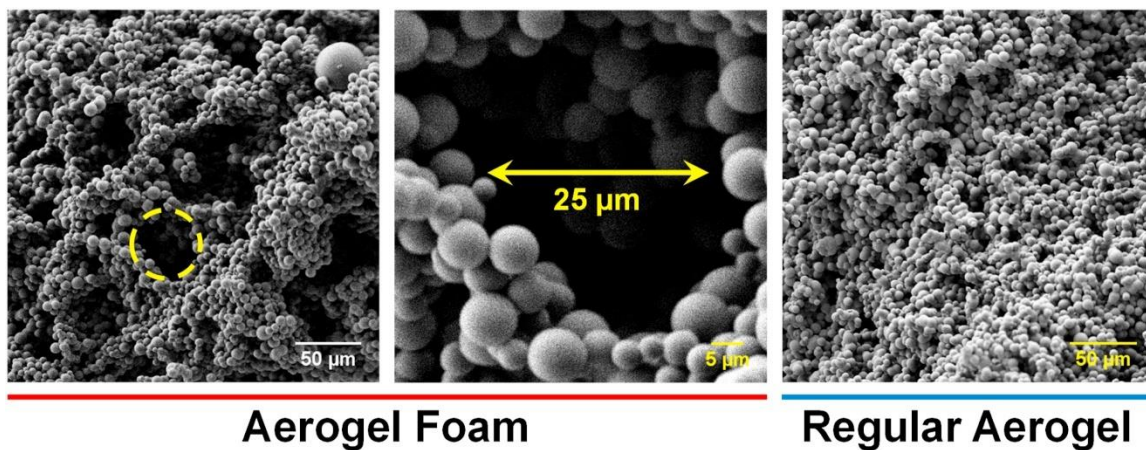
Figure 2. SEM images of an aerogel foam (PIR-PUR-P1 sample) in comparison with a regular PIR-PUR aerogel.
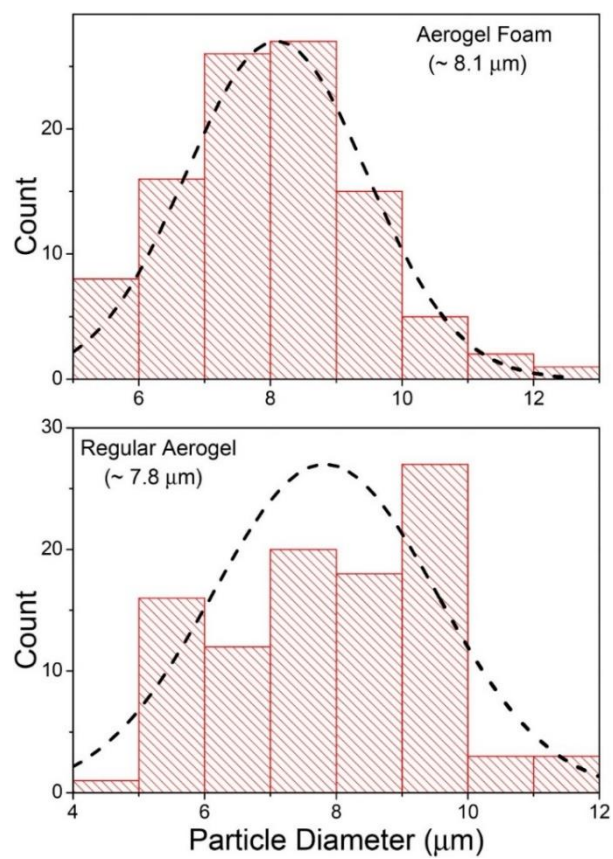
Figure 3. Particle size distribution of a regular PIR-PUR and of an aerogel foam.

The air dissolved in the sol during gelation formed bubbles during depressurization, leading to the formation of macrovoids surrounded by the pore structure of the regular aerogel. Based on Figure 2, the size of a typical macrovoid was around 25 μm. It is worth mentioning that the processes of bubble nucleation (void formation) and growth (phase separation) may both be affected by many factors including gas solubility, diffusivity, and bubble surface tension, which are also functions of the foaming temperature and pressure. However, the size of the voids depends on the pressure difference between the inside of the bubble and the surrounding medium. Therefore, either by increasing the sol internal pressure or lowering the external pressure during the depressurization stage, the size of the macrovoids can be potentially controlled. Larger macrovoids either due to supercritical drying or by increasing the pressure difference between the interior of the bubble and the surrounding medium can lead to aerogel materials with higher porosities.

SEM analysis of a material's morphology is a qualitative characterization method and in most cases the results are simply articulated verbally. A thorough quantitative analysis would require numerical image processing which is outside the scope of this report. In order to quantify the effect of the pressurized gelation on the pore morphology of aerogel foams versus that of a regular aerogel, the SEM images in Figure 2 were analyzed using the ImageJ software package (Radial Profile Plot) [14] as follows (see Figure 4): First, the integrated intensity at a given distance from a randomly selected reference point was defined by the sum of the pixel values around a circle with the reference point as its center and the given distance as its radius (see Figure 4, Inset); Subsequently, the integrated intensities were divided by the number of pixels in the circle to obtain the normalized integrated intensities. Of course, for this analysis to be valid, the SEM images

had to be captured at the same magnification, same brightness, same exposure time, etc. The normalized integrated intensities were used as indicators of the radial particle distribution as a function of the radial distance from the center point of the SEM images. According to Figure 4, there is a distinct peak in the radial profile of the regular PIR-PUR aerogels at 10–20 μm. With 8 μm average particle diameter (see above), this peak shows that aerogel particles, and therefore the porous space created in between, are distributed evenly at the vicinity of the center point of the SEM image. Since the selection of the center point was random, this assertion is valid for the entire material. This conclusion is consistent with the SEM image of the regular aerogels (Figure 2). However, this picture is no longer valid in the aerogel foams: as data of Figure 4 show, in that case we have three macrovoids around the SEM center point. Interestingly, the radial profiles of both the regular aerogel and the aerogel foam are converging as the sampling radius increases above 60 μm. However, the converging intensity value of aerogel foams is 34% lower than the corresponding value of a regular aerogel. That percent difference between the converged intensities is in the same range as the percent difference of bulk densities between regular PIR-PUR aerogel and aerogel foams. This observation suggests that the normalized integrated intensities can be used to quantify morphology related differences in nanostructured materials and we intend to explore it further.

2.3. THERMAL PROPERTIES

The thermal diffusivities, R, of a regular aerogel and aerogel foams were measured using the laser flash method as a non-contact, non-destructive, and highly accurate method [14,15]. The R values are listed in Table 2.
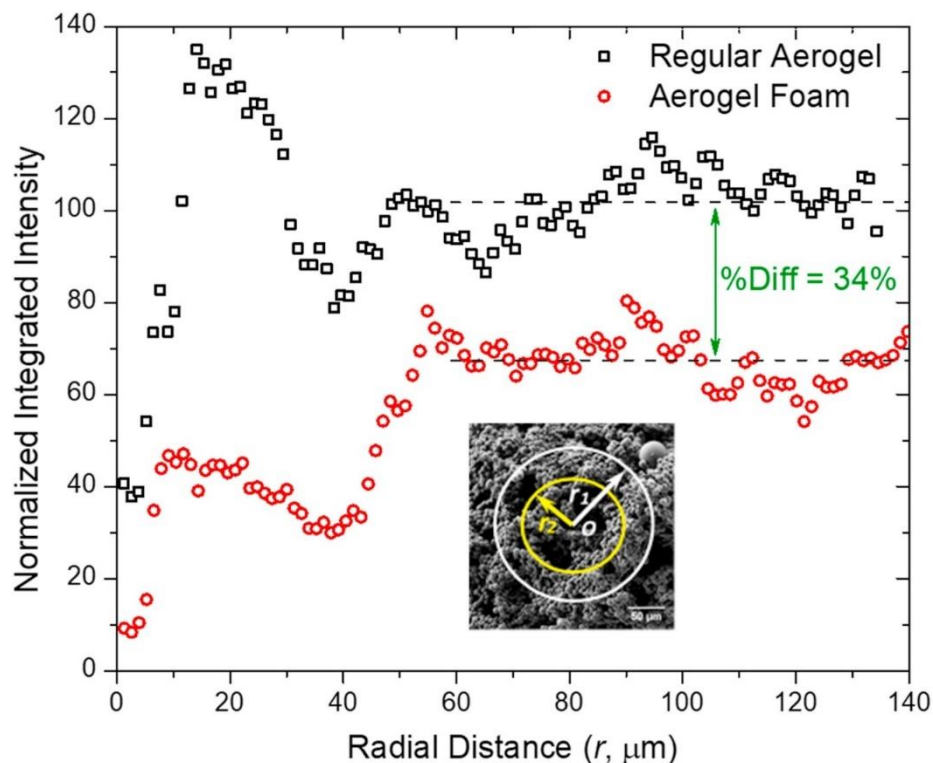
Figure 4. Normalized integrated intensities of the regular aerogel and aerogel foam (PIR-PUR-P1) as a function of the radial distance, r, from a randomly selected center point (O) in the SEM – see Inset. (Data are used to quantify the void space distribution.)

Due to the increase in porosity and the presence of new voids in the aerogel foams relative to the regular aerogel, the air thermal diffusivity is expected to be higher in aerogel foams relative to regular aerogels. However, that increase in thermal diffusivities is apparently moderated by a reduction of the amount of solid material in the skeletal framework, and as a result the thermal diffusivities of the two materials remain within error about equal to one another (Figure 5a). Thermal conductivities (k) were then calculated from the corresponding thermal diffusivities (R) using the relationship $k = R \times c_p \times \rho_b$, where c_p and ρ_b are the specific heat capacity and the bulk density, respectively. Here, the specific heat capacity was considered equal for all materials (1.711 ± 0.074 J g−1 K−1)

[12]. The thermal conductivities of the regular aerogel and aerogel foams are included in Table 2. Signifying the solid network contribution, the thermal conductivities of the aerogel foams were notably lower (by 25%) compared to the corresponding values of regular aerogels prepared with the same monomer concentration (Figure 5b). This further underlines the fact that heat transfer between pore-filling air and the PIR-PUR walls of the aerogel foam is negligible [17]. Therefore, with a significant reduction in bulk density (about 30%), the heat transfer contribution of the PIR-PUR phase is significantly reduced and subsequently the total thermal conductivity in the aerogel foams is also reduced proportionally compared to the regular aerogel.
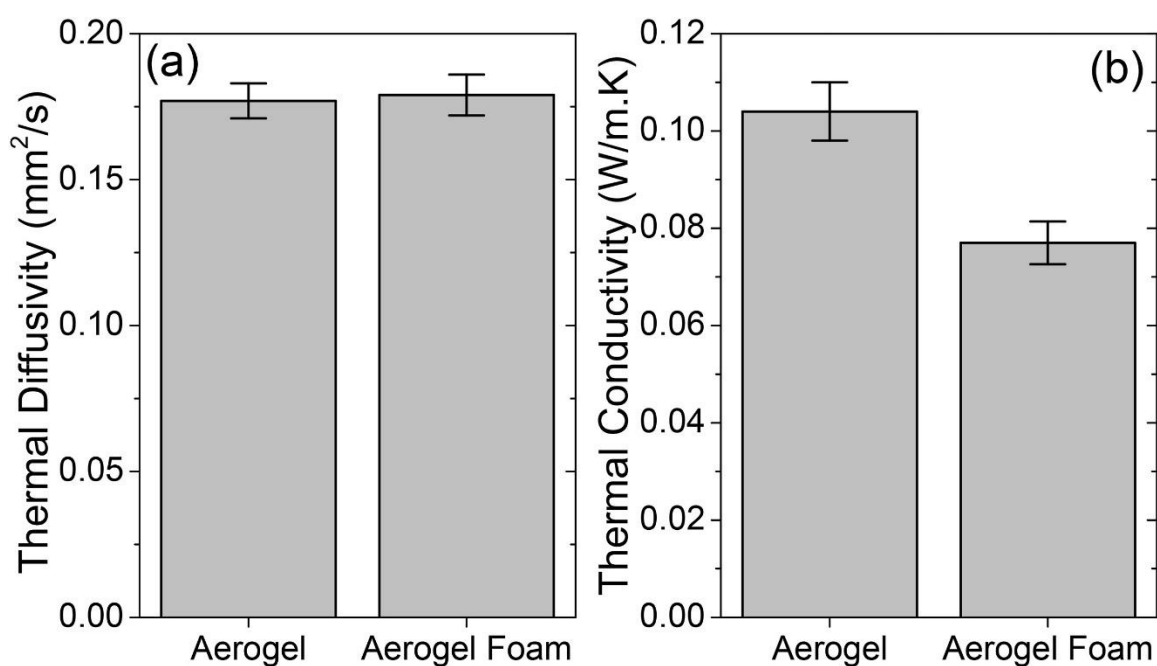
Figure 5. (a) Average thermal diffusivity and (b) average thermal conductivity of the regular PIR-PUR aerogel and of the corresponding aerogel foams at room temperature.

2.4. OIL ABSORPTION PROPERTIES

Figure 6 shows the percent mass gain of the regular aerogel and aerogel foam (PIR-PUR-P1) as a function of time when corresponding samples were submerged in engine oil (density of 0.8 g/cm^3). The aerogel foam shows a peak mass gain of 219%, which was reached in a little over 1 min. The peak mass gain for regular aerogel was 165%, which was reached at roughly the same time. Both samples maintained this peak mass gain. However, as it was expected, due to the higher porosity of aerogel foams, those samples were 36% more absorbent (29% improvement in terms of volume uptake) than the regular aerogel samples. In fact, that increase in oil absorption capacity far exceeds the increase in porosity (10%), which might be attributed to greater swelling due to lower density. It is interesting to note that aerogel foams released a minimal amount of oil during the experiments, whereas the regular aerogel sample released a significantly larger volume of oil. Thus, aerogel foams demonstrate better oil retention and absorption than regular aerogels.

Table 2. Thermal diffusivity and thermal conductivity of a regular PIR-PUR aerogel and aerogel foams at room temperature.

Name	Thermal diffusivity (mm^2 s^{-1})	Thermal conductivity (W m^{-1} K^{-1})
Regular Aerogel (PIR-PUR)	0.177 ± 0.006	0.104 ± 0.006
Aerogel Foam (PIR-PUR-P1)	0.192 ± 0.001	0.082 ± 0.010
Aerogel Foam (PIR-PUR-P2)	0.169 ± 0.011	0.076 ± 0.007
Aerogel Foam (PIR-PUR-P3)	0.175 ± 0.008	0.074 ± 0.005
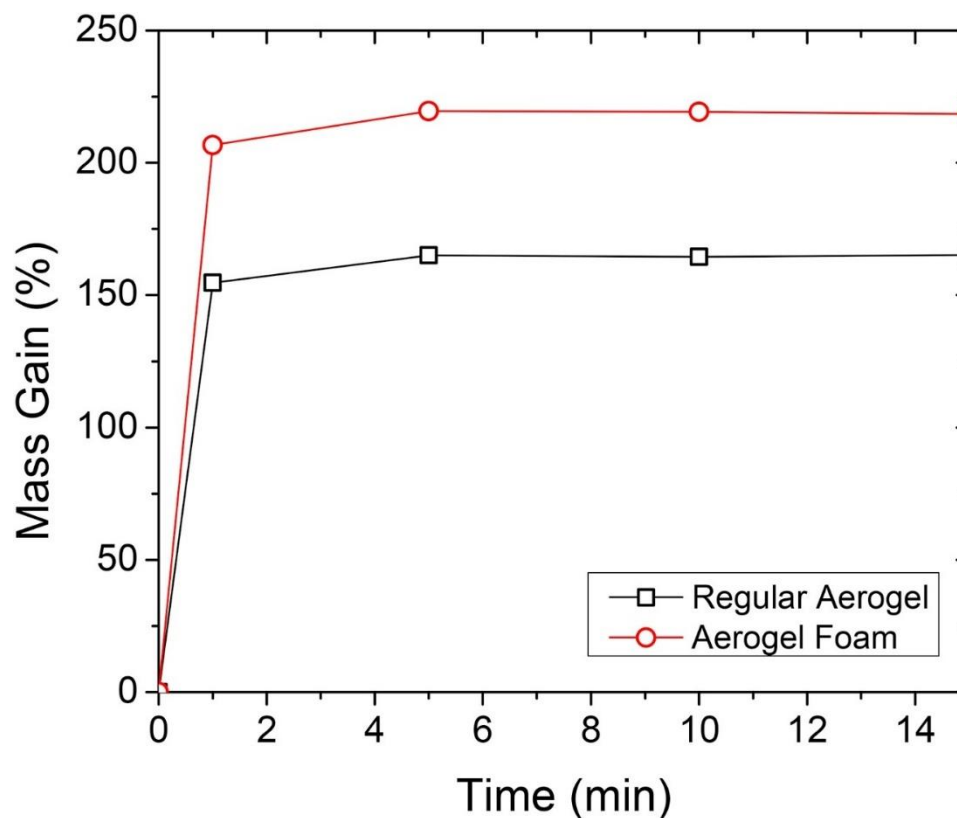
Figure 6. Percent mass gain of the regular aerogel and aerogel foam (PIR-PUR-P1) upon submerging in engine oil as a function of time.

3. CONCLUSIONS

In summary, polymeric aerogels with foam-like porosity surrounded by regular structural characteristics of the corresponding aerogels were prepared using a pressurized sol-gel approach. The procedure of injecting high-pressure air into the gelation vessel containing a proper sol is indeed an environmentally friendly and low-cost method for producing aerogel foams. Aerogel foams exhibited significantly lower bulk density, higher porosity, and lower thermal conductivity compared to their regular aerogel counterparts. Further research will be conducted to control the effects of gelation temperature and

injected air pressure. With aerogels demonstrating applications such as oil-spill cleaning, CO2 capturing, blood fractionating, air freshener release, mosquito repellant release, filter for hemodialysis, and so on, it is speculated that aerogel foams will demonstrate further quantitative improvements in all these applications.

4. EXPERIMENTAL

Materials: Acetone, acetonitrile, and ethylene glycol were obtained from Fisher Scientific (Hampton, NH). Desmodur N330A was supplied by Covestro (Pittsburgh, PA). Dibutyltin dilaurate, 95% (DBTDL) was obtained from Alfa Aesar (Haverhill, MA). Five-millimeter plastic vials were used as molds. All purchased materials were used without further processing.

Setup for gelation under pressure: A 6" threaded steel pipe was attached to a high-pressure vessel via a ball valve and a flange. The other end was closed with a steel cap. An air compressor was attached to the vessel through a pressure gauge. To reach higher pressures, a more powerful air compressor was attached to the gauge. Figure S2 in the Supporting Information shows the setup for the pressurized so-gel synthesis. The sol is poured into the steel pipe when the ball valve is closed and then sealed with the steel cap. The total volume of the gelation vessel is roughly 100 mL. A total of 90 mL sol was used to allow space for the expansion of the pressurized sample.

Synthesis: Monomeric compounds Desmodur N3300A and ethylene glycol were dissolved separately in acetone and acetonitrile (exact amounts are listed in Table S1 of the Supporting Information). The two solutions were combined and stirred for 5 min at room

temperature. Dibutyltin dilaurate catalyst was then added, and the solution was stirred for an additional 5 min. The solution was poured into the gelation vessel, where it was pressurized with an air compressor and allowed to gel and age for 2 h at room temperature. For sample removal, the cap of the gelation vessel was loosened and tightened repeatedly to allow gradual depressurization in stages. The sample was allowed to equilibrate for several minutes during each depressurization step, totaling approximately 45 min. The samples were then washed successively twice with acetone, acetonitrile, and finally pentane for a period of 8 h in each bath. Pentane-filled wet-gels were allowed to dry at room temperature and pressure for 24 h. The resulting aerogels were cured in a convection oven at 50 °C for 2 h. A 5 mL aliquot of each sol was set aside in an unpressurized clear syringe and was left for gelation. These control samples were processed in the same way as the aerogel foams.

Basic material characterization: Bulk densities (ρ_b) were determined from the weight and the physical dimensions of the samples. Skeletal densities (ρ_s) were determined with helium pycnometry using a Micromeritics AccuPyc II 1340 instrument. Samples for skeletal density measurements were outgassed for 24 h at room temperature under vacuum before analysis. Porosities (Π) as a percent of empty space were determined from the ρ_b and ρ_s values via $\Pi = 100 \times [(\rho_s - \rho_b)/\rho_s]$.

Scanning electron microscopy: SEM images were captured from Au/Pd (60/40) coated samples on a Hitachi Model S-4700 field emission microscope.

Thermal conductivity: The total thermal conductivities of all samples were calculated at 23 °C via $k = R \times c_p \times \rho_b$, as has been described recently [16]. The thermal diffusivity, R, of each sample was determined at room temperature and atmospheric

pressure with a Netzsch NanoFlash Model LFA 447 flash diffusivity instrument using disk samples (~1 cm in diameter, 2–3 mm thick) [9,18].

Oil absorption capability: Two small beakers filled with engine oil (Castrol Ltd., Liverpool, UK) were prepared. The samples were lowered into the beakers, then allowed to soak for an allotted time period. The samples were then removed from the beaker and placed in Petri dishes, where they sat to dry for 1 min. After this drying interval, the samples were squeezed, and then were placed back into the oil.

DECLARATION OF COMPETING INTEREST

ACKNOWLEDGEMENTS

SUPPORTING INFORMATION

Table S.1. Exact amounts used for the sol preparation of regular aerogel and aerogel foams (total vol. 90 mL).

Material	Volume (mL)	Mass (g)
Desmodur N3300A	10.91	12.77
Ethylene Glycol	2.12	2.48
Acetonitrile	57.72	45.36
Acetone	19.12	15.12
Dibutylin Dilaurate	0.13	0.13
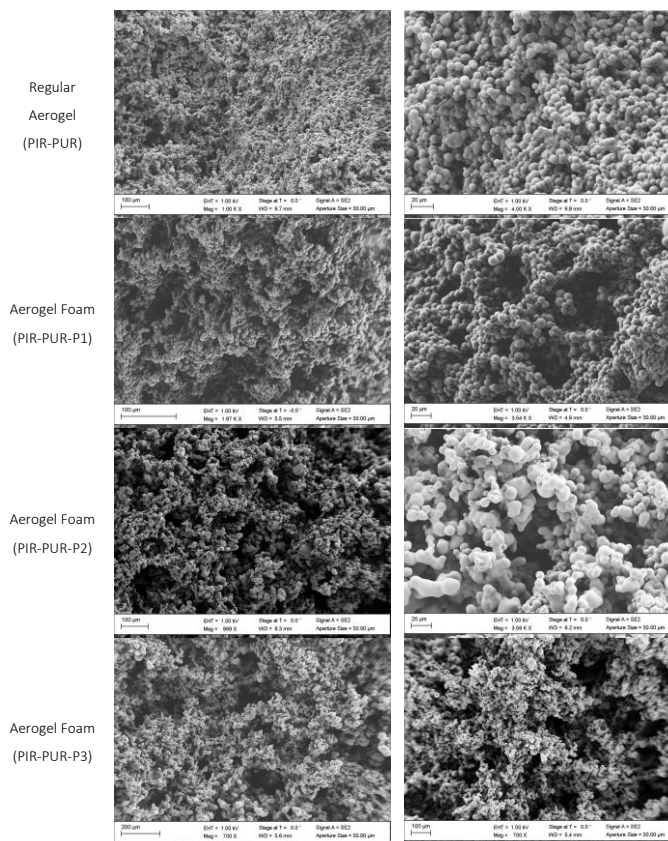
Figure S.1. The SEM images of the regular aerogel and aerogel foams at different magnifications.

(1) High pressure steel cap
(2) Pressure vessel as a gelation mold
(3) High pressure ball valve
(4) High pressure flange
(5) High pressure air tank
(6) Pressure gauge
(7) Air compressor inlet
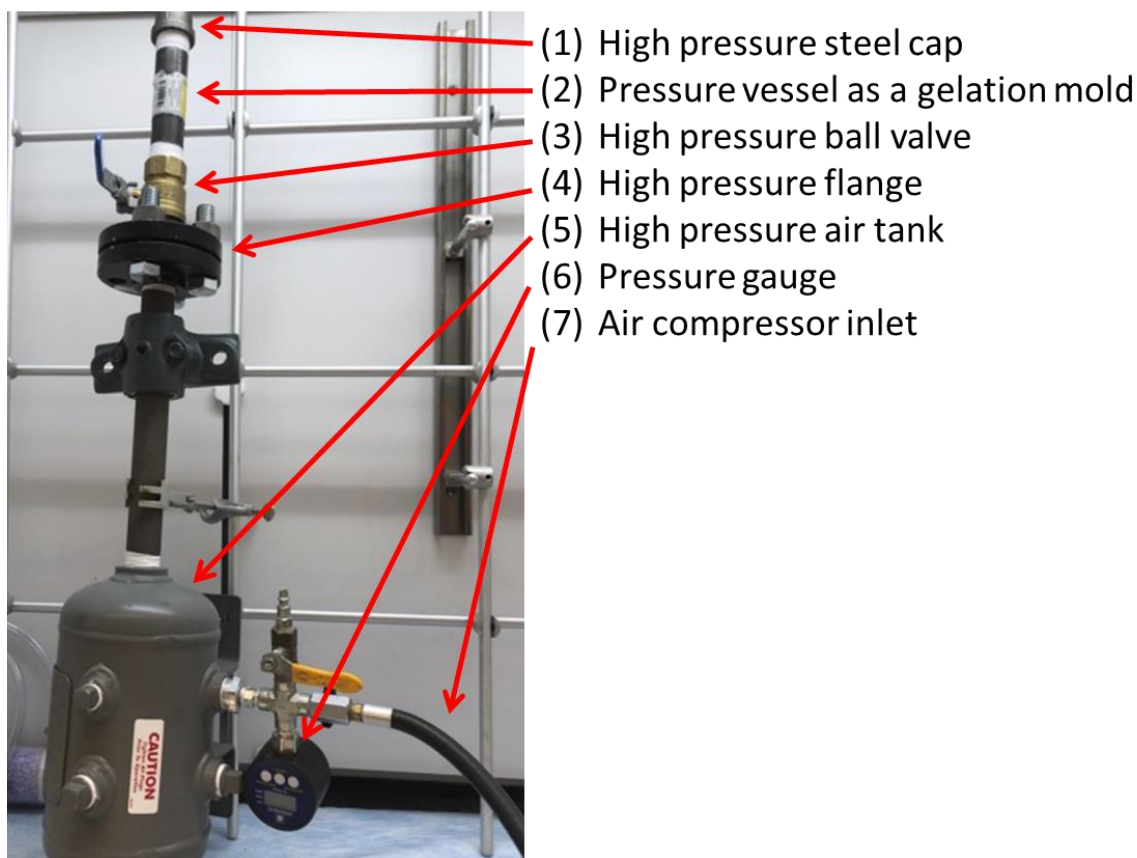
Figure S.2. Photograph of the pressurized mold for the synthesis of PIR-PUR aerogel foam.

REFERENCES

[1] A.C. Pierre, History of aerogels. Aerogels Handb., Springer, New York, NY, 2011, pp. 3–18, https://doi.org/10.1007/978-1-4419-7589-8_1.

[2] A.C. Pierre, A. Rigacci, SiO2 aerogels. Aerogels Handb., Springer New York, New York, NY, 2011, pp. 21–45, https://doi.org/10.1007/978-1-4419-7589-8_2.

[3] A.M. Kraynik, M.K. Neilsen, Elastic behavior of cellular solids. Encycl. Mater. Sci. Technol., Elsevier, 2001, pp. 2387–2389, https://doi.org/10.1016/b0-08-043152-6/00421-6.

[4] G. Wypych, Introduction. Handb. Foam. Blowing Agents, Elsevier, 2017, pp. 1–2, https://doi.org/10.1016/b978-1-895198-99-7.50003-9.

[5] N. Teo, S.C. Jana, Open cell aerogel foams via emulsion templating, Langmuir 33 (2017) 12729–12738, https://doi.org/10.1021/acs.langmuir.7b03139.

[6] N. Leventis, S. Mulik, X. Wang, A. Dass, V.U. Patil, C. Sotiriou-Leventis, H. Lu, G. Churu, A. Capecelatro, Polymer nano-encapsulation of templated mesoporous silica monoliths with improved mechanical properties, J. Non-Cryst. Solids 354 (2008) 632–644, https://doi.org/10.1016/j.jnoncrysol.2007.06.094.

[7] N. Teo, Z. Gu, S.C. Jana, Polyimide-based aerogel foams, via emulsion-templating, Polymer 157 (2018) 95–102, https://doi.org/10.1016/j.polymer.2018.10.030.

[8] S. Gu, S.C. Jana, Open cell aerogel foams with hierarchical pore structures, Polymer 125 (2017) 1–9, https://doi.org/10.1016/j.polymer.2017.07.085.

[9] C. Chidambareswarapattar, P.M. McCarver, H. Luo, H. Lu, C. Sotiriou-Leventis, N. Leventis, Fractal multiscale nanoporous polyurethanes: flexible to extremely rigid aerogels from multifunctional small molecules, Chem. Mater. 25 (2013) 3205–3224, https://doi.org/10.1021/cm401623h.

[10] S. Donthula, C. Mandal, T. Leventis, J. Schisler, A.M. Saeed, C. Sotiriou-Leventis, N. Leventis, Shape memory superelastic poly(isocyanurate-urethane) aerogels (PIR-PUR) for deployable panels and biomimetic applications, Chem. Mater. 29 (2017) 4461–4477, https://doi.org/10.1021/acs.chemmater.7b01020.

[11] J.P. Vareda, A. Lamy-Mendes, L. Dur˜aes, A reconsideration on the definition of the term aerogel based on current drying trends, Microporous Mesoporous Mater. 258 (2018) 211–216, https://doi.org/10.1016/j.micromeso.2017.09.016.

[12] S. Donthula, C. Mandal, J. Schisler, T. Leventis, M.A.B. Meador, C. Sotiriou-Leventis, N. Leventis, Nanostructure-dependent marcus-type correlation of the shape recovery rate and the young's modulus in shape memory polymer aerogels, ACS Appl. Mater. Interfaces 10 (2018) 23321–23334, https://doi.org/10.1021/acsami.8b06234.

[13] T. Taghvaee, S. Donthula, P.M. Rewatkar, H. Majedi Far, C. Sotiriou-Leventis, N. Leventis, K -Index, A descriptor, predictor, and correlator of complex nanomorphology to other material properties, ACS Nano 13 (2019) 3677–3690, https://doi.org/10.1021/acsnano.9b00396.

[14] (n.d. ImageJ. https://imagej.nih.gov/ij/. (Accessed 20 April 2021) accessed.

[15] S. Min, J. Blumm, A. Lindemann, A new laser flash system for measurement of the thermophysical properties, Thermochim. Acta 455 (2007) 46–49, https://doi.org/10.1016/j.tca.2006.11.026.

[16] S. Malakooti, G. Qin, C. Mandal, R. Soni, T. Taghvaee, Y. Ren, H. Chen, N. Tsao, J. Shiao, S.S. Kulkarni, C. Sotiriou-Leventis, N. Leventis, H. Lu, Low-cost, ambientdried, superhydrophobic, high strength, thermally insulating, and thermally resilient polybenzoxazine aerogels, ACS Appl. Polym. Mater. 1 (2019) 2322–2333, https://doi.org/10.1021/acsapm.9b00408.

[17] K. Sakai, Y. Kobayashi, T. Saito, A. Isogai, Partitioned airs at microscale and nanoscale: thermal diffusivity in ultrahigh porosity solids of nanocellulose, Sci. Rep. 6 (2016) 1–7, https://doi.org/10.1038/srep20434.

[18] D.P. Mohite, S. Mahadik-Khanolkar, H. Luo, H. Lu, C. Sotiriou-Leventis, N. Leventis, Polydicyclopentadiene aerogels grafted with PMMA: II. Nanoscopic characterization and origin of macroscopic deformation, Soft Matter 9 (2013) 1531–1539, https://doi.org/10.1039/C2SM27606B.

II. A COBALT SUNRISE: THERMITES BASED ON LiClO₄-FILLED Co(0) *AEROGELS* PREPARED *FROM* POLYMER-CROSSLINKED COBALTIA *XEROGEL* POWDERS

Parwani M. Rewatkar, Rushi U. Soni, Chariklia Sotiriou-Leventis[*] and Nicholas Leventis[*]

Department of Chemistry, Missouri University of Science and Technology, Rolla, MO 65409, U.S.A. [*]Corresponding authors: Tel.: 573-341-4391 (N.L.); 573-341-4353 (C.S.-L.). E-mail: leventis@mst.edu; cslevent@mst.edu

ABSTRACT

A new route to metallic aerogels that bypasses use of supercritical fluids and handling fragile wet-gel and aerogel precursors is exemplified by the carbothermal synthesis of monolithic Co(0) aerogels from compressed cobaltia xerogel powders coated conformally (crosslinked) at the primary particle level with a carbonizable polyurea. Residual carbon is removed and carbon-free samples are obtained by high-temperature treatment of as-prepared Co(0) aerogels under a flowing stream of H_2O/H_2 that prevents oxidation of the Co(0) network. The durability of Co(0) aerogels is demonstrated under harsh processing conditions in their application as thermites. For this, Co(0) aerogel discs are infiltrated with $LiClO_4$ from a melt, and are ignited at about 1100 °C with an electric resistor. As Co(0) "burns" to CoO, temperature exceeds 1500 °C, and the heat released ($55._2 \pm 2$ kcal mol^{-1}) is near to both the theoretical value (-58.47 kcal mol^{-1}) and that from well-known pressed-pellet iron/perchlorate thermites (66.6 kcal mol^{-1}). The advantage of nanostructured thermites based on Co(0) aerogels is the efficiency (100%) by which the metal is consumed during its reaction with $LiClO_4$ filling the pores.

Keywords: cobalt, aerogel, xerogel, carbothermal, thermite

TOC Graphic
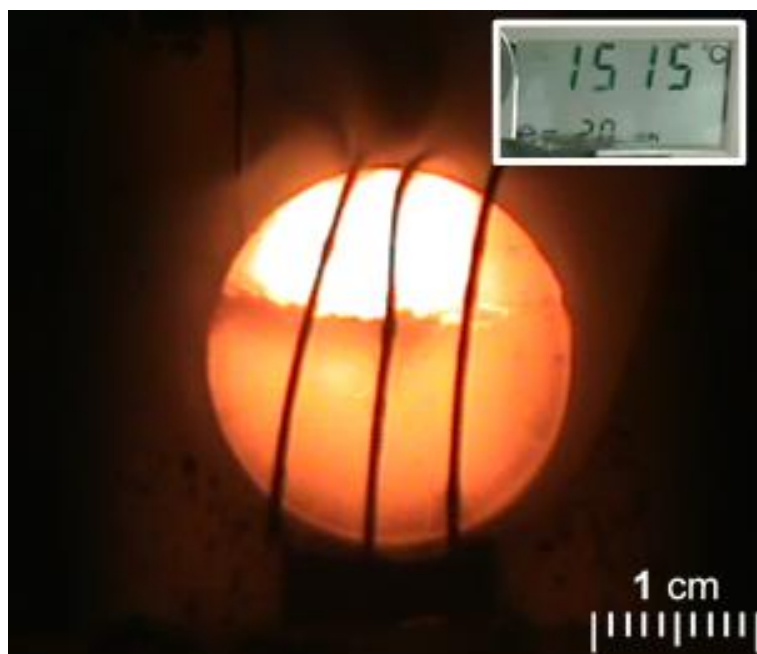
1. INTRODUCTION

Aerogels are open solid colloidal or polymer networks that are obtained by removing the swelling agents from a gel without substantial volume reduction or network compaction.[1] That definition has been expanded to include materials whose precursors are "regular" aerogels derived via the sol-gel route.[2,3] The most well-known class of materials in that category is carbon aerogels, but it also includes several porous metals and porous ceramics (*e.g.*, carbides, nitrides). Thus, although nanoporous metal foams can be prepared from suitable metal complex precursors *via*, for example, combustion synthesis,[4] and while

monolithic noble metal aerogels can be prepared *via* direct sol-gel destabilization of colloids of noble metal nanoparticles,[5,6,7] a large sub-set of monolithic metallic aerogels can be prepared *via* carbothermal reduction of interpenetrating aerogel networks of a nanostructured oxide and a carbonizable polymer.[8,9,10,11,12] Interestingly, carbothermal reduction of interpenetrating xerogel networks takes place consistently at about 400 $^{\circ}$C below the temperature needed for the exact same reduction in the corresponding aerogels, pointing to the importance of the proximity of the reactants at the nanoscopic level.[13] Thereby, the carbothermal route to metallic aerogels could be improved if the carbonizable polymer coats conformally the oxide network. That type of composite aerogels are referred to as polymer-crosslinked or X-aerogels, and are obtained by reaction of surface functional groups on wet-gels with suitable monomers.[14,15,16,17]

The X-aerogel route was first employed toward carbothermal synthesis of isomorphic SiC aerogels from polyacrylonitrile-crosslinked silica aerogel monoliths.[1] Unfortunately, however, any benefits from crosslinking are negated by the long diffusion time needed in order for crosslinking reagents and solvents to infiltrate the interior of large monolithic wet-gels, and thus reach, react and latch on the skeletal nanoparticles throughput. That issue is further compounded by the drying process of wet-gel to aerogels that typically involves converting the pore-filling solvent into a supercritical fluid (SCF) that is vented off like a gas. Alternatively, we have demonstrated recently that large monolithic SiC and Si_3N_4 aerogels can be prepared by pyrolysis of compressed compacts of X-silica *xerogel powders* obtained from suspensions of sol-gel particles, which in turn were obtained by disrupting gelation of silica sols with vigorous stirring.[18] That method does not involve molding and handling fragile wet-gels and/or aerogels, and bypasses the

use of SCF for drying wet-gels into aerogels, or the need for long drying times for converting wet-gels into xerogels. That is, the short time/distance that reagents and solvents need to diffuse over in order to access the interior of the wet-gel grains of the suspension cuts down the crosslinking process from days to minutes. High porosity was created when the crosslinking polymer reacted away during carbothermal reduction of silica toward the carbide or the nitride.

Here, that methodology is extended to large-size monolithic metallic Co(0) aerogels, for which a route through monolithic aerogel precursors could not have even been practical, as reportedly only a few selected cobaltia sols can gel, and they do so with great difficulty (gelation time ~ 10 days).[19] The durability of the newly prepared Co(0) aerogels was probed under extreme processing conditions: the porous space of Co(0) aerogels was filled almost completely with molten $LiClO_4$, the resulting composites did not shrink, remained monolithic and were demonstrated as thermites[20] analogous to pressed $Fe(0)/KClO_4$ pellets that are used in thermal batteries.[21,22] Thermal batteries include an electrolytic salt that becomes an ionic conductor after melting through the heat provided by a thermite. Alternatively, the electrolytic salt can form an ionic conductor by dissolution, thereby the same concept has been extended to wet-condition indicators.[23]

2. RESULTS AND DISCUSSION

The overall process to Co(0) aerogels and their operation as thermites is summarized in Scheme 1. Synthetic procedures are detailed in the Experimental section. Comprehensive materials characterization data have been compiled in Table S.1 of

Appendix I in Supporting Information. The sections below discuss the rationale, chemical transformations, and characterization data of the various intermediates along processing.
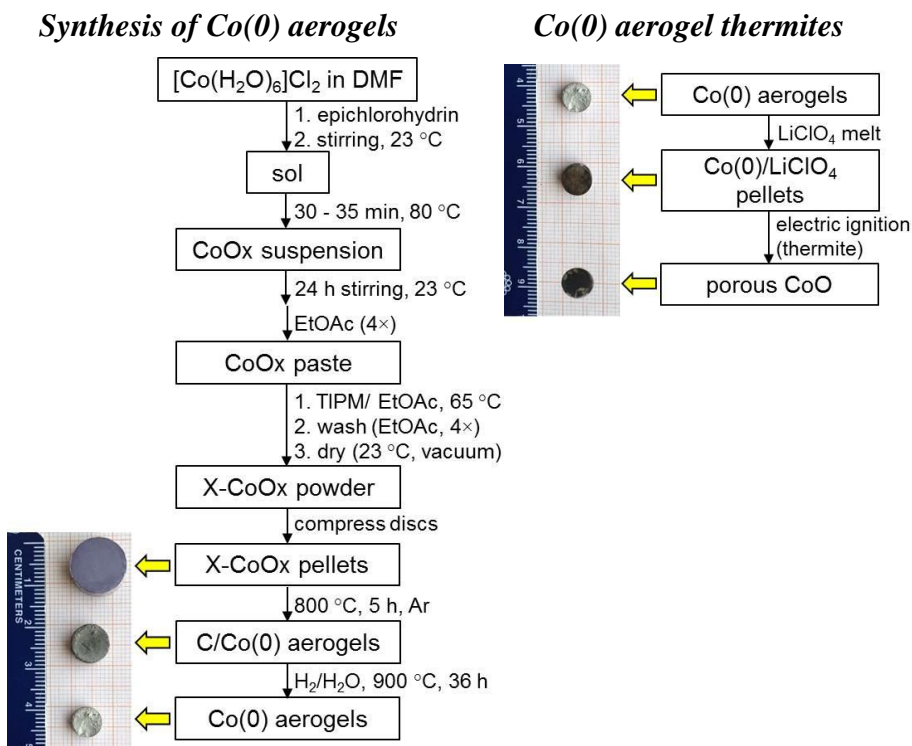
Scheme 1. Synthesis of Co(0) aerogels and their implementation as thermites.

2.1. PREPARATION OF COBALTIA (CoOx) POWDER

Cobaltia (CoOx) suspensions were produced from DMF sols *via* reaction of $[Co(H_2O)_6]Cl_2$ with a proton acceptor (epichlorohydrin).[24,25,26] For characterization purposes part of the suspension was centrifuged and the precipitate was washed and dried under vacuum. Importantly, the $[Co(H_2O)_6]Cl_2$ salt is pink, but its DMF solutions were blue suggesting that octahedral $[Co(H_2O)_6]^{2+}$ was in equilibrium with tetrahedral $[CoCl_4]^{2-}$ (Scheme 2, Eq 1).[27] The position of that equilibrium was evaluated by titrating a DMF

solution of $[Co(H_2O)_6](NO_3)_2$ (at the same concentration as in the sol: 0.43 M) with aqueous HCl. Figure 1 shows that the spectrum of the $[Co(H_2O)_6]Cl_2$ in DMF was practically the same as the spectrum of the nitrate salt plus 4 mol equivalents of HCl, suggesting that gelation of the hexahydtate salt with epichlorohydrin (Scheme 2, Eq 2) was convoluted with Eq 1, the equilibrium of which lies to the left. Reasonably, Eq 1 is expected to be also involved at the surface of the CoOx particles resulting from Eq 3. Indeed, prior TEM work has shown that cobaltia nanoparticles do form in our sol.[13] Furthermore, the thermogravimetric (TGA) profile of CoOx (Figure 2a) shows two mass loss events in the 200-400 °C range (pointed at by blue arrows); reasoning by analogy to $Co(OH)_2$ and $Co_2(OH)_3Cl$,[19,28] the first mass loss, which is observed at around 220 °C, is assigned to dehydroxylation of –OH capped cobaltia nanoparticles, while the second one, at around 300 °C, involves loss of chlorine from –Cl capped particles. Presence of a significant amount of surface –Cl caps suggests a reduced aptitude for cobaltia nanoparticles to develop interparticle Co–O–Co bridges, which are a prerequisite for gelation. Notwithstanding the reasons that prevent large-scale gelation, as outlined in the Introduction, this work bypasses the need to make monolithic cobaltia aerogels (or xerogels) toward metallic Co(0) aerogels.

The multidisperse irregular grains of the precipitate from Equation 3 (Figure 3a-left) had an internal nanostructure typical of an oxide sol-gel materials (xerogel or aerogel) (Figure 3a-right). The skeletal density, ρ_s, of the CoOx xerogel powder was 3.137 ± 0.003 g cm^{-3} and the BET surface area, σ, was 62.4 m^2 g^{-1}. The primary particle diameter was about 31 nm [$= 6 / (\rho_s \times \sigma)$], and agreed with the minimum particle size in SEM (Figure 1a-right) and previous TEM results.[13] In TGA (Figure 2a), the CoOx xerogel powder lost
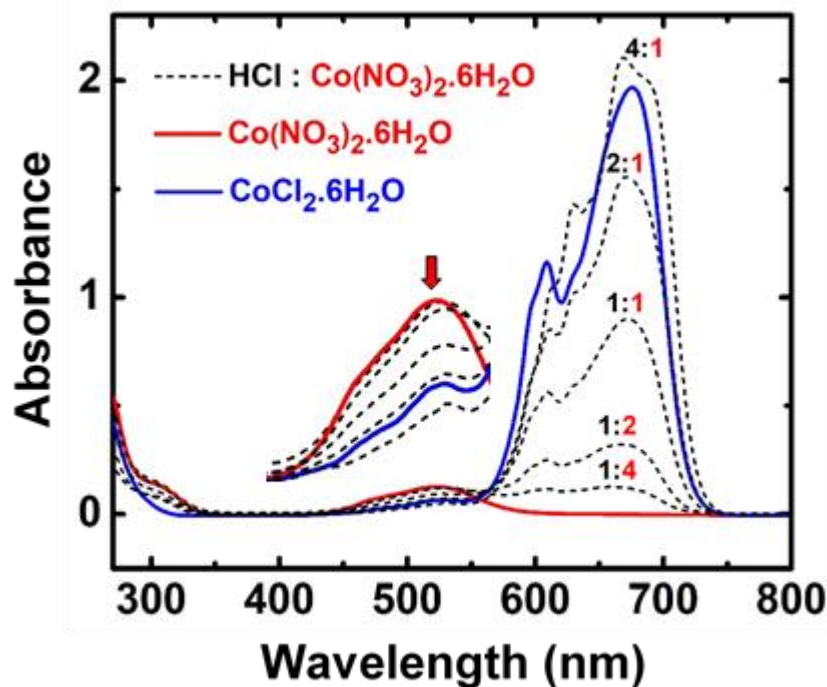
Figure 1. Spectrophotometric titration of a $[Co(H_2O)_6](NO_3)_2$ solution in DMF (0.43 M – red line) with HCl (black dashed lines – fractions denote the HCl : $[Co(H_2O)_6](NO_3)_2$ mol/mol ratio. As the concentration of HCl increases, the intensity of the absorption at 523 nm decreases (red arrow pointing down) and the intensity at 675 nm increases. The blue line shows the spectrum of $[Co(H_2O)_6]Cl_2$ in DMF at the same concentration (0.43 M). (Concentrations of the cobalt complexes were equal to those used in the sol. Spectra were taken from undiluted solutions using a sample holder with an optical path of 0.09 mm.).
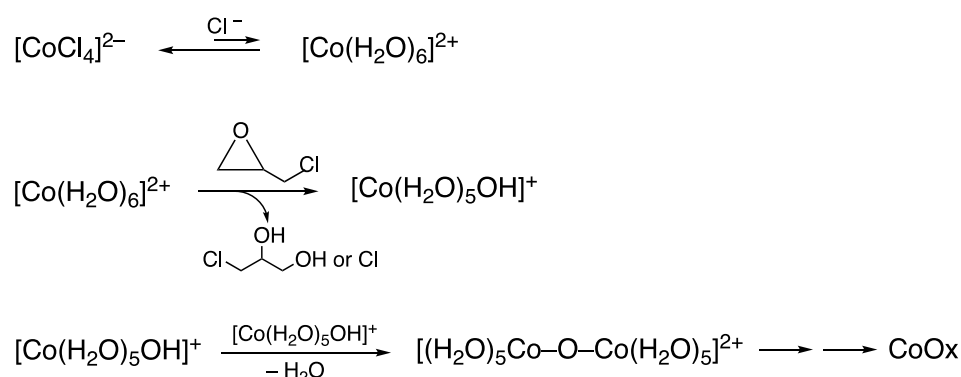
Scheme 2. Chemical processes during preparation of cobaltia (CoOx).

about 3% of its mass by 200 °C (attributed to solvent), and another 25% by 400 °C, attributed to dehydroxylation and loss of Cl as discussed above. By 900 °C, TGA under O_2 (Figure 2a) yielded a 73.20% w/w residue that was identified with XRD as Co_3O_4 (Figure 2b); by 1000 °C the residue was reduced to 68.49% w/w and was identified as CoO (Figure 2b). Thereby, CoOx contained about 54% w/w Co.

2.2. CROSSLINKING OF CoOx WITH A CARBONIZABLE POLYUREA – PREPARATION OF X-CoOx

Crosslinking was carried out by adding an aromatic triisocyanate (TIPM – see Eq 4) to CoOx suspensions and heating (Scheme 1). The size of the grains in the new material (X-CoOx) remained unchanged; under high magnification, skeletal particles were still visible, albeit a massive uptake of polymer. While both CoOx and X-CoOx powders were attracted by laboratory magnets, treating X-CoOx powder with aqueous HCl (12 M) yielded a residue that was not magnetic. TGA under O_2 showed that CoOx had been removed almost completely – the residue at 1000 °C was 3.3% w/w (Figure 2a).

Solid-state ^{13}C NMR (Figure S.1 of Appendix II in Supporting Information) showed that the residue was chemically identical to polyurea (PUA) obtained *via* reaction of TIPM with water (Eq 4).[26]

(1)
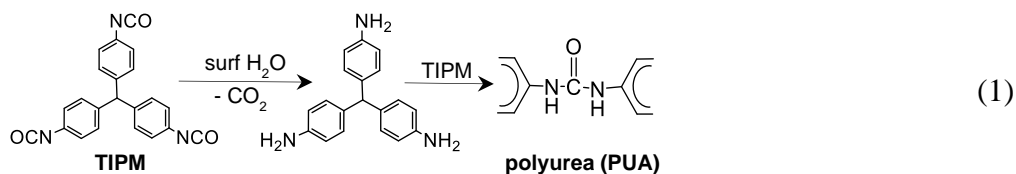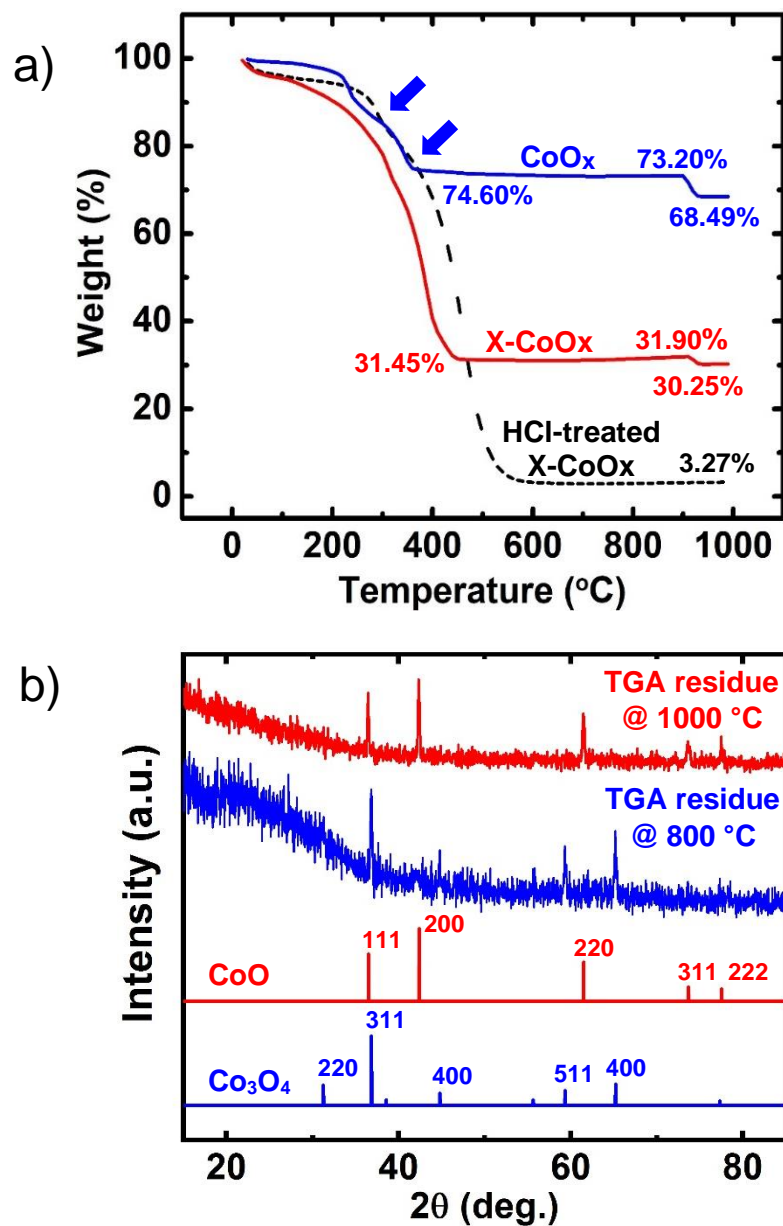
Figure 2. a) TGA under O_2 at 5 °C min^{-1} of: CoOx (blue line), X-CoOx (red line), and HCl-treated X-CoOx (dashed black line). Blue arrows point at the two decomposition steps of CoOx in the 200-400 °C range (see text). b) Referring to part (a) (blue line): XRD of the residue from TGA under O_2 collected at 800 °C and at 1000 °C, as indicated.
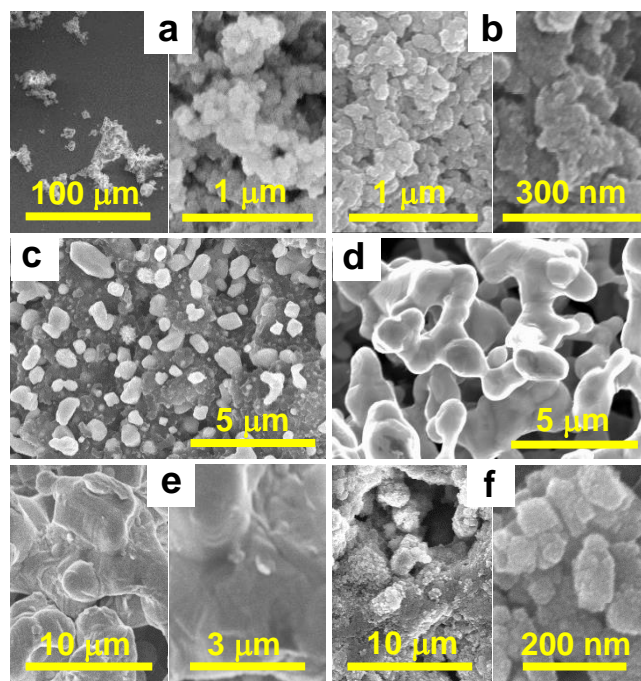
Figure 3. SEM of: a) CoOx powder (left: grains; right: interior of the grains). b) X-CoOx compressed disc at two magnifcations. c) As-prepared Co(0)/C (before carbon removal). d) Co(0)-800: Co(0) after carbon removal with H_2O/H_2 at 800 ^{o}C. e) Co(0)-900: Co(0) after carbon removal with H_2O/H_2 at 900 ^{o}C. f) Monolithic CoO after ignition of LiClO$_4$-loaded Co(0)-900 aerogels and washing with water.

The skeletal density of the X-CoOx powder dropped to $\rho_s = 1.734 \pm 0.003$ g cm^{-3}, and the BET surface area also decreased to $\sigma = 36.2$ m^2 g^{-1}. Lower ρ_s and σ values increased the apparent particle diameter to about 96 nm. Concurrently, the specific pore volume in the 1.7-300 nm range, $V_{1.7\text{-}300\_nm}$ (Table S.1), decreased to 0.11 cm^3 g^{-1} (from 0.35 cm^3 g^{-1} in CoOx), consistent with PUA coating the primary CoOx particles, and filling the space in between them. At 1000 ^{o}C under O$_2$, X-CoOx gave a TGA residue of 30.3% w/w (CoO – see Figures 2a and 2b), therefore it was concluded that X-CoOx contained 23.8% w/w Co.

Considering the skeletal density of X-CoOx as the weighted average of the ρ_s values of CoOx (3.137 ± 0.003 g cm^{-3}) and of TIPM-derived polyurea (1.24 g cm^{-3}),[29] the PUA-to-CoOx mass ratio in X-CoOx was calculated equal to 0.74:0.26. Given that: (a) at 800 °C under Ar, the char yield of TIPM-derived polyurea is 56% w/w,[29] and (b) that char consists of 81% w/w C (the balance being N/O in ~1:1 atomic ratio),[29] the carbon yield of X-CoOx at 800 °C was expected to be about 33.6% w/w. Since X-CoOx contains 23.8 w/w Co (see last paragraph above), the expected C:Co mol/mol ratio from carbonization of X-CoOx was equal to 7.0. Given that at 800 °C CoOx yields Co_3O_4 (Figure 2b), the reduction process at 800 °C requires 2 mol of C per mol of Co_3O_4 for conversion to Co(0) and CO_2.[10] Therefore, it was concluded that the expected C:Co ratio from X-CoOx was sufficient for reduction of the latter to Co(0).

2.3. COMPACTION OF X-CoOx POWDER TO DISCS

Using different dies, X-CoOx powder was compressed under 10,000 psi into different size discs (see Experimental Section). The compaction pressure has not been optimized; the value of 10,000 psi was selected because it is within the typical range used for compressing pellets for infrared spectroscopy, therefore it is easily accessible in most laboratories, rendering reproduction of this work rather straightforward. Compaction did not alter the oxidation state of cobalt. In XPS, the Co 2p spectra of CoOx powder, compressed CoOx powder (at 10,000 psi) and compressed X-CoOx (at 10,000 psi) discs were identical (Figure 4), consisting of two major peaks corresponding to the Co $2p_{1/2}$ and Co $2p_{3/2}$ energy levels (at around 797 and 781 eV, respectively), with a spin-energy separation of about 15.8 eV, and two higher-energy satellite features at around 802 and 785

eV, all characteristic of Co(II) species.[30,31] Just like the X-CoOx powders, compressed X-CoOx discs were attracted by laboratory magnets.

Gram magnetic susceptibilities were measured and the values were reduced to magnetic susceptibilities per gram of Co. Thus, the susceptibilities per gram of Co of the CoOx powder and of the $[Co(H_2O)_6]Cl_2$ complex were close to one another (193.35 and 179.94, respectively; theoretical value for the hexahydrated complex: 164.76 – all in cgs units $\times 10^{-6}$); similarly, the susceptibilities per gram of Co of the X-CoOx powder and of the X-CoOx compressed discs were higher, yet close to one another (229.70 and 233.07, respectively – again in cgs units $\times 10^{-6}$), suggesting a direct chemical interaction (bonding) between Co(II) and the polymer, as expected from crosslinking,[14] and that interaction was not altered under 10,000 psi.

The skeletal density of the X-CoOx compacts (1.673 ± 0.009 g cm^{-3}) was practically unchanged from that of the loose X-CoOx powder (see Section 2.2). Based on the ρ_s value and the bulk density of the compact discs (1.340 ± 0.007 g cm^{-3}), their porosity was calculated at 19.9 % v/v. The values of $V_{1.7-300\_nm}$ and σ (0.0561 cm^3 g^{-1}, and 19.5 m^2 g^{-1}, respectively) were about half relative to those of the X-CoOx powders.

The majority of the specific pore volume (62%) was assigned to pores with >300 nm in diameter. Fussion of the X-CoOx aggregates as well as macroporosity, presumably created when grains of X-CoOx were squeezed together, were both evident in SEM (Figure 3b).
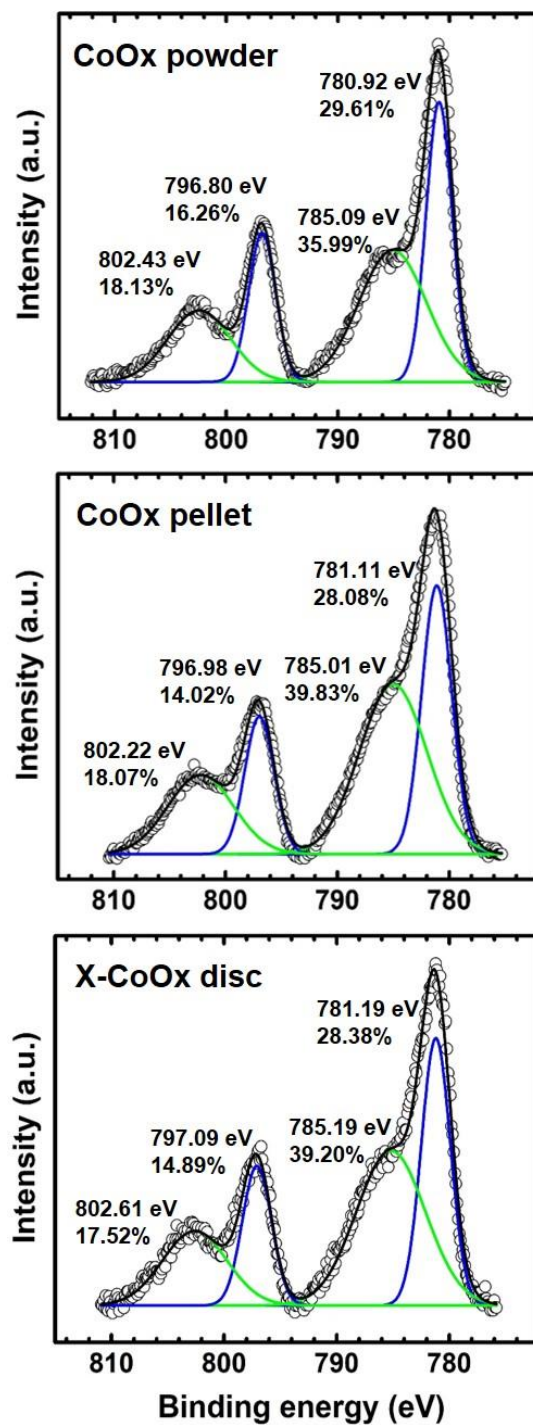
Figure 4. High resolution Co 2p XPS spectra of CoOx powder (top), a CoOx compressed pellet (middle), and of a X-CoOx compressed disc (bottom).

2.4. CARBOTHERMAL REDUCTION OF X-CoOx COMPACT DISCS AND REMOVAL OF RESIDUAL CARBON

Reduction of X-CoOx compacts was carried out at 800 $^{\circ}$C under flowing Ar (Scheme 1). Discs came out black and remained monolithic. Their bulk density was 2.14 $\pm$ 0.02 g cm^{-3}. XRD showed only one crystalline phase, α-Co (Figure 5), but the skeletal density (3.80 $\pm$ 0.09 g cm^{-3}) was much lower than the density of metallic Co (8.90 g cm^{-3}). SEM showed bright metallic protrusions embedded in amorphous matter (Figure 3c). CHN analysis yielded 41.55 $\pm$ 0.2 % C w/w. Despite shrinkage (31.5$_6$ $\pm$ 0.19 % in linear dimensions – see Table S.1), the porosity (44% v/v) was >2$\times$ than the porosity of the X-CoOx compressed discs (19.9 % v/v). In TGA under O_2, the product lost 31.31% of its mass up to 900 $^{\circ}$C and an additional 4.49% by 1000 $^{\circ}$C (Figure 6). The first mass loss was attributed to unreacted carbon and conversion of Co(0) to Co_3O_4, while the second mass loss was due to conversion of Co_3O_4 to CoO (as discussed in conjunction with Figure 2). By either value, the atomic ratio of unreacted C-to-Co(0) was 4.83, which is in reasonable agreement with the after-pyrolysis expected atomic ratio of C:Co (7.0), and the 1:2 mol/mol stoichiometry of the reduction of Co_3O_4 to Co(0) and CO_2 (see above).[10]

A demanding application of Co(0) aerogels is as thermites for thermal batteries.[20,21] Because of the confined space in the latter devices, combustion of residual carbon would cause an explosion. A second cause of explosion is the rapid heating and expansion of the pore filling air.[11,32] This type of explosion is facilitated by weakening of the metallic network under oxidative carbon removal (*e.g.*, with O_2 at 600 $^{\circ}$C).[32] Thereby, our approach here was first to remove carbon under conditions that would provide an overwhelmingly reducing environment around Co(0), and second to fill the pores with the oxidant (LiClO$_4$) almost completely.
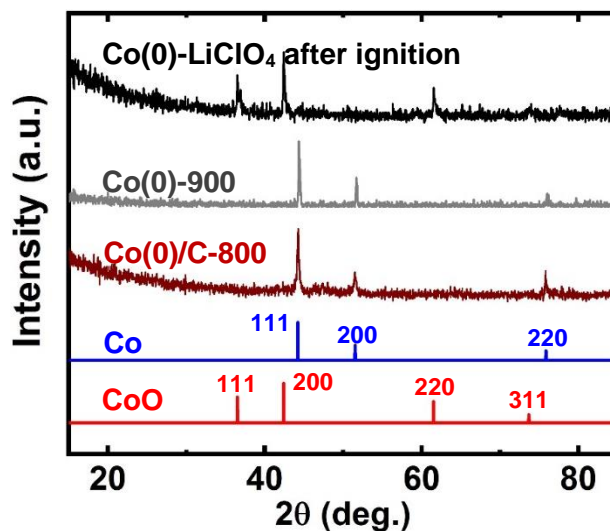
Figure 5. Powder XRD spectra of samples as shown. Numerical extensions denote the temperature of the last processing step (see text).

Carbon was removed with water vapor using H_2 as the carrier gas at two different temperatures, 800 °C and 900 °C. (It is noted that if the carrier gas for the water vapor is Ar, while all other conditions remain the same, Co(0) is oxidized completely to CoO – by XRD, data not shown.) In SEM, the 800 °C samples had a more open structure than the 900 °C samples (compare Figures 3d and 3e). (For further comparison of the properties of the two materials refer to Table S.1) For thermites, we opted to proceed with the 900 °C samples, because smaller pores had the tendency to retain molten $LiClO_4$ longer, thus minimizing its spillage, which may reduce the amount of oxidizer available for combustion of the Co(0) network. Post carbon-removal CHN analysis yielded C: $0.12 \pm 0.02\%$ w/w; H: $-0.03 \pm 0.00_5\%$ w/w; N: $0.02 \pm 0.00_5\%$ w/w. XRD showed only one crystalline phase (α-Co) over a flat baseline (Figure 5). TGA under N_2 of carbon-free Co(0) aerogels showed essentially a flat profile up to 1000 °C (Figure 6). TGA under O_2 showed first a 135.9%

mass increase up to 922.2 °C (expected for Co(0)-to-Co$_3$O$_4$: 136.20% w/w), and a subsequent decrease to 127.3% (expected for Co(0)-to-CoO: 127.15%). (The chemical identity of the two residues at the two temperatures was confirmed with XRD – just as in Figure 2b.)
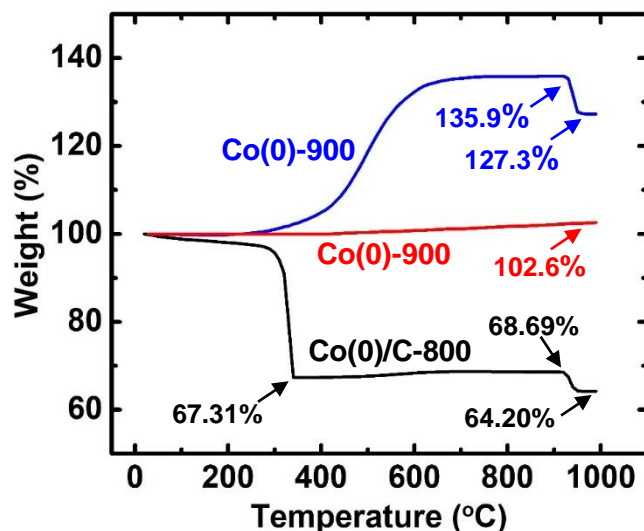
Figure 6. TGA (at 5 °C min^{-1}) of samples and conditions as follows. <u>Black line</u>: Under O$_2$ of an as-prepared Co(0)/C-800 disc; <u>Blue line</u>: Under O$_2$ of a carbon-free Co(0)-900 disc; <u>Red line</u>: Under N$_2$ of a carbon-free C(0)-900 disc. Numerical extensions denote the temperature of the last processing step (see text).

Macroscopically, Co(0) aerogels from the 900 °C treatment for carbon removal (referred to as Co(0)-900 samples) were silvery-gray and extremely sturdy with a Young's modulus = 689 ± 10 MPa and ultimate compressive strength = 1035 ± 19 MPa at over 80% strain (see Figure S.2 of Appendix III in Supporting Information). By comparison, the Young's moduli of ceramic SiC and Si$_3$N$_4$ aerogels made by the same method described here (*i.e.*, from xerogel powders) were much lower (37 and 59 MPa, respectively),[18] and iron aerogels made from interpenetrating networks had to be annealed at 1,200-1,300 °C to

reach the same density as the Co(0)-900 aerogels, yet their Young's modulus was less than half (316 MPa).[32] The distribution of open pores in the Co(0)-900 samples was centered at 11 μm (by Hg-intrusion – see Figure S.3 of Appendix IV in Supporting Information). The skeletal density of the same samples was 8.2 ± 0.1 g cm^{-3} (versus 8.90 g cm^{-3} for pure Co(0)) indicating 7.45% v/v of closed porosity along the metallic framework. Consistent with SEM, the BET surface area was low (0.46 m^2 g^{-1}). However, given that intimate contact of solid-state reagents is as important, or even more so, than how finely divided are the reagents (as pointed out in the Introduction, xerogels react more efficiently than corresponding aerogels[13]) the low surface area of Co(0)-900 was of low concern as long as the porous space was large enough to accommodate the amount of oxidizer (LiClO$_4$) needed for complete consumption of Co(0). Indeed, from skeletal and bulk density data (3.16 ± 0.07 g cm^{-3}), open porosity was sufficiently high (62% v/v), and it should be able to accommodate the amount of LiClO$_4$ needed for complete combustion of the Co(0) in the aerogel discs.

2.5. FILLING THE POROUS SPACE OF Co(0) AEROGELS WITH LiClO$_4$ AND INGNITION

Co(0) aerogels were filled with LiClO$_4$ via capillary action from a melt in a sublimation apparatus under vacuum at 270 °C. *CAUTION:* This is a highly energetic system, and all safety rules must be obeyed at all times (see Experimental section).

The Co(0)-LiClO$_4$ pellets did not shrink relative to the Co(0) aerogels (Scheme 1 and Table S.1). α-Co remained the only Co(0) phase. Based on bulk and skeletal density data ($3.8_6 \pm 0.20$ g cm^{-3} and $4.12_2 \pm 0.056$ g cm^{-3}, respectively) the porosity of the LiClO$_4$-loaded Co(0) pellets was reduced to 6.4 % v/v (from 62% v/v before infiltration with

LiClO$_4$). Based either on those skeletal density data, or the mass gain of the Co(0)-LiClO$_4$ pellets, the amount of LiClO$_4$ was 1.01 ± 0.01 mol/mol relative to the amount required for complete combustion *via* Eq 5.

$$4 \, Co(0) \; + \; LiClO_4 \longrightarrow 4 \, CoO \; + \; LiCl \tag{2}$$

For ignition, a Nichrome wire was wrapped around the Co(0)-LiClO$_4$ discs (Figure 7). Ignition started at one of the contact points of the disc with the wire, when the temperature of the latter was approximately 1100°C (calculated as described in the Experimental section). Once ignition started, the electric power to the wire was disconnected and further combustion was self-sustained. A very bright glow spread rapidly throughout the disk. Quickly, that glow turned red and then ceased altogether. It took about 20 s from ignition to complete combustion (see Ignition Movies). Using an infrared pyrometer, the disc temperature reached 1515 °C. Discs shrunk slightly during combustion (Table S.1), but kept their shape. Post-combustion, discs were washed with water and were dried. Yet, they remained monolithic (Scheme 1), and the only crystalline phase was CoO (Figure 5). Fused CoO particles were <100 nm in size (Figure 3f). The ρ_s value of the CoO network was 5.06 ± 0.03 g cm^{-3} (density of CoO = 6.44 g cm^{-3}), pointing to 27% v/v of closed porosity. The skeletal and the bulk density ($2.68_6 \pm 0.023$ g cm^{-3}) of the CoO discs together gave an open porosity of 47% v/v. The sum of open and closed porosity (74% v/v) was near the sum of those values in the Co(0)-900 aerogels (70% v/v).
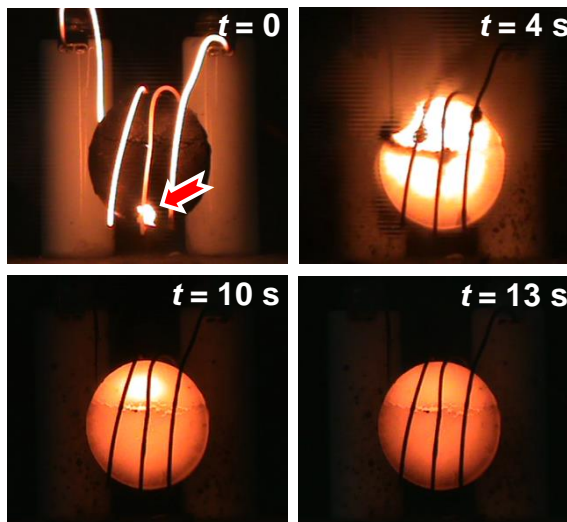
Figure 7. Ignition ($t = 0$) and combustion of a $LiClO_4$-infiltrated Co(0)-900 aerogel disc (21.8 diam. 3.7 mm thick). Arrow shows the point of ignition. The temperature at the center of the disk at $t = 4$ s after ignition reached 1515 °C (see Movie S.M.2).

Ignition of Co(0)-$LiClO_4$ in a bomb calorimeter under high-purity Ar (1 bar, 23 °C) yielded again CoO as the only cobalt phase (identical XRD profile as the one shown in Figure 5 - top). The heat released, -55.17 ± 2.01 kcal per mol of Co(0) reacted, was close to both the theoretical value (-58.47 kcal mol^{-1} from Eq 5), and the heat released from the analogous combustion of Fe(0) to FeO (-66.6 kcal mol^{-1}).[32] Thereby, $LiClO_4$-filled Co(0) aerogels comprise a reasonable alternative to pressed-pellet iron/$KClO_4$ thermites. One advantage of the nanostructured cobalt system over the pressed pellet technology is that Co(0) is consumed completely.

3. CONCLUSION

Deconvolution of the synthesis of monolithic non-oxide aerogels from monolithic aerogel precursors has been extended to smeltable metals. Other possible candidates

include Fe, Ni, Sn and Cu. According to the new method, both metallic and ceramic aerogels can be prepared from X-xerogel powders, relying for porosity on the carbonizable crosslinking polymer reacting away. Using xerogel powders as precursors renders the whole process economic, because it speeds up solvent exchanges and bypasses time-consuming SCF- or freeze-drying. In the present case of Co(0) aerogels, further streamlining was achieved by removing unreacted C with H_2O/H_2. Application of Co(0) aerogels in thermites was a point of departure in order to demonstrate durability at high temperatures, in melts, and in contact with strong oxidizers. It follows that less demanding environments as in liquidized gasses, or electrolytic solutions will be tolerated easily. Applications of Co(0) aerogels in catalysis, as porous electrodes and in magnetic separations are under way.

4. EXPERIMENTAL

4.1. MATERIALS

All reagents and solvents were used as received. Epichlorohydrin (EPH) was purchased from the Sigma Aldrich Chemical Co. Cobalt chloride hexahydrate ($CoCl_2.6H_2O$), and HPLC grade dimethylformamide (DMF) and ethylacetate (EtOAc) were purchased from Fisher Scientific International, Inc. Tris(4-isocyanatophenylmethane) (TIPM) was donated by Covestro LLC (Pittsburg, PA) as a 27% w/w solution in dry EtOAc under the trade name Desmodur RE. Ultra-high purity Ar (grade 5), and H_2 (99.999% purity) gases were purchased from Ozarc Gas (Rolla, MO).

4.1.1. Preparation of CoO$_x$ Suspensions. CoCl$_2$.6H$_2$O (15.756 g, 0.06622 mol) was dissolved in DMF (100 mL) under vigorous stirring. Epichlorohydrin (55 mL, 0.632 mol) was added and the blue solution was heated at 80 °C for 120 min. A suspension (CoOx) started forming in about 15-20 min. After the heating period, the mixture was allowed to cool down to room temperature and stirring continued for another 24 h. The CoO$_x$ suspension was transferred to centrifuge tubes (50 mL, Fischer Scientific), and the solvent was exchanged three times with ethylacetate. All washes and solvent exchanges were carried out with centrifugation for 15-20 min at 2,450 rpm. For each solvent exchange / wash step the new solvent that was brought in was 2× the volume of the compacted slurry (paste) at the bottom of the centrifuge tubes. Before every new centrifugation step, the compacted CoOx slurry was re-suspended with a glass rod. For characterization purposes, a portion of the slurry from the last wash was dried under reduced pressure at 80 ºC into a dry, freely flowing CoO$_x$ powder.

4.1.2. Preparation of Crosslinked X-CoO$_x$ Powder. As-received Desmodur RE (*i.e.,* a solution of TIPM in ethylacetate), 1× the volume of the centrifuged paste, was added to the centrifuge tubes containing the CoO$_x$ slurry from the last ethylacetate wash, the tubes were sealed tightly with their caps, and the suspension was heated in an oven at 65 ºC for 24 h. The mixture was swirled frequently to re-distribute the settled powder and increase the diffusion rate. At the end of the 24 h period, the tubes were allowed to cool to room temperature, they were centrifuged for 15 to 20 min and the suspension was washed 5× with ethylacetate as above. Always, the wash solvent was removed using centrifugation. Again, for all washes, the volume of solvent was 2× the volume of the paste at the bottom of the centrifuge tubes. After removing the solvent from the last ethylacetate wash, the

contents of the tubes were transferred with the aid of small portions of ethylacetate and were combined in a round bottom flask. Ethylacetate was removed and the product was dried under reduced pressure at 80 ºC into a dry, freely flowing X-CoO$_x$ powder.

4.1.3. Preparation of Monolithic Co(0) Aerogels. Dry X-CoO$_x$ powder was compressed into discs using aluminum dies and a hydraulic press operated at 10,000 psi. Two different dies were used yielding two different size discs (diameter/thickness, mm/mm): 41.9/7.6 and 13.0/3.9. Placement of the powder in the dies was carried out in small portions under continuous tapping to ensure even distribution and settling of the X-CoOx powder. Compressed discs were reduced at 800 ºC for 5 h under flowing high-purity Ar. At the end of the heating period, the furnace was allowed to cool down under flowing Ar, pellets were removed and it was found that they contained unreacted carbon. Those samples are referred to as Co(0)/C-800, whereas the numerical extension indicates that temperature of their treatment. Unreacted carbon was removed with H$_2$O-saturated H$_2$. For this, the temperature of the tube furnace was raised to either 800 ºC or 900 ºC under flowing Ar, the gas was switched to H$_2$O-saturated H$_2$ and the temperature was held at that point for 36 h. (Flowing H$_2$ was saturated with water vapor by bubbling through water before directed to the furnace.) At the end of this period, the furnace was allowed to cool down under continuous flow of H$_2$. The resulting samples are refereed to as Co(0)-800 or as Co(0)-900 where the numerical extension indicates the temperature used for their preparation.

4.1.4. Preparation of LiClO$_4$-loaded Co(0)-900 Aerogels. Co(0)-900 samples were degassed at 80 °C overnight under vacuum prior to perchlorate infiltration. The infiltration process was carried out in a sublimation apparatus under vacuum at 270 °C

(melting point of LiClO$_4$ = 236 ^{o}C). The sublimation apparatus containing solid LiClO$_4$ and a hanging Co(0) aerogel pellet at the bottom of the top lid was sealed and heated under vacuum to the intended temperature using a sand bath. The pellet was held in place with a magnetic rod placed inside the "cold" finger of the sublimation apparatus. After LiClO$_4$ melted completely, the magnetic rod was pulled out of the cold finger, and the Co(0)-900 aerogel pellet dropped in the pool of molten LiClO$_4$. In the beginning, the Co(0)-900 pellet floated on the liquid perchlorate, but eventually it sunk as it was filled with the liquid salt. The process took 15 – 20 min. At the end of this period, the pellet was removed from the molten salt, always under vacuum, with the help of a powerful Nd-Fe-B magnet from outside. Subsequently, the apparatus was allowed to cool to room temperature, the vacuum was broken and the perchlorate-infiltrated pellet was removed. The amount of perchlorate was determined gravimetrically.

CUATIONARY NOTE: With the understanding that one deals with a highly energetic system, all safety precautions must be obeyed during infiltration: (a) use of face and body protection; (b) the infiltration vessel must be placed behind a Plexiglass^{TM} shield inside a fume hood; (c) a Class D[33] fire extinguisher must be kept next to the fume hood at all times.

4.2. METHODS

4.2.1. Pyrolytic Synthesis of Co(0). Pyrolytic conversion of X-CoO$_x$ compacts to pure metallic cobalt aerogels was carried out in a programmable MTI GSL1600X-80 tube furnace (outer and inner tubes both of 99.8% pure alumina; outer tube: 1022 mm × 82 mm × 70 mm; inner tube: 610 mm × 61.45 mm × 53.55 mm; length of the heating zone at the

set temperature: 457 mm). The rate of heating and cooling was always maintained at 2.5 °C min^{-1}. All gas flow rates were set at 325 mL min^{-1}.

4.2.2. Ignition of LiClO$_4$-loaded Co(0)-900 Aerogel Pellets. For ignition in the open air, a Nichrome wire (0.65 mm in diameter) was wrapped around LiClO$_4$-loaded Co(0)-900 pellets, and power was supplied to the wire with a Variac. The voltage across the wire (8.5 V) was measured with a multimeter and the electric current flowing through the wire (13.0 A) was measured using a Fluke i400 inductive current probe. Using the diameter of the wire, the current flowing through it, and by consulting tables,[34] the temperature at the point of ignition was about 1,100 °C. That temperature was also confirmed with an infrared thermometer. The whole set-up was placed in a fume hood behind a Plexiglass^{TM} shield. Video was recorded with a Sony Handycam Model DCR-SR68, placed on a tripod. The temperature of the LiClO$_4$-loaded Co(0)-900 pellets during thermite operation was monitored with an Infrared Thermometer (Model 0S3708) from Omega Engineering, Inc. focused at the center of the disc. The maximum temperature recorded was 1515 °C (See Ignition Movie S.M.2).

4.2.3. Physical Characterization. Bulk densities (ρ_b) were calculated from the weight and the physical dimensions of the samples. Skeletal densities (ρ_s) were determined with helium pycnometry using a Micromeritics AccuPyc II 1340 instrument. Samples for skeletal density measurements were outgassed for 24 h at 80 °C under vacuum before analysis. Percent porosities, Π, were determined from the ρ_b and ρ_s values via $\Pi = 100 \times (\rho_s-\rho_b)/\rho_s$.

4.2.4. Thermogravimetric Analysis (TGA). TGA was conducted under N_2 or O_2 with a TA Instruments Model TGA Q50 thermogravimetric analyzer, using a heating rate of 5 °C min^{-1}.

4.2.5. Chemical Characterization. Different methods were applied at different stages of processing as follows.

CHN elemental analysis was conducted with an Exeter Analytical Model CE440 elemental analyzer, calibrated with acetanilide. The combustion furnace was operated at 925 °C. The calibration standard and samples were run three times and results are given as averages.

The crosslinking polymer was identified as TIPM-derived polyurea with solid-state CPMAS ^{13}C NMR on a Bruker Avance III 400 MHz spectrometer with a carbon frequency of 100 MHz, using a 7 mm Bruker MAS probe at a magic angle spinning rate of 5 kHz with broadband proton suppression, and CP TOSS pulse sequence. The Total Suppression of Spinning Sidebands (TOSS) pulse sequence was applied by using a series of four properly timed 180º pulses on the carbon channel at different points of a cycle before the acquisition of the FID, after an initial excitation with a 90º pulse on the proton channel. The 90º excitation pulse on the proton and the 180º excitation pulse on carbon were set to 4.2 µs and 10 µs, respectively. The cross-polarization contact time and the relaxation delay were set at 2000 µs and 5 s, respectively. The number of scans was set at 2,048. Spectra were referenced externally to glycine (carbonyl carbon at 176.03 ppm). Chemical shifts are reported versus TMS (0 ppm). For this, dry X-CoOx powder was treated for 30 min with aqueous HCl (12 M). At the end of the period, the suspension was washed several times with water and several times with acetone. The final slurry was dried under vacuum at 80

°C overnight. X-CoOx powders were attracted by magnets; after removal of the CoOx component with HCl, they were not. The NMR spectrum of the residue was compared with the spectrum of polyurea obtained from the reaction of TIPM with water.

Powder X-ray diffraction (XRD) analysis was performed with powders of the corresponding materials using a PANalytical X'Pert Pro multipurpose diffractometer (MPD) with Cu Kα radiation ($\lambda = 1.54$ Å) and a proportional counter detector equipped with a flat graphite monochromator.

X-ray photoelectron spectroscopic analysis (XPS) was carried out with a Kratos Axis 165 Photoelectron Spectroscopy System. Samples were mixed and ground together with Au powder (5% w/w) as internal reference. Samples were analyzed as powders. Each sample was placed on a piece of conductive carbon tape that was adhered to a stainless steel sample holder. Samples were introduced into the analysis chamber one at a time and the chamber was evacuated at 10^{-8} Torr or lower. No ion sputtering was performed on any of the samples. An Al monochromatic source (150 W) was used for excitation. A charge neutralizer was used to reduce the effects of differential or sample charging. The analysis area was 700×300 microns. Elemental quantification calculations were based on broad survey results from single sweeps at higher sensitivity (Pass energy = 80) and were carried out with the Kratos Axis Vision processing software taking into consideration the appropriate relative sensitivity factors for the particular XPS system. High-resolution elemental scans where carried out at a lower sensitivity (Pass energy = 20), using multiple sweeps to improve the signal-to-noise ratios. Deconvolution of Co 2p spectra was performed with Gaussian function fitting using the OriginPro 8.5.1 software package.

UV-Vis spectroscopy was carried out in DMF solutions of $CoCl_2.6H_2O$, $Co(NO_3)_2.6H_2O$, and $Co(NO_3)_2.6H_2O$ with varying concentrations of HCl using a Cary 5000 UV-Vis Spectrophotometer Model # G9825A. Absorbance was recorded from 270 to 800 nm. Samples were referenced against DMF. The salt concentration in each solution were 0.43 M, equal to the concentration of $CoCl_2.6H_2O$ in the DMF sol used for making CoOx suspensions. Five different solutions of $Co(NO_3)_2.6H_2O$ in DMF were prepared by varying the molar ratio of HCl : $[Co(NO_3)_2.6H_2O]$ as follows: 1:4, 1:2, 1:1, 2:1 and 4:1.

Magnetic susceptibilities were measured with powders of the corresponding samples using a Johnson Matthey Model Mark I Magnetic Susceptibility Balance. A five-point calibration curve was constructed with $CoCl_2.6H_2O$, $CuSO_4.6H_2O$, $K_3[Fe(CN)_6]$, CoO and H_2O. The mass magnetic susceptibility, χ_g (in cgs units), was calculated using the following equation:[35]

$\chi_g = CL(R - R_o)/[1 \times 10^9 (m)]$, where, C = balance calibration constant, L = sample height in cm, R = reading from the digital display when the sample and the tube are in place in the instrument, R_o = reading from the display when the empty sample tube is placed in the instrument, m = sample mass in grams.

4.2.6. Solid Framework Characterization. Scanning electron microscopy (SEM) was conducted with Au-coated samples on a Hitachi Model S-4700 field-emission microscope.

4.2.7. Pore Structure Analysis. N_2-sorption porosimetry at 77 K was conducted with a Micromeritics ASAP 2020 surface area and porosity analyzer. Samples for N_2-sorption analysis were outgassed for 24 h at 80 °C under vacuum before analysis. The pore

size distribution of Co pellet was also probed with Hg-intrusion porosimetry using a Micromeritics AutoPore IV 9500 instrument.

4.2.8. Mechanical Characterization of Co(0) Aerogels. Quasi-static compression testing of Co(0)-900 aerogels at low strain rates (2.5 mm/mm) was conducted on an Instron 4469 Universal Testing Machine using a 50 kN load cell, following testing procedures and specimen length/diameter ratios in the spirit of ASTM D1621-04a (Standard Test Method for Compressive Properties of Rigid Cellular Plastics), as described before.[16] The recorded force as a function of displacement (machine-compliance corrected) was converted into stress as a function of strain.

4.2.9. Calorimetry. The enthalpy of the reaction taking place in $LiClO_4$-impregnated Co(0) was measured in a 200 mL bomb calorimeter (Parr Instrument Company, Model 1108 Oxygen Combustion Vessel and Model 1341 Plain Jacket Calorimeter). The heat capacity of the calorimeter was measured using benzoic acid as standard. The sample was ignited with a Nichrome fuse wire (0.65 mm in diameter, 10 cm in length) connected to the terminal socket on the apparatus head, which in turn was connected to the ignition unit (a Variac). The experiment was carried out by heating the Nichrome wire with a supply of 13.0 A of current for 15 sec under an atmosphere of high-purity Ar. The heat released by the fuse was measured independently with the calorimeter and was taken into consideration in the calculations. After each experiment, the residue was collected and analyzed with XRD.

ACKNOWLEDGEMENTS

SUPPORTING INFORMATION

Appendix I.   Solid-state ^{13}C NMR Data
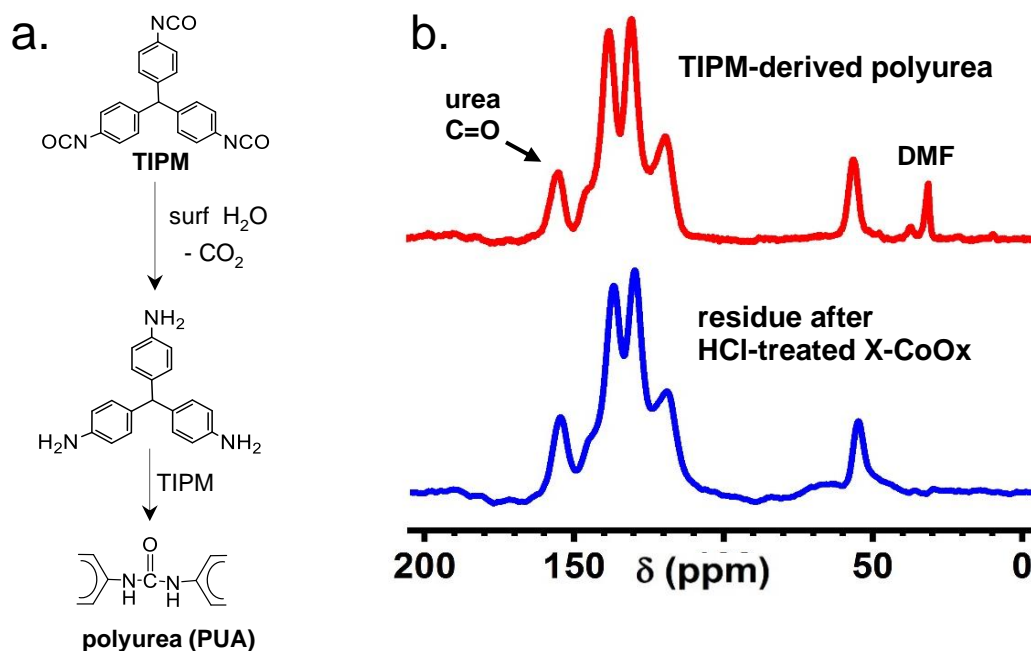
Figure S.1. a) Formation reaction of a TIPM-derived polyurea coating on the surface of the cobaltia nanoparticles. b) Comparison of the solid-state ^{13}C CPTOSS NMR spectrum of TIPM-derived polyurea via reaction of TIPM with water,[S.R.1] with the spectrum of the residue after HCl-treatment of X-CoOx powder.

Appendix II. Material Characterization Data

Table S.1. Materials characterization data along all stages of processing as well as before and after ignition

Sample I.D.	linear shrinkage (%) [b,c]	bulk density, ρ_b (g cm^{-3}) [b]	skeletal density, ρ_s (g cm^{-3}) [d]	porosity, Π (% v/v) [e]	specific pore volume (cm^3 g^{-1})			BET surface area, σ (m^2 g^{-1}) [i]	Average pore diameter Φ (nm) [j]
					V_{Total} [f]	$V_{1.7\text{-}300\_nm}$ [g]	$V_{>300\ nm}$ [h]		
Powders and Compacts									
CoOx powder	-	-	3.137 ± 0.003	-	-	0.3500	-	62.40	-
X-CoOx powder	-	-	1.734 ± 0.003	-	-	0.1124	-	36.20	-
X-CoOx compact	-	1.340 ± 0.007	1.673 ± 0.009	19.87	0.1485	0.0561	0.0924	19.53	30.41
Monoliths from Compacts after Pyrolysis at 800 °C / Ar									
C/Co-800 monolith	31.56 ± 0.19	2.134 ± 0.020	3.802 ± 0.091	43.88	0.2345	0.0221	0.2124	62.69	14.87
Monoliths after Carbon Removal (H$_2$O/H$_2$) at the Temperatures Indicated as Extensions to the Sample I.D.s									
Co(0)-800 monolith [a]	42.14 ± 0.32	1.685 ± 0.063	8.127 ± 0.043	79.25	0.4704	0.0014	0.4690	1.34	1404.18
Co(0)-900 monolith [a]	45.78 ± 0.73	3.155 ± 0.073	8.237 ± 0.113 [b]	61.69	0.1979	0.0006	0.1973	0.46	1720.87 [11325.74]
Co(0)-900 monolith loaded with LiClO$_4$ [a]	no differential shrinkake	3.860 ± 0.201	4.122 ± 0.056	6.35	-	-	-	-	-
LiClO$_4$-loaded Discs after Ignition									
Co(0)-900/LiClO$_4$ after ignition	47.90 ± 0.61	3.762 ± 0.124	5.382 ± 0.265	30.11	-	-	-	-	-
Co(0)-900/LiClO$_4$ after ignition & wash	no additional shrinkage	2.686 ± 0.023	5.060 ± 0.029	46.91	-	-	-	-	-

[a] The numerical extension of Co(0) indicates the last processing temperature. [b] Average of 3 samples. [c] Shrinkage = 100 × (mold diameter – sample diameter)/(mold diameter). All shrinkges are reported with respect to the X-CoOx compact. [d] Single sample, average of 50 measurements. [e] Porosity, $\Pi = 100 \times (\rho_s - \rho_b)/\rho_s$. [f] V_{Total} was calculated via $V_{Total} = (1/\rho_b) - (1/\rho_s)$. [g] $V_{1.7\text{-}300\ nm}$ from N$_2$- BJH desorption volume. [h] $V_{>300\ nm}$ was calculated by subtracting $V_{1.7\text{-}300\ nm}$ from V_{Total}. [i] BET surface area from N$_2$ sorption. [j] For the first number, V was calculated via $4V/\sigma$ by setting $V_{Total} = (1/\rho_b) - (1/\rho_s)$; the number in [brackets] is the peak maximum from the pore size distribution curve obtained using Hg-intrusion porosimetry (see Appendix IV).

Appendix III.   Mechanical Characterization of a Co(0)-900 Aerogel Monolith
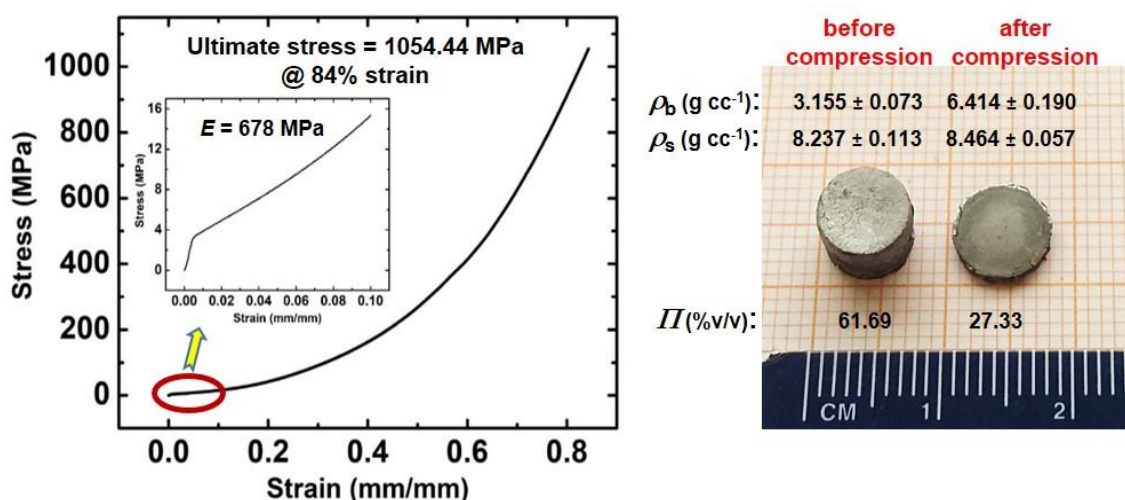
Figure S.2. Quasi-static (2.5 mm min^{-1}) compression testing of a cylindrical Co(0)-900 aerogel monolith (6 mm in length, 3 mm in diameter). The experiment was repeated two times with different monoliths. (The numerical extension in Co(0)-900 indicates the processing temperature at which flowing H_2O/H_2 was used in order to remove unreacted carbon from Co(0)/C-800 aerogels.)

Appendix IV.   Hg-intrusion Porosimetry of a Co(0)-900 Aerogel Disc
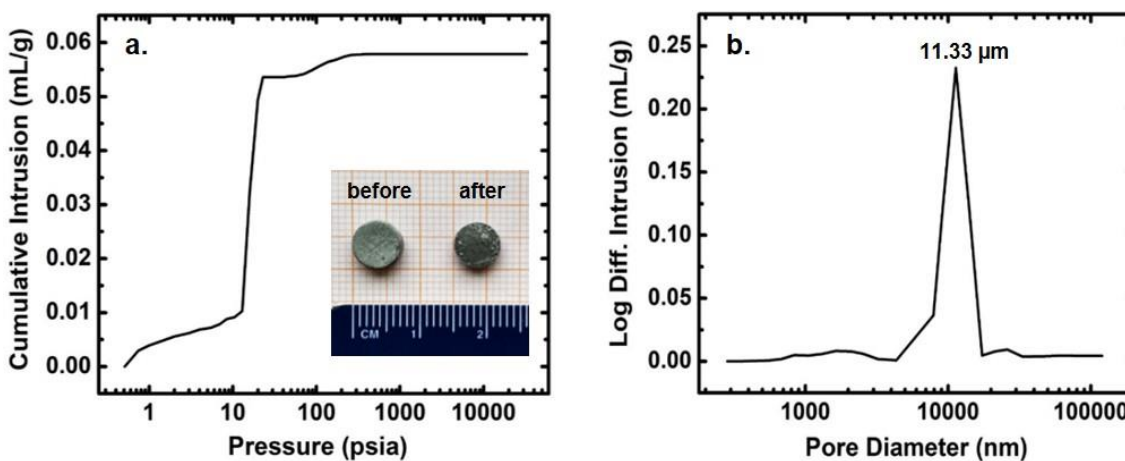
Figure S.3. a) Hg-intrusion isotherm. b) Pore size distribution of a Co(0)-900 aerogel disc. (The numerical extension in Co(0)-900 indicates the processing temperature at which flowing H_2O/H_2 was used in order to remove unreacted carbon from Co(0)/C-800 aerogels.)

Appendix V.   Supplementary References

S.R.1   Leventis, N.; Sotiriou-Leventis, C.; Saeed, A. M.; Donthula, S.; Far H. M.; Rewatkar, P. M.; Kaiser, H.; Robertson, J. D.; Lu, H.; Churu, G. Nanoporous Polyurea from a Triisocyante and Boric Acid: A Paradigm of a General Reaction Pathway for Isocyanates and Mineral Acids. *Chem*. *Mater.* **2016**, *28*, 67−78.

REFERENCES

1. Leventis, N.; Sadekar, A.; Chandrasekaran, N.; Sotiriou-Leventis, C. Click Synthesis of Monolithic Silicon Carbide Aerogels from Polyacrylonitrile-Crosslinked 3D Silica Networks. *Chem. Mater.* **2010**, *22*, 2790–2803.

2. Vareda J. P.; Lamy-Mendes, A.; Durães, L. A Reconsideration on the Definition of the Term Aerogel based on Current Drying Trends. *Microporous Mesoporous Mater*. **2018**, *258*, 211–216.

3. Du, A.; Zhou, B.; Zhang, Z.; Shen, J. A Special Material or a New State of Matter: A Review and Reconsideration of the Aerogel. *Materials* **2013**, *6*, 941–968.

4. Tappan, B. C.; Steiner, S. A.; Luther, E. P. Nanoporous Metal Foams. *Angew. Chem. Int. Ed.* **2010**, *49*, 4544–4565.

5. Cai, B.; Dianat, A.; Hübner, R. Liu, W.; Wen, D.; Benad, A.; Sontag, L.; Gemming, T.; Cuniberti, G.; Eychmüller, A. Multimetallic Hierarchical Aerogels: Shape Engineering of the Building Blocks for Efficient Electrocatalysis. *Adv. Mater.* **2017**, *29*, 1605254.

6. Liu, W.; Herrmann, A.-K.; Bigall, N. C.; Rodriguez, P.; Wen, D.; Oezaslan, M.; Schmidt, T. J.; Gaponik, N.; Eychmüller, A. Noble Metal Aerogels–Synthesis, Characterization, and Application as Electrocatalysts. *Acc. Chem. Res.* **2015**, *48*, 154–162.

7. Wen, D.; Herrmann, A.-K.; Borchardt, L.; Simon, F.; Liu, W.; Kaskel, S.; Eychmüller, A. Controlling the Growth of Palladium Aerogels with High-Performance toward Bioelectrocatalytic Oxidation of Glucose. *J. Am. Chem. Soc.* **2014**, *136*, 2727–2730.

8. Wakayama, H.; Fukushima, Y. Porous Platinum Fibers Synthesized Using Supercritical Fluid. *Chem. Commun.* **1999**, 391–392.

9. Bozbag, S. E.; Sanli, D.; Erkey, C. Synthesis of Nanostructured Materials Using Supercritical CO_2: Part II. Chemical Transformations. *J. Mater. Sci.* **2012**, *47*, 3469–3492.

10. Shen, Y. Carbothermal Synthesis of Metal-functionalized Nanostructures for Energy and Environmental Applications. *J. Mat. Chem. A* **2015**, *3*, 13114–13188.

11. Mahadik-Khanolkar, S.; Donthula, S.; Bang, A.; Wisner, C.; Sotiriou-Leventis, C.; Leventis, N. Polybenzoxazine Aerogels. 2. Interpenetrating Networks with Iron Oxide and the Carbothermal Synthesis of Highly Porous Monolithic Pure Iron(0) Aerogels as Energetic Materials. *Chem. Mater.* **2014**, *26*, 1318–1331.

12. Leventis, N.; Chandrasekaran, N.; Sotiriou-Leventis, C.; Mumtaz, A. Smelting in the Age of Nano: Iron Aerogels. *J. Mater. Chem.* **2009**, *19*, 63–65.

13. Leventis, N.; Chandrasekaran, N.; Sadekar, A. G.; Mulik, S.; Sotiriou-Leventis, C. The Effect of Compactness on the Carbothermal Conversion of Interpenetrating Metal Oxide / Resorcinol-Formaldehyde Nanoparticle Networks to Porous Metals and Carbides. *J. Mater. Chem.* **2010**, *20*, 7456–7471.

14. Leventis, N. Three Dimensional Core-Shell Superstructures: Mechanically Strong Aerogels. *Acc. Chem. Res.* **2007**, *40*, 874–884.

15. Leventis, N.; Sotiriou-Leventis, C.; Zhang, G.; Rawashdeh, A.-M. M. Nano Engineering Strong Silica Aerogels. *NanoLetters* **2002**, *2,* 957–960.

16. Leventis, N.; Sotiriou-Leventis, C.; Mulik, S.; Dass, A.; Schnobrich, J.; Hobbs, A.; Fabrizio, E. F.; Luo, H.; Churu, G.; Zhang, Y.; Lu, H. Polymer Nanoencapsulated Mesoporous Vanadia with Unusual Ductility at Cryogenic Temperatures. *J. Mater. Chem.* **2008**, *18*, 2475–2482.

17. Meador, M. A. B.; Capadona, L. A.; MacCorkle, L.; Papadopoulos, D. S.; Leventis, N. Structure-Property Relationships in Porous 3D Nanostructures as a Function of Preparation Conditions: Isocyanate Cross-Linked Silica Aerogels. *Chem. Mater.* **2007**, *19*, 2247-2260.

18. Rewatkar, P. M.; Taghvaee, T.; Saeed, A. M.; Donthula, S.; Mandal, C.; Chandrasekaran, N.; Leventis, T.; Shruthi, T. K.; Sotiriou-Leventis, C.; Leventis, N. Sturdy, Monolithic SiC and Si_3N_4 Aerogels from Compressed Polymer-Cross-Linked Silica Xerogel Powders. *Chem. Mater.* **2018**, *30*, 1635–1647.

19. Peterson, G. R.; Hung-Low, F.; Gumeci, C.; Bassett, W. P.; Korzeniewski, C.; Hope-Weeks, L. J. Preparation−Morphology−Performance Relationships in Cobalt Aerogels as Supercapacitors. *ACS Appl. Mater. Interfaces* **2014**, *6*, 1796–1803.

20. Overviews of Recent Research on Energetic Materials. In Advanced Series in Physical Chemistry; Shaw, R. W., Brill, T. B., Thompson, D. L., Eds.; World Scientific Publishing, Co.: London, U.K., 2005; Vol. 16.

21. Guidotti, R. A.; Masset, P. Thermally Activated ("Thermal") Battery Tchnology Part I: An Overview. *J. Power Sources* **2006**, *161*,1443−1449.

22. Guidotti, R; Odinek, J; Reinhardt, F. W. Characterization of $Fe/KClO_4$ Heat Powders and Pellets. *J. Energ. Mater.* **2006**, *24*, 271−305.

23. Leventis, N.; Galison, W. A. Apparatus for Detecting Moisture in Garments. U.S. Patent No. 5,796,345 (1998).

24. Gash, A. E.; Tillotson, T. M.; Satcher, J. H.; Poco, J. F.; Hrubesh, L. W.; Simpson, R. L. Use of Epoxides in the Sol−gel Synthesis of Porous Iron(III) Oxide Monoliths from Fe(III) Salts. *Chem. Mater.* **2001**, *13*, 999−1007.

25. Fears, T. M.; Sotiriou-Leventis, C.; Winiarz, J. G.; Leventis, N. Economical Synthesis of Vanadia Aerogels via Epoxide-Assisted Gelation of $VOCl_3$. *J. Sol-Gel Sci. Technol.* **2016**, *77*, 244–256.

26. Leventis, N.; Vassilaras, P.; Fabrizio, E. F.; Dass, A. Polymer Nanoencapsulated Rare Earth Aerogels: Chemically Complex but Stoichiometrically Similar Core-Shell Superstructures with Skeletal Properties of Pure Compounds. *J. Mater. Chem.* **2007**, *17*, 1502–1508.

27. Greenwood, N. N.; Earnshaw, A. Chemistry of the Elements. Butterworth-Heinemann, Woburn, MA 1998, p 1131.

28. Garciamartinez, O.; Millan, P.; Rojas, R. M.; Torralvo, M. J. Cobalt Basic Salts as Inorganic Precursors of Cobalt Oxides and Cobalt Metal: Thermal Behavior Dependence on Experimental Conditions. *J. Mater. Sci.* **1988**, *23*, 1334−1350.

29. Leventis, N.; Sotiriou-Leventis, C.; Chandrasekaran, N.; Mulik, S.; Larimore, Z. J.; Lu, H.; Churu, G.; Mang, J. T. Multifunctional Polyurea Aerogels from Isocyanates and Water. A Structure-Property Case Study. *Chem. Mater.* **2010**, *22*, 6692–6710.

30. https://xpssimplified.com/elements/cobalt.php (Accessed 05-27-2019)

31. Xie, S.; Liu, Y.; Deng, J.; Yang, J.; Zhao, X.; Han, Z.; Zhang, K.; Dai, H. Insights into the Active Sites of Ordered Mesoporous Cobalt Oxide Catalysts for the Total Oxidation of *o*-xylene. *J. Catal.* **2017**, *352*, 282–292.

32. Leventis, N.; Donthula, S.; Mandal, C.; Ding, M. S.; Sotiriou-Leventis, C. Explosive versus Thermite Behavior in Iron(0) Aerogels Infiltrated with Perchlorates. *Chem. Mater.* **2015**, *27*, 8126–8137.

33. http://www.strikefirstusa.com/2016/05/five-classes-of-fires-fire-extinguishers-stop-them/ (Accessed 05-27-2019)

34. https://web.archive.org/web/20120920075813/http://www.pelicanwire.com/category/formulas-resistance/ (Accessed 05-27-2019)

35. https://www.unf.edu/~michael.lufaso/chem3610L/instructions_magnetic_susceptibility.pdf (Accessed 05-27-2019)

III. PREPARATION OF CARBON AEROGELS FROM POLYMER-CROSSLINKED XEROGEL POWDERS WITHOUT SUPERCRITICAL FLUID DRYING AND THEIR APPLICATION IN HIGHLY-SELECTIVE CO₂ ADSORPTION

Rushi U. Soni, Vaibhav A. Edlabadkar, Daniel Greenan, Parwani M. Rewatkar, Nicholas Leventis[§] and Chariklia Sotiriou-Leventis[*]

Department of Chemistry, Missouri University of Science and Technology, Rolla, MO 65409, U.S.A. [§] Present Address: Aspen Aerogels, 30 Forbes Road, Bldg. B, Northborough, MA 01532, U.S.A. *Address correspondence to this author (Tel.: 573-341-4353; E-mail: cslevent@mst.edu)

ABSTRACT

Carbon aerogels are well known materials for their high porosity and high surface areas. They are typically made from pyrolysis of carbonizable polymeric aerogels, which in turn are synthesized via sol-gel methods. Preparation of those polymeric aerogels involves supercritical fluid drying of wet-gels by replacing the pore-filling solvent with liquid CO_2, which is subsequently vented off as a gas, thus allowing pores to retain their shape and size. In contrast, this report demonstrates an alternative route to monolithic carbon aerogels starting from xerogel powders. This method speeds-up solvent exchanges along sol-gel processing, and bypasses the supercritical fluid drying step, resulting in time, energy, and materials efficient fabrication of carbon aerogels. Specifically, polymer-crosslinked silica xerogel powders were prepared via free-radical surface-initiated polymerization of acrylonitrile (AN) on a suspension of silica particles derived from tetramethylorthosilicate (TMOS) surface-modified with 3-aminopropyltriethoxysilane (APTES)-derived initiator. Alternatively, cross-linked silica xerogel powders were

prepared with a carbonizable polyurea (PUA) derived from the reaction of an aromatic triisocyanate (tris(4-isocyanatophenyl)methane – referred to as TIPM) with –OH, –NH$_2$ and adsorbed water on the surface of a TMOS/APTES-derived silica suspension. Wet-gel powders by either method were dried under vacuum at 50 °C to xerogel powders, which were compressed into pellets. In turn these pellets were carbonized, and were treated with HF to remove silica, and with CO_2 to create microporosity. The resulting monolithic carbon aerogels had porosities up to 83% v/v, BET surface areas up to 1934 m^2 g^{-1}, and could uptake up to 9.15 mmol g^{-1} of CO_2 at 273 K, with high selectivity toward other gasses (H$_2$, N$_2$ and CH$_4$).

Keywords: carbon, aerogel, xerogel, drying, CO_2 adsorption, isosteric heat, selectivity

TOC Graphic
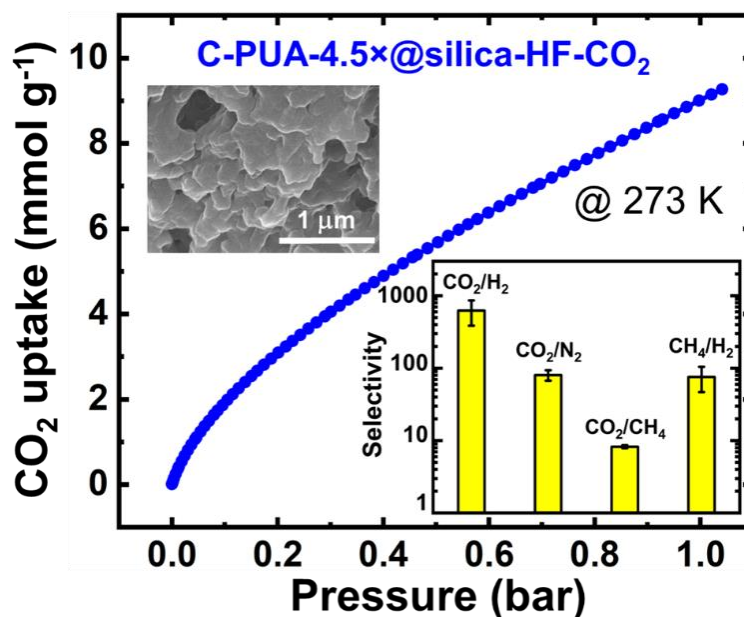
1. INTRODUCTION

Carbon aerogels are electrically conducting low-density materials with high internal surface area consisting typically of over 90% w/w of carbon. They are produced from pyrolysis of carbonizable polymeric aerogels, which in turn are prepared with typical sol-gel chemistry. Applications of carbon aerogels include gas adsorption,[1] gas separation,[2] water purification,[3] catalyst supports,[4] and electrodes for fuel cells.[5] Polymeric precursors of carbon aerogels include aromatic polyureas, polyacrylonitriles, polyamides, polyimides, and most commonly phenolic resins (e.g., those from resorcinol-formaldehyde) including polybenzoxazines.[6–9] The high porosity and surface area of carbon aerogels come from both the innate porosity of the parent polymeric aerogels, and the chemical transformations (decomposition) of the skeletal framework during pyrolysis.

Aerogel-like porous carbon materials have been also demonstrated based on three-dimensional (3D) assemblies of carbon nanotubes,[10,11] carbon nanofibers,[12] templated porous carbons, and graphene-based materials.[13] Finally, the porosity and surface area of all aerogel and aerogel-like porous carbons can be enhanced using the so-called activation (etching) either at low temperatures with reagents such as KOH, NaOH, $ZnCl_2$, $FeCl_2$,[14–17] or at high temperatures, typically in tandem with the carbonization process, using steam, air, or CO_2.[18]

Both the synthesis of polymeric aerogel precursors of carbon aerogels, and the direct 3D assembly of carbonaceous materials into aerogel-like structures involves drying of wet-gels first by extracting the pore-filling solvent with liquid CO_2, and subsequently converting liquid CO_2 to a supercritical fluid (SCF) that is vented off as a gas. This time-

tested method eliminates the surface tension forces of an evaporating solvent through the delicate skeletal framework of the wet gel, and thus preserves its volume and structure in the final dry form (the aerogel). On the downside, use of supercritical fluids is a high-pressure, energy-intensive process. When it comes to preparation of monolithic carbon aerogels with a pre-determined form factor, molding and handling of potentially fragile polymeric wet-gel and aerogel precursors might lower the yield. Furthermore, the size of the monoliths is limited by the size of the pressure vessel. Conversely, if the pore-filling solvent of a wet gel is allowed to evaporate under ambient pressure, surface-tension induced shrinkage is extensive and results in higher-density, low-porosity solids referred to as xerogels.[19] Xerogels can be obtained in the form of powders by drying suspensions of wet-gel microparticles, which in turn are obtained by disrupting long-range gelation of the sol with vigorous stirring. Wet-gel microparticles are easy to handle, and can be dried quickly due to their high surface-to-volume ratio.[20]

Along these lines, a new hybrid approach to aerogels via xerogels was demonstrated recently with the preparation of ceramic (silicon carbide and silicon nitride)[20] and metallic (cobalt)[21] aerogels via pyrolysis of compressed xerogel powder compacts. The xerogel powders consisted of a nanostructured sol-gel oxide network coated conformally (crosslinked) with an about stoichiometrically balanced carbonizable polymer. Carbothermal reduction of the oxide network produced the ceramic or metallic network and created porosity by consuming all carbon in the composite. A small amount of unreacted carbon remaining at the end was removed oxidatively, creating more porosity. The method does not involve SCFs and is capable of furnishing monoliths in various shapes.

In this two-paper sequence, we demonstrate the complementary use of the aerogel-via-xerogel method in the synthesis of carbon aerogels (this report) and graphitic aerogels (next paper). Obviously, in both cases the mol ratio of the carbonizable polymer / inorganic oxide in the corresponding crosslinked xerogel powders had to be tilted heavily towards the polymeric component. For producing regular carbon aerogels (this paper) the oxide partner was silica that can be removed with hydrofluoric acid (HF). For graphitic aerogels, the inorganic component was a sol-gel derived iron or cobalt oxide aerogel network that consumes a small amount of the carbon in order to produce carbothermally *in situ* the graphitization catalyst (Fe(0) or Co(0) nanoparticles), which was removed at the end with aqua regia. Overall, the porosity of regular carbon aerogels was created by (a) decomposition of the carbonizable polymer to carbon; and (b) reactive removal of the silica network. Additional porosity was created by using reactive etching (with CO_2) of the resulting carbon aerogel. The general material properties were similar to those of other carbon aerogels obtained via the traditional method, namely direct pyrolysis of polymeric aerogels from the SCF drying route. In terms of applications, these new types of carbon aerogels were tested for their adsorption capacity towards CO_2 and the values came above average for other CO_2 adsorbers.

More specifically, this paper reports the synthesis of porous carbon aerogels derived from silica xerogels crosslinked with two different carbonizable polymers: an aromatic polyurea (PUA) and polyacrylonitrile (PAN) (Scheme 1). In turn, the silica network was obtained by gelation of tetramethylorthosilicate (TMOS) followed by modification, respectively, with either 3-aminopropyltriethoxysilane (APTES), or with a free radical initiator, which again was a derivative of APTES (Scheme 1). The specific

polyurea and PAN were selected in order to test the applicability of the aerogels-via-xerogels concept to the two major aerogel-crosslinking chemistries, namely with isocyanates, or with surface-initiated free-radical polymerization.[22] In general, PUA- and PAN-crosslinked silica powders, referred to as PUA@silica and PAN@silica, respectively, were compressed into compacts with a hydraulic press and were pyrolyzed at 800 $^{\circ}$C under argon into materials referred to as C-PUA@silica and C-PAN@silica, respectively. C-PUA@silica & C-PAN@silica compacts were etched with HF solutions at room temperature and with CO_2 at 1000 $^{\circ}$C. The sequence of the two etching process on the properties of the final carbon aerogels was studied. PUA-derived carbon aerogels were over 80% porous after the HF/CO_2 etching sequence with surface areas in the range of 1275-1930 m^2 g^{-1}. Carbon aerogels obtained from PAN-crosslinked xerogel powders were 60-85% porous with surface areas in the 843-1433 m^2 g^{-1} range.
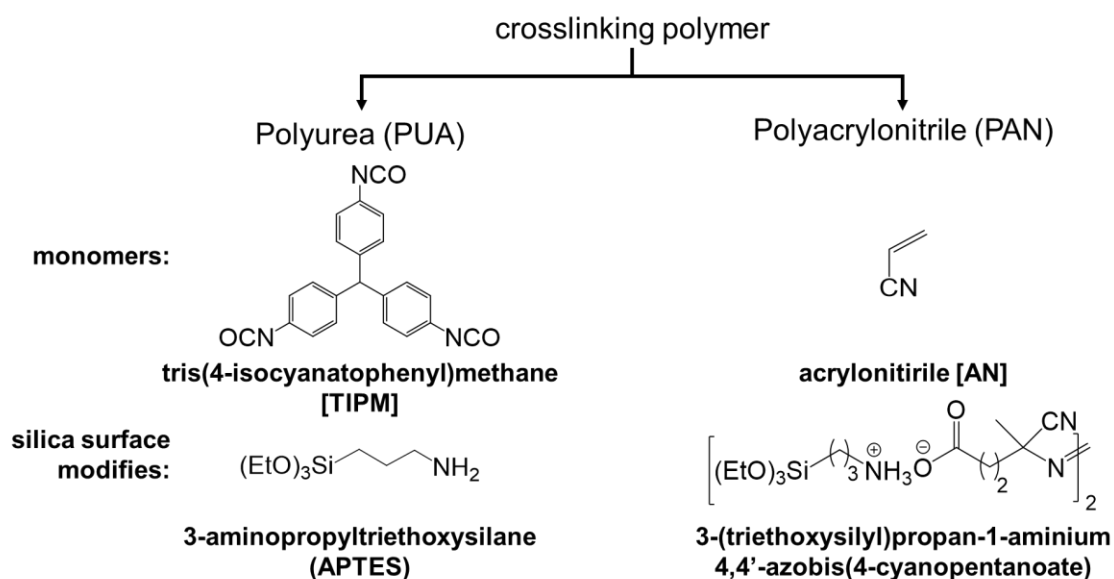
Scheme 1. Monomers and silica surface modifiers for latching of the resulting polymers.

2. RESULTS AND DISCUSSION

2.1. MATERIALS SYNTHESIS

Both carbonizable polymers used in this study, an aromatic polyurea (PUA) and polyacrylonitrile (PAN), were attached on sol-gel derived silica by introducing amine functionality on its surface in two different adaptations of the 3-aminopropyl triethoxysilane (APTES) chemistry.

As shown in Scheme 2A, both routes to carbons from polymer-crosslinked silica xerogel powders started with preparation of sol-gel silica particle suspensions by mixing solution A (TMOS in methanol) with solution B (NH_4OH + water in methanol),[23] followed by adding the combined mixture in hexane under vigorous mechanical stirring.[20] As hydrolysis and condensation of TMOS progressed, the suspended silica particles turned the continuous phase (hexane) milky-white (~20 min).

A. *Preparation of suspensions of silica microparticles*
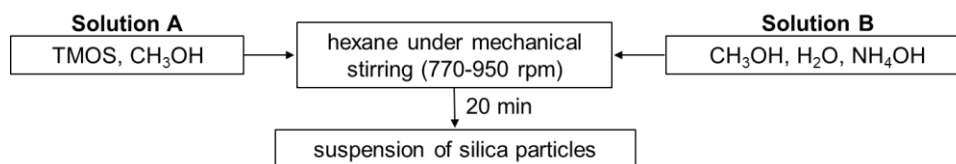
Scheme 2. Synthesis of silica microparticle suspensions, crosslinking with carbonizable polymers, xerogel powders, and xerogel-powder compacts.

B. *Preparation of PUA@silica compacts*
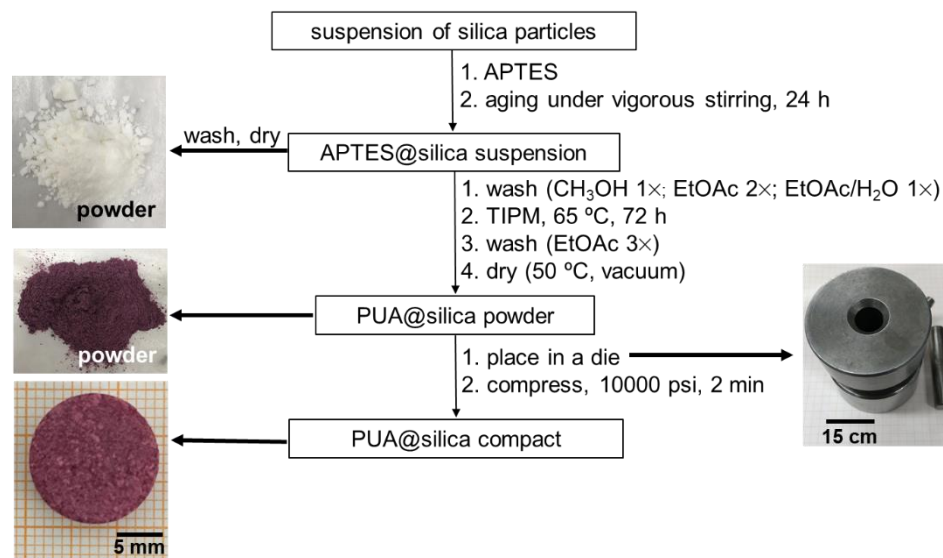
C. *Preparation of PAN@silica compacts*
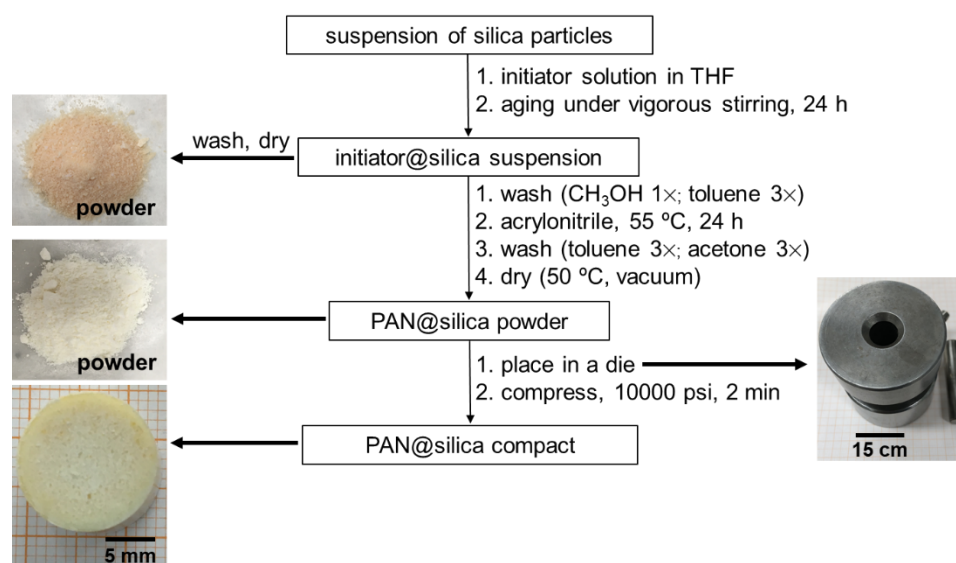
Scheme 2. Synthesis of silica microparticle suspensions, crosslinking with carbonizable polymers, xerogel powders, and xerogel-powder compacts (cont.).

2.1.1. Modification of Silica with Polyurea: PUA@silica Xerogel Powders. As outlined in Scheme 2B, at that point, APTES was added to the suspension of the silica

particles in a 5:1 TMOS:APTES mol/mol ratio. As shown previously, all post-gelation added APTES is attached to the surface of silica down to the primary particle level; in fact, the resulting composition, APTES@silica, is identical to the one obtained when APTES is premixed with TMOS,[20] and that has been considered a proof that hydrolysis and condensation of TMOS is faster than that of APTES.[24,25] The APTES@silica hexane suspension was aged at room temperature under vigorous stirring for 24 h. Conformal coating of the APTES@silica particles with polyurea entails reaction of a multifunctional isocyanate with both the $-NH_2$ groups from the APTES moiety and gelation water remaining adsorbed on the surface of silica.[22,26,27] In order to prepare a reproducible surface for this purpose, excess solvents were removed from the APTES@silica suspension using centrifugation, and the resulting rather thick paste was washed first with ethyl acetate and then with water-saturated ethyl acetate. A small part of the paste from the last centrifugation was separated and dried under vacuum at 50 ºC for characterization purposes. The remaining paste was crosslinked with three different concentrations of Desmodur RE, a commercially-available solution of TIPM (see Scheme 1) in dry ethyl acetate using 1.5×, 3×, or 4.5× mol:mol excess of TIPM relative to the total amount of silicon atoms in APTES@silica. The resulting polyurea cross-linked wet-silica suspension was washed with ethyl acetate and dried under vacuum at 50 ºC to a free-flowing fine xerogel powder that is referred to as PUA-1.5x@silica, PUA-3x@silica or PUA-4.5x@silica, depending on the amount of TIPM used for crosslinking. The first numeral designates the TIPM:silica mol:mol ratio in the crosslinking bath, and the second number the TMOS:APTES mol:mol ratio in silica. For brevity, the samples of the three different formulations are abbreviated as PUA-1.5x@silica, PUA-3x@silica and PUA-4.5x@silica,

and for simplicity, all three samples collectively are referred to as PUA@silica (Scheme 2B).

Using thermogravimetric analysis under O_2 (TGA, see Figure S.1 of Appendix I in Supporting Information), at the high-temperature plateau (> 600 °C) the APTES@silica powder had lost 18.8% of its mass, which was attributed to its organic component. The balance (81.2% w/w) was attributed to SiO_2. Under the same conditions PUA-1.5×@silica, PUA-3×@silica, and PUA-4.5×@silica lost 79.0%, 81.9%, and 87.1% of their masses, respectively, attributed to the sum of the organic component coming from both APTES and the TIPM-derived polyurea. It was then calculated that PUA-2×@silica consisted of 21.0% w/w SiO_2 and 74.1% w/w of TIPM-derived polyurea, and so on as summarized in Table 1. Overall, the amount of polyurea increased from 74.1% to 84.1% as the TIPM:silicon mol:mol ratio increased from 1.5 to 4.5.

2.1.2. Modification of Silica with Polyacrylonitrile: PAN@silica Xerogel Powders. As outlined in Scheme 2C, polyacrylonitrile was coated conformally on the surface of sol-gel derived silica particles via surface-initiated free-radical polymerization of acrylonitrile (AN). As shown in Figure 1A, the surface-confined initiator was the product of the room-temperature, acid-base reaction in anhydrous THF of 4,4′-azobis(4-cyanovaleric acid) (ABCVA), a –COOH group modified derivative of azobisisobutyronitrile (AIBN), and APTES, in an APTES:ABCVA mol/mol ratio of 2:1. In turn, Figure 1B compares the liquid ^{13}C NMR of the APTES/ABCVA reaction mixture with the spectra of the two components. Complete neutralization was confirmed by the conversion of the –COOH group to the carboxylate reflected in the downfield shift of the carboxylic carbon of ABCVA (f: 171 ppm) to 176 ppm (f′: carboxylate).
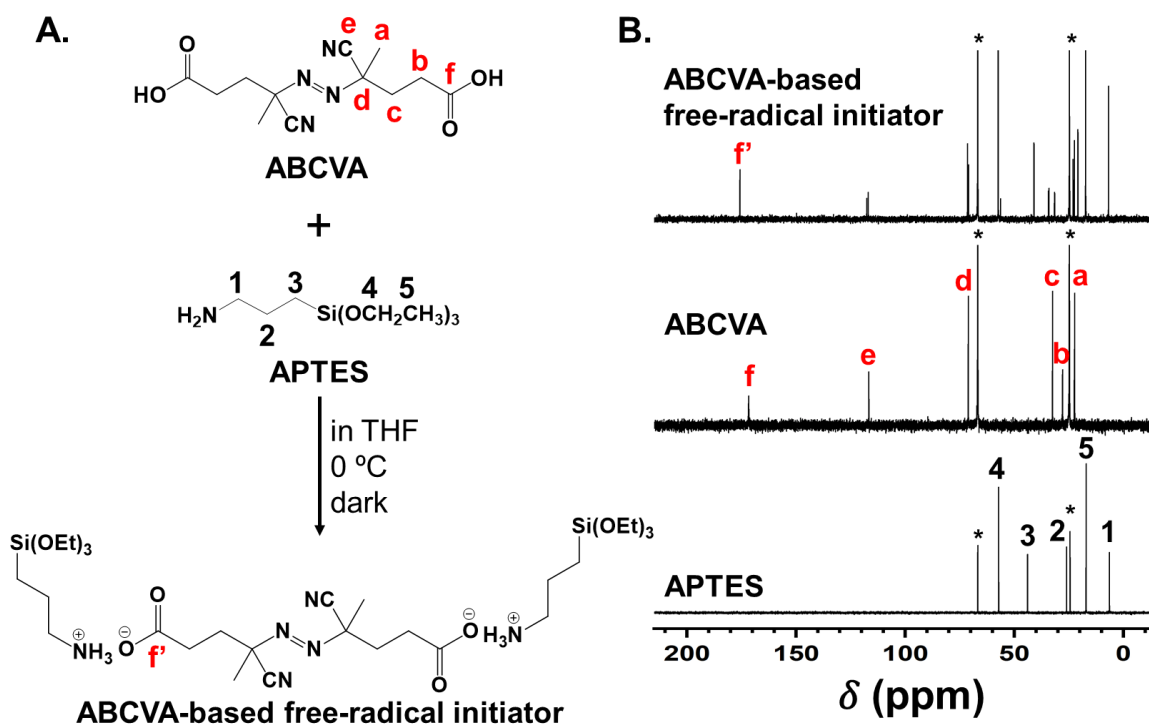
Figure 1. (A) Preparation of the bidentate free-radical initiator used in this study via an acid-base reaction of 4,4'-azobis-4-cyanovaleric acid (ABCVA) and APTES. (B) Liquid ^{13}C NMR spectra in THF-d_8 of APTES, ABCVA, and *3-triethoxysilylpropan-1-aminium 4,4'-azobis(4-cyanovalerate)* (ABCVA-based free-radical initiator). (Solvent peaks are marked with asterisks.)

As a bidentate species, the ABCVA-APTES salt is expected to attach itself on silica from both ends, so that the polymer produced by homolysis of the central -N=N- group would remain surface-bound. This concept is not new,[29,30] however, formation and use of the ABCVA-APTES salt comprises a significant simplification over the previous initiator design, by realizing that linking the –COOH functionality of ABCVA and the –NH$_2$ functionality of APTES as an amide is not necessary, because the simple –NH$_3^+$ $^-$OOC– salt will remain surface-bound as long as APTES remains surface bound and the ionic strength of the solution is zero.

The as-prepared initiator solution was added to a silica suspension prepared as shown in Scheme 2A. The amount of the initiator solution was adjusted so that the final TMOS:APTES ratio would be equal to either 9:1 or 7:3 mol/mol. Those ratios were chosen in order to bracket the TMOS:APTES ratio used in the preparation of PUA@silica (5:1), and thus use this series of materials to probe not only the effect of the polymer, but also the effect of the polymer anchoring sites on the material properties of the final carbons. The resulting suspension was aged for 24 h under vigorous stirring while the apparatus was covered with Al foil. The resulting wet-silica suspension was referred to as initiator@silica. The gelation solvents were removed with centrifugation, and the resulting wet initiator@silica paste was washed with methanol (1×) and then with toluene (3×). For characterization purposes, some of the initiator@silica paste was collected right before the first toluene wash and was dried under vacuum at 23 °C in the dark. Toluene-washed initiator@silica paste was cross-linked with PAN in an acrylonitrile (AN)/toluene solution at 55 °C for 24 h using two different inhibitor-free AN-to-silicon ratios (AN:silicon = 2 and 6 mol/mol). The resulting PAN-crosslinked wet-silica suspension was washed with toluene, and then with acetone and was dried under vacuum at 50 °C to a free-flowing fine xerogel powder that is referred to as PAN-n×@silica(x:y); where "n×" stands for the molar excess of AN over total silicon in the crosslinking bath and, as just described, n× takes the values of 2× and 6×; x:y stands for the TMOS:APTES mol/mol ratio in the formulation of the silica backbone, and as it was described above, it takes the values of 9:1 and 7:3.

Using thermogravimetric analysis under O_2 (TGA, see Figure S.2 of Appendix I in Supporting Information), at the high-temperature plateau (> 600 °C), the initiator@silica powder had lost 22.3% of its mass, attributed to its organic component. The balance (77.7%

w/w) was attributed to SiO_2. Under the same conditions PAN-6×@silica(9:1), PAN-2×@silica(9:1), PAN-6×@silica(7:3), and PAN-2×@silica(7:3) lost 85.1%, 64.0%, 84.0%, and 69.9% of their masses, respectively, attributed to the sum of the organic component coming from both the initiator and PAN. It was then calculated that for example PAN-6×@silica(9:1) consisted of 14.9% w/w SiO_2 and 80.8% w/w of polyacrylonitrile, and so on as summarized in Table 2. Overall, for a given silica:initiator ratio (expressed as 9:1 or 7:3) the amount of PAN in PAN@silica increased as the monomer amount in the crosslinking bath increased. Interestingly, higher amounts of PAN had been uptaken in the PAN@silica composites with lower amounts of initiator; i.e., the percent amounts of PAN in the composites were higher when x:y = 9:1 than when x:y = 7:3.

2.1.3. Processing of PUA@silica and PAN@silica Compacts into Carbon Aerogels. Dry PUA@silica and PAN@silica powders were placed in suitable stainless-steel dies and were compressed with a hydraulic press at 10,000 psi for 2 min (Schemes 2B and 2C). Conversion of PUA@silica compacts to their carbonized products, referred to in general as C-PUA@silica, was carried out by direct heating at 800 ℃ under flowing ultrahigh purity Ar (Scheme 3A)**.** Either under TGA in O_2, or after heating in a tube furnace at 1000 ℃ under flowing O_2, C-PUA-1.5×@silica, C-PUA-3×@silica, and C-PUA-4.5×@silica lost 64.0%, 70.1%, and 75.5% of their mass, respectively, corresponding to the amount of carbon in the composites; the balance was SiO_2. Data are summarized in Table 1. The data agree well with the compositions expected from the parent PUA@silica compacts given the carbonization yield of the TIPM-derived PUA (56% w/w).[28] Following the trend established by PUA in PUA@silica, the percent amount of carbon increased from 64% to 75.5% w/w with increasing the TIPM-to-silicon ratio in the crosslinking bath.

Table 1. Composition of PUA@silica and of carbonized C-PUA@silica xerogel compacts prepared with different TIPM:silicon mol ratios (1.5×, 3×, 4.5×).

sample	1.5×		3×		4.5×	
	PUA or C [% w/w]	SiO$_2$ [% w/w]	PUA or C [% w/w]	SiO$_2$ [% w/w]	PUA or C [% w/w]	SiO$_2$ [% w/w]
PUA@silica	74.1	21.0	77.7	18.1	84.1	12.9
C-PUA@silica (expected)[a]	66.4	33.6	70.6	29.4	78.5	21.5
C-PUA@silica (found)	64.0	36.0	70.1	29.9	75.5	24.5

[a]Calculated based on the composition of PUA@silica and the carbonization yield of TIPM-derived polyurea (56%).[28]

Table 2. Composition of PAN@silica and of carbonized C-PAN@silica xerogel compacts prepared with different acrylonitrile:SiO_2 (n×) and TMOS:APTES (x:y) mol ratios.

sample	6×, (9:1)		2×, (9:1)		6×, (7:3)		2×, (7:3)	
	PAN or C [% w/w]	SiO_2 [% w/w]	PAN or C [% w/w]	SiO_2 [% w/w]	PAN or C [% w/w]	SiO_2 [% w/w]	PAN or C [% w/w]	SiO_2 [% w/w]
PAN@silica	80.8	14.9	53.7	36.0	67.9	16.0	39.7	30.1
C-PAN@silica (expected)[a]	79.1	20.9	51.1	48.9	73.8	26.2	48.0	52.0
C-PAN@silica (found)	75.6	24.4	46.5	53.5	78.4	21.6	49.3	50.7

[a]Calculated based on the composition of PAN@silica and the carbonization yield of PAN (70%).[31,32]

On the other hand, direct heating of PAN@silica compacts at 800 $^{\circ}$C under Ar results in almost complete loss of the organic matter.[30] Conversion of PAN@silica compacts to their carbonized products, requires prior oxidative ring-fusion aromatization of PAN (Scheme 3B).[33]

Modulated differential scanning calorimetry (MDSC) of PAN@silica compacts under O_2 (Figure 2) showed a strong exotherm in the 200-300 $^{\circ}$C range with a maximum at 265 $^{\circ}$C. Guided by the MDSC data, solid-state CPMAS ^{13}C NMR spectra of PAN@silica samples treated under various oxidative conditions showed that complete suppression of the aliphatic protons of PAN, appearing at around 30 ppm, and thereby quantitative ring fusion aromatization, occurred only under prolonged treatment (24 h) at 300 $^{\circ}$C in flowing O_2 (Figure 3). Such aromatized PAN@silica compacts are referred to as A-PAN@silica (Scheme 3B).

Subsequently, A-PAN@silica samples were pyrolyzed at 800 $^{\circ}$C for 5 h under flowing ultrahigh purity Ar and were converted to carbonized PAN@silica compacts, which are referred to in general as C-PAN@silica (Scheme 3B). Either under TGA in O_2, or after heating in a tube furnace at 1000 $^{\circ}$C under flowing O_2, samples C-PAN-6×@silica(9:1), C-PAN-2×@silica(9:1), C-PAN-6×@silica(7:3), and C-PAN-2×@silica(7:3) lost 75.6%, 46.5%, 78.4%, and 49.3% of their masses, respectively, corresponding to the amounts of carbon in the composites; the balance was SiO_2.

Data are summarized in Table 2. The data agree well with the compositions expected from the parent PAN@silica compacts given the carbonization yield of PAN (70% w/w).[31,32] The expected compositions of the C-PAN@silica samples are included in

Table 2. Following the trend established by PAN in PAN@silica, the percent amount of carbon increased with increasing the monomer ratio in the crosslinking bath (see Table 2).

A. Processing of PUA@silica compacts to carbon aerogels

```
                    ┌─────────────────────┐
                    │ PUA@silica compact  │
                    └─────────────────────┘
                              │ pyrolysis, 800 ºC, 5 h, Ar
                              ▼
                    ┌─────────────────────┐
                    │    C-PUA@silica     │
                    └─────────────────────┘
         HF etching │                     │ CO₂ etching, 1000 ºC, 3 h
                    ▼                     ▼
      ┌─────────────────────┐   ┌─────────────────────┐
      │  C-PUA@silica-HF    │   │  C-PUA@silica-CO₂   │
      └─────────────────────┘   └─────────────────────┘
  CO₂ etching, 1000 ºC, 3 h │            │ HF etching
                    ▼                     ▼
  ┌───────────────────────┐   ┌───────────────────────┐
  │ C-PUA@silica-HF-CO₂   │   │ C-PUA@silica-CO₂-HF   │
  └───────────────────────┘   └───────────────────────┘
```
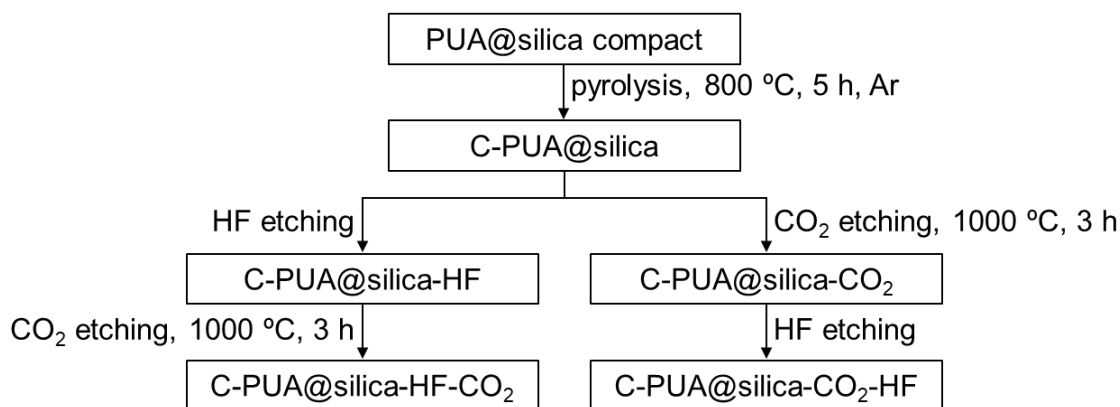
B. Processing of PAN@silica compacts to carbon aerogels

```
                    ┌─────────────────────┐
                    │ PAN@silica compact  │
                    └─────────────────────┘
                              │ aromatization, 300 ºC, 24 h, O₂
                              ▼
                    ┌─────────────────────┐
                    │    A-PAN@silica     │
                    └─────────────────────┘
                              │ pyrolysis, 800 ºC, 5 h, Ar
                              ▼
                    ┌─────────────────────┐
                    │    C-PAN@silica     │
                    └─────────────────────┘
         HF etching │                     │ CO₂ etching, 1000 ºC, 3 h
                    ▼                     ▼
      ┌─────────────────────┐   ┌─────────────────────┐
      │  C-PAN@silica-HF    │   │  C-PAN@silica-CO₂   │
      └─────────────────────┘   └─────────────────────┘
  CO₂ etching, 1000 ºC, 3 h │            │ HF etching
                    ▼                     ▼
  ┌───────────────────────┐   ┌───────────────────────┐
  │ C-PAN@silica-HF-CO₂   │   │ C-PAN@silica-CO₂-HF   │
  └───────────────────────┘   └───────────────────────┘
```
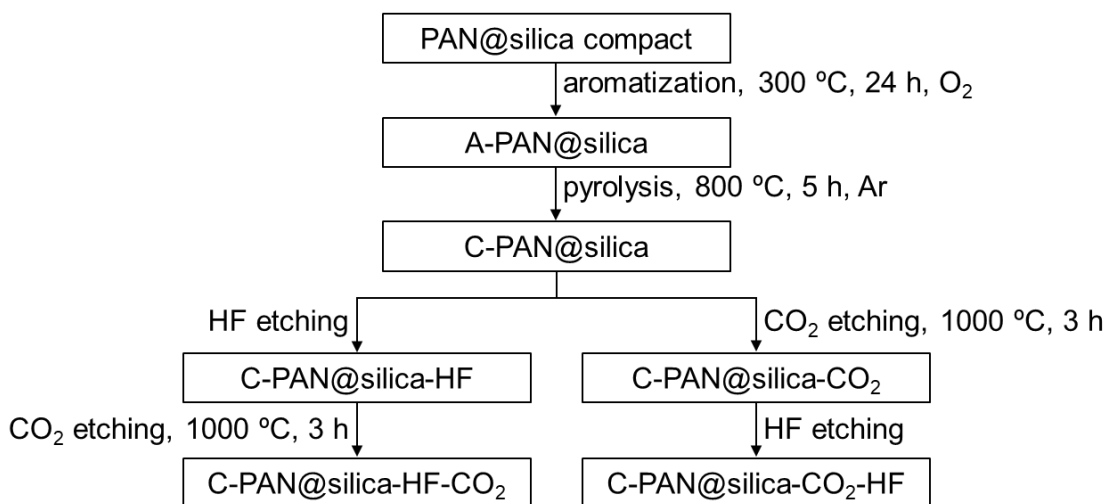
Scheme 3. Further processing of PUA@silica and PAN@silica compacts (see Scheme 1) toward carbon aerogels.
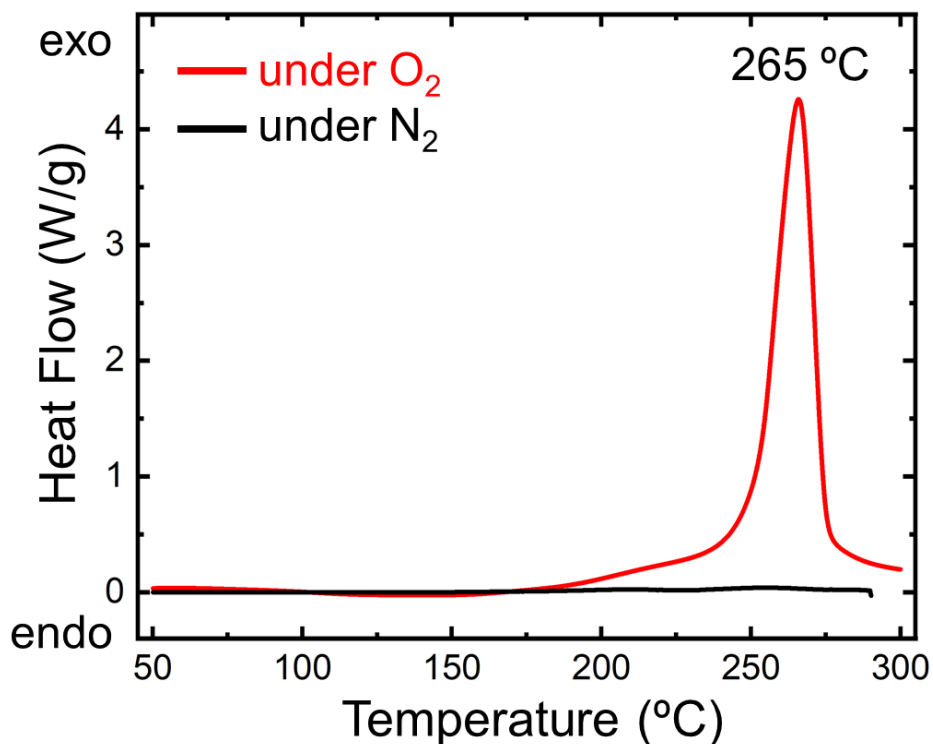
Figure 2. Typical modulated differential scanning calorimetry (MDSC) of PAN@silica samples demonstrated with PAN-6×@silica(9:1) under O_2 or N_2, as indicated (heating rate: 5 ℃ min^{-1}).

2.1.4. Post-carbonization Processing of C-PUA@silica and C-PAN@silica Aerogels. Both carbonized products, C-PUA@silica and C-PAN@silica, were further treated with an aqueous HF solution at room temperature, and with CO_2 gas at 1000 ℃, in either order; i.e., either first with HF followed by high-temperature etching with CO_2, or first with flowing CO_2 gas at 1000 ℃, followed by cooling back to room temperature and treatment with aqueous HF. The two treatments, and their sequence, are shown as extensions to the carbon aerogel names; for example, C-PAN-6×@silica(9:1)-CO_2-HF designates a carbon aerogel resulting from a first treatment of C-PAN@silica with CO_2 at 1000 ℃, followed by treatment with an aqueous HF solution;
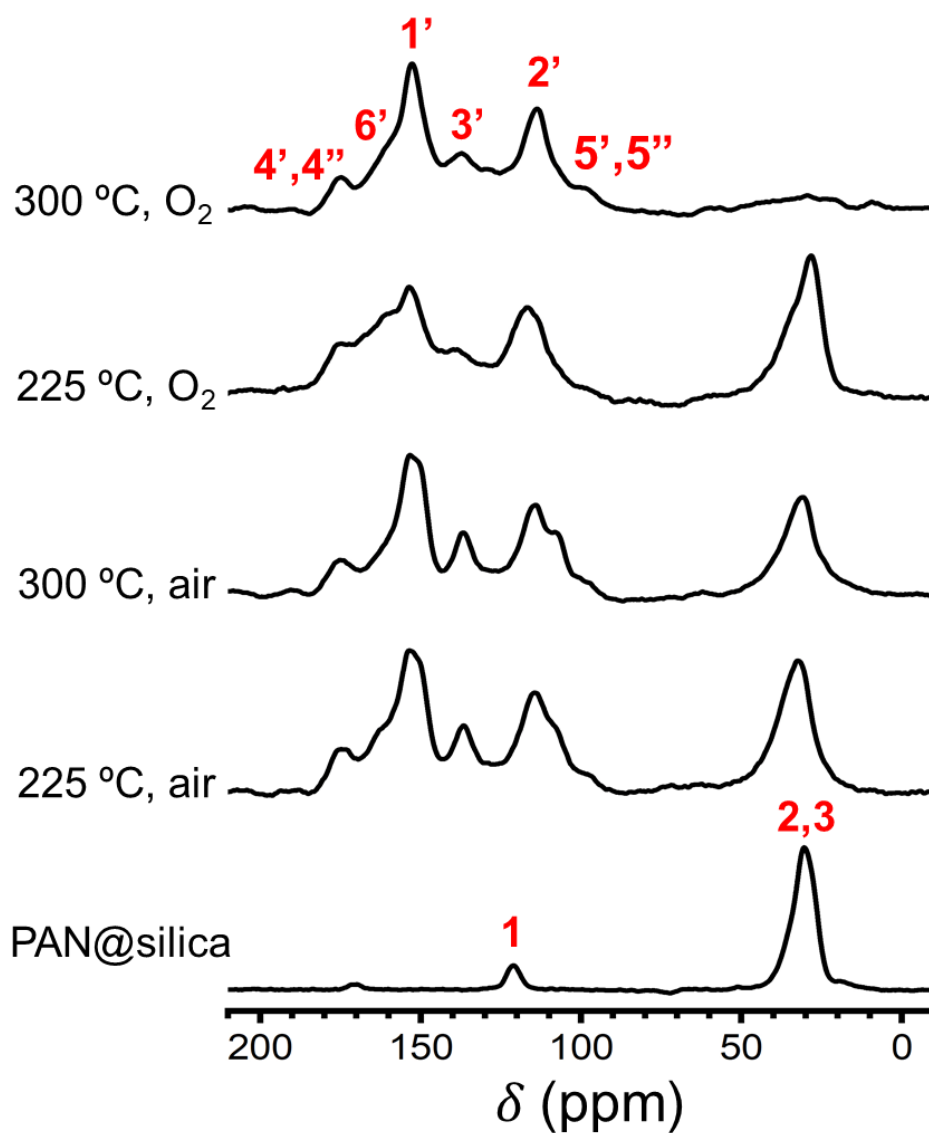
Figure 3. Solid-state CPMAS ^{13}C NMR spectra of the PAN-6×@silica(9:1) system subjected to different oxidation conditions. All pyrolyses were carried out for 24 h. For peak assignments refer to Scheme 5 in Section 2.2b. (The spectra of the fully aromatized samples from all four compositions of the PAN@silica system are shown in Figure S.3 of Appendix II in Supporting Information.).

The carbon framework itself came from PAN-crosslinked silica prepared with a AN:total silicon ratio equal to 6:1 mol/mol, while silica had been formulated with a TMOS:APTES mol/mol ratio equal to 9:1. The HF treatment removed silica from the

carbonized compacts, while etching with CO_2 increased the surface area and created microporosity by removing carbon. Curiously, the two treatments, first with HF or first with CO_2, were not equivalent in terms of their final effect. Although they were identical in terms of processing conditions, and both effective in terms of removing silica (see Section 2.2.3), the materials treated first with HF displayed a much higher overall mass loss than the samples treated first with CO_2 (Table 3). Given that the amount of silicon was the same in every pair of samples, the higher mass loss is attributed to a more efficient removal of carbon when silica was removed first.

2.2. CHEMICAL TRANSFORMATIONS ALONG PROCESSING

2.2.1. The PUA@silica System. Latching of APTES on TMOS-derived silica particles was confirmed with solid-state CPMAS ^{29}Si NMR (Figure 4A). The spectrum of APTES@silica shows a peak at −67 ppm with a shoulder at −59 ppm, which are assigned to the T_3 and T_2 silicon atoms from APTES, respectively, and two peaks at −110 ppm and at −101 ppm with a shoulder at −91 ppm, which are assigned to the Q_4, Q_3, and Q_2 silicon atoms of the TMOS-derived silica (see Scheme 4).The presence of the Q_3 and T_2 silicon atoms points to dangling Si−OH groups, thereby APTES@silica offers two kinds of possible sites for reaction with the isocyanate groups of TIPM: −OH and −NH$_2$. The CPMAS ^{13}C NMR spectrum of the APTES@silica powder (Figure 3B) shows the three $\underline{C}$H$_2$ resonances from APTES of about equal intensity at 43, 24, and 9.5 ppm. The spectrum of the PUA@silica powder was pretty similar to the spectrum of pure TIPM-derived polyurea (also included in Figure 3B for comparison).[34]

For the peak assignment refer to Scheme 4. Due to massive polymer uptake in PUA@silica, the relative intensity of the CH_2 groups from APTES are suppressed. Going back to the solid-state CPMAS ^{29}Si NMR spectra of Figure 3A, it is noted that the $Q_3:Q_4$ peak intensity ratio in PUA@silica is enhanced relative to its value in the spectrum of APTES@silica, which is interpreted as that the triisocyanate (TIPM) being attached to the surface of the silica particles not only via the dangling $-NH_2$ groups of APTES, but also via the innate $-OH$ groups of silica resulting in urethane group formation as shown in Scheme 4.[20]

2.2.2. The PAN@silica System. In addition to the Q_2, Q_3, and Q_4 peaks from silica, the CPMAS ^{29}Si NMR spectrum of initiator@silica (Figure 5A-bottom) shows peaks from the T_3 and T_2 silicon atoms of the APTES part of the initiator. Since the samples shown in Figure 5 were prepared with a TMOS:APTES mol ratio equal to 9:1, the relative intensity of the T-manifold in initiator@silica was lower than its intensity in APTES@silica (Figure 4A).

The solid-state CPMAS ^{13}C NMR spectrum of the initiator@silica powder (Figure 5B) includes the resonances from both APTES and ABCVA. Due to the massive polymer uptake, the solid-state ^{13}C NMR spectrum of the PAN@silica powder showed only the resonances assigned to PAN. Going back to the solid-state CPMAS ^{29}Si NMR spectrum of PAN@silica (Figure 5A), it is noted that the T_3 peak is enhanced relative to its intensity in the spectrum of initiator@silica. This is attributed to the fact that the surface-bound radicals produced by homolytic cleavage of the initiator are *still* bound at the APTES sites, as designed, thereby the polymer extends from those points outward.

Table 3. Mass loss after double etching of carbonized C-PUA@silica and C-PAN@silica compacts (averages of three samples at every composition).

Part A. The PUA@silica system

sample	mass loss relative to the PUA@silica xerogel compacts [% w/w]		
	1.5×	3×	4.5×
C-PUA-n×@silica-HF-CO_2	88 ± 1	86 ± 1	87 ± 1
C-PUA-n×@silica-CO_2-HF	76 ± 2	79 ± 1	80 ± 2

Part B. The PAN@silica system

sample	mass loss relative to the PAN@silica xerogel compacts [% w/w]			
	6×, (9:1)	6×, (9:1)	6×, (9:1)	6×, (9:1)
C-PAN-n×@silica(x:y)-HF-CO_2	73 ± 3	73 ± 3	73 ± 3	73 ± 3
C-PAN-n×@silica(x:y)-CO_2-HF	64 ± 3	64 ± 3	64 ± 3	64 ± 3
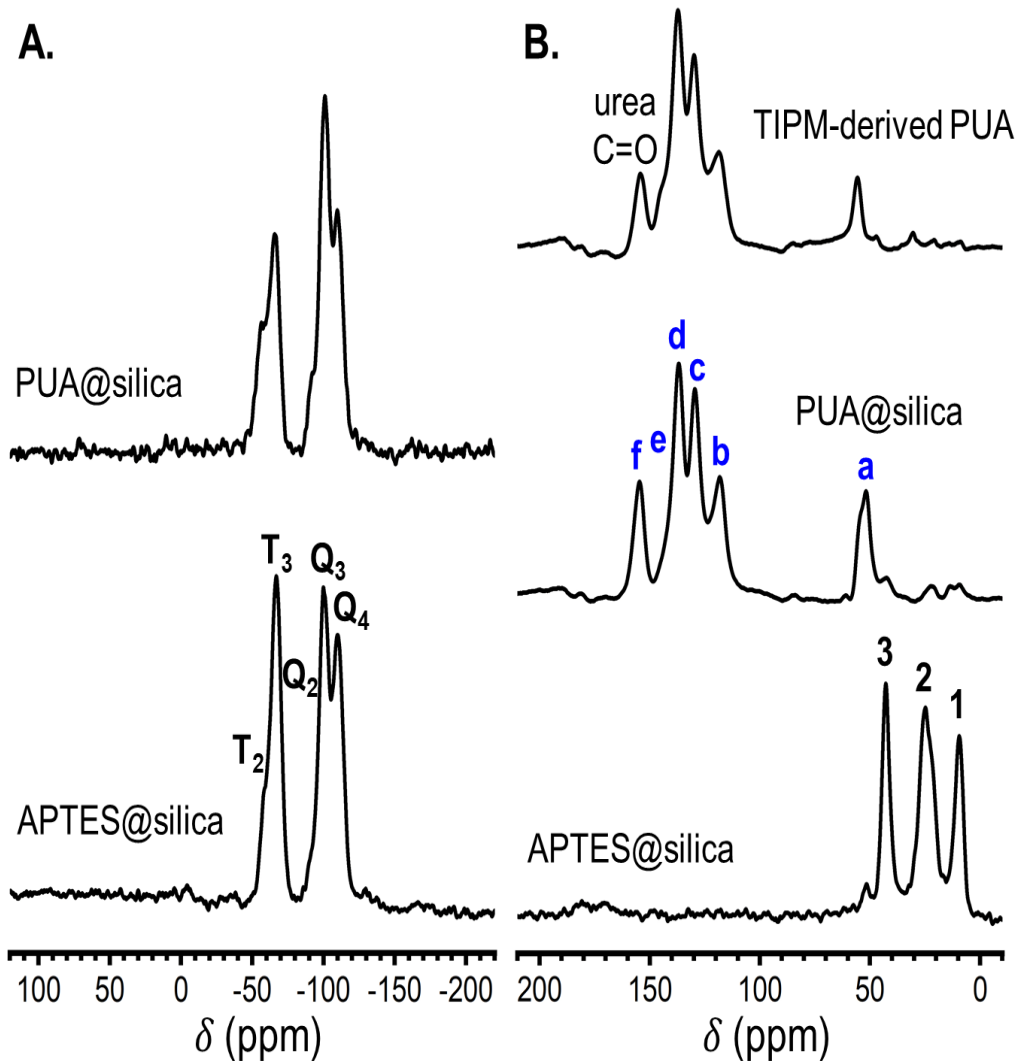
Figure 4. Solid-state CPMAS NMR spectra of representative PUA@silica samples (from the PUA4.5×@silica system) and of relevant controls: (A) ^{29}Si; (B) ^{13}C. For peak assignments refer to Scheme 4. (The spectra of all three different compositions of the PUA@silica system are given in Figures S.4 and S.5 of Appendix III in Supporting Information.)
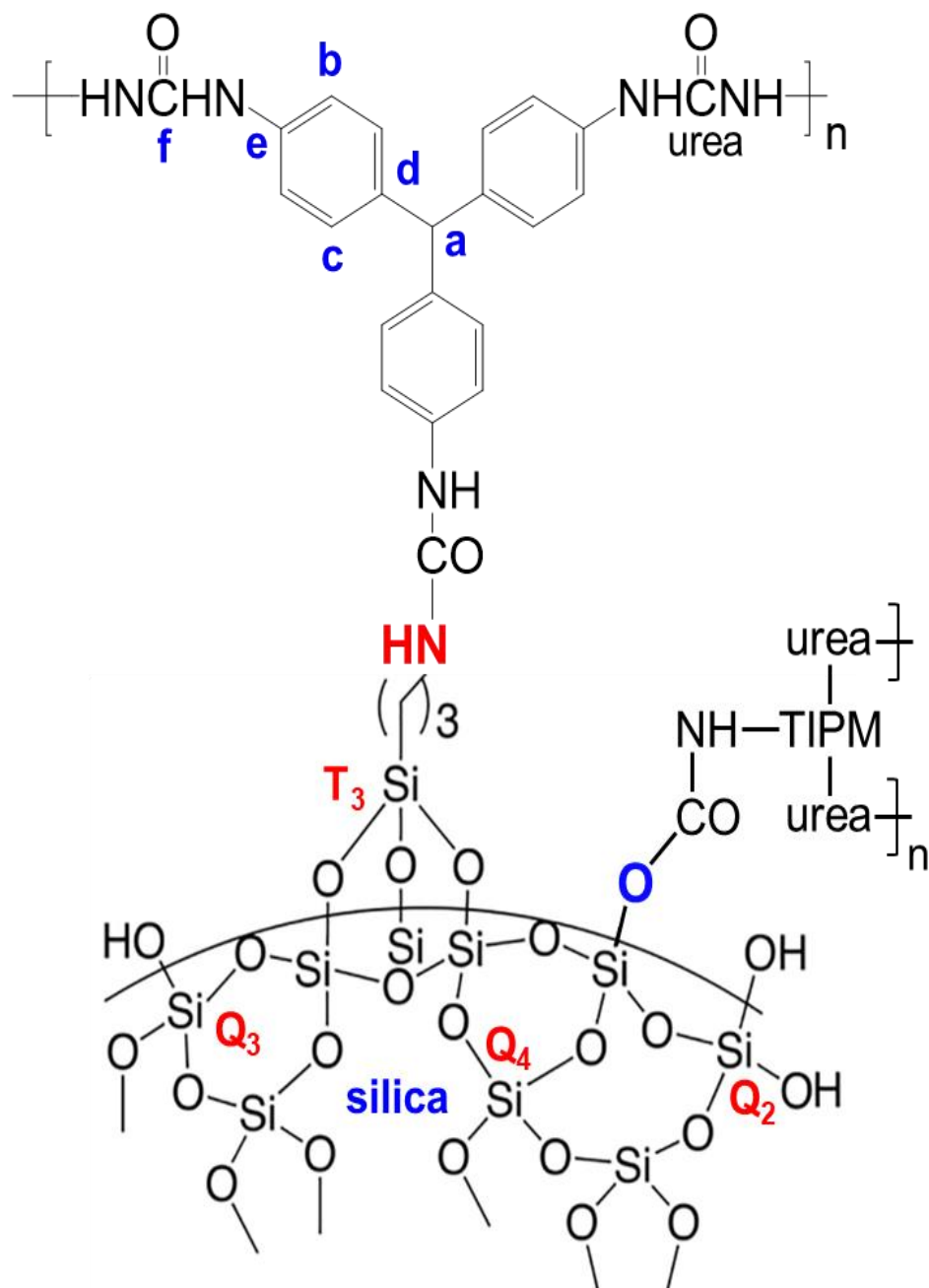
Scheme 4. Latching of TIPM-derived polyurea on the surface of silica.
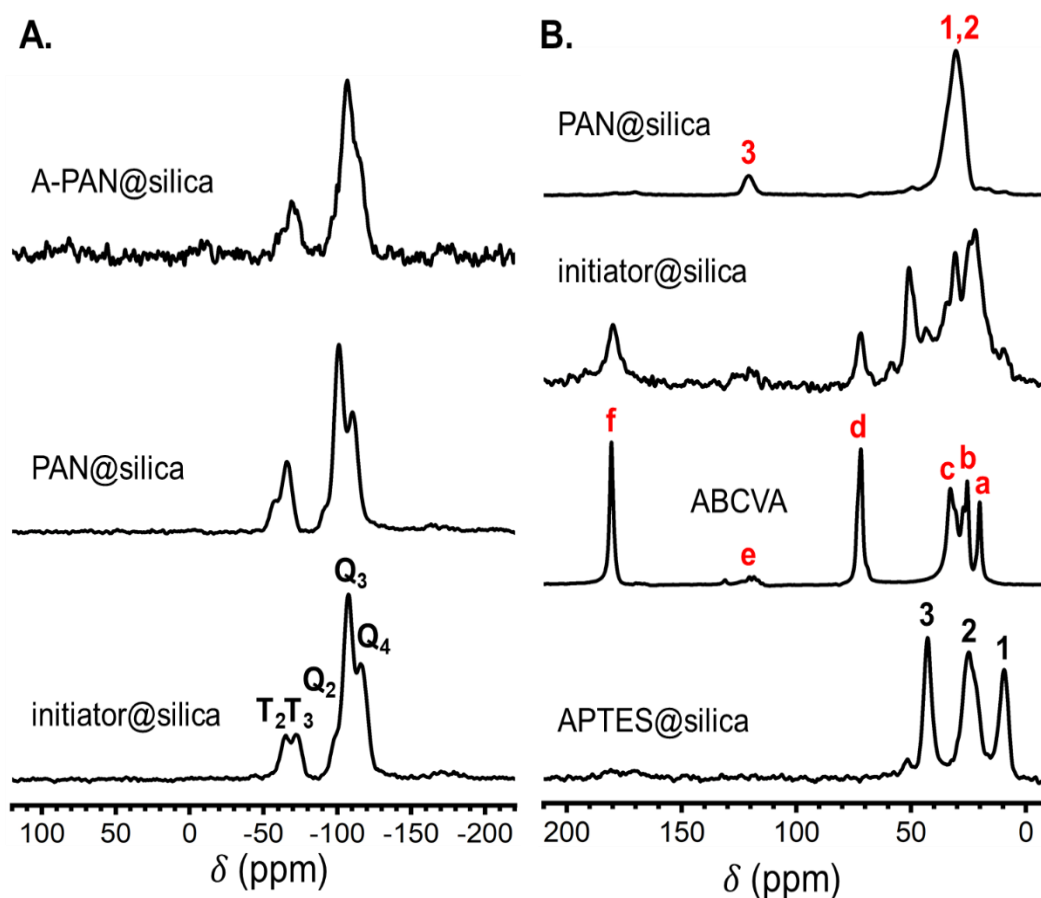
Figure 5. Solid-state CPMAS NMR spectra of representative PAN@silica samples (from the PAN-6×@silica(9:1) system) and of relevant controls: (A) ^{29}Si; (B) ^{13}C. For peak assignments refer to Figure 1 and Scheme 5. (The spectra of all four compositions of the PAN@silica system are given in Figures S.6 and S.7 of Appendix III in Supporting Information.)

The resulting close vicinity of the T_3 Si atoms to the protons of the developing polymer enhances cross-polarization (CP), and therefore the intensity of these silicon atoms increases due to more efficient excitation. Oxidative aromatization of PAN@silica (see Section 2.1.3.) was expected to leave the topographic relationship between the polymer and its anchoring sites more-or-less unperturbed, and indeed the ^{29}Si NMR spectra of A-PAN@silica and PAN@silica were practically identical (compare the middle and top

spectra of Figure 5A). The solid-state ^{13}C NMR spectra of the PAN@silica samples (Figure 3) treated at 300 $^{\circ}$C for 24 h under O_2 are dominated by the resonances that correspond to the idealized structure of fully aromatized PAN (Scheme 5); some lower-intensity resonances that showed up were assigned to pyridonic carbonyls (4' and 4" at around 170 ppm) and to sp^2 carbons on terminal rings (at around 102 ppm - Scheme 5).
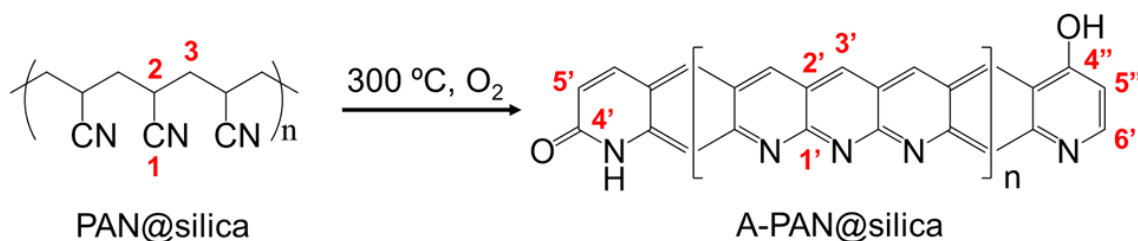
Scheme 5. Conversion of PAN@silica compacts to aromatized-PAN@silica compacts (A-PAN@silica) [The atom numbering is arbitrary and is used to facilitate assignment of the ^{13}C NMR resonances in Figure 3-top.]

2.2.3. PUA@silica– and PAN@silica–derived Carbons and Etched Carbons.

According to EDS (see Figure S.8 and Table S.1 of Appendix IV in Supporting Information), in addition to C and N, carbonized C-PUA@silica and C-PAN@silica contained significant amounts of silicon and oxygen; for example, C-PUA-3x@silica and C-PAN-6x@silica(9:1) contained 13% (Si) / 15% (O) w/w, and 17% (Si) / 16% (O) w/w, respectively. After treatment with HF, the amount of oxygen in C-PUA-3x@silica-HF and in C-PAN-6x@silica(9:1)-HF was reduced drastically to 2.3% and 2.7% w/w, respectively, and neither sample contained any silicon. Thereby, treatment with HF removes silica completely. Both etched samples consisted of C, N and O (no analysis was conducted for H).

High resolution XPS for C, N and O was conducted with carbonized samples in order to elucidate the functional groups those elements are expressed with on the internal surfaces of the samples. Figures 6 and 7 show the O 1s and N 1s spectra of C-PUA@silica and C-PAN@silica, respectively, and include the spectra of the corresponding double-etched C-PUA_or_PAN@silica-HF-CO_2.

The XPS spectra of C-PUA@silica and of C-PAN@silica included peaks at 533.5 eV of O 1s (see Figures 6A and 7A), and at 103.6 eV of Si 2p from SiO_2 (see Figure S.9 of Appendix V in Supporting Information).[35,36] Consistently with the EDS data, the Si 2p peak and the O 1s peak of silica were absent from the spectra of double-etched C-PUA_or_PAN@silica-HF-CO_2 (Figures 6B, 7B) and of C-PUA_or_PAN@silica-CO_2-HF (see Figure S.10 of Appendix V in Supporting Information).

The O 1s spectra of C-PUA@silica and of C-PAN@silica (Figures 6A and 7A) contained also a strong peak at 533.0 eV assigned to ether O, and weak peaks at 531.6 eV and 531.9 eV, respectively, assigned to $-O^-$.[37–39] The N 1s spectra of C-PUA@silica and C-PAN@silica (see Figure 6C and 7C) showed N mainly in pyridinic (398.3–398.4 eV), and pyridonic positions (400.6–400.7 eV; more pyridonic in C-PUA@silica than in C-PAN@silica) and small amounts of nitroxide at 403.8 eV (case of C-PUA@silica), or at 403.3 eV (case of C-PAN@silica).[39–42]
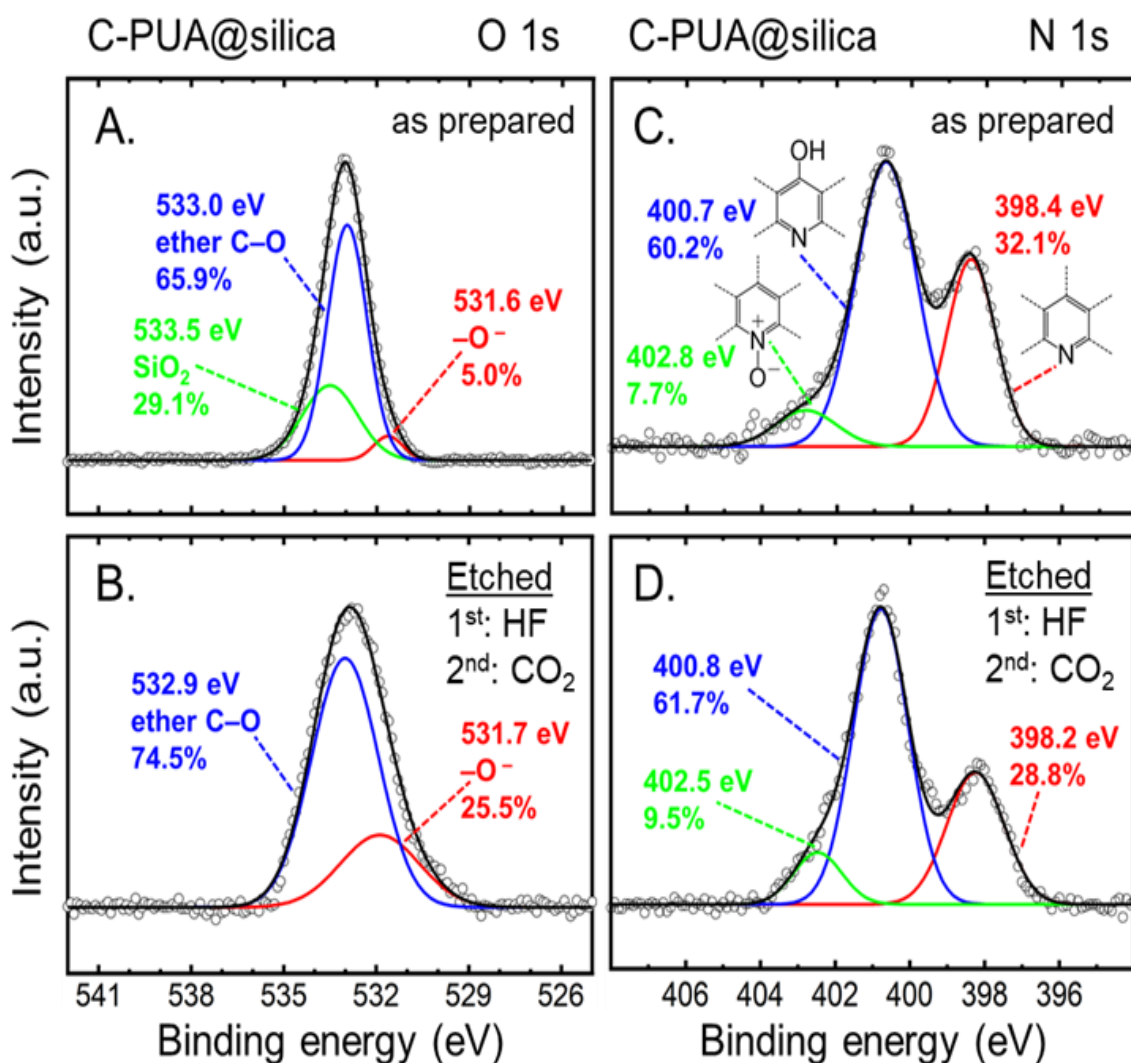
Figure 6. High resolution O 1s (left) and N 1s (right) XPS spectra of: (A,C) C-PUA-4.5×@silica; (B,D) C-PUA-4.5×@silica-HF-CO₂. (For the Si 2p and C 1s spectra, and those of the corresponding –CO₂-HF samples, see Figures S.9–S.12 of Appendix V in Supporting Information.)

The O 1s spectra of double-etched carbon samples contained the same ether O, and –O⁻ peaks, but the intensity of the –O⁻ peak at ~532 eV was increased significantly relative to before the etching processes – from 5% to 25.5% (case of C-PUA@silica-HF-CO₂), and from 8.5% to 25.1% (case of C-PAN@silica-HF-CO₂). Simultaneously, the intensity of the N 1s peaks attributed to pyridonic and nitroxide ($-N^+-O^-$) also increased.
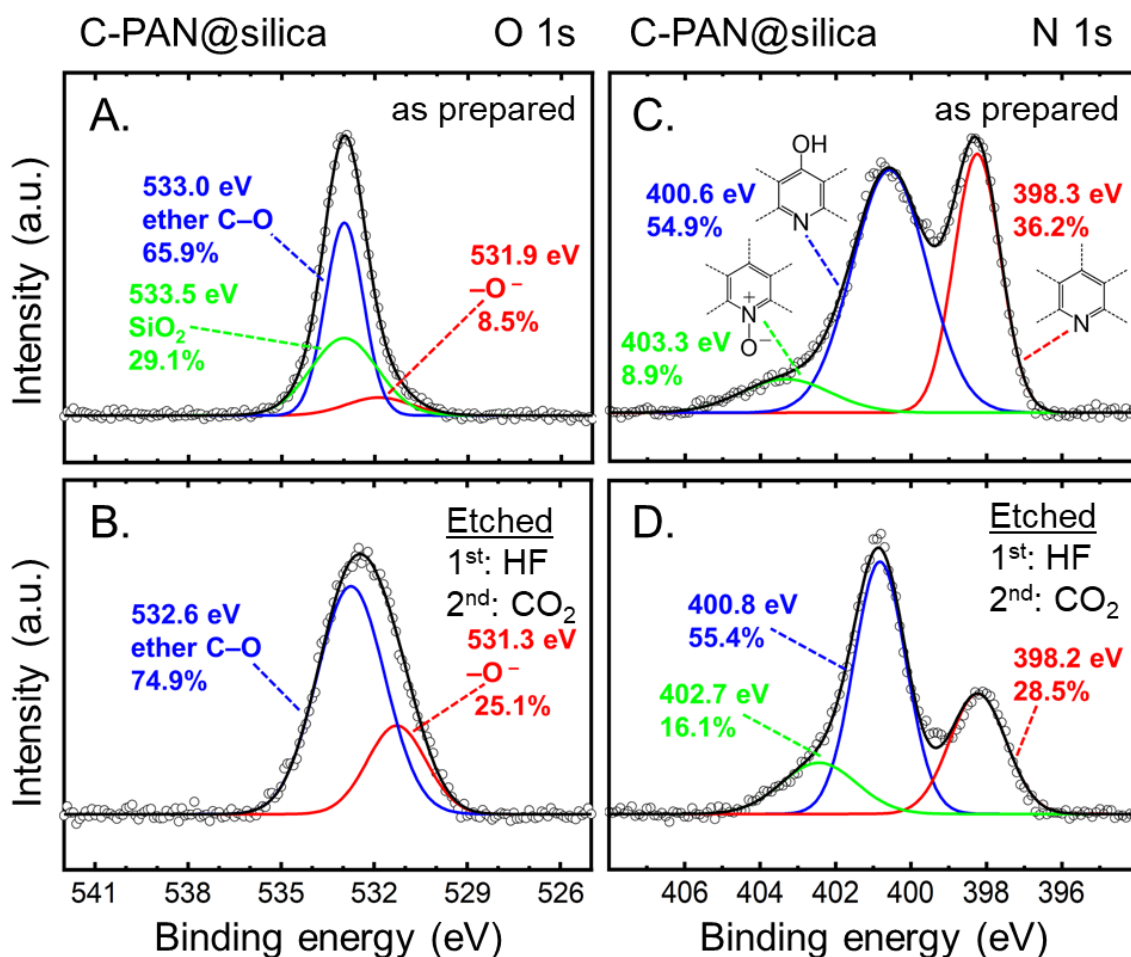
Figure 7. High resolution O 1s (left) and N 1s (right) XPS spectra of: (A,C) C-PAN-6×@silica(9:1); (B,D) C-PAN-6×@silica(9:1)-HF-CO$_2$. (For the Si 2p and C 1s spectra, and those of the corresponding –CO$_2$-HF samples, see Figures S.9–S.12 of Appendix V in Supporting Information.)

For example, the intensity of the latter went from 7.7% to 9.5% (case of C-PUA@silica-HF-CO$_2$ – compare Figures 6C and 6D), and from 8.9% to 16.1% (case of C-PAN@silica-HF-CO$_2$ – compare Figures 7C and 7D).

Similar evolutions in the O 1s and N 1s spectra were observed in double-etched C-PUA_or_PAN@silica-CO$_2$-HF samples (see Figures S.10 and S.11 of Appendix V in Supporting Information). The C 1s spectra (see Figure S.12 of Appendix V in Supporting

Information) support the functional groups identified from the O 1s and N 1s spectra showing peaks at 284.5 eV (aromatic C), 285.3 eV (C=N) and at 287-288 eV for C-O (ether).[43–45]

2.3. MATERIALS CHARACTERIZATION

2.3.1. Bulk Material Properties of PUA@silica, PAN@silica and Carbons thereof. Figure 8 shows typical PUA@silica and PAN@silica compacts along processing. The compacts were prepared with the same die and had the same dimensions. The photographs show that the compacts developed no defects, and the two series were practically indistinguishable at the various stages. Relevant property characterization data for all materials and all formulations considered in this study are summarized in Tables 4 and 5.

The bulk density (ρ_b) of PUA@silica xerogel compacts was in the range of 0.894-1.007 g cm^{-3}; the skeletal density (ρ_s) was in the range of 1.332–1.369 g cm^{-3}. Both ρ_b and ρ_s decreased as the amount of PUA in the composite increased (Table 4). The bulk density (ρ_b) of PAN@silica xerogel compacts was in the range of 1.282-1.441 g cm^{-3} while the skeletal density (ρ_s) was in the range of 1.182-1.373 g cm^{-3}. The trends in ρ_b and ρ_s as a function of the amount of PAN were similar to those in PUA@silica. The operation of squeezing the void space out of PAN@silica compacts was more effective than in PUA@silica. The percent open porosity, Π, calculated from bulk and skeletal density data via $\Pi = 100 \times (\rho_s - \rho_b) / \rho_s$, was in the range of 26-33% v/v for PUA@silica xerogel compacts, and 5-7% v/v for PAN@silica xerogel compacts.
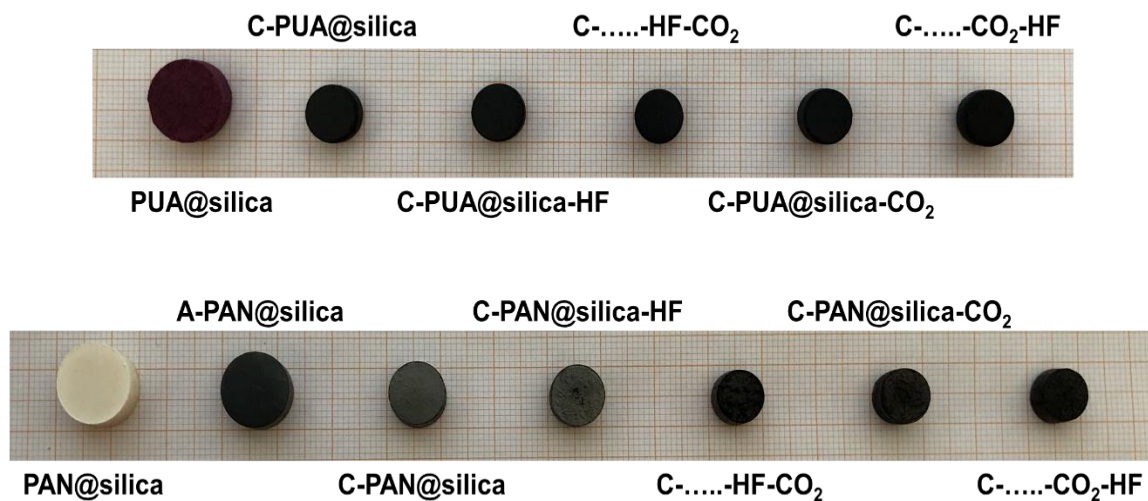
Figure 8. Photographs of PUA-3x@silica and PAN-6x@silica(9:1) compacts, abbreviated as PUA@silica and PAN@silica, respectively, along carbonization and etching.

The carbonization process of the PUA@silica xerogel compacts brought about a linear shrinkage of about 28% for all samples, yet because of the mass loss the porosity increased into the 38-51% v/v range.

For the PAN@silica xerogel compacts, the aromatization process brought about a linear shrinkage of $9 \pm 3\%$ and a slight-to-moderate increase in porosity into the range of 8-24% v/v. The subsequent carbonization of the A-PAN@silica compacts resulted in a total linear shrinkage of up to 22%, and an increase in porosity into the 22%–32% v/v range.

Table 4. Materials characterization data along processing of PUA-n×@silica xerogel compacts with n× =1.5×, 3×, 4.5×.

sample n×	linear shrinkage [%] [a,b]	bulk density, ρ_b [g cm^{-3}] [a]	skeletal density, ρ_s [g cm^{-3}] [c]	porosity, Π [% v/v] [d]	specific pore volume [cm³ g⁻¹]				BET surface area, σ [m² g⁻¹] [i]	average pore diameter [nm] [j]
					V_{Total} [e]	$V_{1.7\text{-}300\ nm}$ [f]	$V_{micropore}$ [g]	$V_{>300\ nm}$ [h]		
PUA-@silica										
1.5×	-	1.007 ± 0.002	1.369 ± 0.001	26	k	k	k	k	k	k
3×	-	0.967 ± 0.022	1.363 ± 0.002	29	k	k	k	k	k	k
4.5×	-	0.894 ± 0.010	1.332 ± 0.001	33	k	k	k	k	k	k
C-PUA@silica										
1.5×	28.37 ± 0.10	1.201 ± 0.015	1.934 ± 0.012	38	0.32	0.01	0.0 [l]	0.31	1.3 (1.1)	954
3×	28.02 ± 0.41	1.082 ± 0.021	1.953 ± 0.021	45	0.41	0.03	0.0 [l]	0.38	11 (3.4)	151
4.5×	28.45 ± 0.34	0.937 ± 0.014	1.901 ± 0.011	51	0.54	0.03	0.0 [l]	0.51	6.7 (0.6)	324
C-PUA@silica-HF										
1.5×	28.58 ± 0.13	0.828 ± 0.016	1.781 ± 0.016	54	0.65	0.32	k	m	394 (82)	6.6
3×	28.46 ± 0.85	0.730 ± 0.013	1.755 ± 0.009	58	0.80	0.13	k	m	353 (70)	9.1
4.5×	28.74 ± 0.55	0.654 ± 0.018	1.788 ± 0.003	63	0.97	0.33	k	m	285 (47)	14
C-PUA@silica-HF-CO₂										
1.5×	32.85 ± 0.83	0.411 ± 0.022	2.353 ± 0.078	83	2.01	0.72	0.74	0.55	1275 (628)	6.3
3×	34.08 ± 0.67	0.334 ± 0.026	1.943 ± 0.031	83	2.48	0.65	0.75	1.08	1724 (708)	6.2
4.5×	34.76 ± 0.47	0.380 ± 0.024	2.133 ± 0.048	82	2.16	1.09	0.86	0.21	1930 (708)	4.5
C-PUA@silica-CO₂										
1.5×	29.79 ± 0.20	1.197 ± 0.003	1.959 ± 0.005	39	0.33	0.02	k	m	170 (149)	7.9
3×	30.09 ± 0.87	1.079 ± 0.092	2.154 ± 0.007	50	0.46	0.11	k	m	404 (345)	4.7
4.5×	32.30 ± 0.46	0.876 ± 0.023	1.985 ± 0.002	56	0.64	0.10	0.25	0.29	845 (598)	3.1
C-PUA@silica-CO₂-HF										
1.5×	29.93 ± 0.16	0.749 ± 0.027	1.953 ± 0.017	62	0.82	0.51	0.21	0.10	1149 (669)	2.9
3×	31.15 ± 0.61	0.558 ± 0.035	1.846 ± 0.029	70	1.25	0.76	0.42	0.07	1220 (630)	4.1
4.5×	33.62 ± 0.39	0.510 ± 0.033	1.982 ± 0.013	74	1.46	0.68	0.62	0.16	1331 (611)	4.8

[a]Average of three samples. [b]Shrinkage relative to the PUA@silica xerogel compact. [c]Single sample, average of 50 measurements. [d]Porosity, Π = $100 \times (\rho_s - \rho_b)/ \rho_s$. [e]$V_{Total}$ was calculated via $V_{Total} = (1/\rho_b) - (1/\rho_s)$. [f]$V_{1.7\text{-}300\_nm}$ was calculated via the BJH desorption cumulative pore volume. [g]$V_{micropore}$ was calculated with N_2-sorption data at $P/P_o \leq 0.1$ using a low-pressure N_2 dosing routine at 77 K and the Dubinin–Radushkevich (DR) method for data analysis. [h]$V_{>300\ nm} = V_{Total} - (V_{micropore} + V_{1.7\text{-}300\_nm})$. [i]Numbers in (parentheses): Micropore surface areas calculated via t-plot method. [j]Average pore diameters were calculated via the $4 \times V/\sigma$ method by setting $V = V_{Total} = (1/\rho_b) - (1/\rho_s)$. [k]Too small – could not be measured. [l]Presumed. [m]Was not calculated because of [h] and [k].

Table 5. Materials characterization data along processing of PAN-n×@silica(x:y) xerogel compacts with n× = 2× and 6×, and (x:y) = (9:1) and (7:3).

sample n×, (x:y)	linear shrinkage [%] [a,b]	bulk density, ρ_b [g cm^{-3}] [a]	skeletal density, ρ_s [g cm^{-3}] [c]	porosity, Π [% v/v] [d]	specific pore volume [cm³ g⁻¹]				BET surface area, σ [m² g⁻¹] [i]	average pore diameter [nm] [j]
					V_{Total} [e]	$V_{1.7\text{-}300\_nm}$ [f]	$V_{micropore}$ [g]	$V_{>300\,nm}$ [h]		
PAN@silica										
6×, (9:1)	-	1.143 ± 0.012	1.223 ± 0.003	7	[k]	[k]	[k]	[k]	[k]	[k]
2×, (9:1)	-	1.122 ± 0.004	1.182 ± 0.002	5	[k]	[k]	[k]	[k]	[k]	[k]
6×, (7:3)	-	1.202 ± 0.029	1.288 ± 0.002	7	[k]	[k]	[k]	[k]	[k]	[k]
2×, (7:3)	-	1.282 ± 0.003	1.373 ± 0.002	7	[k]	[k]	[k]	[k]	[k]	[k]
A-PAN@silica										
6×, (9:1)	9.87 ± 0.51	1.314 ± 0.016	1.504 ± 0.002	13	[k]	[k]	[k]	[k]	[k]	[k]
2×, (9:1)	6.14 ± 0.25	1.426 ± 0.016	1.554 ± 0.005	8	[k]	[k]	[k]	[k]	[k]	[k]
6×, (7:3)	9.60 ± 0.12	1.294 ± 0.018	1.548 ± 0.003	17	[k]	[k]	[k]	[k]	[k]	[k]
2×, (7:3)	12.00 ± 0.16	1.351 ± 0.005	1.773 ± 0.001	24	[k]	[k]	[k]	[k]	[k]	[k]
C-PAN@silica										
6×, (9:1)	20.67 ± 0.74	1.339 ± 0.011	1.918 ± 0.007	30	0.23	0.00	0.0 [l]	0.23	0.47 (0.42)	1938
2×, (9:1)	14.56 ± 0.15	1.443 ± 0.025	1.851 ± 0.019	22	0.15	0.01	0.0 [l]	0.14	7.9 (4.8)	76.6
6×, (7:3)	20.87 ± 0.34	1.289 ± 0.013	1.905 ± 0.010	32	0.25	0.01	0.0 [l]	0.24	6.3 (2.3)	159
2×, (7:3)	22.25 ± 0.56	1.463 ± 0.025	1.997 ± 0.004	27	0.18	0.00	0.0 [l]	0.18	3.0 (1.9)	368
C-PAN@silica-HF										
6×, (9:1)	21.01 ± 0.37	1.139 ± 0.027	1.761 ± 0.009	35	0.31	0.18	[k]	[m]	193 (41)	6.5
2×, (9:1)	15.54 ± 0.24	0.679 ± 0.013	1.781 ± 0.006	62	0.91	0.57	[k]	[m]	474 (69)	7.7
6×, (7:3)	21.79 ± 0.28	0.778 ± 0.018	1.783 ± 0.004	56	0.73	0.60	[k]	[m]	442 (39)	5.6
2×, (7:3)	23.35 ± 0.62	0.639 ± 0.013	1.753 ± 0.008	64	1.00	0.56	[k]	[m]	618 (119)	6.5

Table 5. Materials characterization data along processing of PAN-n×@silica(x:y) xerogel compacts with n× = 2× and 6×, and (x:y) = (9:1) and (7:3) (cont.).

C-PAN@silica-HF-CO$_2$										
6×, (9:1)	25.57 ± 0.70	0.725 ± 0.025	1.878 ± 0.018	61	0.85	0.34	0.37	0.14	843 (491)	4.0
2×, (9:1)	26.45 ± 0.44	0.339 ± 0.029	1.814 ± 0.040	81	2.40	1.49	0.60	0.91	1433 (323)	6.7
6×, (7:3)	27.15 ± 1.47	0.630 ± 0.024	2.180 ± 0.022	71	1.13	0.44	0.42	0.27	1024 (535)	4.4
2×, (7:3)	34.34 ± 0.14	0.413 ± 0.030	2.340 ± 0.017	82	2.00	1.39	0.56	0.05	1419 (369)	5.6
C-PAN@silica-CO$_2$										
6×, (9:1)	23.92 ± 0.68	1.258 ± 0.025	2.132 ± 0.013	41	0.33	0.01	k	m	226 (187)	5.8
2×, (9:1)	19.62 ± 0.70	1.305 ± 0.026	2.193 ± 0.007	40	0.31	0.02	k	m	267 (124)	4.7
6×, (7:3)	28.45 ± 0.84	1.030 ± 0.012	2.099 ± 0.025	51	0.50	0.01	k	m	169 (98)	11.9
2×, (7:3)	26.67 ± 1.16	1.452 ± 0.016	2.036 ± 0.004	29	0.20	0.02	k	m	465 (361)	1.7
C-PAN@silica-CO$_2$-HF										
6×, (9:1)	24.02 ± 0.64	0.778 ± 0.055	1.799 ± 0.001	57	0.73	0.24	0.29	0.20	416 (214)	7.0
2×, (9:1)	20.19 ± 0.45	0.506 ± 0.019	1.968 ± 0.014	74	1.47	0.77	0.42	0.28	1167 (264)	5.0
6×, (7:3)	26.60 ± 0.89	0.621 ± 0.010	1.919 ± 0.013	68	1.09	0.46	0.44	0.19	994 (451)	4.4
2×, (7:3)	28.01 ± 1.20	0.576 ± 0.014	1.846 ± 0.005	69	1.19	0.72	0.43	0.04	1142 (263)	4.2

[a]Average of three samples. [b]Shrinkage relative to the PAN@silica xerogel compact. [c]Single sample, average of 50 measurements. [d]Porosity, $\Pi = 100 \times (\rho_s - \rho_b)/\rho_s$. [e]$V_{Total}$ was calculated via $V_{Total} = (1/\rho_b) - (1/\rho_s)$. [f]$V_{1.7-300\_nm}$ was calculated via the BJH desorption cumulative pore volume. [g]$V_{micropore}$ was calculated with N_2-sorption data at $P/P_o \leq 0.1$ using a low-pressure N_2 dosing routine at 77 K and the Dubinin–Radushkevich (DR) method for data analysis. [h]$V_{>300\ nm} = V_{Total} - (V_{micropore} + V_{1.7-300\_nm})$. [i]Numbers in (parentheses): Micropore surface areas calculated via t-plot method.

Overall, although the loss of mass due to the carbonization process did create some void space, the porosity never exceeded 51% v/v (case of C-PUA@silica), while in C-PAN@silica the porosity was significantly lower, never exceeded 32% v/v. In contrast, the subsequent etching processes with HF and CO_2, and especially their sequence, had a profound effect on the porosity, surface areas and pore size distribution.

After etching C-PUA@silica compacts with HF, ρ_b and ρ_s decreased as expected from the fact that silica was removed. Samples did not shrink further, and the porosities of C-PUA@silica-HF were higher (in the 54%–63% v/v range) relative to those of C-PUA@silica (38%–51% v/v). On the other hand, when C-PUA@silica samples were etched with CO_2 first, linear shrinkage increased somewhat, which apparently compensated for the mass loss, and ρ_b remained about the same; ρ_s, however, increased consistent with removing carbon while silica stayed behind. The porosities of C-PUA@silica-CO_2 were slightly higher (39%–56% v/v) than those of C-PUA@silica (38%–51% v/v) and slightly lower than those of C-PUA@silica-HF (54%–63% v/v).

What was remarkable at this point though was that further etching of C-PUA@silica-HF with CO_2 propelled the porosity of the resulting C-PUA-silica-HF-CO_2 into the 82%–83% v/v range. On the contrary, the porosity of the C-PUA-CO_2-HF samples remained significantly lower, in the 62%–74% v/v range. Meanwhile, the shrinkages of all double-etched samples converged to the level noted for the samples etched first with CO_2 (i.e., of C-PUA@silica-CO_2).
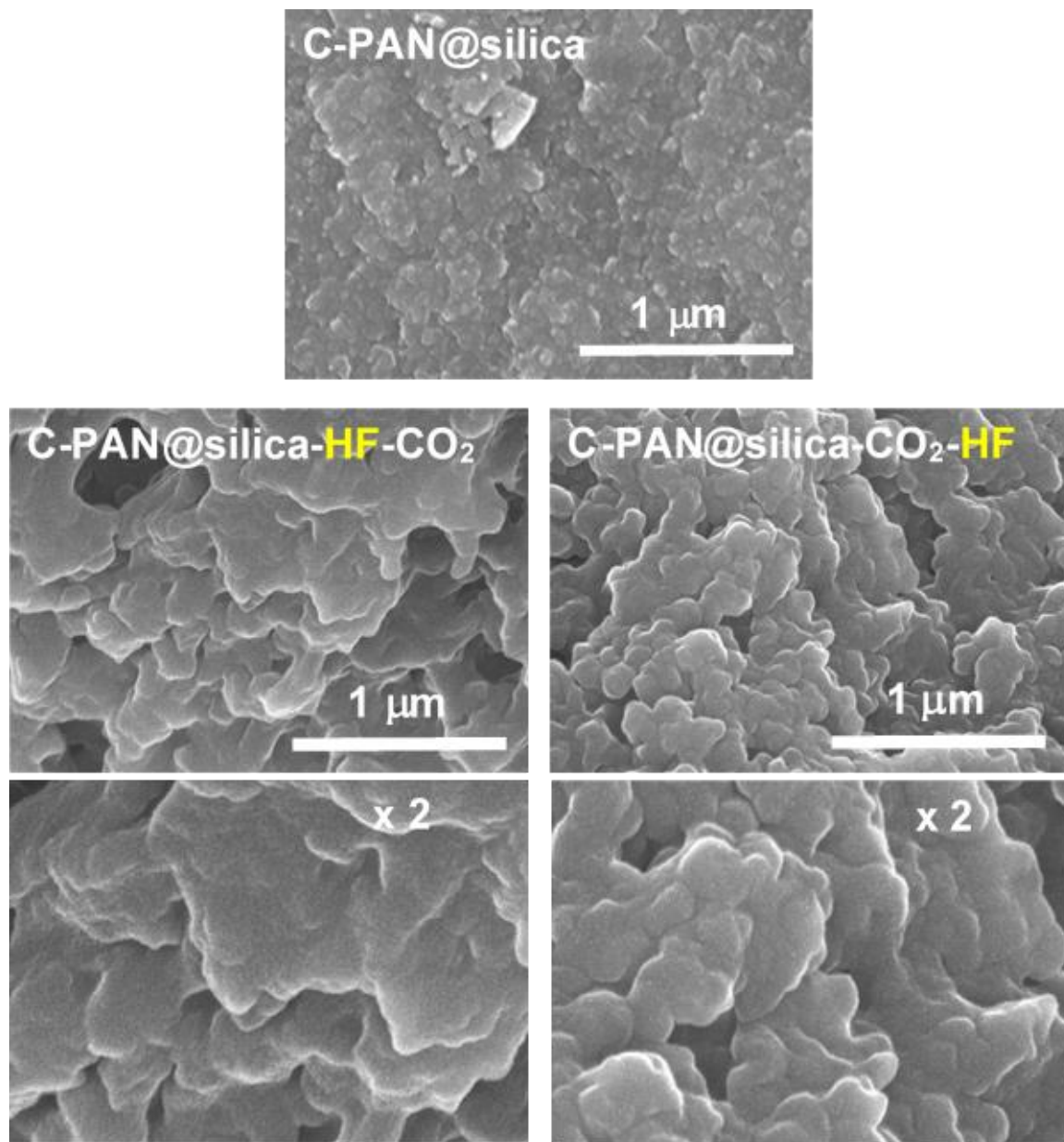
Figure 9. Typical SEM images along processing represented by carbonized C-PAN-6×@silica(9:1) and its double-etched derivatives at two different magnifications, as indicated. (The etching process that applied first is highlighted yellow in the material name.)

Similarly, after HF-etching C-PAN@silica compacts shrank by about an additional 5% in linear dimensions, and both ρ_b and ρ_s decreased due to the mass ensuing loss (Table

5). The porosities of C-PAN@silica-HF were higher (in the 35%–64% v/v range) relative to those of C-PAN@silica (22%–32% v/v). Consistent with what was found with etching of C-PUA@silica, if C-PAN@silica is etched with CO_2 first, the shrinkage is higher (about an additional 25%) and the porosity is lower (in the 29%-51% v/v range) than the porosity of the carbon samples etched first with HF (in the 35%–64% v/v range). A second etching with CO_2, or HF, respectively, equalized the shrinkages, and consistent with what was found with double etching of the C-PUA@silica samples, the porosities of the samples etched with HF first, i.e., of C-PAN@silica-HF-CO_2, were significantly higher (in the range of 61%–82% v/v) than the porosities of the C-PAN@silica-CO_2-HF (in the 57%–74% v/v range).

The differences in the porosities of the terminal carbons as a function of the sequence of treatment with HF versus CO_2 were also accompanied by differences in the pore structure and surface areas.

2.3.2. The Nanostructure of Carbon Aerogels Derived from PUA@silica and PAN@silica Compacts, and a Model for the Etching Processes. Microscopically (SEM), internal cleaved surfaces of all PUA@silica and PAN@silica compacts were smooth. Some roughness appeared after carbonization, yet the materials remained compact. Void space and some structure at the sub-micron level were generated after etching with HF and CO_2, but the new surfaces still appeared smooth. Those changes are illustrated in Figure 9 using C-PAN-6×@silica(9:1) and its double-etched derivatives as an example. One definite conclusion from SEM imaging is that the etching processes generated some macroporosity, but owing to the apparent smoothness of the macroporous

surfaces it was decided to rely on N_2 sorption as a higher resolution probe of the pore structure in the meso- and micropore size regimes.

The evolution of the N_2-sorption isotherms of C-PUA@silica and C-PAN@silica upon further treatment with HF and then CO_2, or with CO_2 and then HF is shown in Figures 10 and 11, respectively. Both systems follow the same pattern. To begin with, the adsorption of N_2 by either C-PUA@silica or C-PAN@silica was negligibly small, suggesting that the porosities reported above (38%–51% v/v, and 22%–32% v/v, respectively) corresponded to macropores with >300 nm in diameter. Things got different by a first treatment with HF versus CO_2.

In both cases the N_2 uptake increased, but only the isotherms of C-PUA@silica-HF and C-PAN@silica-HF showed the characteristic hysteresis loops of mesoporosity; in both types of materials a first treatment with CO_2 yielded a sharp rise of the isotherms at low pressures, characterizing microporosity (cases of C-PUA@silica-CO_2 and C-PAN@silica-CO_2). Indeed, BJH analysis of the desorption branches of the isotherms of all four carbons (i.e., of C-PUA@silica-HF or –CO_2 and C-PAN@silica-HF or –CO_2) yielded meaningful pore size distributions in the mesopore range only for C-PUA@silica-HF and C-PAN@silica-HF (see Insets in Figures 10 and 11). Subsequent treatment with the second etching agent resulted in materials with N_2-sorption isotherms indicating the presence of both mesopores and micropores, irrespective of their origin.

The BJH plots of all four terminal doubly etched materials show similar pore size distributions centered at similar pore diameters, a little less than 10 nm; the distribution maxima were slightly larger in materials etched first with HF (blue lines – see Figure 12). A final note on the isotherms is that the shape of the desorption branches of all C-

PAN@silica-HF, -HF-CO_2 and –CO_2-HF indicates ink-bottle types of mesopores. That kind of shape was not as well-defined in the corresponding cases of the PUA-derived samples.
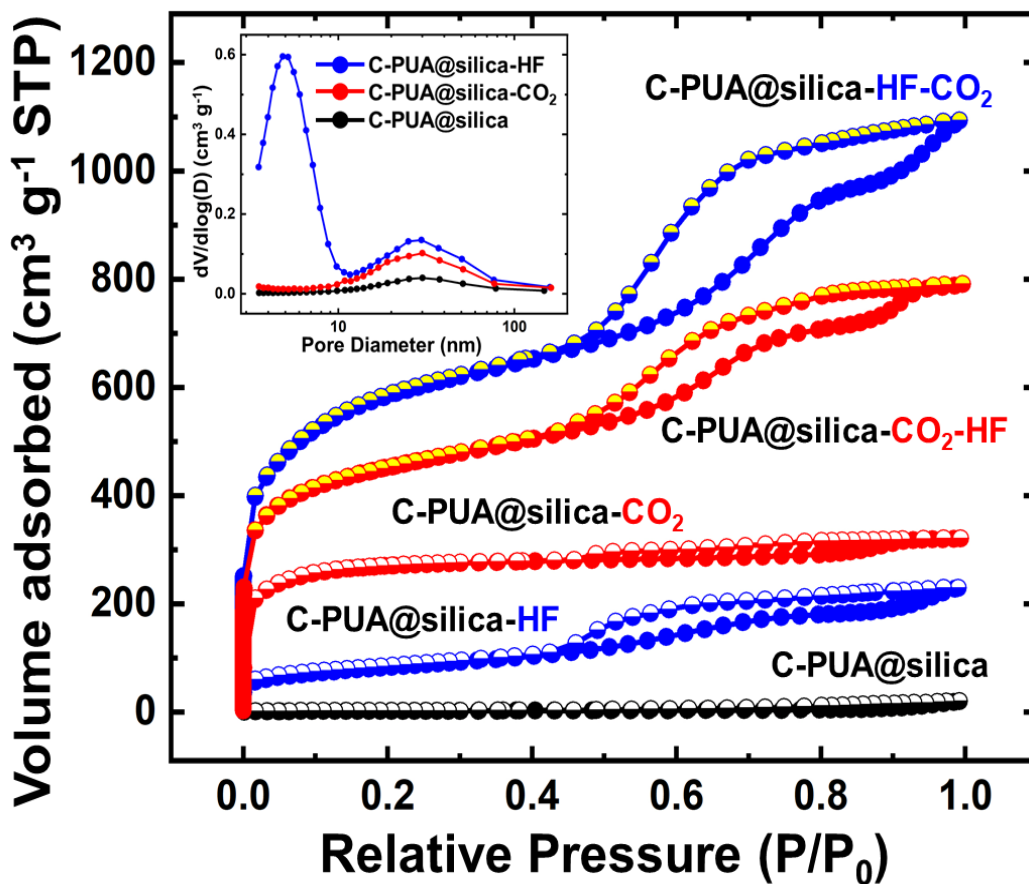
Figure 10. N_2-sorption isotherms at 77 K of carbonized C-PUA-4.5×@silica compacts after each processing step. (Inset: BJH pore size distributions for the lower three isotherms according to the color coding.)

Consistently, the total volume of N_2 uptaken by samples etched first with HF, that is C-PUA@silica-HF-CO_2 and C-PAN@silica-HF-CO_2, was significantly higher than that of C-PUA@silica-CO_2-HF and C-PAN@silica-CO_2-HF.
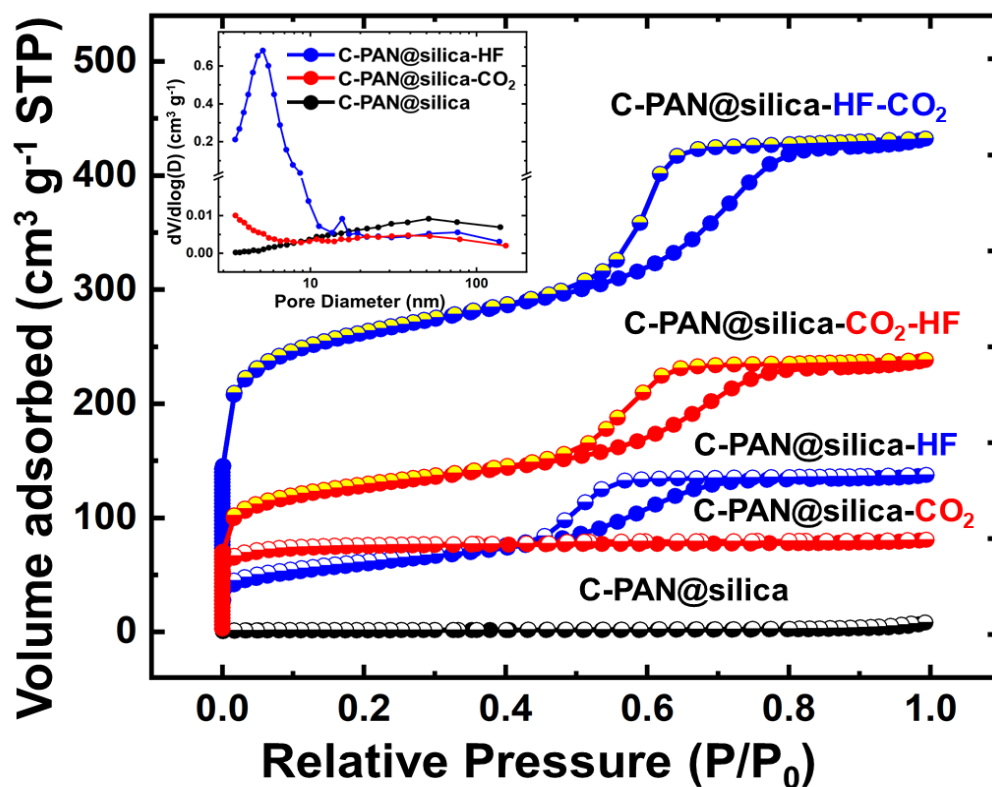
Figure 11. N₂-sorption isotherms at 77 K of carbonized C-PAN-6×@silica-(9:1) compacts after each processing step. (Inset: BJH pore size distributions for the lower three isotherms according to the color coding.)
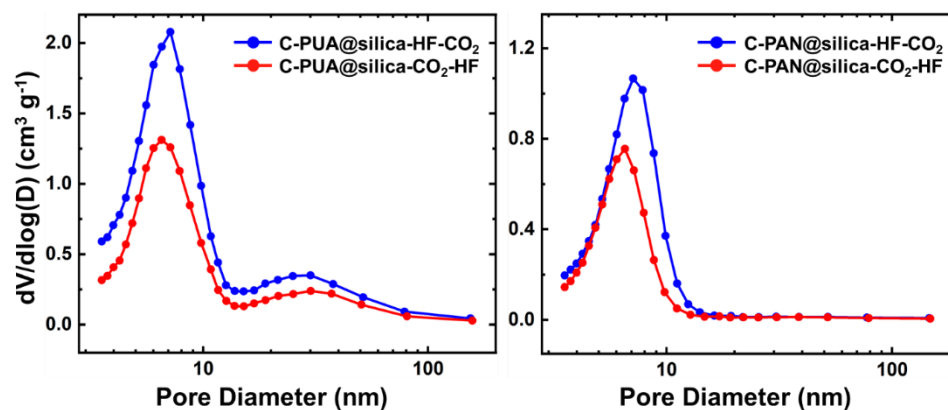
Figure 12. Pore-size distributions using the BJH desorption method of carbonized and double-etched compacts: C-PUA-4.5×@silica (left) and C-PAN-6×@silica(9:1) (right). The etching sequence is color coded as shown in the legends inside the frames: HF-CO₂ in blue, versus CO₂-HF in red.

That behavior matched the trends in the porosity as described in the previous section, and is also reflected on the corresponding surface areas (Tables 4 and 5). Specifically, the BET surface areas of C-PUA@silica and C-PAN@silica were very low (1.3–11.0 m^2 g^{-1}, and 0.47–7.9 m^2 g^{-1}, respectively). Upon treatment with HF the BET surface area of C-PUA@silica-HF jumped in the 285–394 m^2 g^{-1} range (20% assigned to micropores) while the BET surface area of C-PAN@silica-HF jumped in the 193–618 m^2 g^{-1} range (only 5% to 20% was assigned to micropores). On the other hand, a first etch with CO_2 increased the surface areas of the corresponding samples roughly up to the same ranges as the HF treatment did, however, in the case of C-PUA@silica-CO_2 over 70% of the new surface area was assigned to micropores, and 50%–80% in the case of C-PAN@silica-CO_2.

Treatment with the second etching agent propelled BET surface areas up to 1930 m^2 g^{-1} (case of C-PUA-4.5×@silica-HF-CO_2), 37% of which was assigned to micropores, and up to 1433 m^2 g^{-1} (22% assigned to micropores – case of C-PAN-2×@silica(9:1)-HF-CO_2). Complete data for all samples are presented in Tables 4 and 5 for reference and further analysis by the interested reader.

The pore structure of the double-etched samples was also probed with low-pressure N_2-sorption using a low-pressure transducer. The derived micropore volumes, $V_{micropore}$, are included in Tables 4 and 5, and in all cases $V_{1.7–300\_nm} + V_{micropore} < V_{Total}$ (the latter calculated from bulk and skeletal density data via $V_{Total} = (1/\rho_b) – (1/\rho_s)$), meaning that, in agreement with conclusions arrived from SEM, all samples included a certain amount of macropores with sizes > 300 nm. A second observation is that in general, $V_{micropore}$ were lower in samples etched first with CO_2.

Overall, percent mass loss, porosity values (Π), specific pore volumes V_{Total} and $V_{\text{micropore}}$, and BET surface areas were higher in double-etched samples that were treated first with HF. Since the mechanism of action of CO_2 is via a comproportionation reaction with C to CO, it is reasonable to suggest that silica protects the carbon is in contact with. As illustrated in Scheme 6, if silica is removed first, more surface area of carbon becomes accessible to the etching effect of CO_2.

2.4. PROBING MICROPOROSITY WITH CO_2, AND APPLICATION OF DOUBLY-ETCHED PUA@SILICA– AND PAN@SILICA–DERIVED CARBON AEROGELS TO HIGHLY SELECTIVE CO_2 CAPTURE

Conventional carbon aerogels with microporosity lined with O and N heteroatoms have shown high capacity for CO_2 adsorption.[1,8] Since this property has a clearly defined application in CO_2 sequestration, it was deemed suitable as a basis for comparison with other conventional carbon aerogels obtained via direct pyrolysis of polymeric aerogels. Fully reversible, with no hysteresis, CO_2 adsorption isotherms at two different temperatures (273 K and 298 K) and up to 1 bar (corresponding to partial pressure $P/P_o = 0.03$) of all carbon samples of this study double-etched in either sequence are shown in Figure 13. Cross-referencing with Tables 4 and 5, maximum CO_2 uptake (from Figure 13) in both the PUA– and PAN–derived, and double-etched (in either sequence) carbon aerogel systems was observed with the lower-density, higher-porosity, higher micropore volume and lower micropore surface area samples, namely with C-PUA-4.5×@silica-HF-CO_2 (9.15 mmol g^{-1}) and C-PUA-4.5×@silica-CO_2-HF (6.13 mmol g^{-1}), as well as with C-PAN-2×@silica(7:3)-HF-CO_2 (6.56 mmol g^{-1}) and C-PAN-2×@silica(7:3)-CO_2-HF
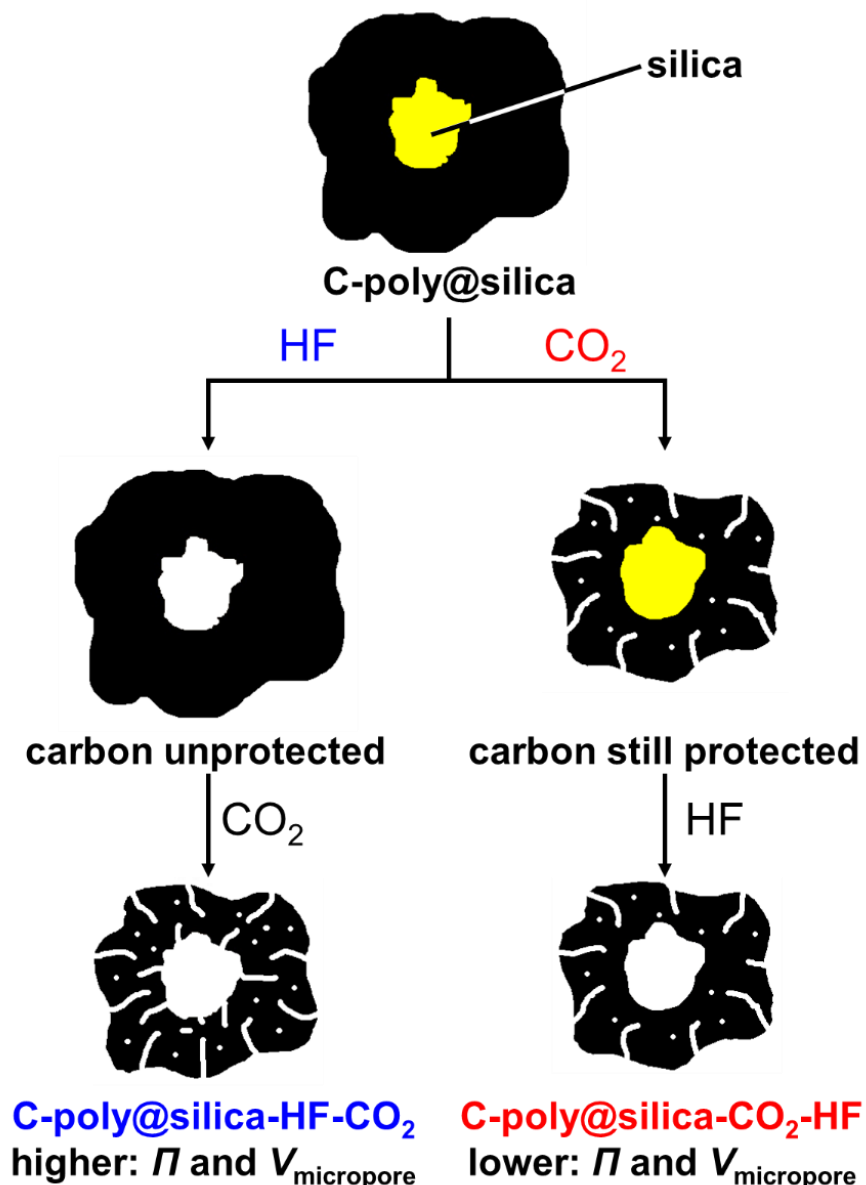
Scheme 6. Etching model of carbonized C-PUA@silica and C-PAN@silica with HF and CO_2 in either sequence. (poly = PUA or PAN; micropores are shown as white wiggly lines penetrating into the bulk of carbon.)

(5.30 mmol g^{-1}). PAN–derived carbon aerogels adsorbed lower amounts of CO_2 than their PUA-derived analogues. Consistently, a lower CO_2 uptake was observed with samples obtained through the CO_2/HF etching sequence compared with their counterparts obtained

through the HF/CO_2 sequence. Overall, most samples displayed levels of CO_2 uptake that were amongst what has been observed before with other carbon aerogels (around 5-6 mmol g^{-1}).[1] By the same token, however, the best performer, C-PUA-4.5×@silica-HF-CO_2 (9.15 mmol g^{-1}), was above the best performers in the literature (e.g., phenolic resin-based activated carbon microspheres,[46] or carbon nanotube superstructures),[47] yet lower than certain CO_2-etched carbon aerogels from pyrolysis of low-density resorcinol-formaldehyde aerogels, which have shown CO_2 uptake up to 14.8 ± 3.9 mmol g^{-1}.[1]
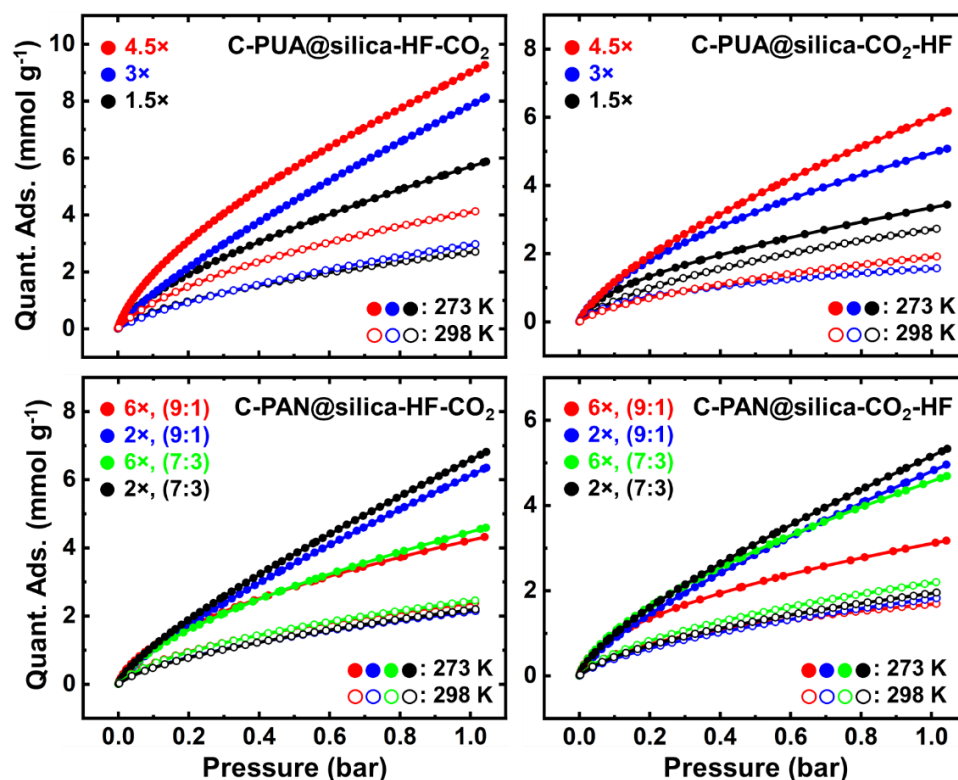
Figure 13. CO_2 adsorption isotherms of all etched carbon aerogels of this study at two different temperatures as shown. (For clarity only the adsorption branches are shown, but all isotherms were reversible without hysteresis).

The involvement of the micropores in the CO_2 uptake was investigated by comparing the experimental CO_2 uptake with values calculated by assuming: (a) monolayer coverage of the BET surface area with CO_2 (0.17 nm^2 per molecule);[48] monolayer coverage of only the micropore surface area; and (c) micropore volume filling with CO_2 in a state that resembles liquid CO_2 (density of the state = 1.023 g cm^{-3}).[49,50] Micropore volumes were calculated using the Dubinin-Radushkevich (DR) method on low-pressure N_2-sorption data at 77 K and on CO_2 adsorption data at 0 ℃, or the Density Functional Theory (DFT) method on the CO_2 adsorption data at 0 ℃.

All relevant data are summarized in Table 6. It is noted, however, that since the $DR(CO_2)$ data are not independent of the CO_2 uptake, they were not considered in pore filling with CO_2; instead, they were used for cross checking the consistency of the pore volumes calculated via the $DR(N_2)$ method, and it is noted that in general the two micropore volumes agree with one another. Subsequently, both $DR(N_2)$ and $DR(CO_2)$ were used for calculating average micropore sizes.

The amounts of CO_2 uptaken at the highest points of the isotherms of Figure 13 were lower than the amounts of CO_2 that would provide monolayer coverage of the corresponding BET surface areas. On the other hand, independently of the polymer system or the etching sequence, all double-etched materials showed similar micropore size distributions by the DFT method applied on the CO_2 adsorption isotherms (see Figure S.13 of Appendix VI in Supporting Information), and similar specific micropore volumes (all around 0.08-0.12 cm^3 g^{-1}); filling those DFT-derived micropore volumes with CO_2 typically requires only 2–3 mmol g^{-1} of CO_2, exception being the case of C-PUA-4.5×@silica-HF-CO_2 (requires 4.2 mmol g^{-1}), yet in all cases the amount of CO_2 required

to fill those micropore volumes was much below the experimentally observed values of CO_2 uptake (Table 6). Then, as summarized in Figure 14, in general, we observe that whenever the average micropore diameter from the $DR(N_2)$ and the $DR(CO_2)$ methods was approximately 3-4 nm, the amount of CO_2 uptaken was found near the amount required for monolayer coverage of the micropores.

When the average micropore diameter was < 3 nm, the amount of CO_2 uptaken was less, to significantly lesser than what was required for monolayer coverage of the micropores; when the average micropore diameter was > 4 nm the CO_2 uptaken was more, to significantly more than the amount required for monolayer coverage of the micropores, yet it always remained less than the amount of CO_2 required to fill the "micropore" volumes that were calculated with the $DR(N_2)$ method. In other words, CO_2 seems to fill all sub-nanometer micropores (accounted for by the $DFT(CO_2)$ method), and continues to cover the surfaces of small pores falling in the region between what is still defined formally as micropores and the small end of mesopores.

In that region there appears to be a pore-size threshold (in the 3–4 nm range), below which micropores are not coated with CO_2 completely, and above which CO_2 keeps on accumulating on already adsorbed CO_2, but never fills those small mesopores completely. It is speculated that in both cases the ultimate amount of CO_2 uptaken is controlled by the fact that the entropic penalty of new CO_2 molecules entering the small pores can no longer be ignored.[51]
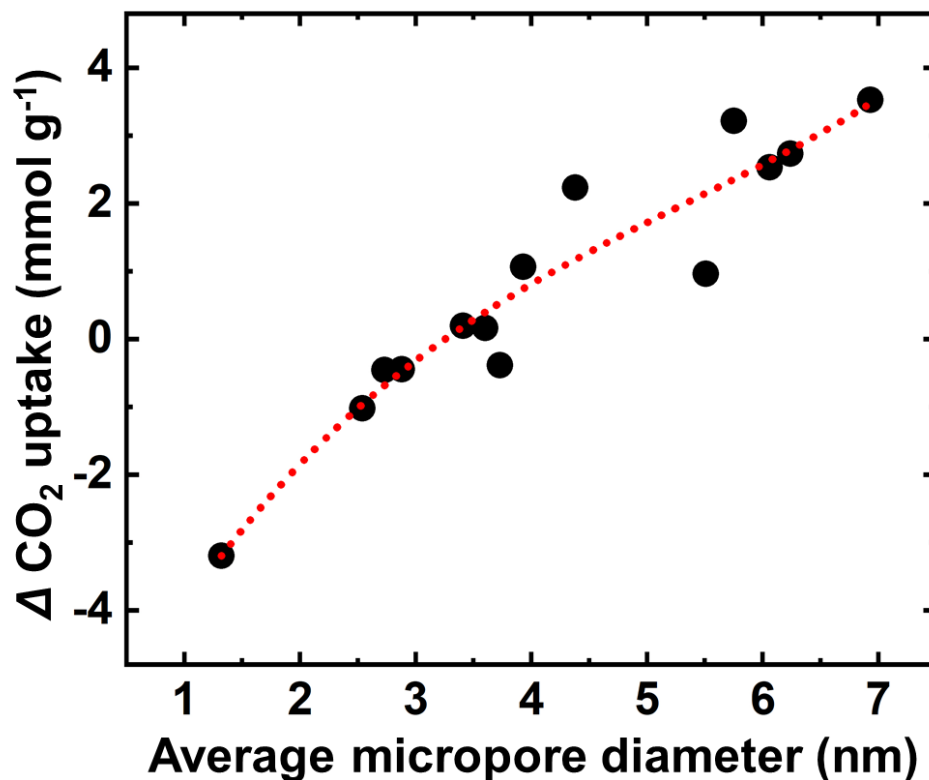
Figure 14. Differential (Δ) experimental from expected CO_2 uptake versus average micropore diameter for all carbonized and double-etched PUA@silica and PAN@silica xerogel compacts. The expected CO_2 uptake was calculated from micropore monolayer coverage (see footnote "g" in Table 6). Average micropore diameters were calculated as described in footnote "e" of Table 6. Dotted line is a third-order polynomial fit.

Further insight in the interaction of CO_2 with the surface of the carbon aerogels was obtained by calculating the isosteric heat of adsorption of CO_2 (Q_{st}) by the four doubly etched-carbon aerogels with the highest CO_2 uptake capacities amongst their peers: C-PUA-4.5×@silica-HF-CO_2 & -CO_2-HF, and C-PAN-2×@silica(7:3)-HF-CO_2 & -CO_2-HF. Q_{st} is defined as the negative of the differential change in the total enthalpy of a closed system, and values were calculated as a function of the CO_2 uptake using Virial fitting on the CO_2 adsorption isotherms at two different temperatures (273 K and 298 K – see Experimental Section and Appendix VII in Supporting Information).

Table 6. Micropore analysis and CO_2 uptake at 0 °C by all carbonized and double-etched xerogel compacts.

sample	Specific micropore volume [cm³ g⁻¹]			Micropore diameter [nm] via 4 × V/(micropore area)[d]			CO₂ uptake [mmol g⁻¹] at 273 K, 1 bar				
							measured experimentally	calculated from			
								surface areas		specific micropore volumes	
	DR(N₂)[a]	DR(CO₂)[b]	DFT(CO₂)[c]	V from DR(N₂)	V from DR(CO₂)	average[e]		BET[f]	Micropore[g]	DR(N₂)[h]	DFT(CO₂)[i]
C-PUA@silica-HF-CO₂											
1.5×	0.74	0.43 ± 0.01	0.11 ± 0.01	4.71	2.74 ± 0.07	3.73	5.75 ± 0.17	12.5	6.1	17.2	2.6 ± 0.1
3×	0.75	0.64 ± 0.03	0.12 ± 0.01	4.24	3.64 ± 0.15	3.93	7.98 ± 0.15	16.8	6.9	17.4	2.7 ± 0.1
4.5×	0.86	0.69 ± 0.01	0.18 ± 0.01	4.86	3.91 ± 0.05	4.38	9.15 ± 0.10	18.9	6.9	20.0	4.2 ± 0.1
C-PUA@silica-CO₂-HF											
1.5×	0.21	0.23 ± 0.01	0.08 ± 0.01	1.26	1.49 ± 0.04	1.32	3.34 ± 0.10	11.2	6.5	4.9	1.8 ± 0.1
3×	0.42	0.38 ± 0.01	0.12 ± 0.01	2.67	2.27 ± 0.03	2.54	5.13 ± 0.09	11.9	6.2	9.8	2.7 ± 0.1
4.5×	0.62	0.48 ± 0.02	0.08 ± 0.03	4.06	2.74 ± 0.17	3.60	6.13 ± 0.07	13.0	6.0	14.4	2.0 ± 0.4
C-PAN@silica-HF-CO₂											
6×, (9:1)	0.37	0.30 ± 0.01	0.11 ± 0.01	3.01	2.46 ± 0.07	2.73	4.34 ± 0.11	8.2	4.8	8.6	2.6 ± 0.1
2×, (9:1)	0.60	0.52 ± 0.02	0.10 ± 0.01	7.43	6.39 ± 0.05	6.93	6.68 ± 0.29	14.0	3.2	14.0	2.3 ± 0.1
6×, (7:3)	0.42	0.35 ± 0.01	0.11 ± 0.01	3.14	2.58 ± 0.04	2.88	4.78 ± 0.14	10.0	5.2	9.8	2.5 ± 0.1
2×, (7:3)	0.56	0.50 ± 0.02	0.10 ± 0.01	6.07	5.43 ± 0.22	5.75	6.82 ± 0.12	13.9	3.6	13.0	2.4 ± 0.1
C-PAN@silica-CO₂-HF											
6×, (9:1)	0.29	0.30 ± 0.01	0.08 ± 0.01	5.42	5.65 ± 0.16	5.51	3.05 ± 0.09	4.1	2.1	6.7	1.9 ± 0.1
2×, (9:1)	0.42	0.38 ± 0.02	0.08 ± 0.01	6.36	5.78 ± 0.35	6.06	5.11 ± 0.27	11.4	2.6	9.8	1.9 ± 0.1
6×, (7:3)	0.44	0.33 ± 0.01	0.10 ± 0.01	3.90	2.95 ± 0.06	3.41	4.60 ± 0.08	9.7	4.4	10.2	2.3 ± 0.1
2×, (7:3)	0.43	0.39 ± 0.01	0.09 ± 0.01	6.54	5.86 ± 0.020	6.24	5.30 ± 0.12	11.2	2.6	10.0	2.1 ± 0.1

[a]Via the Dubinin–Radushkevich (DR) method from N_2-sorption data obtained at 77 K using a low-pressure transducer (P/P$_o$ ≤ 0.01). Single experiment; [b]Via the DR method from CO_2 adsorption data at 273 K up to relative pressure of 0.015; [c]Using the same data as in footnote (b) and applying the DFT method. Pore volumes correspond to pores <1 nm in size; [d]Calculated as indicated using the micropore surfaces areas obtained from N_2-sorption data via the t-plot method; [e]Calculated via 4 × V/(micropore area), where $V = [V_{DR(N2)} + V_{DR(CO2)}]/2$; [f]Calculated by dividing the BET surface area over the CO_2 cross sectional area (0.17 nm^2),[48] over the Avogadro's number; [g]Calculated by dividing the micropore surface area obtained from N_2-sorption data via the t-plot method over the CO_2 cross sectional area (0.17 nm^2), over Avogadro's number; [h,i]Calculated by assuming that micropore volumes (via the DR(N_2) and the DFT(CO_2) methods – see footnotes a and c, respectively) are filled with liquid CO_2 (the density of liquid CO_2 at 273 K, was taken equal to the density of adsorbed CO_2 (1.023 g cm^{-3}).[49,50] Errors were calculated by applying rules of propagation of error.

The plots of the Q_{st} values of the four materials versus the CO_2 uptake are shown in Figure 15. The intercept of any Q_{st} plot at zero CO_2 uptake is referred to as Q_0, and is the energy of interaction of CO_2 with the surface of the adsorber. In general, Q_0 values >40 kJ mol^{-1} are generated by chemisorption while lower values by physisorption.

The Q_0 values of the four double-etched samples, C-PUA-4.5×@silica-HF-CO$_2$ & -CO$_2$-HF and C-PAN-2×@silica(7:3)-HF-CO$_2$ & -CO$_2$-HF, were in the range of 27-32 kJ mol^{-1} (see Table S.4 of Appendix VII in Supporting Information). Those values can be attributed to ether weak chemisorption or strong physisorption, and their numerical proximity reflects the fact that irrespective of the polymeric origin of the carbons implemented in this study, or their etching sequence, the surfaces of all systems are lined with the same functional groups (refer to the XPS data in Section 2.2.3 above, and in Appendix V of the Supporting Information). Physisorption may involve quadrupolar interactions between quadrupolar CO_2 and quadrupolar nitrogen-rich sites.[52] Those interactions are favored in smaller micropores (yielding higher Q_0 values)[53] where quadrupolar fields come closer to one another and may interact better with the adsorbate.[54,55] On the other hand, a special kind of weak chemisorption of CO_2 on the surface of carbon may involve nucleophilic attack of surface $-O^-$ (for example from nitroxide) and $-N:$ (for example from pyridinic and pyridonic sites) onto CO_2 toward surface-bound carbonate or carbamate, respectively. The reaction of CO_2 with surface $-O^-$ is nearly isoenthalpic, while its reaction with $-N:$ is slightly endothermic.[1,8]
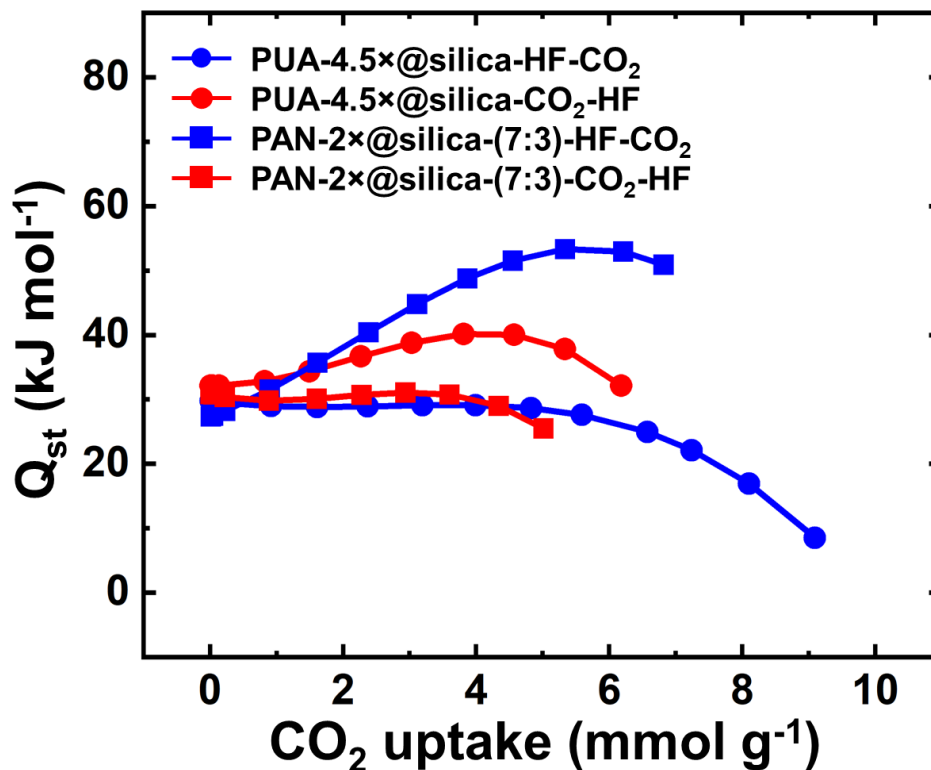
Figure 15. Isosteric heats of CO_2 adsorption of the four samples of this study with the highest CO_2 uptakes as a function of the latter. (For clarity, only one every four points is shown.)

Beyond initial interaction with the surface walls, it is noted from Figure 14 that in the cases of C-PUA-4.5×@silica-HF-CO_2 and C-PAN-2×@silica(7:3)-CO_2-HF the isosteric heats, Q_{st}, remain about flat until about monolayer coverage (~6 mmol g^{-1}) and afterwards curve downwards – meaning that pore filling starts becoming less favorable. Incidentally, those are also the samples with the highest CO_2 uptake amongst all the PUA- and PAN-derived carbons, respectively (Table 6). On the other hand, at first the Q_{st} values of the other two samples, C-PUA-4.5×@silica-CO_2-HF and C-PAN-2×@silica(7:3)-HF-CO_2, take upward trends as the CO_2 uptake increases, but again they both turn downwards as pore filling progresses. Interestingly, the former two samples, whose Q_{st} plots remain

substantially flat, happen to have surfaces O-rich, while the latter two samples, whose Q_{st}

plots curve upwards, are N-rich: by XPS, the O:N ratios of the HF-CO_2 etched C-PUA and

C-PAN are 1.85 versus 0.43, respectively, while the O:N ratio of CO_2-HF etched C-PUA

and C-PAN are 0.69 versus 1.02, respectively (see Table S.2 in Appendix V of the

Supporting Information).

A CO_2 uptake model consistent with all data suggests that in the case of O-rich C-

PUA-4.5×@silica-HF-CO_2 and C-PAN-2×@silica(7:3)-CO_2-HF, CO_2 is mostly adsorbed

via energy-neutral Eq. 1 with surface $-O^-$, and continues for sometime

$$-O^- + CO_2 \longrightarrow surface-O-CO-O^- \tag{1}$$
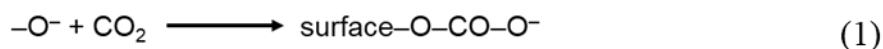
beyond monolayer coverage according to also energy neutral Eq. 2.

$$-O^- + CO_2 \longrightarrow surface-O-CO-O^- \xrightarrow{CO_2} surface-O-CO-O-CO-O^- \tag{2}$$
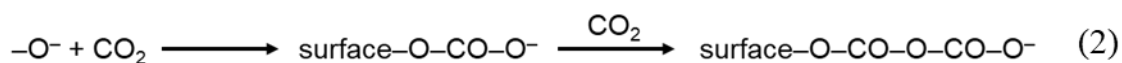
Since the micropore volume of PUA-4.5×@silica-HF-CO_2 according to the DR(N_2)

method is larger (0.86 cm^3 g^{-1}) than the micropore volume of C-PAN-2×@silica(7:3)-CO_2-

HF (0.43 cm^3 g^{-1}), eventually filling of the former proceeds beyond filling of the latter,

resulting in 9.15 mmol g^{-1} versus 5.30 mmol g^{-1} of CO_2 uptake, respectively.

On the other hand, in the case of double-etched carbon aerogels with N-rich

surfaces, C-PUA-4.5×@silica-CO_2-HF and C-PAN-2×@silica(7:3)-HF-CO_2, the

micropore volume of the latter material is less (0.37 cm^3 g^{-1}) than that of the former (0.62

cm^3 g^{-1}), therefore it gets filled faster, the favorable quadrupole interactions increase as the

free space decreases, and consequently the Q_{st} curve moves upward; in fact the CO_2 uptake

by C-PAN-2×@silica(7:3)-HF-CO_2 (6.82 mmol g^{-1}) is well above what is needed for

monolayer coverage of its micropores (3.6 mmol g^{-1}) and close to what is needed for filling them completely (8.6 mmol g^{-1}).

Overall, the lining of the pores is important for increased CO_2 uptake, and consistently with our previous studies, O–lining is as important as N, or even more so. Coverage starts with filling smaller (<1 nm) micropores and continues with monolayer coverage of small mesopores. Depending on the pore size, multilayer coverage continues until smaller mesopores (those probed with CO_2 adsorption and low-pressure N_2 sorption) are partially filled.

For practical applications a highly CO_2-absorbing material should also be selective toward other gasses. For example, for pre-combustion separation, a CO_2-absorbing material should be selective against H_2 and CH_4, while for post-combustion purposes, selectivity towards N_2 is desired. The adsorption isotherms of CH_4 and H_2 at 273 K, 1 bar for both double-etched C-PUA-4.5×@silica and C-PAN-2×@silica(7:3) are shown in Figure 16. The maximum gas uptake values are summarized in Table S.5 of Appendix VIII in Supporting Information. The isotherms were fitted with a Virial-type equation that allowed calculation of the Henry's constants, K_H, for each gas and material (see Experimental Section). Then, selectivities were calculated as the ratios of the K_H values (see Table S.6), and are compared in bar-graph forms in Figure 17.

The uptake of H_2 and N_2 was quite low as compared to CO_2 adsorption for carbon aerogels derived from PUA and PAN. The selectivity of C-PUA-4.5×@silica aerogels toward CO_2 versus H_2 was 624 ± 238 and 288 ± 86 for the HF-CO_2 and the CO_2-HF varieties of the material, respectively; the corresponding selectivity toward CO_2 versus N_2 was in the range of 70-80 for both varieties of the material. The significant difference in

the CO_2/H_2 selectivities of C-PUA-4.5×@silica carbon aerogels from the two etching processes is attributed to the fact that the CO_2 adsorption of the HF-CO_2 variety was 50% higher than that of the CO_2-HF material (9 vs 6 mmol g^{-1}, respectively), while the H_2 adsorption was similar (0.06-0.08 mmol g^{-1}) for all the double-etched PUA-derived carbon aerogels.

The selectivities of the C-PAN-2×@silica-(7:3) samples toward CO_2 versus H_2 were in the range of 780-863, while the CO_2/N_2 selectivities were in the range of 73-92 for materials from both etching processes. On the other hand, the adsorption of CH_4 was high compared to N_2 and H_2 (up to 2.6 mmol g^{-1} – see Table S.5 of Appendix VIII in Supporting Information), which has been attributed to the high polarizability of CH_4.[56,57] As a result, selectivities of CO_2 toward methane for both PUA- and PAN-derived carbon aerogels, by both etching processes, were low, typically less than 25.

Overall, all PUA- and PAN-derived carbon aerogels by the method described here, showed high selectivities towards H_2, which is favorable for pre-combustion CO_2 capture. Relevant to post-combustion applications (CO_2-N_2 separation), selectivities in the range of 71-97 were at par with those from amide networks,[58] organic cages,[59] certain conjugated organic polymers,[52] and other microporous carbon derived from phenolic aerogels.[1]
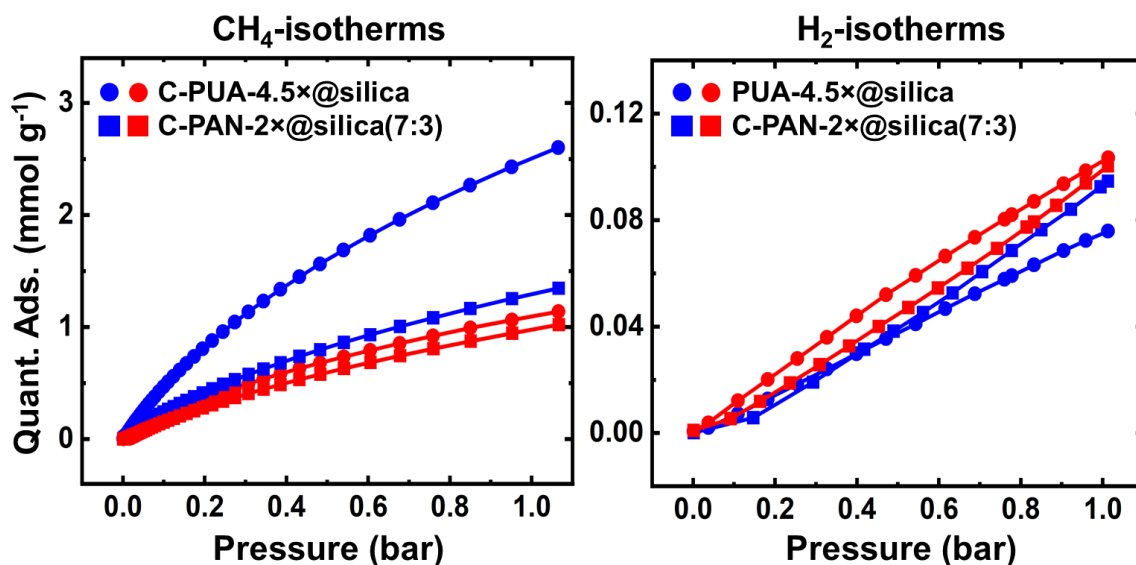
Figure 16. Representative CH_4 (left) and H_2 (right) adsorption isotherms at 273 K for C-PUA-4.5×@silica-HF-CO_2 (blue circles), C-PUA-4.5×@silica-CO_2-HF (red circles), C-PAN-2×@silica(7:3)-HF-CO_2 (blue squares), and C-PAN-2×@silica(7:3)-CO_2-HF (red squares). (For clarity only adsorption is shown, but all isotherms are reversible without any hysteresis. One every two points is shown in the H_2 adsorption isotherms.)

3. CONCLUSION

Viewing sol-gel derived silica suspensions as removable templates for the accumulation of carbonizable polymers, we have demonstrated an alternative synthetic route to highly porous carbon aerogel monoliths from compressed polymer-crosslinked xerogel powders. The new process is energy efficient due to bypassing supercritical-fluid drying or freeze-drying, time efficient due to faster solvent exchanges within the grains of wet-gel particles, and material efficient due to the reduced number of solvent exchanges required for xerogelling versus aerogelling. Post carbonization etching processes control BET/micropore surface areas as well as micro- and meso-porosities in the final carbon-
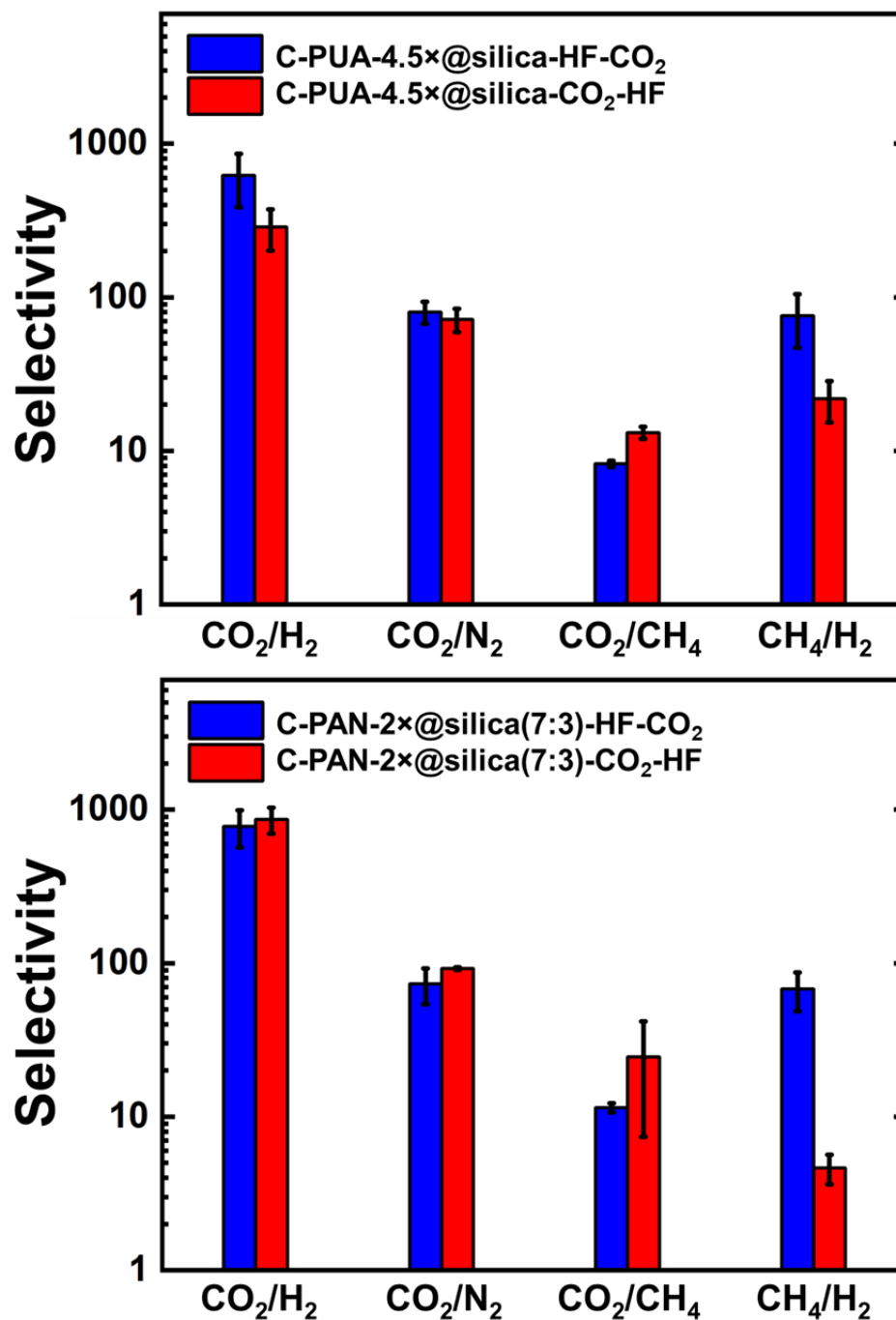
Figure 17. Relative selectivities at 273 K for the gases shown of double-etched carbon aerogels derived from PUA@silica (top) and from PAN@silica (bottom). (Selectivities were calculated as the ratios of the corresponding Henry's constants obtained by Virial fitting of the isotherms at 273 K of Figure 16.)

-aerogels. The microporosity of those carbons can be utilized for high and selective CO_2 adsorption at par with the best CO_2 adsorbers considered in the literature. The method of preparing monolithic carbon aerogels from xerogel powders is generalizable and can be applied to other metal-oxide aerogels besides silica. For example, in the next paper of this issue, silica has been replaced with iron and cobalt oxide networks yielding graphitic aerogels at temperatures considered low for graphitization (e.g., $\leq$1,500 °C).

4. EXPERIMENTAL

4.1. MATERIALS

All reagents and solvents were used as received unless noted otherwise. Ammonium hydroxide (NH_4OH, ACS reagent), 3-aminopropyltriethoxysilane (APTES), sodium hydroxide pellets (NaOH), anhydrous sodium sulfate (Na_2SO_4, ACS certified), and hydrofluoric acid (HF, 48-51% solution in water, ACS reagent) were purchased from Fisher Scientific. Tetramethylorthosilicate (TMOS), 4,4'-azobis(4-cyanopentanoic acid) (ABCVA, $\geq$98% *-trans*), anhydrous tetrahydrofuran (THF), and acrylonitrile ($\geq$99%, contains 35-45 ppm monomethyl ether hydroquinone (MEHQ) as inhibitor) were purchased from the Sigma Aldrich Chemical Company. Acrylonitrile was extracted three times with 3.0 M aqueous sodium hydroxide solution to remove the inhibitor, and dried using sodium sulfate. The inhibitor-free acrylonitrile was stored in a refrigerator at 0 °C and used within a month. HPLC grade solvents including hexane, methanol (CH_3OH), ethyl acetate (EtOAc) and toluene were purchased from Fisher Scientific. Technical grade acetone was purchased from Univar (St. Louis, MO). Tris(4-isocyanatophenyl)methane

(TIPM) was donated by Covestro LLC (Pittsburg, PA) as a 27% w/w solution in dry EtOAc under the trade name Desmodur RE. Ultra-high purity Ar (grade 5), N_2 (grade 4.8), O_2 (grade) and Ar (99.99999%) gases were purchased from AirGas (Rolla, MO).

4.1.1. Preparation of APTES@silica Powder (Refer to Schemes 2A and 2B).

In a typical process, hexane (43 mL, 3× the volume of the intended sol) was added under flowing dry (with a drying tube) Ar (99.99999%) to a three-neck round bottom flask equipped with a mechanical stirrer and a drying tube. To that flask, solution A consisting of 4.5 mL of CH_3OH and 3.85 mL (0.026 mol) of TMOS, and solution B consisting of 4.5 mL of CH_3OH, 1.5 mL (0.083 mol) of water and 40 µL NH_4OH were added successively at room temperature under vigorous stirring (770 – 950 rpm). As soon as the mixture developed fine particles and turned white (approximately 20 min), 1.28 mL (0.0065 mol) of APTES (approximately 1/3× the volume of TMOS) was added to the flask, and the reaction mixture was stirred at the same rate for 24 h at room temperature. The resulting APTES@silica suspension was transferred to centrifuge tubes (50 mL, Fisher Scientific) and the solvent was exchanged twice with ethyl acetate and once with water-saturated ethyl acetate ($EtOAc/H_2O$). After standing for 15 h in $EtOAc/H_2O$, the APTES@silica suspension was either processed to PUA@silica powder (see next section) or dried under vacuum at 50 ºC for further characterization. All washes and solvent exchanges were carried out with centrifugation for 15-20 min at 2450 rpm. Each time, the supernatant solvent was removed and the volume of the new solvent that was brought in was 2× the volume of the compacted slurry (paste) at the bottom of the centrifuge tubes. Before every new centrifugation step, the compacted slurry was re-suspended with vigorous agitation with Vortex-Genie (Model no. K-550-G, Scientific Industries) and a glass rod.

4.1.2. Preparation of PUA@silica Powder (Refer to Scheme 2B). In a typical procedure, TIPM solution as received (4× the volume of the centrifuged paste) was added to the centrifuge tubes (50 mL, Fisher Scientific, Cat. no. 06-443-18) containing the APTES@silica slurry from the last EtOAc/H_2O wash, the tubes were sealed tightly with their caps, and the suspension was heated in an oven at 65 ºC for 72 h. For different formulations of PUA@silica powders, different amounts of TIPM solution 4.5×, 3×, and 1.5× mol (6×, 4×, and 2× v/v relative to 1× v/v of APTES@silica paste) were used for cross-linking relative to 1× mol of APTES@silica. The mixture was swirled slowly every 10 to 12 h to re-distribute the settled powder and increase the diffusion rate. At the end of the 3-day period, the tubes were allowed to cool to room temperature, and they were centrifuged for 15 to 20 min followed successively by three ethyl acetate washes. The wash solvent was always removed by centrifugation. Again, for all washes, the volume of solvent added was twice the volume of the paste at the bottom of the tubes. After removing the solvent from the last ethyl acetate wash, the contents of the tubes were transferred with the aid of small portions of ethyl acetate and were combined in a round bottom flask. Ethyl acetate was removed, and the product was dried under reduced pressure (water aspirator connected via a drying tube) at 50 ºC into a dry, freely flowing PUA@silica powder.

4.1.3. Preparation of initiator@silica Powder (Refer to Scheme 2C). Hexane (43 mL, 3× the volume of the intended sol) was added under flowing dry (with a drying tube) Ar (99.99999%) to a three-neck round bottom flask equipped with a mechanical stirrer and a drying tube. To that flask, solution A consisting of 4.5 mL of CH_3OH and 3.85 mL (0.0260 mol) of TMOS, and solution B consisting of 4.5 mL of CH_3OH, 1.5 mL (0.0830 mol) of water and 40 µL NH_4OH were added successively at room temperature

under vigorous stirring (770 – 950 rpm). As soon as the mixture developed fine particles and turned white (approximately 20 min), a third solution consisting of 0.67 mL (0.0028 mol) of APTES (TMOS:APTES = 9:1 mol/mol) and 0.4049 g (0.0014 mol) of ABCVA (APTES:ABCVA = 2:1 mol/mol) dissolved in 8.70 mL anhydrous THF at 0 ℃ in an amber-glass Erlenmeyer flask, was added to the flask. The reaction mixture was stirred at the same rate for 24 h at room temperature. The resulting initiator@silica suspension was transferred to centrifuge tubes and the solvent was exchanged once with methanol and thrice with toluene. After this solvent exchange, the initiator@silica suspension was either processed to PAN@silica powder (see next section) or was washed with acetone three times and dried under vacuum at 50 ℃ for further characterization. All washes and solvent exchanges were carried out with centrifugation for 15 to 20 min at 2450 rpm. Each time, the supernatant solvent was removed and the volume of the new solvent that was brought in was 2× the volume of the compacted slurry (paste) at the bottom of the centrifuge tubes. Before every new centrifugation step, the compacted slurry was re-suspended with vigorous agitation using Vortex-Genie (Model no. K-550-G, Scientific Industries) and a glass rod.

4.1.4. Preparation of PAN@silica Powder (Refer to Scheme 2C). In a typical procedure, 13.5 mL inhibitor-free acrylonitrile in 5 mL toluene (acrylonitrile:toluene = 2.7:1 by v/v) was added in a round bottom flask containing the above obtained initiator@silica slurry from the toluene wash. The mixture was heated at 55 ℃ and stirred using a magnetic stirrer at 400 rpm. At the end of the 24 h period, the mixture was allowed to cool to room temperature and then the slurry was centrifuged for 15 to 20 min followed successively by three toluene washes and three acetone washes. Always, the wash solvent

was removed by centrifugation. Again, for all washes, the volume of solvent added was twice the volume of the paste at the bottom of the tubes. After removing the solvent from the last acetone wash, the contents of the tubes were transferred with the aid of small portions of acetone and were combined in a round bottom flask. Acetone was removed and the product was dried under reduced pressure (water aspirator connected via a drying tube) at 50 ℃ in to a dry, freely flowing PAN@silica powder.

4.1.5. Preparation, Carbonization and Post-carbonization Etching of PUA@silica and PAN@silica Compacts (Refer to Schemes 2 and 3). Dry PUA@silica and PAN@silica powders were compressed into various cylindrical monolithic objects using a stainless-steel die and a hydraulic press operated at 10,000 psi. Placement of the powders in the die was carried out in small portions under continuous tapping.

Compressed PUA@silica compacts were converted to carbonized C-PUA@silica compacts pyrolytically at 800 ℃ for 5 h under flowing ultrahigh purity Ar using a programmable MTI GSL1600X-80 tube furnace (outer and inner tubes both of 99.8% pure alumina; outer tube: 1022 mm × 82 mm × 70 mm; inner tube: 610 mm × 61.45 mm × 53.55 mm; heating zone at set temperature: 457 mm). The gas flow was always set at 325 mL min^{-1}.

Compressed PAN@silica compacts were first aromatized to A-PAN@silica compacts pyrolytically at 300 ℃ for 24 h under flowing O_2, and then these A-PAN@silica compacts were converted to C-PAN@silica compacts pyrolytically at 800 ℃ for 5 h under flowing ultrahigh purity Ar.

Carbonized C-PUA@silica and C-PAN@silica compacts were subjected further to two etching processes. Hydrofluoric acid (HF, 48-51% w/w in water) treatment of

carbonized C-PUA@silica and C-PAN@silica compacts was carried out in high-density polyethylene (HDPE) vials (20 mL, Cat. no. 03-337-23, Fisher Scientific) capped with rubber septa (Cat. no. CG-3024-03, ChemGlass Life Sciences) under reduced pressure (using a water aspirator) until no more bubbles were observed coming out from the carbonized compacts. Subsequently, these compacts were washed three times with distilled water and three times with acetone in the same HDPE vials, under reduced pressure, for 15 min each time. Finally, washed compacts were dried in a vacuum oven at 80 ℃ for 24 h. CO_2 etching was carried out in a tube furnace at 1000 ℃ for 3 h under flowing CO_2, before or after HF treatment.

4.2. METHODS

4.2.1. Physical Characterization. Bulk densities (ρ_b) were calculated from weight and physical dimensions of the samples. Skeletal densities (ρ_s) were measured using helium pycnometry on a Micromeritics AccuPyc II 1340 instrument. Samples for skeletal density measurements were outgassed for 24 h at 80 ℃ under vacuum before analysis. Percent porosities (Π) were determined from the ρ_b and ρ_s values via $\Pi = 100 \times [(\rho_s - \rho_b)/ \rho_s]$.

4.2.2. Chemical Characterization. Different methods were applied at different stages of processing as follows.

Liquid ^{13}C NMR spectra were recorded with 400 MHz Varian Unity Inova NMR instrument (100 MHz carbon frequency). The cross-linked polymer was identified as polyacrylonitrile with solid-state CPMAS ^{13}C NMR on a Bruker Avance III 400 MHz spectrometer with a carbon frequency 100 MHz, using 7 mm Bruker MAS probe at a magic angle spinning rate of 5 kHz with broadband proton suppression and CP total suppression

of spinning side bands (TOSS) pulse sequence. The TOSS pulse sequence was applied by using a series of four properly timed 180º pulses on the carbon channel at different points of a cycle before the acquisition of the FID, after an initial excitation with a 90º pulse on the proton channel. The 90º excitation pulse on the proton and the 180º excitation pulse on carbon were set to 4.2 and 10 µs, respectively. The cross-polarization contact time and the relaxation delay were set at 3000 µs and 5 s, respectively. The number of scans was set at 2048. Spectra were referenced externally to glycine (carbonyl carbon at 176.03 ppm). Chemical shifts were reported versus tetramethylsilane (TMS, 0 ppm). Solid-state ^{29}Si NMR spectra were also obtained on the same Bruker Avance III 400 MHz spectrometer with a 59.624 MHz silicon frequency using again a 7 mm Bruker MAS probe and magic angle spinning at 5 kHz, using cross-polarization pulse sequence. The cross-polarization contact time and the relaxation delay were set at 3000 µs and 5 s, respectively. The number of scans was set at 16384. ^{29}Si NMR spectra were referenced externally to neat TMS (0 ppm).

X-ray photoelectron spectroscopic analysis (XPS) was carried out with a ThermoFischer Scientific Nexsa X-ray Photoelectron Spectrometer System. Samples were mixed and ground together with Au powder (5% w/w) as an internal reference. Deconvolution of the spectra was performed with Gaussian function fitting using the OriginPro 9.7 software package.

4.2.3. Thermal Characterization. Thermogravimetric Analysis (TGA) was conducted under air at 1000 ºC with Fischer Scientific Isotemp muffle furnace using a heating rate of 10 ºC min^{-1}. TGA was also conducted under O_2 with a TA instrument Model TGA Q50 analyzer, using heating rate of 5 ºC min^{-1}.

Modulated Differential Scanning Calorimetry (MDSC) was conducted under N_2 from -30 ℃ to 350 ℃, with a heating rate of 5 ℃ min^{-1} using a TA Instruments Differential Scanning Calorimeter Model Q2000.

4.2.4. Structural Characterization. Scanning electron microscopy (SEM) and Energy Dispersive X-ray Spectroscopy (SEM-EDX) was conducted with Au/Pd (60/40) coated samples on a Hitachi Model S-4700 field-emission microscope. Samples were placed on the stub using C-dot. Thin sticky copper strips were cut and placed on the edges and top of the sample, leaving space for the analysis.

4.2.5. Pore Structure Analysis. The pore structure was probed with N_2-sorption porosimetry at 77 K using either a Micromeritics ASAP 2020 or a TriStar II 3020 surface area and porosimetry analyzer. Before porosimetry, samples were outgassed for 24 h under vacuum at 120 ℃. Data were reduced to standard conditions of temperature and pressure (STP). Total surface areas were determined via the Brunauer-Emmett-Teller (BET) method from the N_2-sorption isotherms. Micropore analysis was conducted with low-pressure N_2-sorption at 77 K using a Micromeritics ASAP 2020 instrument equipped with a low-pressure transducer, or with CO_2 adsorption up to 760 Torr (relative pressure $P/P_0 = 0.03$) at 273 K using the Micromeritics TriStar II 3020 system mentioned above. Micropore surface areas were calculated via t-plot analysis of the isotherms using the Harkins and Jura Model. Pore size distributions were determined with the Barret-Joyne-Halenda (BJH) equation applied to the desorption branch of the N_2-sorption isotherms.

4.2.6. Isosteric Heats of CO_2 Adsorption (Q_{st}). Q_{st} values were calculated using the Virial fitting method. For this, the CO_2 adsorption isotherms at 273 K and 298 K were

fitted simultaneously with a Virial-type Equation (3) using the OriginPro 2020 9.7.0 software package.

$$\ln P = \ln N + \frac{1}{T}\sum_{i=0}^{m} a_i N^i + \sum_{i=0}^{n} b_i N^i$$

(3)

[P is pressure in Torr, N is the adsorbed amount in mmol g^{-1}, T is the absolute temperature, a_i and b_i are the Virial coefficients, and m and n are the number of coefficients needed in order to fit the isotherms adequately]. Using the least squares method, the values of m and n were gradually increased until the sum of the squared deviations of the experimental points from the fitted isotherm was minimized. All data were fitted well with $m = 3$ and $n = 1$ (see Table S.3 in Appendix VII of the Supporting Information). The values of a_o to a_m were introduced into Equation (4), and the isosteric heats of adsorption (Q_{st}) were calculated as a function of the surface coverage (N).

$$Q_{st} = -R\sum_{i=0}^{m} a_i N^i$$

(4)

[R is the gas constant (8.314 J mol^{-1} K^{-1}) and Q_{st} is given in kJ mol^{-1}]. The common term in Equation (4) for all N, Q_0, corresponds to $i = 0$ and is given by Equation (5).

$$Q_0 = -Ra_0$$

(5)

Q_0 is the heat of adsorption as coverage goes to zero and is a sensitive evaluator of the affinity of the adsorbate for the surface. Q_0 values are summarized in Table S.4 of Appendix VII in Supporting Information.

4.2.7. Relative Adsorption Selectivities. Relative adsorption studies for CO_2, CH_4, N_2, and H_2 were done on Micromeritics TriStar II 3020 surface area and porosimetry analyzer at 273 K up to 1 bar. Adsorption selectivities for one gas versus another were calculated as the ratios of the respective Henry's constants, K_H. The latter were calculated via another type of a Virial model, whereas the single-component adsorption isotherms for each gas at 273 K were fitted according to Equation (6).

$$\ln N = \ln P + K_1 + K_2 N + K_3 N^2 + ... = \ln P + \sum_{i=1}^{m} K_i N^{i-1}$$

(6)

Fitting was carried out using the least squares method by varying the number of terms, until a suitable number of terms, m, described the isotherms adequately. Coefficients K_1, K_2, ... K_m are characteristic constants for a given gas-solid system and temperature. The Henry's constant for each gas, K_H, is the limiting value of N/P as $P \rightarrow 0$ and is given by Equation (7).[60]

$$K_H = \lim_{P \to 0} \left(\frac{N}{P} \right) \cong e^{K_1}$$

(7)

To calculate standard deviations, all isotherms obtained experimentally for each component were fitted individually. The K_H values from all isotherms were averaged, and the average values were used to calculate selectivities by taking the ratios. Standard deviations for the ratios were calculated using rules for propagation of error.

ACKNOWLEDGEMENTS

SUPPORTING INFORMATION

Appendix I. Thermogravimetric analysis (TGA) data
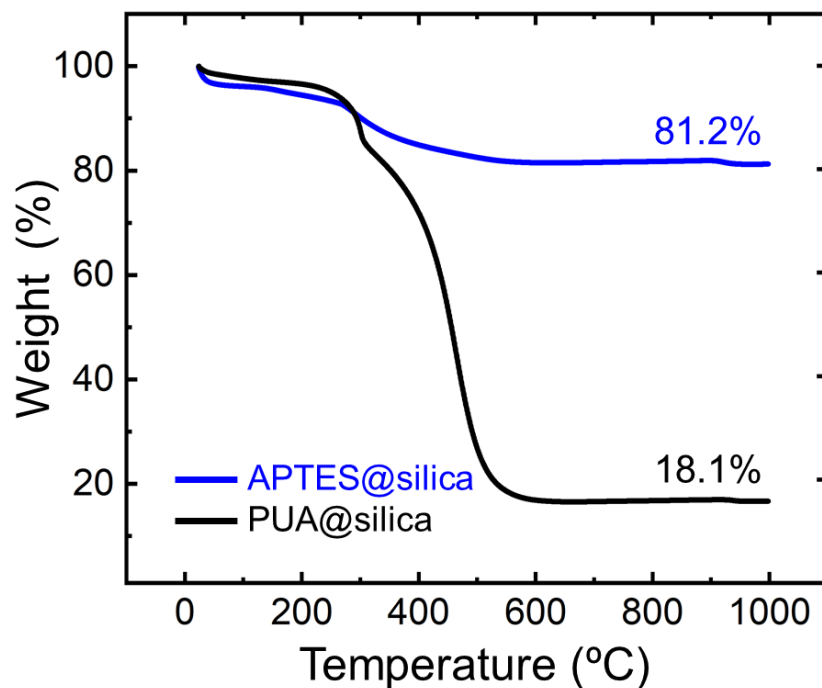
Figure S.1. TGA under O_2 at 5 ºC min^{-1} of APTES@silica (blue line, 81.2% residue) and of PUA-3×@silica (black line, 18.1% residue).
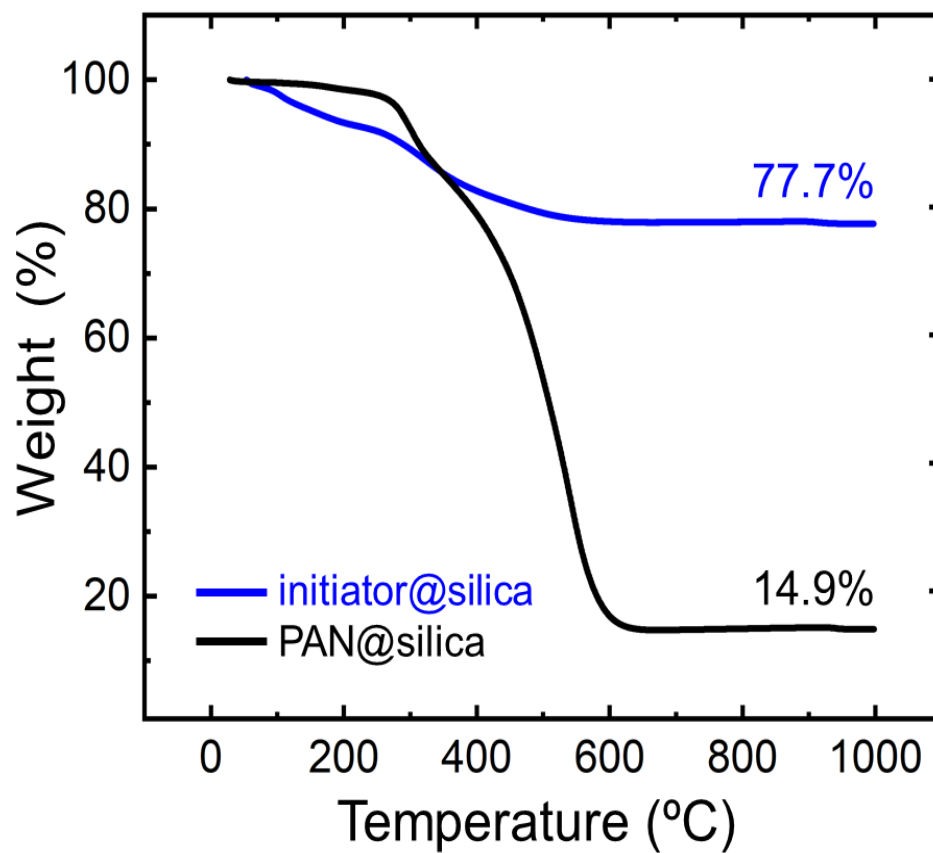
Figure S.2. TGA under O_2 at 5 ºC min^{-1} of initiator@silica (blue line, 77.7% residue) and of PAN-6×@silica-(9:1) (black line, 14.9% residue).

Appendix II. CPMAS ^{13}C NMR spectra of all fully aromatized A-PAN-n×@silica(x:y) compacts
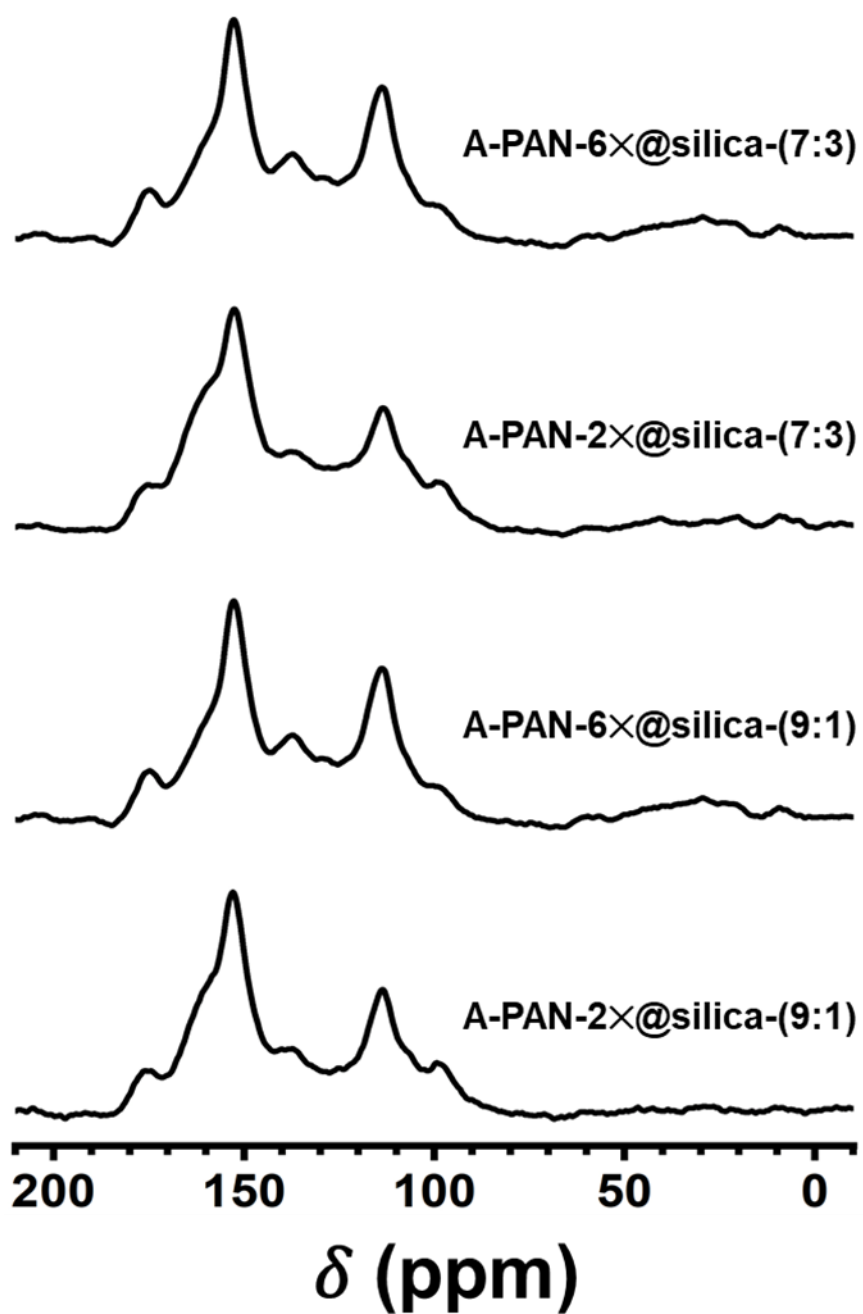
Figure S.3. Solid-state CPMAS ^{13}C NMR spectra of all fully aromatized A-PAN@silica compacts as shown. (Full aromatization: 300 ^{o}C / O$_2$ / 24 h)

Appendix III. Solid-state ^{29}Si and ^{13}C CPMAS NMR spectra of all as-prepared PUA@silica and PAN@silica compacts
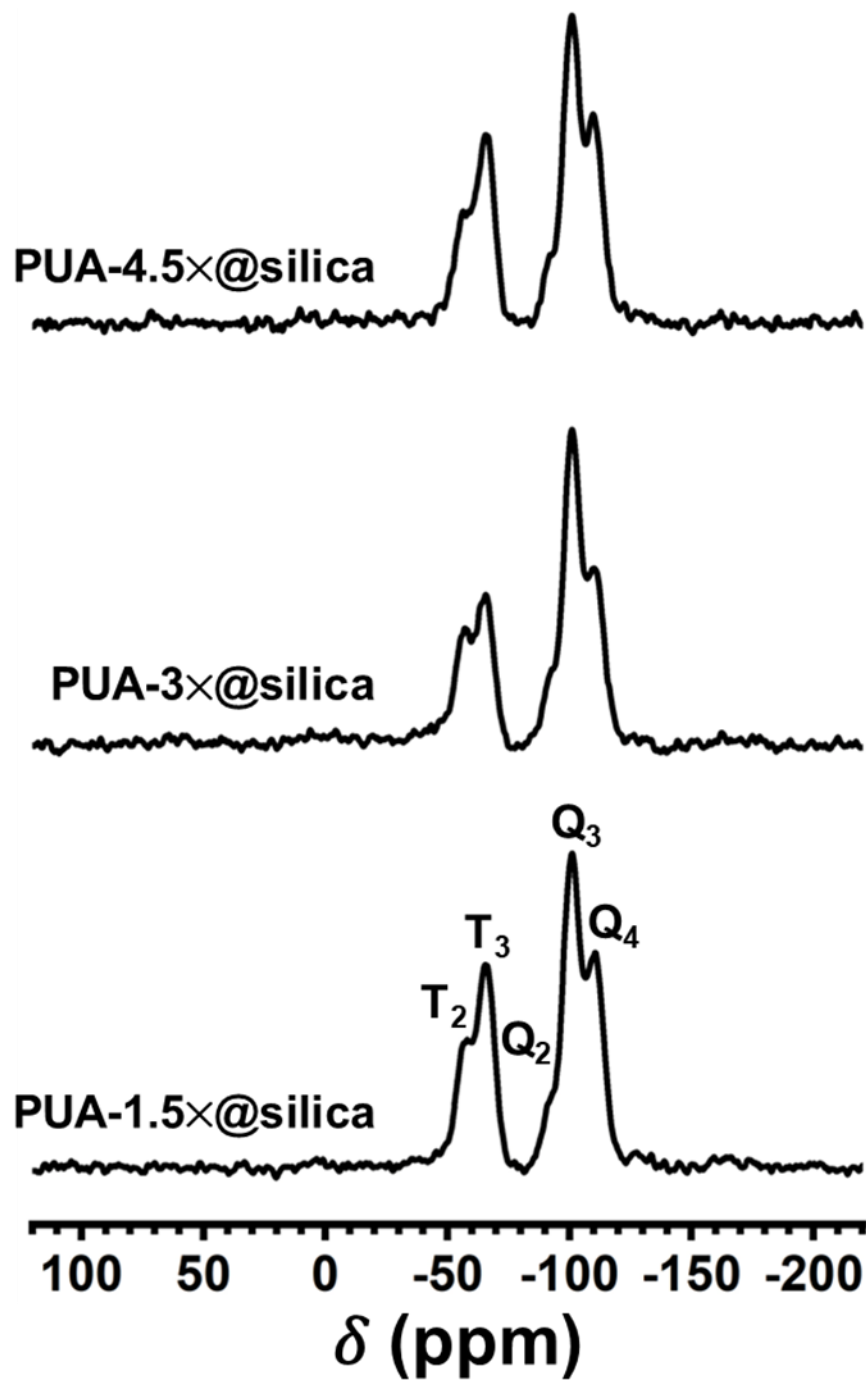
Figure S.4. Solid-state CPMAS ^{29}Si NMR spectra of the three as-prepared PUA@silica compacts, as shown.
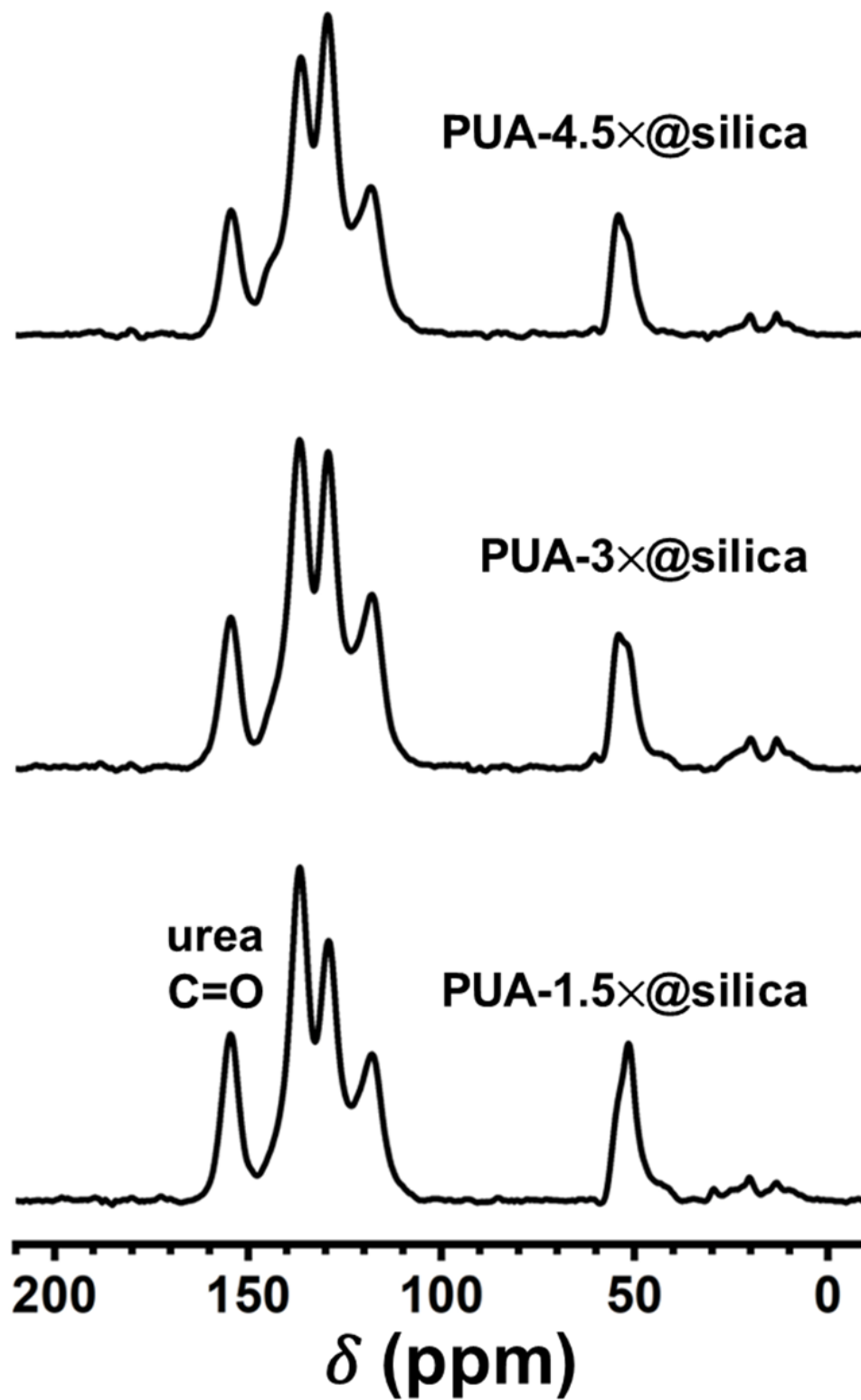
Figure S.5. Solid-state CPMAS ^{13}C NMR spectra of the three as-prepared PUA@silica compacts, as shown.
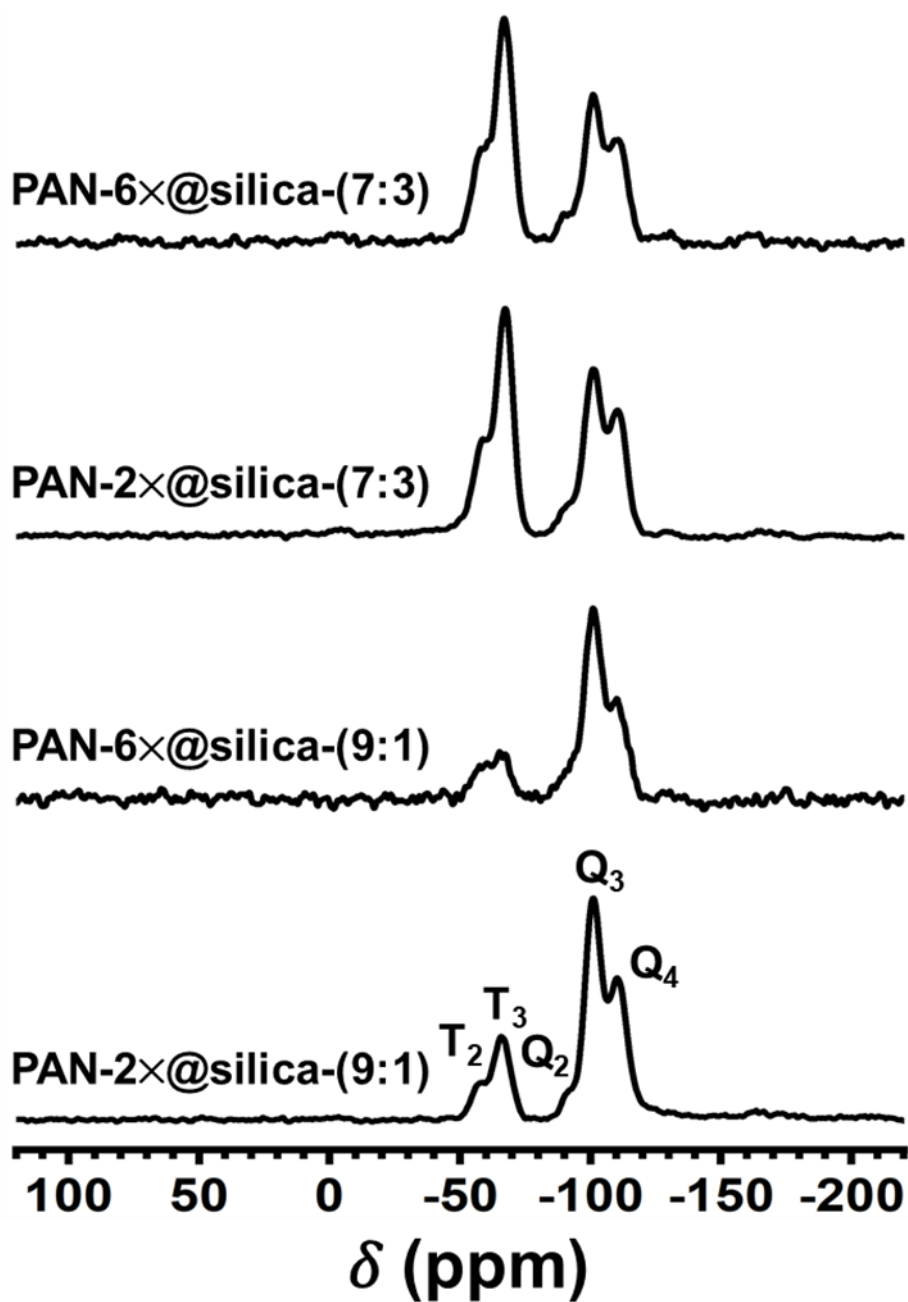
Figure S.6. Solid-state CPMAS ^{29}Si NMR spectra of the four as-prepared PAN@silica compacts, as shown.
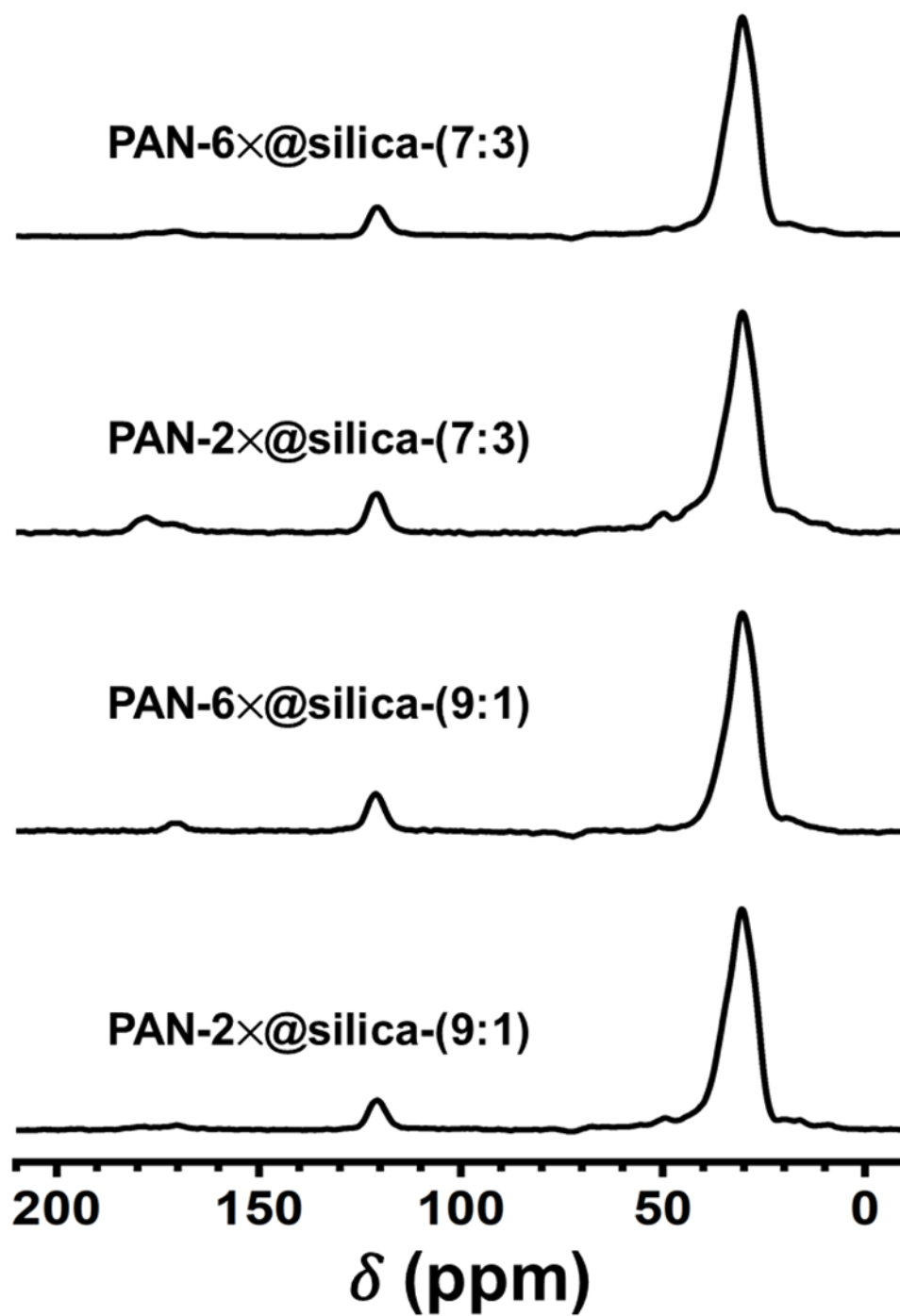
Figure S.7. Solid-state CPMAS ^{13}C NMR spectra of the four as-prepared PAN@silica compacts, as shown.

Appendix IV. EDS data of carbonized PUA@silica and PAN@silica samples, before and after HF treatment.
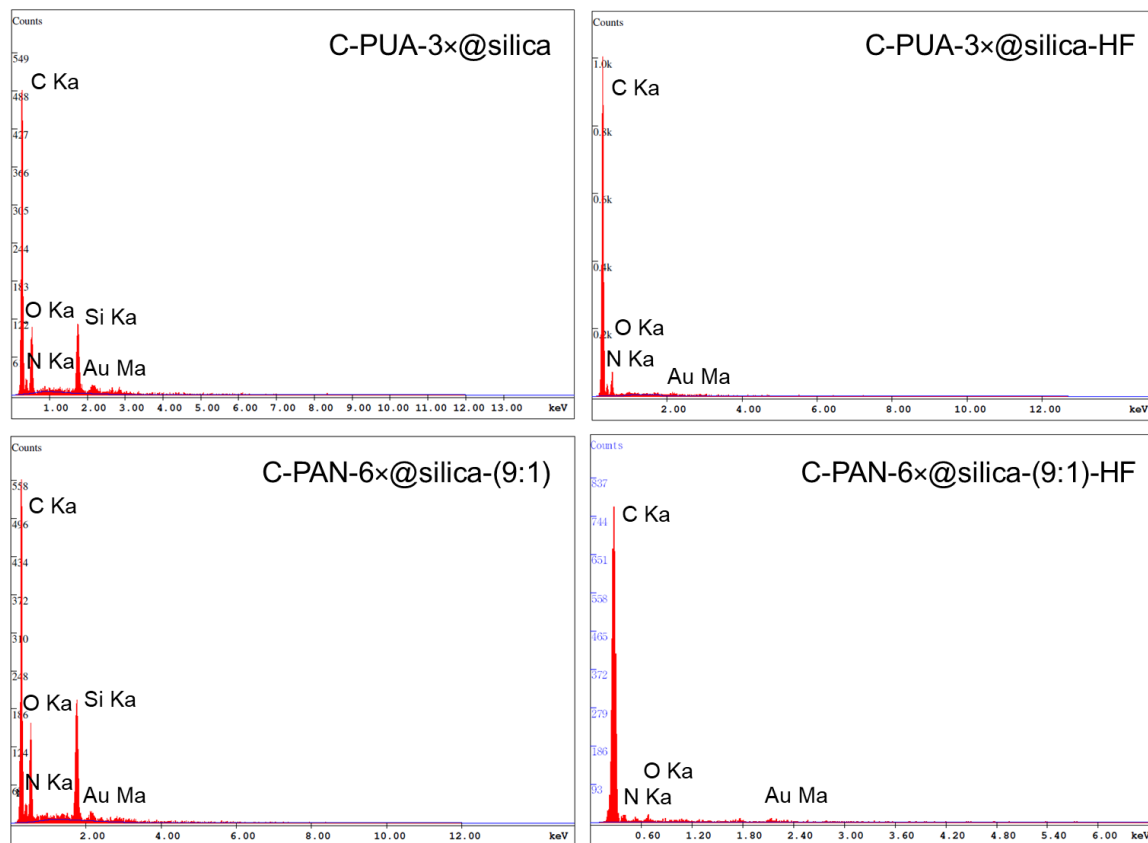
Figure S.8. EDS data of C-PUA-3×@silica, C-PUA-3×@silica-HF, C-PAN-6×@silica(9:1), and C-PAN-6×@silica(9:1)-HF samples. Weight and atomic percent of individual elements are given in Table S.1.

Table S.1. Percent elemental composition via EDS of C-PUA-3×@silica, C-PUA-3×@silica-HF, C-PAN-6×@silica(9:1), and C-PAN-6×@silica(9:1)-HF samples.

sample	weight %					
	C	N	O	Si	Au	Total
C-PUA-3×@silica	59.95	7.95	14.69	12.36	5.05	100.00
C-PUA-3×@silica-HF	87.95	7.05	2.27	0.00	2.73	100.00
C-PAN-6×@silica(9:1)	55.32	8.15	15.59	16.50	4.44	100.00
C-PAN-6×@silica(9:1)-HF	89.36	4.62	2.62	0.00	3.40	100.00
	atomic %					
	C	N	O	Si	Au	Total
C-PUA-3×@silica	71.60	8.14	13.17	6.31	0.78	100.00
C-PUA-3×@silica-HF	94.71	3.09	1.90	0.00	0.29	100.00
C-PAN-6×@silica(9:1)	68.01	8.60	14.39	8.67	0.33	100.00
C-PAN-6×@silica(9:1)-HF	95.51	2.01	2.12	0.00	0.36	100.00

Appendix V. XPS data of carbonized samples before and after etching with HF and CO_2 with either sequence.

Table S.2. Elemental quantification data with XPS.

sample	atomic %				O/N
	C	O	N	Au	
C-PUA-4.5×@silica-HF-CO$_2$	89.61	6.44	3.48	0.47	1.85
C-PUA-4.5×@silica-CO$_2$-HF	91.57	3.11	4.50	0.82	0.69
C-PAN-2×@silica(7:3)-HF-CO$_2$	89.95	2.95	6.86	0.24	0.43
C-PAN-2×@silica(7:3)-CO$_2$-HF	86.44	6.22	6.09	1.25	1.02
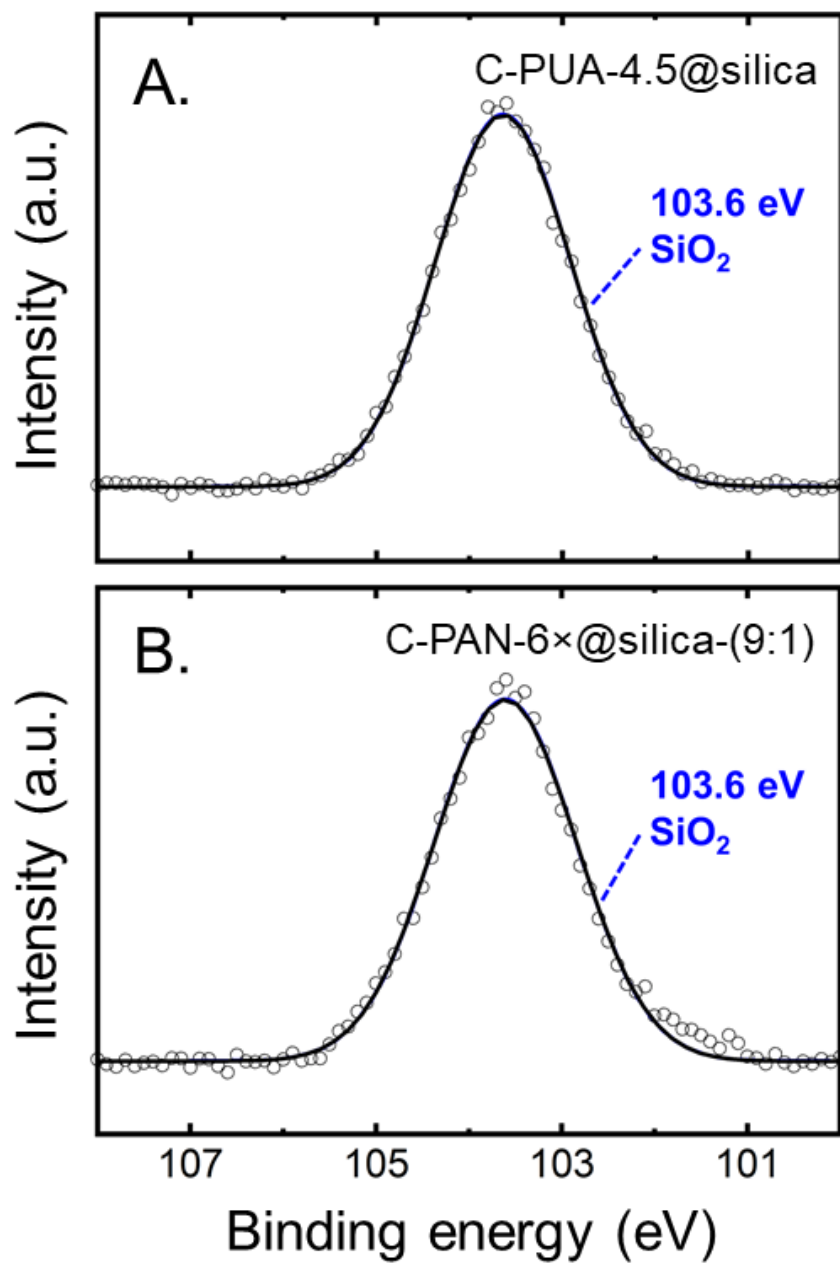
Figure S.9. High resolution Si 2p spectra of: (A) C-PUA-4.5×@silica; and (B) C-PAN-6×@silica(9:1).
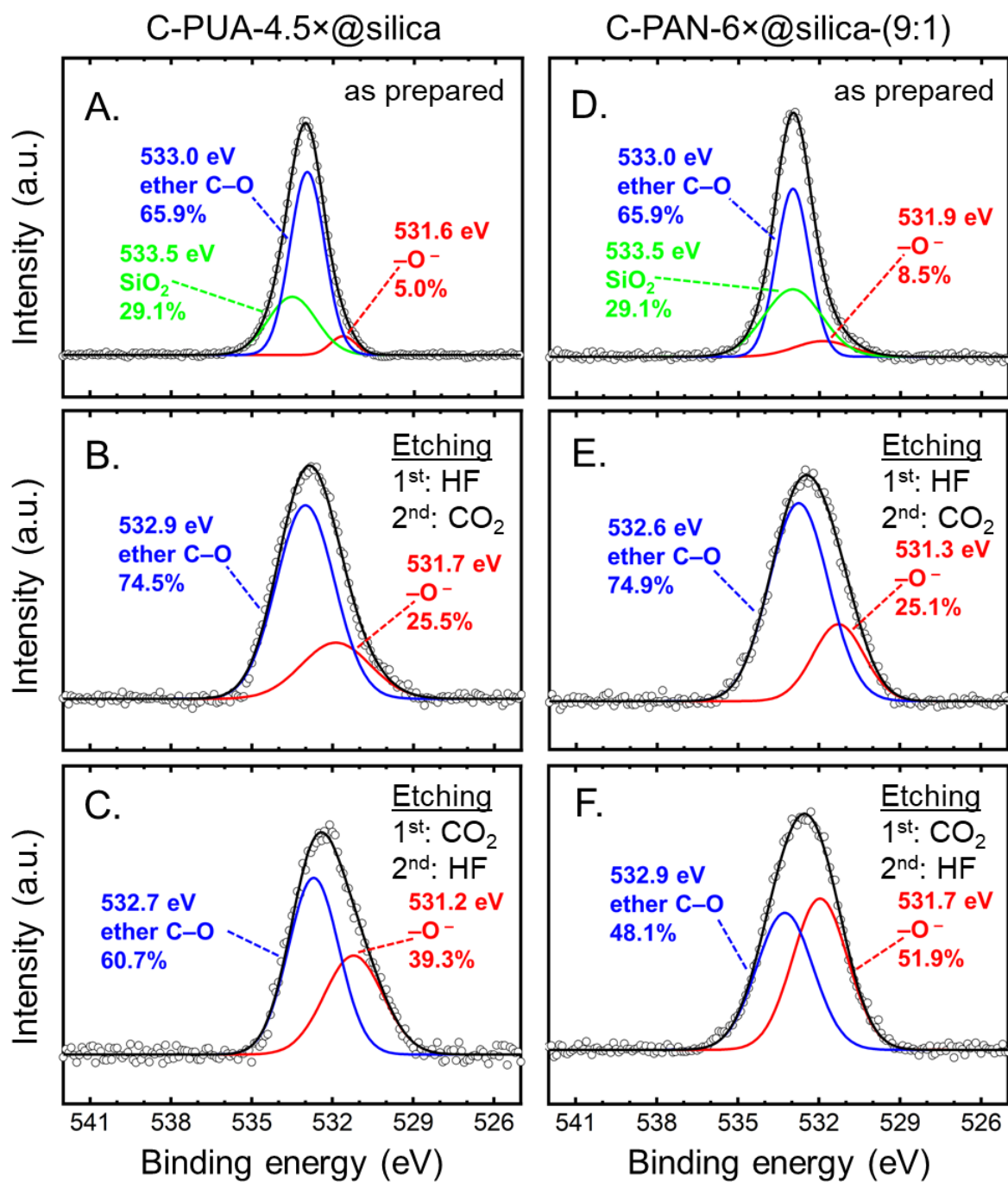
Figure S.10. Comparative high-resolution O 1s XPS spectra of: (A) C-PUA@silica; (B) C-PUA@silica-HF-CO$_2$; (C) C-PUA@silica-CO$_2$-HF; (D) C-PAN@silica; (E) C-PAN@silica-HF-CO$_2$; and (F) C-PAN@silica-CO$_2$-HF. The specific sample formulations were PUA-4.5×@silica and PUA-6×@silica(9:1), respectively.
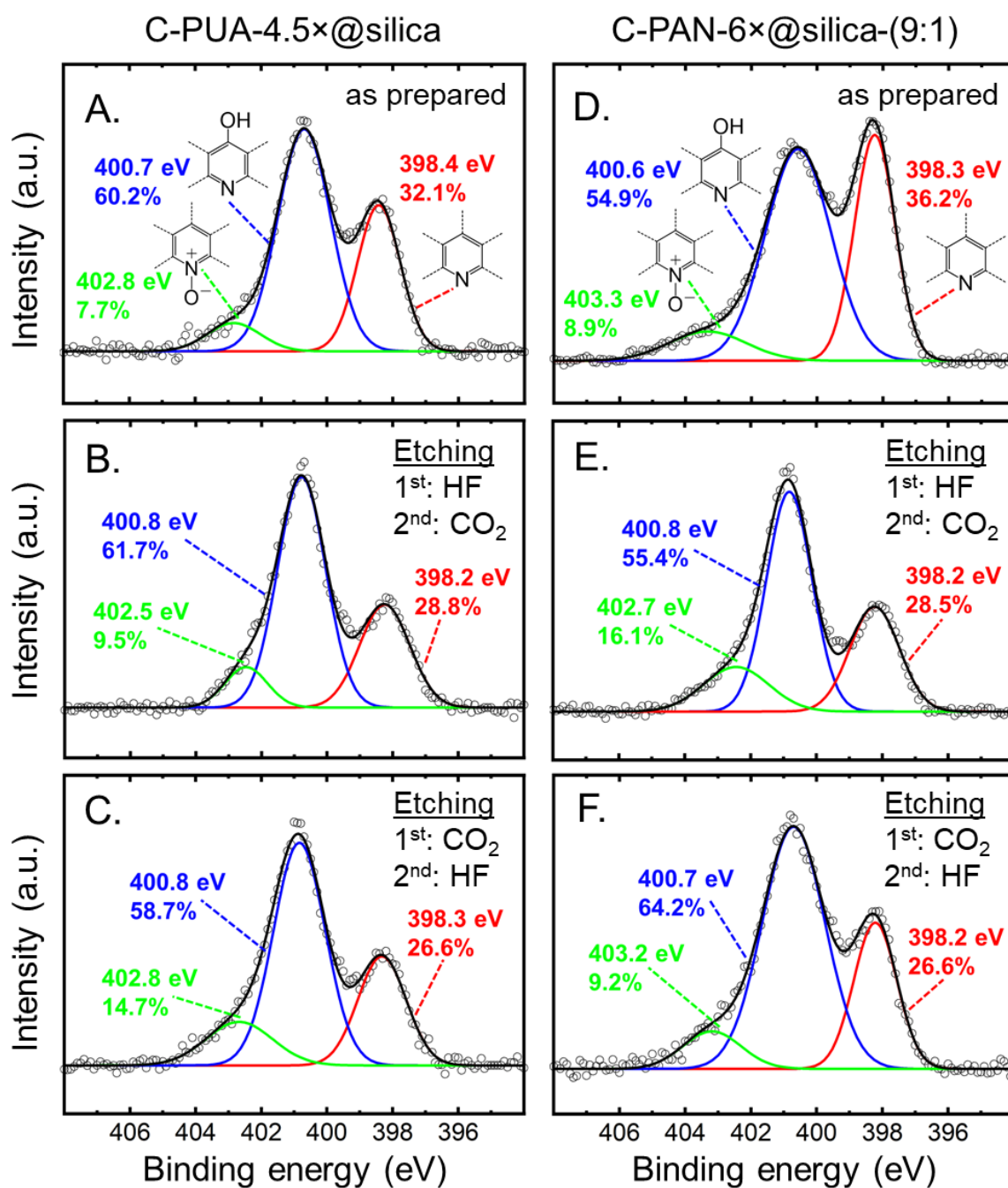
Figure S.11. Comparative high-resolution N 1s XPS spectra of: (A) C-PUA@silica; (B) C-PUA@silica-HF-CO_2; (C) C-PUA@silica-CO_2-HF; (D) C-PAN@silica; (E) C-PAN@silica-HF-CO_2; and (F) C-PAN@silica-CO_2-HF. The specific sample formulations were PUA-4.5×@silica and PUA-6×@silica(9:1), respectively.
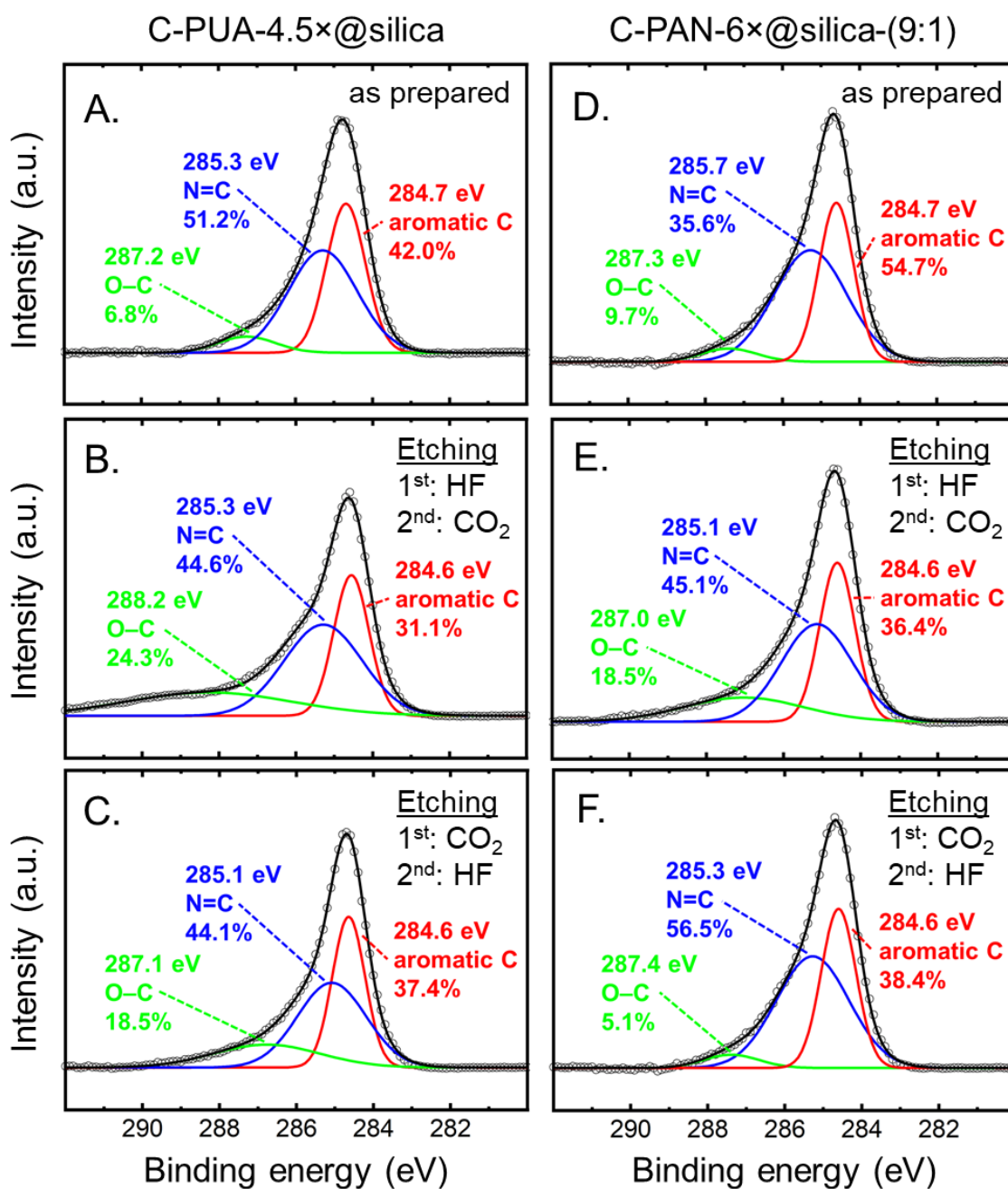
Figure S.12. Comparative high-resolution C 1s XPS spectra of: (A) C-PUA@silica; (B) C-PUA@silica-HF-CO_2; (C) C-PUA@silica-CO_2-HF; (D) C-PAN@silica; (E) C-PAN@silica-HF-CO_2; and (F) C-PAN@silica-CO_2-HF. The specific sample formulations were PUA-4.5×@silica and PUA-6×@silica(9:1), respectively.

Appendix VI. Micropore size distribution by the CO_2/DFT method.
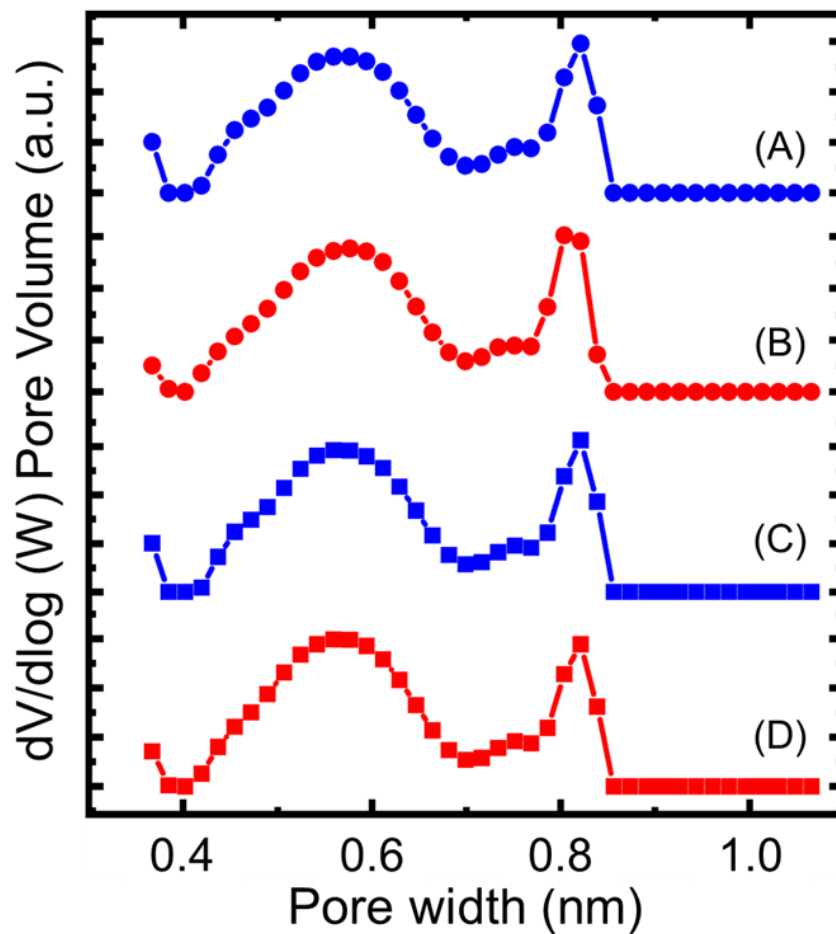
Figure S.13. Micropore size distribution obtained with the DFT method applied to CO_2 adsorption data at 273 K up to 1 bar for (A) C-PUA-4.5×@silica-HF-CO_2; (B) C-PUA-4.5×@silica-CO_2-HF; (C) C-PAN-2×@silica(7:3)-HF-CO_2; and (D) C-PAN-2×@silica(7:3)- CO_2-HF compacts.

Appendix VII. Virial fitting of CO_2 isotherms at 273 K and 298 K.

Table S.3. CO_2 adsorption data at two different temperatures (blue: 273 K; red: 298 K). The two isotherms were fitted simultaneously using a Virial equation for calculating the isosteric heats of adsorption, Q_{st}, as a function of CO_2 uptake. Corresponding Virial fitting parameters for calculating Q_{st} and Q_0 are shown in the data tables. (m, n: No. of terms used for Virial fitting.)

C-PUA-4.5×@silica-HF-CO_2 ($m = 3$, $n = 1$)		
Parameters	Value	Standard Error
a_0	-3582.00698	138.31745
a_1	171.57971	66.69309
a_2	-76.95994	10.60571
a_3	9.79411	1.77201
b_0	15.89187	0.49969
b_1	0.26564	0.23538
red X^2	5.20×10^{-3}	
R^2	0.99251	
Q_0	30	

C-PUA-4.5×@silica-CO_2-HF ($m = 3$, $n = 1$)		
Parameters	Value	Standard Error
a_0	-3863.62729	136.80972
a_1	35.57652	105.64754
a_2	-188.80624	20.77019
a_3	29.63731	4.63783
b_0	17.52914	0.49256
b_1	1.44581	0.38339
red X^2	5.72×10^{-3}	
R^2	0.99205	
Q_0	32	

Table S.3. CO_2 adsorption data at two different temperatures (blue: 273 K; red: 298 K). The two isotherms were fitted simultaneously using a Virial equation for calculating the isosteric heats of adsorption, Q_{st}, as a function of CO_2 uptake. Corresponding Virial fitting parameters for calculating Q_{st} and Q_0 are shown in the data tables. (*m*, *n*: No. of terms used for Virial fitting.) (cont.)

C-PAN-2×@silica(7:3)-HF-CO_2 ($m = 3$, $n = 1$)		
Parameters	Value	Standard Error
a_0	-3281.16924	56.30262
a_1	-471.29074	37.73858
a_2	-128.42041	8.22055
a_3	20.00839	1.78324
b_0	15.51151	0.20312
b_1	2.81486	0.14048
red X^2	9.50×10^{-4}	
R^2	0.99849	
Q_0	27	

C-PAN-2×@silica(7:3)-CO_2-HF ($m = 3$, $n = 1$)		
Parameters	Value	Standard Error
a_0	-3710.00363	152.41408
a_1	295.39309	100.50895
a_2	-203.29792	28.90699
a_3	33.92967	7.25744
b_0	16.73648	0.55291
b_1	0.64408	0.39113
red X^2	6.80×10^{-3}	
R^2	0.99132	
Q_0	31	

Table S.4. Maximum CO_2 adsorption at 1 bar at two different temperatures (273 K and 298 K) and summary of the Q_0 values from Table S.3.

sample	CO_2 uptake [mmol g^{-1}] [a]		Q_0 [b]
	at 273 K	at 298 K	
C-PUA-4.5×@silica-HF-CO_2	9.15 ± 0.10	4.13 ± 0.01	30
C-PUA-4.5×@silica-CO_2-HF	6.13 ± 0.07	1.91 ± 0.01	32
C-PAN-2×@silica(7:3)-HF-CO_2	6.82 ± 0.12	2.17 ± 0.04	27
C-PAN-2×@silica(7:3)-CO_2-HF	5.30 ± 0.12	1.95 ± 0.01	31

[a]Average of at least three measurements. [b]Isosteric heats of adsorption at zero coverage, Q_0 (kJ mol^{-1}), using Virial fitting from CO_2 adsorption data at 273 K and 298 K (see Table S.3 above, and Experimental Section in the main article).

Appendix VIII. Adsorption selectivities of various gasses at 273 K.

Table S.5. Maximum gas adsorption data for CO_2, H_2, N_2 and CH_4 at 273 K / 1 bar.[a]

sample	CO_2 [mmol g^{-1}]	H_2 [mmol g^{-1}]	CH_4 [mmol g^{-1}]	N_2 [mmol g^{-1}]
C-PUA-4.5×@silica-HF-CO_2	9.15 ± 0.10	0.08 ± 0.01	2.57 ± 0.04	0.28 ± 0.05
C-PUA-4.5×@silica-CO_2-HF	6.13 ± 0.07	0.11 ± 0.07	1.14 ± 0.01	0.20 ± 0.01
C-PAN-2×@silica(7:3)-HF-CO_2	6.82 ± 0.12	0.11 ± 0.03	1.34 ± 0.01	0.19 ± 0.03
C-PAN-2×@silica(7:3)-CO_2-HF	5.30 ± 0.12	0.09 ± 0.01	1.03 ± 0.05	0.16 ± 0.01

[a]Average of at least three measurements.

Table S.6. Henry's constants and relative selectivity data for CO_2, H_2, N_2 and CH_4 at 273 K / 1 bar.

sample	Henry's constants [mmol g^{-1} mbar^{-1}] [a,b]				Relative selectivities [a,c]			
	K_{H_CO2}	K_{H_H2}	K_{H_N2}	K_{H_CH4}	CO_2/H_2	CO_2/N_2	CO_2/CH_4	CH_4/H_2
C-PUA-4.5×@silica-HF-CO$_2$	42.2 ± 1.4	0.068 ± 0.026	0.53 ± 0.08	5.1 ± 0.17	624 ± 238	80 ± 13	8.2 ± 0.4	76 ± 29
C-PUA-4.5×@silica-CO$_2$-HF	24.6 ± 1.7	0.085 ± 0.025	0.34 ± 0.05	1.9 ± 0.12	288 ± 86	72 ± 12	13 ± 1.2	22 ± 6.5
C-PAN-2×@silica(7:3)-HF-CO$_2$	30.3 ± 1.2	0.039 ± 0.011	0.41 ± 0.07	2.7 ± 0.18	780 ± 212	73 ± 19	11 ± 0.8	68 ± 19
C-PAN-2×@silica(7:3)-CO$_2$-HF	22.3 ± 4.4	0.026 ± 0.005	0.24 ± 0.02	0.12 ± 0.02	863 ± 167	92 ± 1.7	25 ± 17	4.6 ± 1.1

[a]Average of at least three measurements. [b]Henry's constants (K_H) were obtained by applying Virial-type fitting to the isotherms at 273 K (see Experimental Section in the main article). [c]Adsorption selectivities were calculated by taking the ratios of the corresponding K_H values. Errors in selectivities were calculated by applying propagation of error rules to the ratios of the K_H values.

REFERENCES

(1)   Majedi Far, H.; Rewatkar, P. M.; Donthula, S.; Taghvaee, T.; Saeed, A. M.; Sotiriou-Leventis, C.; Leventis, N. Exceptionally High CO_2 Adsorption at 273 K by Microporous Carbons from Phenolic Aerogels: The Role of Heteroatoms in Comparison with Carbons from Polybenzoxazine and Other Organic Aerogels. *Macromol. Chem. Phys.* **2019**, *220* (1), 1–16. https://doi.org/10.1002/macp.201800333.

(2)   Park, J.; Jung, M.; Jang, H.; Lee, K.; Attia, N. F.; Oh, H. A Facile Synthesis Tool of Nanoporous Carbon for Promising H_2, CO_2, and CH_4 Sorption Capacity and Selective Gas Separation. *J. Mater. Chem. A* **2018**, *6* (45), 23087–23100. https://doi.org/10.1039/c8ta08603f.

(3)   Li, Z.; Xu, J.; Sun, D.; Lin, T.; Huang, F. Nanoporous Carbon Foam for Water and Air Purification. *ACS Appl. Nano Mater.* **2020**, *3* (2), 1564–1570. https://doi.org/10.1021/acsanm.9b02347.

(4)   Lam, E.; Luong, J. H. T. Carbon Materials as Catalyst Supports and Catalysts in the Transformation of Biomass to Fuels and Chemicals. *ACS Catal.* **2014**, *4* (10), 3393–3410. https://doi.org/10.1021/cs5008393.

(5)   Xue, Y.; Xie, J.; He, M.; Liu, M.; Xu, M.; Ni, W.; Yan, Y. M. Porous and High-Strength Graphitic Carbon/SiC Three-Dimensional Electrode for Capacitive Deionization and Fuel Cell Applications. *J. Mater. Chem. A* **2018**, *6* (39), 19210–19220. https://doi.org/10.1039/c8ta06657d.

(6)   Far, H. M.; Donthula, S.; Taghvaee, T.; Saeed, A. M.; Garr, Z.; Sotiriou-Leventis, C.; Leventis, N. Air-Oxidation of Phenolic Resin Aerogels: Backbone Reorganization, Formation of Ring-Fused Pyrylium Cations, and the Effect on Microporous Carbons with Enhanced Surface Areas. *RSC Adv.* **2017**, *7* (81), 51104–51120. https://doi.org/10.1039/c7ra10958j.

(7)   Mahadik-Khanolkar, S.; Donthula, S.; Sotiriou-Leventis, C.; Leventis, N. Polybenzoxazine Aerogels. 1. High-Yield Room-Temperature Acid-Catalyzed Synthesis of Robust Monoliths, Oxidative Aromatization, and Conversion to Microporous Carbons. *Chem. Mater.* **2014**, *26* (3), 1303–1317. https://doi.org/10.1021/cm403483p.

(8)   Saeed, A. M.; Rewatkar, P. M.; Majedi Far, H.; Taghvaee, T.; Donthula, S.; Mandal, C.; Sotiriou-Leventis, C.; Leventis, N. Selective CO_2 Sequestration with Monolithic Bimodal Micro/Macroporous Carbon Aerogels Derived from Stepwise Pyrolytic Decomposition of Polyamide-Polyimide-Polyurea Random Copolymers. *ACS Appl. Mater. Interfaces* **2017**, *9* (15), 13520–13536. https://doi.org/10.1021/acsami.7b01910.

(9) Sadekar, A. G.; Mahadik, S. S.; Bang, A. N.; Larimore, Z. J.; Wisner, C. A.; Bertino, M. F.; Kalkan, A. K.; Mang, J. T.; Sotiriou-Leventis, C.; Leventis, N. From "Green" Aerogels to Porous Graphite by Emulsion Gelation of Acrylonitrile. *Chem. Mater.* **2012**, *24* (1), 26–47. https://doi.org/10.1021/cm202975p.

(10) Chang, J.; Zhang, Q.; Lin, Y.; Zhou, C.; Yang, W.; Yan, L.; Wu, G. Carbon Nanotubes Grown on Graphite Films as Effective Interface Enhancement for an Aluminum Matrix Laminated Composite in Thermal Management Applications. *ACS Appl. Mater. Interfaces* **2018**, *10* (44), 38350–38358. https://doi.org/10.1021/acsami.8b12691.

(11) Zou, J.; Liu, J.; Karakoti, A. S.; Kumar, A.; Joung, D.; Li, Q.; Khondaker, S. I.; Seal, S.; Zhai, L. Ultralight Multiwalled Carbon Nanotube Aerogel. *ACS Nano* **2010**, *4* (12), 7293–7302. https://doi.org/10.1021/nn102246a.

(12) Ieamviteevanich, P.; Palaporn, D.; Chanlek, N.; Poo-Arporn, Y.; Mongkolthanaruk, W.; Eichhorn, S. J.; Pinitsoontorn, S. Carbon Nanofiber Aerogel/Magnetic Core-Shell Nanoparticle Composites as Recyclable Oil Sorbents. *ACS Appl. Nano Mater.* **2020**, *3* (4), 3939–3950. https://doi.org/10.1021/acsanm.0c00818.

(13) Kuang, J.; Liu, L.; Gao, Y.; Zhou, D.; Chen, Z.; Han, B.; Zhang, Z. A Hierarchically Structured Graphene Foam and Its Potential as a Large-Scale Strain-Gauge Sensor. *Nanoscale* **2013**, *5* (24), 12171–12177. https://doi.org/10.1039/c3nr03379a.

(14) Wang, J.; Kaskel, S. KOH Activation of Carbon-Based Materials for Energy Storage. *J. Mater. Chem.* **2012**, *22* (45), 23710–23725. https://doi.org/10.1039/c2jm34066f.

(15) Tseng, R. L. Mesopore Control of High Surface Area NaOH-Activated Carbon. *J. Colloid Interface Sci.* **2006**, *303* (2), 494–502. https://doi.org/10.1016/j.jcis.2006.08.024.

(16) Chang, B.; Wang, Y.; Pei, K.; Yang, S.; Dong, X. $ZnCl_2$-Activated Porous Carbon Spheres with High Surface Area and Superior Mesoporous Structure as an Efficient Supercapacitor Electrode. *RSC Adv.* **2014**, *4* (76), 40546–40552. https://doi.org/10.1039/c4ra06418f.

(17) Bedia, J.; Belver, C.; Ponce, S.; Rodriguez, J.; Rodriguez, J. J. Adsorption of Antipyrine by Activated Carbons from $FeCl_3$-Activation of Tara Gum. *Chem. Eng. J.* **2018**, *333* (September 2017), 58–65. https://doi.org/10.1016/j.cej.2017.09.161.

(18) Zbair, M.; Ainassaari, K.; El Assal, Z.; Ojala, S.; El Ouahedy, N.; Keiski, R. L.; Bensitel, M.; Brahmi, R. Steam Activation of Waste Biomass: Highly Microporous Carbon, Optimization of Bisphenol A, and Diuron Adsorption by Response Surface Methodology. *Environ. Sci. Pollut. Res.* **2018**, *25* (35), 35657–35671. https://doi.org/10.1007/s11356-018-3455-3.

(19) Scherer, G. W. in *Xerogels Encyclopedia of Materials: Science and Technology*; Eds.: Buschow, K. H. J., Cahn, R. W., Flemings, M. C., Ilschner, B., Kramer, E. J., Mahajan, S., Veyssière, P., Eds.; Elsevier: New Jersey, **2001**, pp. 9797-9799.

(20) Rewatkar, P. M.; Taghvaee, T.; Saeed, A. M.; Donthula, S.; Mandal, C.; Chandrasekaran, N.; Leventis, T.; Shruthi, T. K.; Sotiriou-Leventis, C.; Leventis, N. Sturdy, Monolithic SiC and Si_3N_4 Aerogels from Compressed Polymer-Cross-Linked Silica Xerogel Powders. *Chem. Mater.* **2018**, *30* (5), 1635–1647. https://doi.org/10.1021/acs.chemmater.7b04981.

(21) Rewatkar, P. M.; Soni, R. U.; Sotiriou-Leventis, C.; Leventis, N. A Cobalt Sunrise: Thermites Based on $LiClO_4$-Filled Co(0) Aerogels Prepared from Polymer-Cross-Linked Cobaltia Xerogel Powders. *ACS Appl. Mater. Interfaces*. **2019**, *11* (25), 22668-22676. https://doi.org/10.1021/acsami.9b04734.

(22) Soni, R. U.; Edlabadkar, V. A.; Rewatkar, P. M.; Doulah, A. S. ud; Leventis, N.; Sotiriou-Leventis, C. Graphitic Carbon Aerogels from Compressed Powders of Polyacrylonitrile-Crosslinked Iron Oxide and Cobalt Oxide Xerogel Powders. *Chem. Mater.* **2021**, *xx* (xx), xx.

(23) Leventis, N. Three-Dimensional Core-Shell Superstructures: Mechanically Strong Aerogels. *Acc. Chem. Res.* **2007**, *40* (9), 874–884. https://doi.org/10.1021/ar600033s.

(24) Leventis, N.; Elder, I. A.; Rolison, D. R.; Anderson, M. L.; Merzbacher, C. I. Durable Modification of Silica Aerogel Monoliths with Fluorescent 2,7-Diazapyrenium Moieties. Sensing Oxygen near the Speed of Open-Air Diffusion. *Chem. Mater.* **1999**, *11* (10), 2837–2845. https://doi.org/10.1021/cm9901966.

(25) Hüsing, N.; Schubert, U.; Mezei, R.; Fratzl, P.; Riegel, B.; Kiefer, W.; Kohler, D.; Mader, W. Formation and Structure of Gel Networks from $Si(OEt)_4$/$(MeO)_3Si(CH_2)_3NR'_2$ Mixtures ($NR'_2 = NH_2$ or $NHCH_2CH_2NH_2$). *Chem. Mater.* **1999**, *11* (2), 451–457. https://doi.org/10.1021/cm980756l.

(26) Zha, J.; Roggendorf, H. Sol–Gel Science, the Physics and Chemistry of Sol–Gel Processing, Ed. by C. J. Brinker and G. W. Scherer, Academic Press, Boston 1990, Xiv, 908 Pp., Bound—ISBN 0-12-134970-5. *Adv. Mater.* **1991**, *3* (10), 522. https://doi.org/https://doi.org/10.1002/adma.19910031025.

(27) Leventis, N.; Sotiriou-Leventis, C.; Zhang, G.; Rawashdeh, A. M. M. Nanoengineering Strong Silica Aerogels. *Nano Lett.* **2002**, *2* (9), 957–960. https://doi.org/10.1021/nl025690e.

(28) Zhang, G.; Dass, A.; Rawashdeh, A. M. M.; Thomas, J.; Counsil, J. A.; Sotiriou-Leventis, C.; Fabrizio, E. F.; Ilhan, F.; Vassilaras, P.; Scheiman, D. A.; McCorkle, L.; Palczer, A.; Johnston, J. C.; Meador, M. A.; Leventis, N. Isocyanate-Crosslinked Silica Aerogel Monoliths: Preparation and Characterization. *J. Non. Cryst. Solids* **2004**, *350*, 152–164. https://doi.org/10.1016/j.jnoncrysol.2004.06.041.

(29) Leventis, N.; Sotiriou-Leventis, C.; Chandrasekaran, N.; Mulik, S.; Larimore, Z. J.; Lu, H.; Churu, G.; Mang, J. T. Multifunctional Polyurea Aerogels from Isocyanates and Water. A Structure-Property Case Study. *Chem. Mater.* **2010**, *22* (24), 6692–6710. https://doi.org/10.1021/cm102891d.

(30) Mulik, S.; Sotiriou-Leventis, C.; Churu, G.; Lu, H.; Leventis, N. Cross-Linking 3D Assemblies of Nanoparticles into Mechanically Strong Aerogels by Surface-Initiated Free-Radical Polymerization. *Chem. Mater.* **2008**, *20* (15), 5035–5046. https://doi.org/10.1021/cm800963h.

(31) Leventis, N.; Sadekar, A.; Chandrasekaran, N.; Sotiriou-Leventis, C. Click Synthesis of Monolithic Silicon Carbide Aerogels from Polyacrylonitrile-Coated 3D Silica Networks. *Chem. Mater.* **2010**, *22* (9), 2790–2803. https://doi.org/10.1021/cm903662a.

(32) Li, J.; Huang, X.; Chen, L. X-Ray Diffraction and Vibrational Spectroscopic Studies on PAN-LiTFSI Polymer Electrolytes. *J. Electrochem. Soc.* **2000**, *147* (7), 2653. https://doi.org/10.1149/1.1393585.

(33) Wang, Y.-X.; Wang, Q. Evaluation of Carbonization Tar in Making High Performance Polyacrylonitrile-Based Carbon Fibers. *J. Appl. Polym. Sci.* **2007**, *104* (2), 1255–1259. https://doi.org/https://doi.org/10.1002/app.25754.

(34) Usami, T.; Itoh, T.; Ohtani, H.; Tsuge, S. Structural Study of Polyacrylonitrile Fibers During Oxidativi Thermal Degradation by Pyrolysis-Gas Chromatography, Solid-State[13]C Nuclear Magnetic Resonance, and Fourier Transform Infrared Spectroscopy. *Macromolecules* **1990**, *23* (9), 2460–2465. https://doi.org/10.1021/ma00211a009.

(35) Leventis, N.; Sotiriou-Leventis, C.; Saeed, A. M.; Donthula, S.; Majedi Far, H.; Rewatkar, P. M.; Kaiser, H.; Robertson, J. D.; Lu, H.; Churu, G. Nanoporous Polyurea from a Triisocyanate and Boric Acid: A Paradigm of a General Reaction Pathway for Isocyanates and Mineral Acids. *Chem. Mater.* **2016**, *28* (1), 67–78. https://doi.org/10.1021/acs.chemmater.5b03117.

(36) Gross, T.; Ramm, M.; Sonntag, H.; Unger, W.; Weijers, H. M.; Adem, E. H. An XPS Analysis of Different SiO_2 Modifications Employing a C 1s as Well as an Au 4f7/2 Static Charge Reference. *Surf. Interface Anal.* **1992**, *18* (1), 59–64. https://doi.org/https://doi.org/10.1002/sia.740180110.

(37) Bertoncello, R.; Glisenti, A.; Granozzi, G.; Battaglin, G.; Caccavale, F.; Cattaruzza, E.; Mazzoldi, P. Chemical Interactions in Titanium- and Tungsten-Implanted Fused Silica. *J. Non. Cryst. Solids* **1993**, *162* (3), 205–216. https://doi.org/10.1016/0022-3093(93)91239-Y.

(38) Kim, C. M.; Jeong, H. S.; Kim, E. H. NEXAFS and XPS Characterization of Molecular Oxygen Adsorbed on Ni(100) at 80 K. *Surf. Sci.* **2000**, *459* (1), 457–461. https://doi.org/10.1016/S0039-6028(00)00512-4.

(39) Figueiredo, J. L.; Pereira, M. F. R. The Role of Surface Chemistry in Catalysis with Carbons. *Catal. Today* **2010**, *150* (1–2), 2–7. https://doi.org/10.1016/j.cattod.2009.04.010.

(40) Figueiredo, J. L.; Pereira, M. F. R.; Freitas, M. M. A.; Órfão, J. J. M. Modification of the Surface Chemistry of Activated Carbons. *Carbon N. Y.* **1999**, *37* (9), 1379–1389. https://doi.org/10.1016/S0008-6223(98)00333-9.

(41) Chen, J.; Mao, Z.; Zhang, L.; Tang, Y.; Wang, D.; Bie, L.; Fahlman, B. D. Direct Production of Nitrogen-Doped Porous Carbon from Urea via Magnesiothermic Reduction. *Carbon N. Y.* **2018**, *130*, 41–47. https://doi.org/10.1016/j.carbon.2017.12.125.

(42) Moon, I. K.; Lee, J.; Lee, H. Highly Qualified Reduced Graphene Oxides: The Best Chemical Reduction. *Chem. Commun.* **2011**, *47* (34), 9681–9683. https://doi.org/10.1039/c1cc13312h.

(43) Inagaki, M.; Toyoda, M.; Soneda, Y.; Morishita, T. Nitrogen-Doped Carbon Materials. *Carbon N. Y.* **2018**, *132*, 104–140. https://doi.org/10.1016/j.carbon.2018.02.024.

(44) Riedo, E.; Comin, F.; Chevrier, J.; Schmithusen, F.; Decossas, S.; Sancrotti, M. Structural Properties and Surface Morphology of Laser-Deposited Amorphous Carbon and Carbon Nitride Films. *Surf. Coatings Technol.* **2000**, *125* (1–3), 124–128. https://doi.org/10.1016/S0257-8972(99)00591-5.

(45) Scharf, T. W.; Ott, R. D.; Yang, D.; Barnard, J. A. Structural and Tribological Characterization of Protective Amorphous Diamond-like Carbon and Amorphous CN_x Overcoats for next Generation Hard Disks. *Journal of Applied Physics.* **1999**, pp. 3142–3154. https://doi.org/10.1063/1.369654.

(46) Yan, X.; Xu, T.; Chen, G.; Xu, S.; Yang, S. Field-Emission Properties of Diamond-like-Carbon and Nitrogen-Doped Diamond-like-Carbon Films Prepared by Electrochemical Deposition. *Appl. Phys. A Mater. Sci. Process.* **2005**, *81* (1), 41–46. https://doi.org/10.1007/s00339-004-3069-0.

(47) Wickramaratne, N. P.; Jaroniec, M. Importance of Small Micropores in CO_2 Capture by Phenolic Resin-Based Activated Carbon Spheres. *J. Mater. Chem. A* **2013**, *1* (1), 112–116. https://doi.org/10.1039/c2ta00388k.

(48) Adeniran, B.; Mokaya, R. Low Temperature Synthesized Carbon Nanotube Superstructures with Superior CO_2 and Hydrogen Storage Capacity. *J. Mater. Chem. A* **2015**, *3* (9), 5148–5161. https://doi.org/10.1039/c4ta06539e.

(49) Webb, P. A.; Orr, C. *Analytical Methods in Fine Particle Technology*; Micromeritics Instrument Corporation: Norcross, GA, **1997**, pp. 61–66.

(50) Cazorla-Amorós, D.; Alcaniz-Monge, J.; Linares-Solano, A. Characterization of Activated Carbon Fibers by CO_2 Adsorption. *Langmuir* **1996**, *12* (11), 2820–2824. https://doi.org/10.1021/la960022s.

(51) Cazorla-Amorós, D.; Alcañiz-Monge, J.; De La Casa-Lillo, M. A.; Linares-Solano, A. CO_2 as an Adsorptive to Characterize Carbon Molecular Sieves and Activated Carbons. *Langmuir* **1998**, *14* (16), 4589–4596. https://doi.org/10.1021/la980198p.

(52) Smit, B.; Reimer, J. R.; Oldenburg, C. M.; Bourg, I. C. *Introduction to Carbon Capture and Sequestration: The Berkeley Lectures on Energy*, Vol. 1.; Imperial College Press: London, **2014**, pp. 281-354.

(53) Patel, H. A.; Je, S. H.; Park, J.; Jung, Y.; Coskun, A.; Yavuz, C. T. Directing the Structural Features of N_2-Phobic Nanoporous Covalent Organic Polymers for CO_2 Capture and Separation. *Chem. - A Eur. J.* **2014**, *20* (3), 772–780. https://doi.org/10.1002/chem.201303493.

(54) Germain, J.; Fréchet, J. M. J.; Svec, F. Nanoporous Polymers for Hydrogen Storage. *Small* **2009**, *5* (10), 1098–1111. https://doi.org/10.1002/smll.200801762.

(55) Xydias, P.; Spanopoulos, I.; Klontzas, E.; Froudakis, G. E.; Trikalitis, P. N. Drastic Enhancement of the CO_2 Adsorption Properties in Sulfone-Functionalized Zr- and Hf-UiO-67 MOFs with Hierarchical Mesopores. *Inorg. Chem.* **2014**, *53* (2), 679–681. https://doi.org/10.1021/ic402430n.

(56) Yang, X.; Yu, M.; Zhao, Y.; Zhang, C.; Wang, X.; Jiang, J. X. Hypercrosslinked Microporous Polymers Based on Carbazole for Gas Storage and Separation. *RSC Adv.* **2014**, *4* (105), 61051–61055. https://doi.org/10.1039/c4ra09394a.

(57) Bag, S.; Kanatzidis, M. G. Chalcogels: Porous Metal-Chalcogenide Networks from Main-Group Metal Ions. Effect of Surface Polarizability on Selectivity in Gas Separation. *J. Am. Chem. Soc.* **2010**, *132* (42), 14951–14959. https://doi.org/10.1021/ja1059284.

(58) Rallapalli, P.; Prasanth, K. P.; Patil, D.; Somani, R. S.; Jasra, R. V.; Bajaj, H. C. Sorption Studies of CO_2, CH_4, N_2, CO, O_2 and Ar on Nanoporous Aluminum Terephthalate [MIL-53(Al)]. *J. Porous Mater.* **2011**, *18* (2), 205–210. https://doi.org/10.1007/s10934-010-9371-7.

(59) Jin, Y.; Voss, B. A.; Noble, R. D.; Zhang, W. A Shape-Persistent Organic Molecular Cage with High Selectivity for the Adsorption of CO_2 over N_2. *Angew. Chemie - Int. Ed.* **2010**, *49* (36), 6348–6351. https://doi.org/10.1002/anie.201001517.

(60) Zulfiqar, S.; Mantione, D.; El Tall, O.; Sarwar, M. I.; Ruipérez, F.; Rothenberger, A.; Mecerreyes, D. Nanoporous Amide Networks Based on Tetraphenyladamantane for Selective CO_2 Capture. *J. Mater. Chem. A* **2016**, *4* (21), 8190–8197. https://doi.org/10.1039/c6ta01457g.

(61) Sing, K. S. W.; Rouquerol, J. *5 Classical Interpretation of Physisorption Isotherms at the Gas – Solid Interface*; *In Adsorption by Powders and Porous Solids, Second Edition* Principles, Methodology and Applications. Eds: Rouquerol, F.; Rouquerol, J.; Sing, K. S. W.; Liewwllyn, P.; Maurin, G. Academic Press, Oxford, **2014**, pp. 159-189.

IV. PREPARATION OF GRAPHITIC CARBON AEROGELS FROM POLYACRYLONITRILE-CROSSLINKED IRON OXIDE AND COBALT OXIDE XEROGEL POWDERS ANDTHEIR EVALUATION IN LITHIUM-ION BATTERIES

Rushi U. Soni, Vaibhav A. Edlabadkar, Parwani M. Rewatkar, ABM Shaheen ud Doulah, Santhoshkumar Sundaramoorthy, Amitava Choudhury, Nicholas Leventis[§] and Chariklia Sotiriou-Leventis[*]

Department of Chemistry, Missouri University of Science and Technology, Rolla, MO 65409, U.S.A. [§] Present Address: Aspen Aerogels, 30 Forbes Road, Bldg. B, Northborough, MA 01532, U.S.A. *Address correspondence to this author (Tel.: 573-341-4353; E-mail: cslevent@mst.edu)

ABSTRACT

We demonstrate the Fe- or Co-catalyzed preparation of graphitic carbon aerogels that bypasses the typical use of supercritical fluid drying, and takes place at much lower temperatures (800 to 1500 °C) than conventional graphitization (2500-3300 °C). The process starts with preparation of polyacrylonitrile (PAN)-crosslinked iron and cobalt oxide xerogel powders via surface-initiated free-radical polymerization of acrylonitrile on the solid, porous networks of sol-gel-derived suspensions of the oxides. The resulting wet-gel powders were dried under vacuum at 50 °C to xerogel powders, which were compressed into desirable form factors, e.g., discs or cylinders. These compacts were then aromatized (300 °C, O_2), and subsequently carbonized in the range of 800 °C to 1500 °C under Ar. Carbothermal reduction of the oxide networks by the newly produced carbon yielded catalytic-toward-graphitization Fe(0) or Co(0) nanoparticles embedded within the carbons. Post-pyrolysis, those metallic nanoparticles were removed with aqua

regia leaving behind pure graphitic carbon aerogels. Chemical characterization of materials up to aromatization was carried out with solid-state ^{13}C NMR; characterization of the terminal graphite aerogels was based on powder-XRD, Raman, TEM, SEM, XPS and N_2-sorption. Porosities in the range of 63% to 78% v/v were created during aromatization, and mainly during pyrolytic carbonization. The micromorphology varied with the catalyst; with iron, it also varied with the temperature. In the latter case, structures included nanorods, nanofibers, and stacked platelets; in the case of cobalt invariably all materials looked like figs. The best quality graphite aerogels were obtained with iron at 1500 ºC. These materials consisted of 99.8% w/w graphitic carbon, the crystallite domain size along the (002) plane reached 170 Å, and the crystallite width along the a-axis was 70 nm. Those materials were introduced into coin cells with a Li foil as a counter electrode, and were evaluated as lithium intercalation electrodes. Their redox potential was stable upon cycling at the expected value of +0.3 V vs. Li^+/Li. The charge capacity was also stable, but significantly lower (~100 mAh g^{-1}) than the theoretically expected value (~372 mA h g^{-1}). That was attributed to the formation of a solid-electrolyte interface over the entire surface area of the graphite electrode that deactivated a significant part of its "bulk."

Keywords: graphitic carbon, aerogel, xerogel, catalytic graphitization, anodes, lithium-ion batteries

TOC Graphic
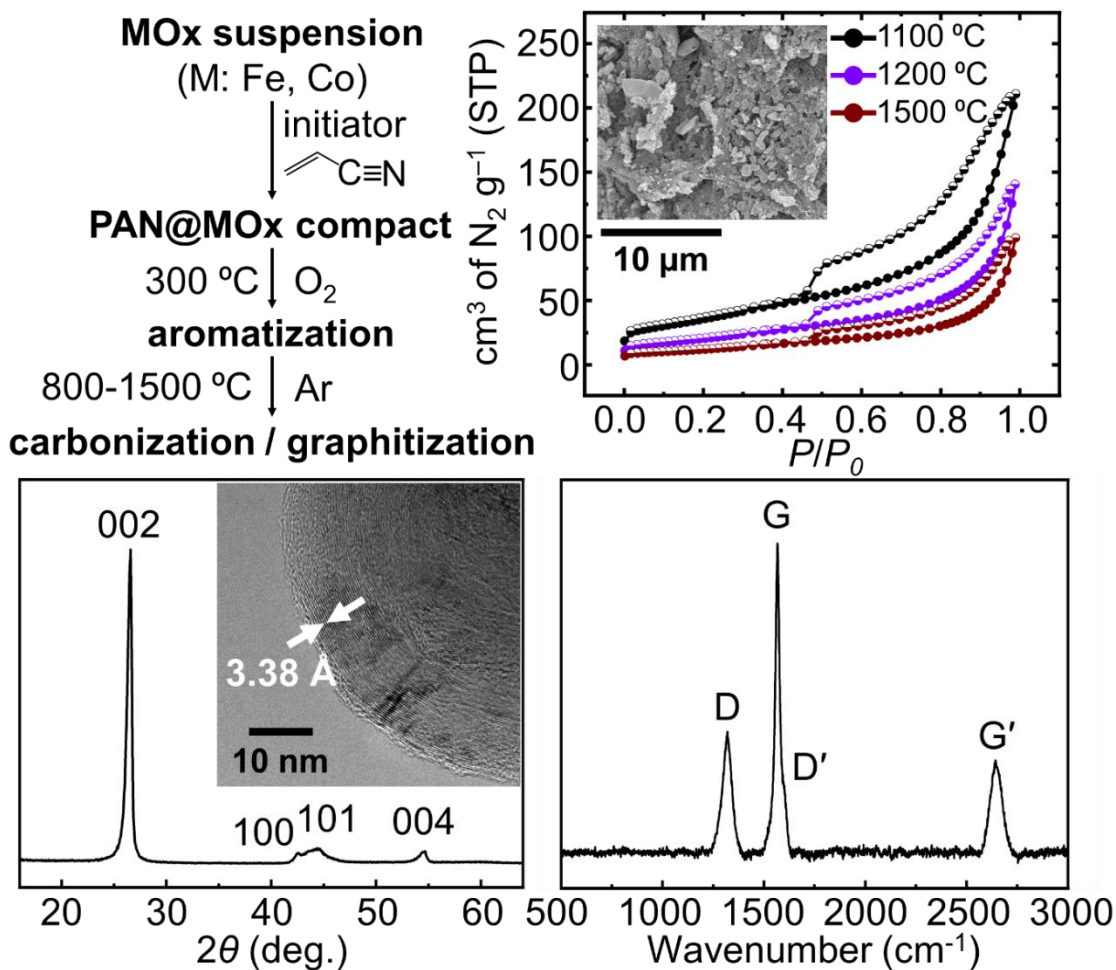
1. INTRODUCTION

Graphite is a chemically inert, thermodynamically stable allotrope of carbon with high electrical and thermal conductivity.[1–3] Porous graphitic carbon, with its open porosity and tunable surface area, can be an attractive electrode material for use in electrochemical energy generation and storage (supercapacitors, batteries and fuel cells),[4–7] as catalyst

support,[8,9] in superlubrication,[10,11] water purification,[12] and for thermal management applications, e.g., efficient heat removal in nanoelectronic devices based on the high thermal conductivity of graphite.[13,14] Graphite is mostly mined, however, separation and purification of natural graphite to technology-relevant grade graphite is an elaborate, low-yield and environmentally unfriendly process.[1] Since, natural graphite is a non-renewable resource, and in addition porous graphite is not even a natural product, various methods for the synthesis of high-quality graphite have been developed. For porous graphitic carbons in particular, typical methods include: (a) high temperature chemical vapor deposition (CVD);[15] (b) high temperature or/and pressure treatment of amorphous carbons and amorphous carbon precursors;[16–18] and (c) catalytic graphitization of amorphous carbon.[19] The challenge of the high-temperature methods is to retain porosity; thereby, akin to those methods is the use of so-called hard[20–23] and soft templates.[24,25] On the other hand, graphitization catalysts reduce the graphitization temperature, but the challenge now is placed with the molecular/nano-level mixing of the carbon to be graphitized, or the carbon precursor, and the catalyst. Graphitization catalysts include metals like Fe, Co, Ni, and Mn.[19,24,26,27]

A special class of porous carbons, which has comprised the point of departure for graphitic aerogels, is referred to as carbon aerogels.[28] Carbon aerogels are obtained by pyrolysis of polymeric aerogels, which in turn are synthesized using sol-gel chemistry.[29–31] Graphitization of carbon aerogels has been carried out by both, high temperature treatment (2300 °C),[32] and catalytically with metallic iron nanoparticles created *in situ* and remaining embedded throughout the carbon; an example of the latter method includes

decomposition of ferrocene-derived monomers used in the synthesis of carbonizable polyamide aerogels.[9]

The route from polymer aerogels to carbon aerogels to graphite aerogels provides many advantages in terms of well-defined porosity, particle morphology, continuous 3D hierarchical structures, and the ability to obtain monolithic gels or powders tailored to specific applications. However, this method, starting from polymeric aerogels to ultimately obtain graphitic carbon aerogels involves handling of extremely fragile wet gels, and supercritical CO_2 drying, which is a lengthy, energy and materials intensive process. Conversely, recently (2018, 2019) we demonstrated the synthesis of ceramic (carbide, nitride),[33] and metallic aerogels[34] from pyrolysis of compressed xerogel powders of a suitable sol-gel-derived oxide network coated conformally with a carbonizable polymer. In order to favor formation of the metallic or ceramic network, the stoichiometric balance of the carbonizable polymer to the oxide was carefully adjusted. Then, as described in the previous article of this issue,[35] if the oxide network is silica and the carbonizable polymer is introduced in a large stoichiometric excess, the aerogel-via-xerogel method can be extended to the preparation of amorphous carbon aerogels. In fact this aerogel-via-xerogel route to amorphous carbon aerogels is more efficient in terms of time, energy and materials consumption relative to the classic method to carbon aerogels from pyrolysis of polymeric aerogels.

At this point, reasoning that, unlike silica, if the sacrificial inorganic support of the carbonizable polymer is also a graphitization catalyst precursor, then the aerogel-via-xerogel methodology can be expanded into the synthesis of graphitic aerogels. For this, two relevant metal oxide (MOx) networks were obtained by gelation of the corresponding

metal chloride hydrates ($FeCl_3.6H_2O$ and $CoCl_2.6H_2O$), and were modified with a bidentate free-radical initiator derived from 4,4′-azobis(4-cyanovaleric acid) (ABCVA). Surface-initiated polymerization of acrylonitrile over those skeletal networks yielded iron or cobalt oxide powders coated conformally with polyacrylonitrile (PAN) at the nanoscopic level. These powders are referred to as PAN@FeOx and PAN@CoOx, respectively, and were compressed into shaped compacts; the latter were first aromatized at 300 ºC under O_2, and then they were pyrolytically graphitized at different temperatures (Temp) from 800 ºC to 1500 ºC under ultrahigh purity argon. The resulting materials are referred to as G-PAN_{Temp}@Fe and G-PAN_{Temp}@Co, respectively. "G" refers to the graphitization process occurring during pyrolysis, and "@Metal" refers to the fact that several sol-gel derived metal oxide networks (including FeOx and CoOx), brought in intimate contact with carbonizable polymers undergo carbothermal reduction[36,37] to the corresponding pure metals.[34,38–41] Post pyrolysis, all inorganic components were removed with aqua-regia, and the resulting pure graphitic aerogels, referred to as G-PAN_{Temp}_*from*_Fe and G-PAN_{Temp}_*from*_Co, respectively, consisted of up to 99.8% w/w of graphitic carbon and were 63-78% v/v porous materials.

2. RESULTS AND DISCUSSION

2.1. SYNTHESIS OF GRAPHITIC CARBON AEROGELS FROM COMPRESSED, POLYACRYLONITRILE-CROSSLINKED, IRON AND COBALT OXIDE XEROGEL POWDERS

As described in the following sections, the aerogel-via-xerogel process to graphite aerogels starts with preparation of metal oxide (MOx) wet-gel particle suspensions,

continues with cross-linking with polyacrylonitrile (PAN), followed by aromatization of PAN, then pyrolytic graphitization and finally by removal of residual inorganic components (matals and metal carbides).

2.1.1. Preparation of Iron Oxide (FeOx) and Cobalt Oxide (CoOx) Wet-Gel Particle Suspensions. Suspensions of wet-gel iron oxide and cobalt oxide particles were prepared in dimethylformamide (DMF) as shown in Schemes 1A and 1B, that is via reaction of the corresponding hydrated metal ions, $[Fe(H_2O)_6]Cl_3$ and $[Co(H_2O)_6]Cl_2$, with epichlorohydrin that acts as a proton acceptor according to Equations 1 and 2 leading to Fe-O-Fe and Co-O-Co bridge formation, and eventually to the oxides.[34,40–42] The epichlorohydrin-to-hydrated metal chloride ratio was fixed to 10:1 mol/mol according to previously published procedures.[34,38]

For the given composition of the FeOx sol, gelation was diverted from monoliths to wet-gel suspensions using vigorous stirring of the sol in a non-solvent (hexane). On the other hand, hydrated Co(II) chlorides do not generally gel into monoliths, but they rather form suspensions of wet CoOx gel particles;[34,39] therefore stirring with a non-solvent for getting to the latter was not needed. The MOx suspensions (M: Fe or Co) were washed with DMF and toluene.

$$[M(H_2O)_6]^{n+} \xrightarrow[\substack{Cl^- \\ \downarrow}]{} [M(H_2O)_5(OH)]^{(n-1)+} \tag{1}$$

$$[M(H_2O)_5(OH)]^{(n-1)+} \xrightarrow[-H_2O]{[M(H_2O)_5(OH)]^{(n-1)+}} [(H_2O)_5M\text{-}O\text{-}M(H_2O)_5]^{2(n-1)+} \longrightarrow MOx \text{ gel suspension} \tag{2}$$
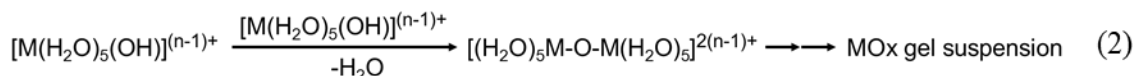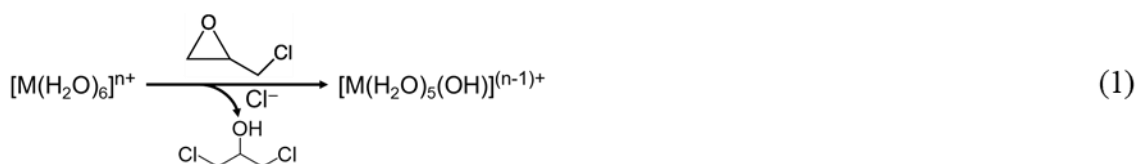
A. Synthesis of wet-gel suspensions of iron oxide particles (FeOx)
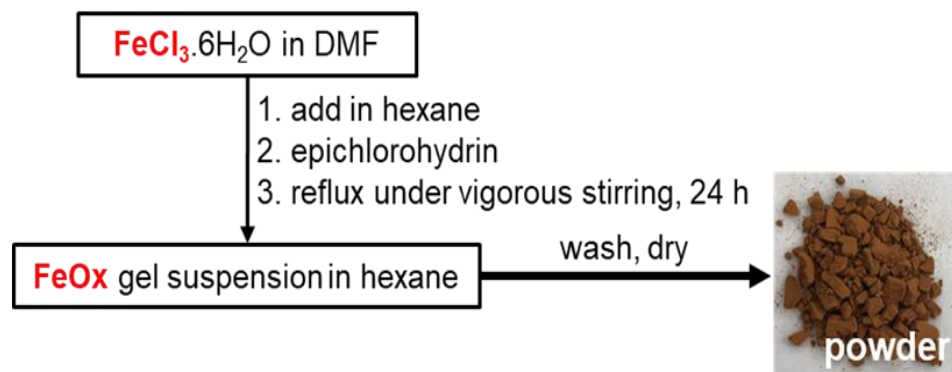
B. Synthesis of wet-gel suspensions of cobalt oxide particles (CoOx)
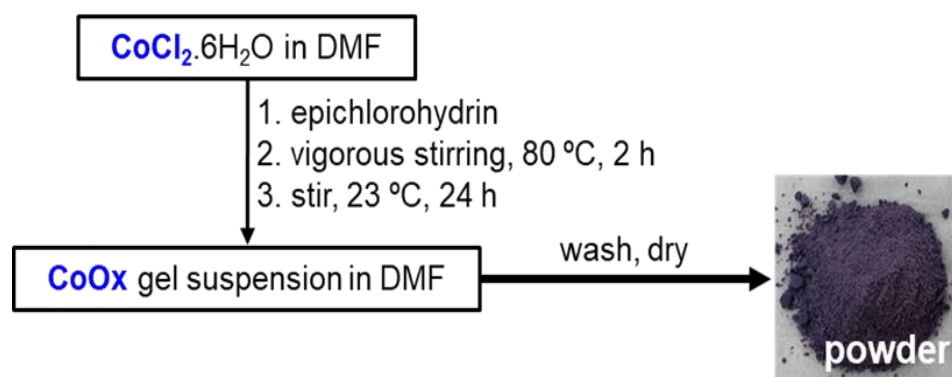
Scheme 1. Synthesis of polyacrylonitrile-crosslinked metal oxide xerogel powders and compacts.

C. Synthesis of polyacrylonitrile-crosslinked metal oxide xerogel powders and PAN@MOx compacts
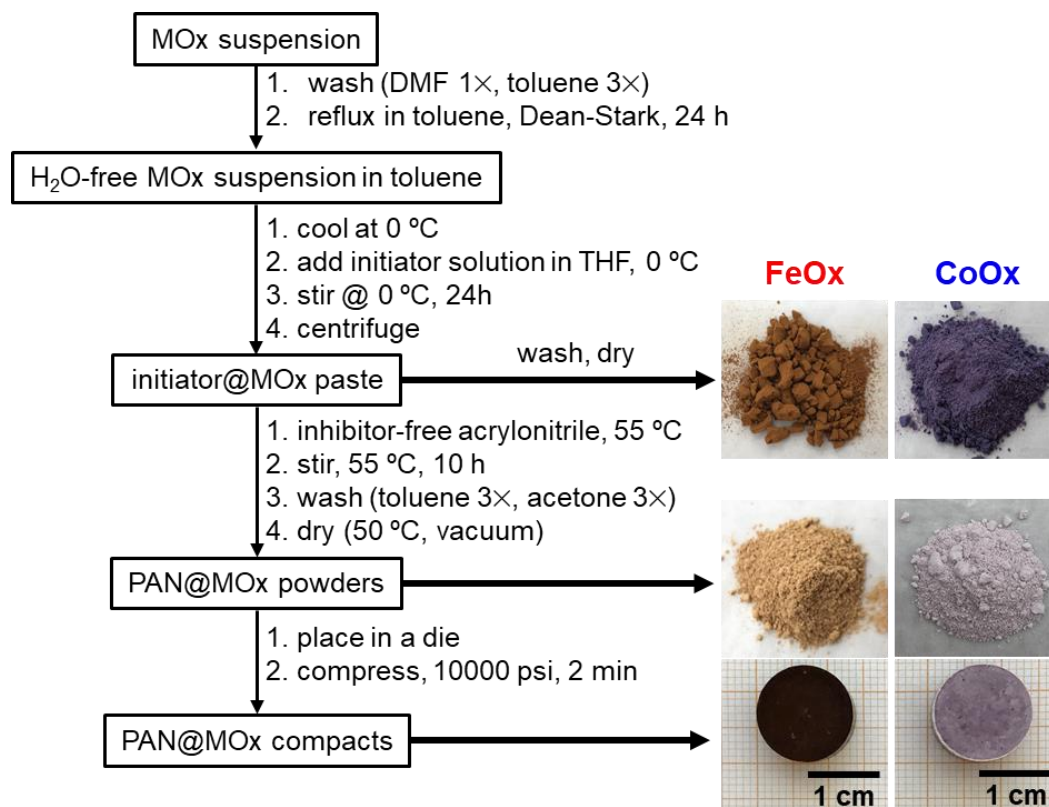
Scheme 1. Synthesis of polyacrylonitrile-crosslinked metal oxide xerogel powders and compacts (cont.).

2.1.2 Crosslinking of FeOx and CoOx Wet-Gel Particles with Acrylonitrile; Preparation of Polyacrylonitrile-Crosslinked Metal-Oxide Xerogel Powders (PAN@MOx). Toluene-exchanged wet-gel suspensions of MOx particles were further exchanged with refluxing toluene in an apparatus equipped with a Dean-Stark in order to remove residual water. This is because, although the initiator we employed here was based on 4,4'-azobis(4-cyanopentanoic acid) (ABCVA – see Figure 1A) as in previous

studies,[35,43–45] the chemistry of its latching into the MOx surface had not only to be different from before, but as it turned out it was also incompatible with water. Specifically, it is noted that both the amide route,[43–45] and the salt route[35] of attaching ABCVA to silica used 3-aminopropyltriethoxysilane (APTES) as a bridging moiety. APTES contains silicon. Here, in order to avoid contamination of the final graphite aerogels with silica or silicon carbide, ABCVA was activated for surface attachment differently: it was first converted into an anhydride that was expected to react with OH groups on the oxide surface, and thus get linked to the oxide network from both of its ends as a bidentate di-ester, in analogy to previous work where ABCVA was linked as a bidentate di-amide.[43–45] As a result of using a bidentate free-radical initiator, the polymer produced by thermal cleavage of the central azo group (-N=N-) of ABCVA would remain surface-bound. Thus, referring to Figure 1, ABCVA was put to react with ethyl chloroformate in a EtOCOCl:ABCVA = 2:1 mol/mol ratio in anhydrous THF at 0 ℃ in an amber-colored Erlenmeyer flask. Triethylamine (Et_3N, in a EtOCOCl:Et_3N = 1:1 mol/mol) was included in the reaction mixture to neutralize HCl. The progress of the reaction was followed visually via the formation of a precipitate (triethylammonium chloride salt ($Et_3NH^+ Cl^-$)) that was completed within 20-25 min.

This solution was centrifuged, and the supernatant liquid contained the activated ABCVA-based free-radical initiator, the identity of which was confirmed with liquid ^{13}C NMR (see Figure 1B and discussion in Section 2.3). Had not all residual water been removed from the MOx suspension before introducing the free radical initiator it might had caused hydrolysis of the terminal anhydride groups, resulting in PAN formation in the interparticle space within the MOx particles. That might be desirable under certain circumstances, but this route was not considered here.
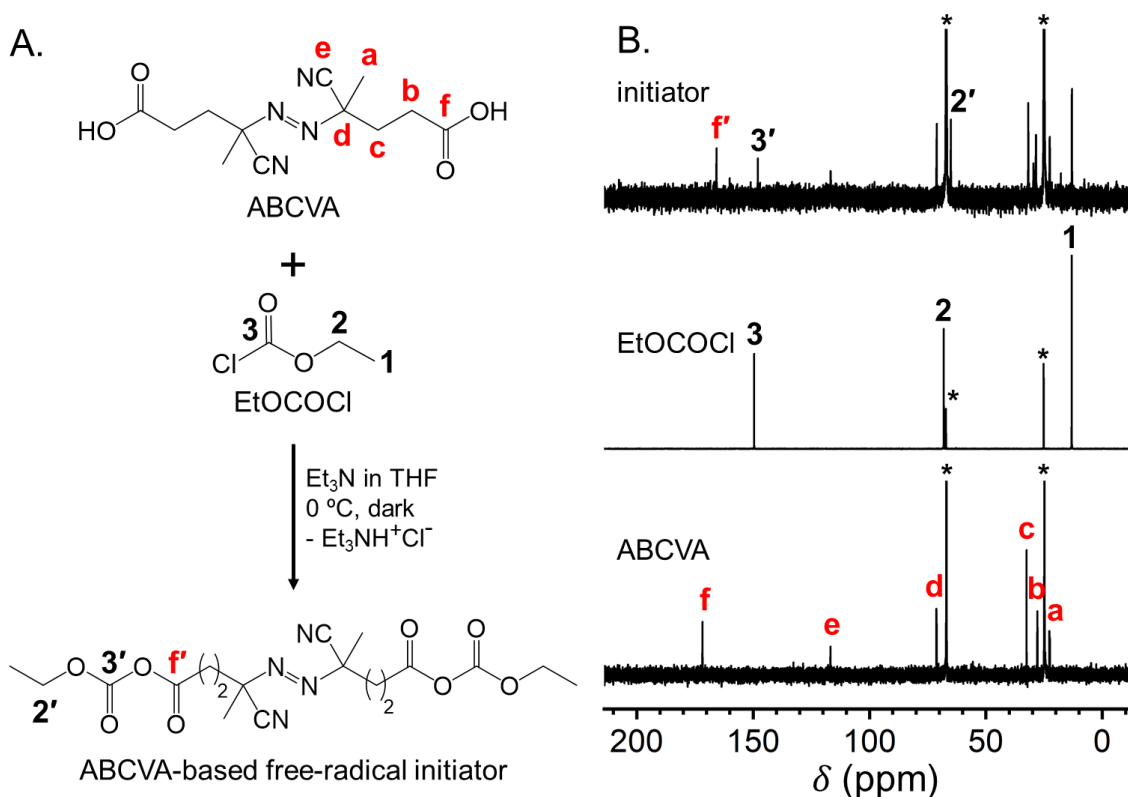
Figure 1. (A) Preparation of the bidentate free-radical initiator used in this study via reaction of 4,4'-azobis-4-cyanovaleric acid (ABCVA) and ethyl chloroformate (EtOCOCl). (B) Liquid ^{13}C NMR spectra in THF-d$_8$ of ABCVA, EtOCOCl and *4,4'-azobis(4-cyano(ethylcarbonic)pentanoic anhydride)* (ABCVA-based free-radical initiator). (Solvent peaks are marked with asterisks.)

The THF solution of the ABCVA-based free-radical initiator was added to the water-free MOx suspension in toluene at 0 ºC and the mixture was stirred for 24 h. The initiator uptake by MOx was monitored periodically with ^{13}C liquid NMR of the supernatant liquid, and the uptake was considered complete when the initiator resonances disappeared (typically by 24 h). The resulting initiator@MOx suspensions were centrifuged, and the resulting paste-like residues were re-suspended in pure inhibitor-free acrylonitrile. The new suspensions were heated at 55 ºC for 10 h to induce surface-initiated

polymerization of the monomer (Equation 3). The continuous phase (inhibitor-free acrylonitrile) remained liquid, and the off-white polyacrylonitrile-crosslinked metal oxide suspensions were washed with toluene and acetone and were dried at 50 ℃ under vacuum to free-flowing fine xerogel powders referred to as PAN@MOx (Scheme 1C). Subsequently, these powders were placed in suitable stainless-steel dies and were compressed with a hydraulic press at 10,000 psi for 2 min to shaped PAN@MOx compacts (Scheme 1C).

$$\text{(3)}$$
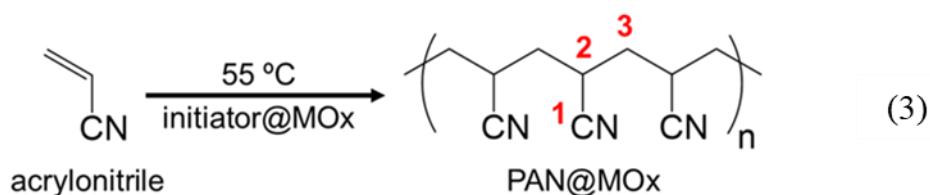
Using thermogravimetric analysis (TGA – see Figure S.1 of Appendix I in Supporting Information) up to 800 ℃ under O_2, initiator@FeOx and initiator@CoOx exhibited mass losses of 33.56% and 26.12%, respectively. Similarly, PAN@FeOx and PAN@CoOx lost 92.42% and 88.24% of their masses, respectively. The residues were analyzed with powder XRD and consisted of Fe_2O_3 and Co_3O_4, respectively.[34,41] Based on these mass losses and the fact that the initiator, being bound on the surface of MOx, stays together with the polymer in the PAN@MOx compacts, it was calculated that PAN@FeOx and PAN@CoOx contained PAN at 87.09% w/w and 84.08% w/w, respectively. (PAN:MOx:initiator mass ratios: for PAN@FeOx, 87.09:8.58:4.33; for PAN@CoOx, 84.08:11.76:4.16)

2.1.3. Processing of PAN@MOx Compacts to Graphitic Carbon Aerogels. Carbonization of the PAN@MOx compacts requires prior aromatization.[46] Otherwise, if

PAN@MOx compacts are heated directly to, say, 800 ℃, they undergo complete loss of the organic matter.[44]
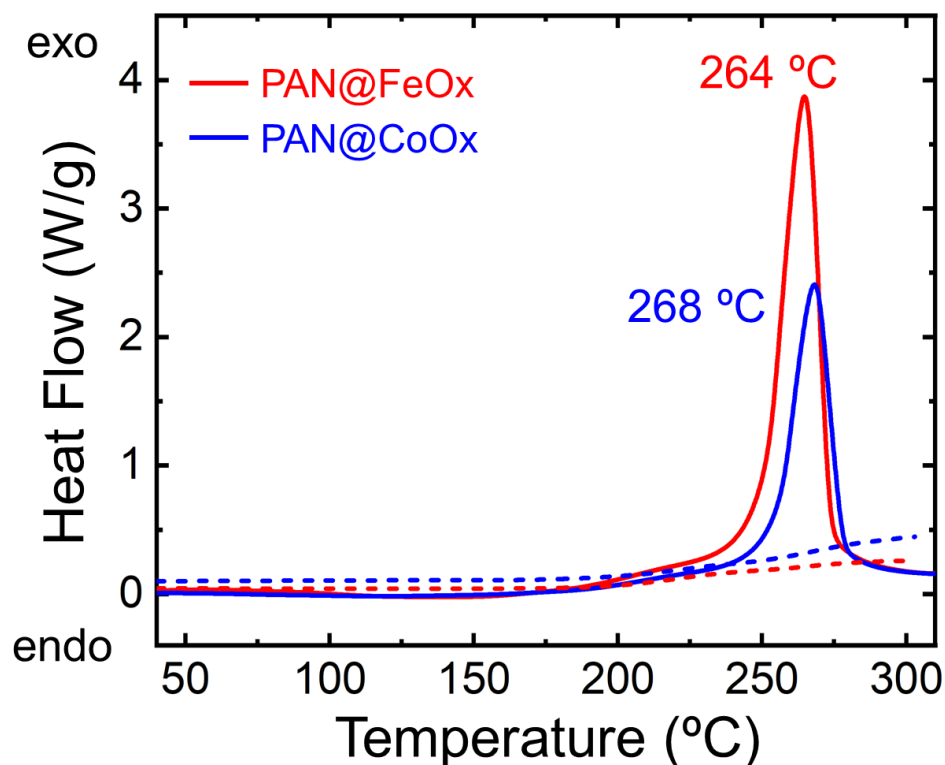
Figure 2. Modulated differential scanning calorimetry (MDSC) of samples as shown under O_2 (solid lines) and under N_2 (dashed lines). (Common heating rate: 5 ℃ min^{-1}).

Heating PAN@FeOx and PAN@CoOx powders under oxygen shows sharp exotherms at 264 ℃ and 268 ℃, respectively (Figure 2). According to the previous article of this issue,[35] complete oxidative aromatization of PAN in PAN@silica samples took place only with pyrolysis after the exotherm. Based on these data, compressed PAN@FeOx and PAN@CoOx compacts were aromatized at 300 ℃ h under flowing O_2 for 24 h (Equation 4). The resulting materials are referred to as
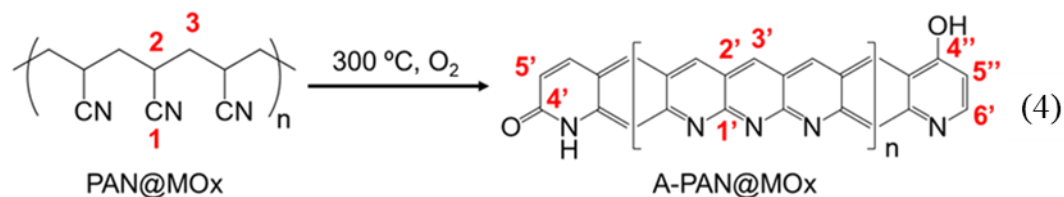
A-PAN@FeOx and A-PAN@CoOx compacts, respectively (Scheme 2). Aromatized compacts were graphitized pyrolytically at different temperatures from 800 ºC to 1500 ºC for 5 h under flowing ultrahigh purity argon. The resulting materials are referred to as G-PAN$_{Temp}$@Fe and G-PAN$_{Temp}$@Co, respectively. Subsequently, these compacts were treated with aqua regia to remove all inorganic components (oxides and carbides), then they were washed with water and acetone, and finally were dried at 80 ºC under vacuum (Scheme 2), to the respective pure metal-free graphitized samples referred to as G-PAN$_{Temp}$_*from*_Fe and G-PAN$_{Temp}$_*from*_Co. All pyrolyzed compacts, before and after aqua regia treatment, were sturdy and kept their monolithic shapes (see Figures 3 & 4). The evolution of the material and chemical properties along processing are discussed in Sections 2.2 and 2.3. Based on the data presented in these two sections, it was concluded that the best quality graphite was contained within G-PAN$_{1500}$_*from*_Fe. Electrochemical characterization of that material is presented in Section 2.4.

2.2. EVOLUTION OF THE MACRO AND MICROSCOPIC PROPERTIES ALONG PROCESSING

General material properties of PAN@MOx and their derivatives along aromatization, graphitization and treatment with aqua regia are presented in Tables S.1 and S.2 of Appendix II in Supporting Information. In brief, the bulk densities (ρ_b) of
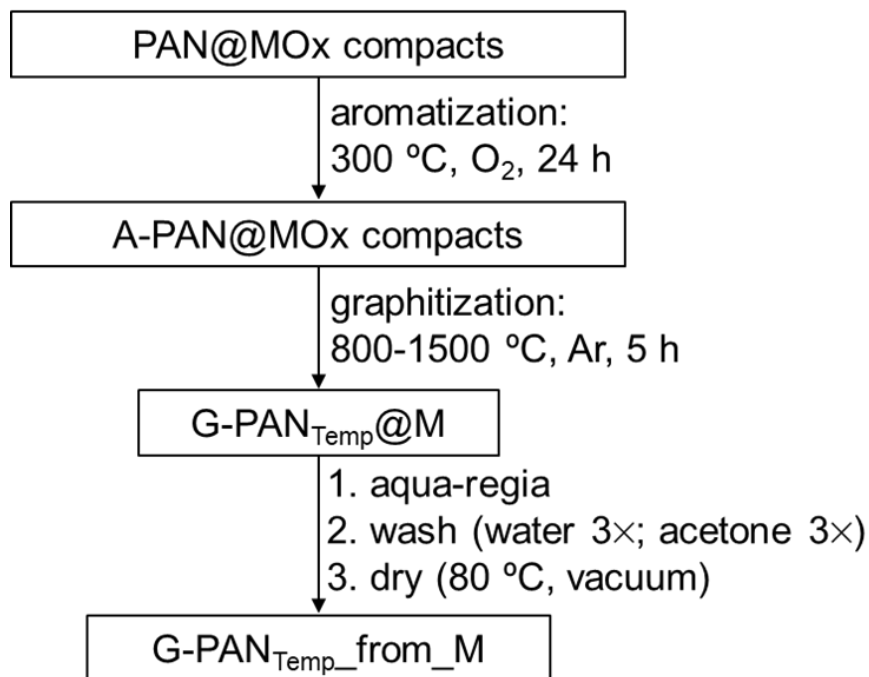
Scheme 2. Further processing of PAN@MOx compacts to graphitic carbon aerogels.
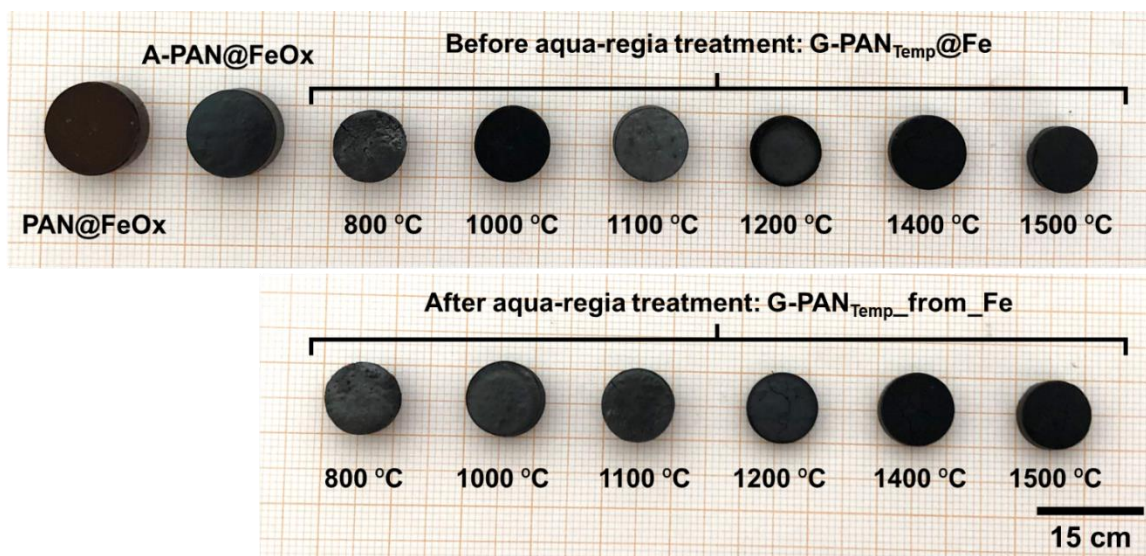
Figure 3. Photographs of the PAN@FeOx system along processing at different temperatures toward graphite aerogels.
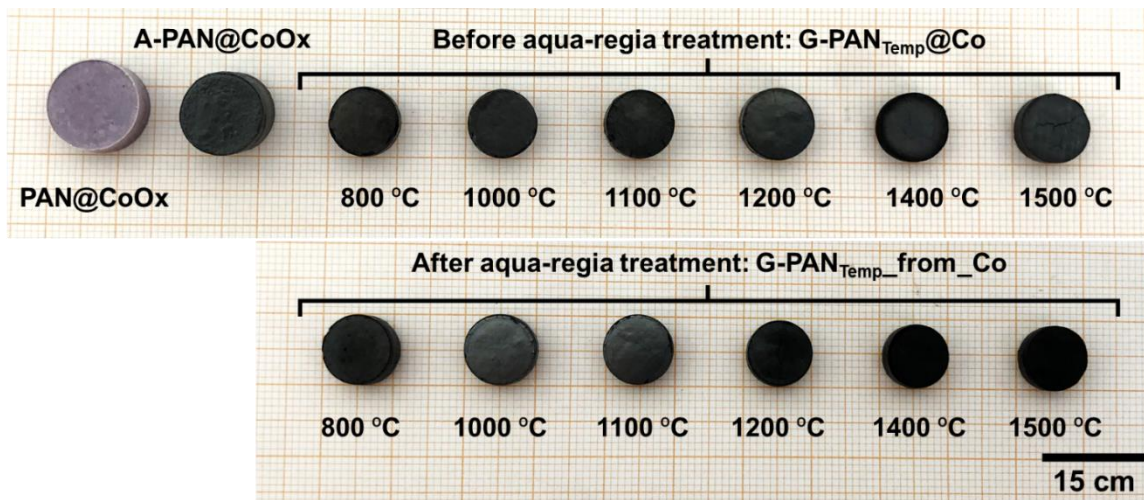
Figure 4. Photographs of the PAN@CoOx system along processing at different temperatures toward graphite aerogels.

PAN@FeOx and PAN@CoOx xerogel compacts were very close to one another (1.228 g cm^{-3} and 1.239 g cm^{-3}, respectively) reflecting the similar formulation and processing of the two types of compacts. The corresponding skeletal densities (ρ_s) were different due the different metal oxides (1.304 g cm^{-3} and 1.412 g cm^{-3}, respectively). The open porosity, Π, calculated as percent of empty space via $\Pi = 100 \times (\rho_s - \rho_b)/\rho_s$, was found very low, at 6% v/v and 12% v/v for PAN@FeOx and PAN@CoOx xerogel compacts, respectively. Considering these property values as the point of departure, aromatization of the PAN@FeOx and PAN@CoOx xerogel compacts (see Equation 4) brought about similar mass losses in the two materials (32% w/w and 28% w/w, respectively) that were matched by similar linear shrinkages (16% and 14%, respectively – refer to Figures 3 and 4), and the densities of A-PAN@FeOx and A-PAN@CoOx were somewhat reduced (1.11 g cm^{-3} and 1.23 g cm^{-3}, respectively) relative to those of the starting PAN@FeOx and PAN@CoOx compacts. At the same time skeletal densities were increased (to 1.858 g cm^{-}

^{3} and 1.773 g cm^{-3}, respectively), and the porosities of the aromatized samples were increased to 40% w/w and 31% w/w.

Further pyrolysis of A-PAN@MOx at temperatures ranging from 800 ^{o}C to 1500 ^{o}C resulted in further mass losses, all falling roughly in the range of 50-75% w/w, including both as-prepared and samples treated with aqua regia (Figure 5). It is noted that relative to as-prepared samples, treatment with aqua regia caused an additional 5-10% of mass loss, owing to removal of the inorganic components. However, similarities not-withstanding, the mass-loss profiles were different in the two series of materials (from Fe and from Co – see Figure 5): The mass losses by G-PAN$_{Temp}$@Fe, and consequently by G-PAN$_{Temp}$_$from$_Fe, leveled off at Temp = 1100 ^{o}C, while G-PAN$_{Temp}$@Co kept on loosing more mass all the way to the maximum pyrolysis temperature employed in this study (1500 ^{o}C). The origin of this discrepancy might be related to the formation of iron carbide at ≤1100 ^{o}C, as well as to the different activity of the two metals as graphitization catalysts (refer to Section 2.3 below).

Now, focusing on the final metal-free carbon aerogels (G-PAN$_{Temp}$_$from$_M), Figure 6 summarizes several of their general material properties. For the original data, as well as the corresponding properties before treatment with aqua regia, refer to Tables S.1 and S.2 of Appendix II in Supporting Information.

The mass yield of G-PAN$_{Temp}$_$from$_M (Figure 6A) follows a reverse trend from the mass loss data of Figure 5: the yield of G-PAN$_{Temp}$_$from$_Fe initially decreases with the pyrolysis temperature, but it levels off at around 24-27% w/w at ≥1100 ^{o}C; the yield of G-PAN$_{Temp}$_$from$_Co decreases continuously with the pyrolysis temperature from 46% at 800 ^{o}C to 24% at 1500 ^{o}C.
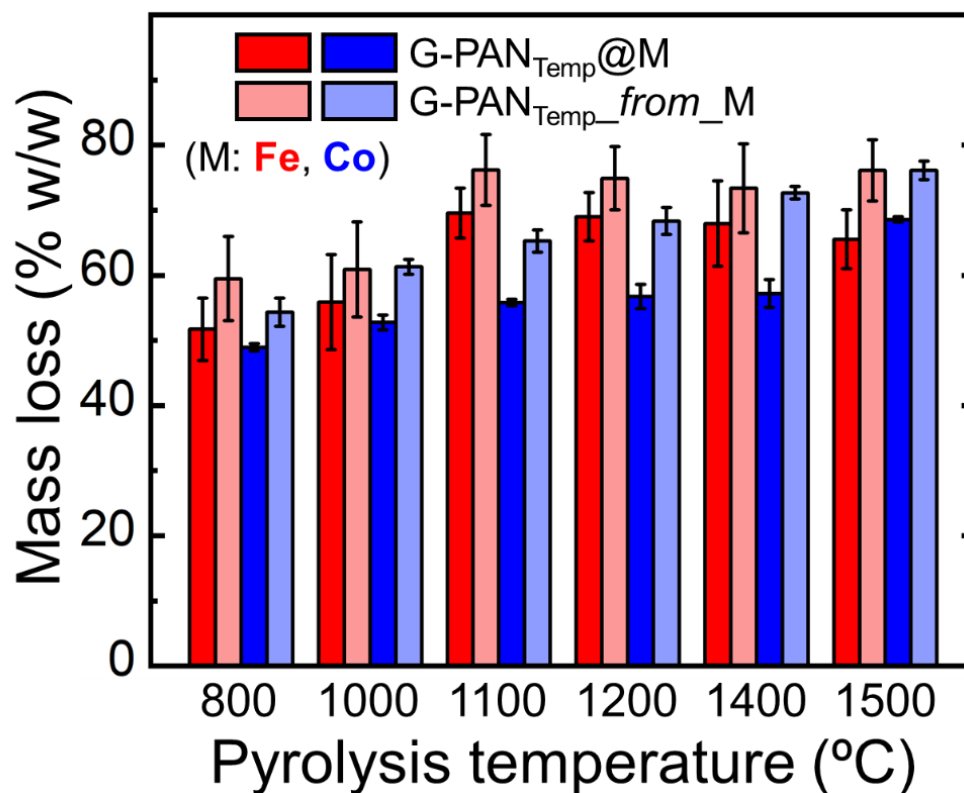
Figure 5. Mass loss of all carbon aerogels before (dark-color bars) and after treatment with aqua regia (light-color bars). Red bars: Fe; Blue bars: Co.

Consistently with the perception created by the photographs of Figures 3 and 4, Figure 6B confirms that along aromatization and beyond all G-PAN$_{Temp}$_*from*_Fe and G-PAN$_{Temp}$_*from*_Co samples shrank uniformly in a similar fashion: in the 20-31% range up to 1400 °C, with a final boost up to 36% by G-PAN$_{1500}$_*from*_Fe, and in the 23-26% range up to 1400 °C, with a final boost up to 39% by G-PAN$_{1500}$_*from*_Co.

The effect of increasing mass loss (Figure 5) and decreasing mass yield with increasing pyrolysis temperature (Figure 6A) was stronger than the effect of shrinkage, and the bulk density of both systems, ρ_b, decreased with increasing pyrolysis temperature (Figure 6C). Within that framework, above 1100 °C, the bulk densities of G-

PAN$_{Temp}$_*from*_Fe were by 0.12-0.18 g cm^{-3} lower than the densities of the corresponding G-PAN$_{Temp}$_*from*_Co.

The skeletal densities, ρ_s, of all G-PAN$_{Temp}$_*from*_M carbons (M: Fe or Co – all skeletal densities in the range 1.94-2.15 g cm^{-3} – see Tables S.1 and S.2 in Supporting Information) were lower than those of pure graphite (2.26 g cm^{-3}),[47] but significantly higher than the density of glassy carbon (1.5 g cm^{-3}).[48,49] Within that overall range of ρ_s values, there was a higher variation in the ρ_s values of G-PAN$_{Temp}$_*from*_Fe (2.021 ± 0.009 g cm^{-3} at 1500 °C versus 2.143 ± 0.009 g cm^{-3} at 1000 °C) than in the ρ_s values of G-PAN$_{Temp}$_*from*_Co (2.009 ± 0.005 to 2.073 ± 0.006 g cm^{-3} at the corresponding temperatures). The subtle, yet unilateral decline in the ρ_s values of both systems as the pyrolysis temperature increased is the opposite from what is expected from the temperature dependence of graphitization of amorphous carbon.[32,50,51]

A plausible reason is creation of closed porosity. At any rate, the combination of the decline in both the ρ_b and ρ_s values as the pyrolysis temperature increased, yielded a shallow climb in the porosities of both systems from 63% to 78% v/v in the G-PAN$_{Temp}$_*from*_Fe series of samples, and from 59% to 71% v/v in the G-PAN$_{Temp}$_*from*_Co series (Figure 6D).

Interestingly, the porosities of the corresponding samples before removal of the inorganic components were in the same ranges: 62-72% v/v in the case of G-PAN$_{Temp}$@Fe, and 57-66% v/v in the case of G-PAN$_{Temp}$@Co, in agreement with the small amounts of FeOx and CoOx in PAN@FeOx and PAN@CoOx.
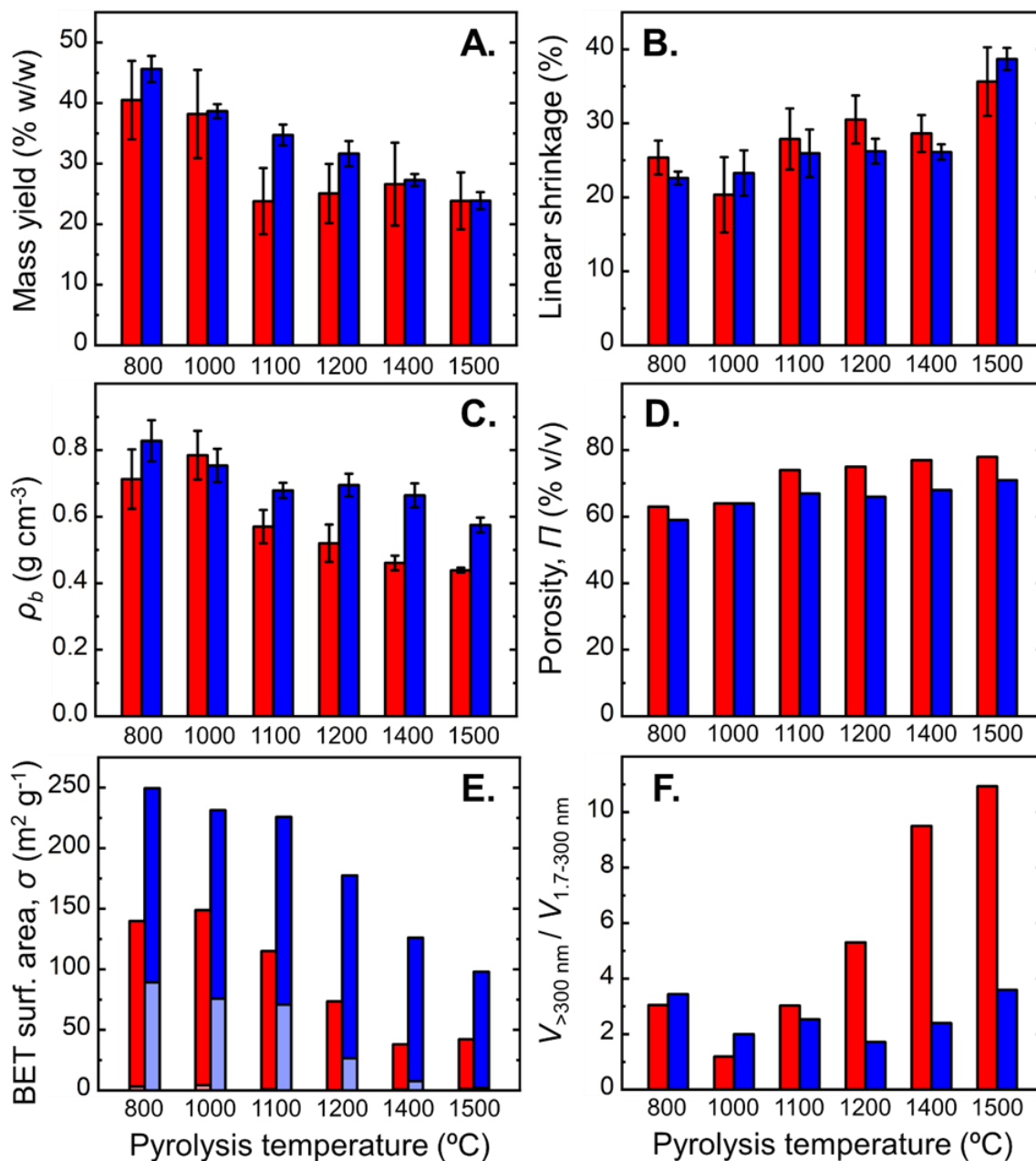
Figure 6. Selected material properties of all final carbon aerogels after aqua regia treatment. Red bars: G-PAN$_{Temp\_from\_}$Fe; Blue bars: G-PAN$_{Temp\_from\_}$Co. (A,B) Mass yield and Linear shrinkage with respect to the initial PAN@MOx compacts, (M: Fe, Co); (C) ρ_b: Bulk density; (D) Porosity, Π, as percent of empty space; (E) Full bar lengths: BET surface areas; lighter lower parts: fraction of the BET surface areas allocated to micropores; (F) Specific pore volume ratio as a gauge of macroporosity (see text).

As we have seen so far, macroscopically, G-PAN$_{Temp}$_*from*_Fe and G-PAN$_{Temp}$_*from*_Co evolved similarly as the pyrolysis temperature increased, and appeared similar in all aspects. Microscopically, however, the picture was different (Figure 7 and Appendix III in Supporting Information). The morphology of post-aqua regia G-PAN$_{Temp}$_*from*_Fe was different at different pyrolysis temperatures: it varied from an almost featureless landscape up to Temp = 1000 ^{o}C sprinkled, here and there, with some up-to-5 micron long rods (pointed at by arrows), to a structure consisting partially of rods with beads, partially of strings-of-beads and partially of stacks of thin sheets at 1100 ^{o}C, to a random distribution of platelets at 1400 ^{o}C, and to a hard-to-describe mixture of the above features at 1500 ^{o}C.

On the other hand, post aqua regia G-PAN$_{Temp}$_*from*_Co consisted uniformly of similar structures that albeit their different length scales, all were reminiscent of the interior of a fig (Figure 7 – right column). Occasionally, at intermediate temperatures one may distinguish flat features like the one pointed at with an arrow in the image of the G-PAN$_{1100}$_*from*_Co sample. Another interesting feature is that practically all samples were clearly macroporous, with the majority of pores at sizes > 300 nm. Finally, intrigued by the macroscopic similarity of the Fe- and Co-derived samples (Figures 3 and 4) and motivated by their microscopic differentiation, it was decided to formally test their mechanical strength under quasi-static compression (see Appendix IV in Supporting Information). Although, as mentioned above, all samples appeared sturdy, under formal conditions Fe-derived samples were clearly stronger and stiffer. For example, the ultimate compressive strength/Young's modulus of G-PAN$_{1500}$@Fe (ρ_b = 0.748 g cm^{-3}) were found equal to 53 MPa / 95 MPa, while those of G-PAN$_{1500}$@Co (ρ_b = 0.740 g cm^{-3}) were found equal to 22

MPa / 41 MPa. After treatment with aqua regia, the ultimate compressive strength/Young's modulus of G-PAN$_{1500}$_*from*_Fe ($\rho_b = 0.439$ g cm^{-3}) were found equal to 38 MPa / 71 MPa, and of G-PAN$_{1500}$_*from*_Co ($\rho_b = 0.575$ g cm^{-3}) were found equal to 13 MPa / 21 MPa.

A more detailed view of the skeletal framework and the porous structure of all aromatized and further-pyrolyzed products was obtained with N$_2$-sorption porosimetry at 77 K. PAN@FeOx and PAN@CoOx xerogel compacts were not analyzed for N$_2$-sorption due to their negligible porosity. The evolution of isotherms with processing temperature of just and post-aromatized samples, before and after treatment with aqua regia, is shown in Figure 8. Surface area and pore volume comparisons of all post-aqua regia samples obtained by pyrolysis of fully aromatized samples in the 800-1500 °C range are presented in Figures 6E and 6F, respectively. (All individual isotherms and pore size distributions for all samples before and after treatment with aqua regia are presented in Appendix V of the Supporting Information. Data extracted from those isotherms are summarized in Tables S.1 and S.2 of Appendix II in Supporting Information.)

A-PAN@FeOx and A-PAN@CoOx compacts showed very low levels of N$_2$-sorption, and the BET surface areas (σ), were 13 m^2 g^{-1} and 1 m^2 g^{-1}, respectively. Upon pyrolysis at 800 °C the maximum quantity of N$_2$ adsorbed by both G-PAN$_{800}$@Fe and G-PAN$_{800}$@Co jumped into the vicinity of 170 cm^3 g^{-1}, and the 140-250 m^2 g^{-1} range, respectively, as $P/P_o \rightarrow 1$. The isotherms were Type IV, with Type B hysteresis loops characterized by a sharp decrease in the desorption branch at around P/P_o ~0.45, and indicating multiple pore types with broad distributions of diameters typically associated with slit-like pores formed by parallel plates.[52]
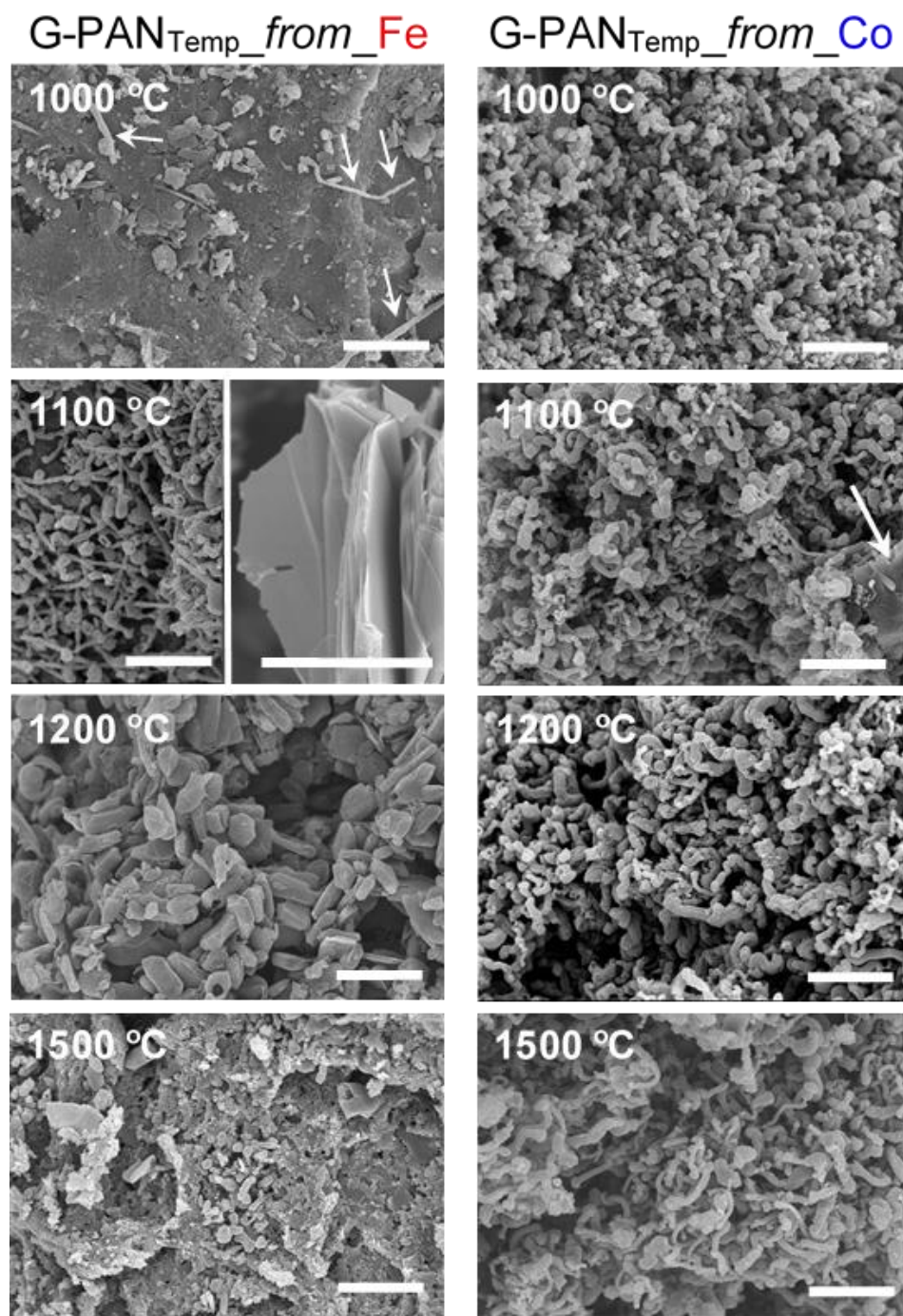
Figure 7. Representative SEMs of samples as shown. All scale bars at 5 microns. The split image of G-PAN$_{1100}$_from_Fe shows two different areas of the same sample (see text). (For SEM images at two magnifications of all samples before and after treatment with aqua regia refer to Appendix III in Supporting Information.)
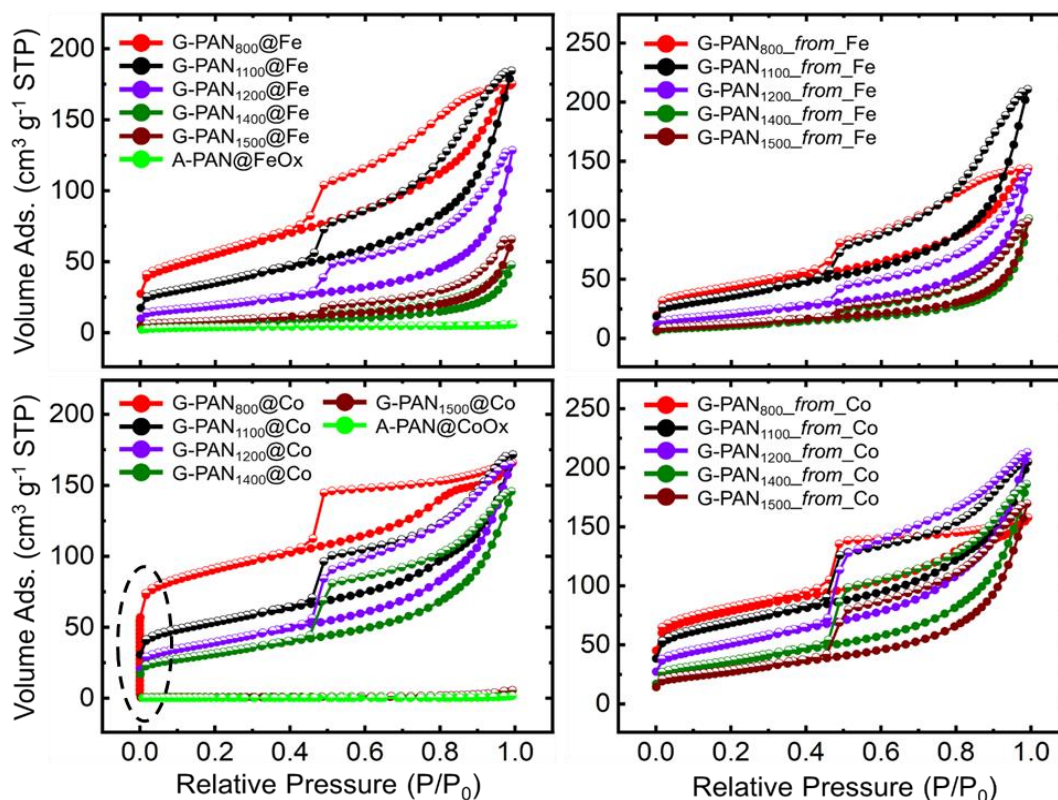
Figure 8. N$_2$-sorption isotherms at 77 K of PAN@FeOx compacts (top row) and of PAN@CoOx compacts (bottom row) graphitized at different temperatures, as indicated. <u>Left Column</u>: before treatment with aqua-regia. <u>Right Column:</u> after treatment with aqua-regia. The dashed oval marks the region of N$_2$ uptake by micropores.

Upon pyrolysis at 1000 ^{o}C and higher, the maximum amount of N$_2$ adsorbed kept on decreasing with increasing temperature; that decrease was quite drastic in the case of G-PAN$_{800}$@Fe and was accompanied by a change in the shape of the hysteresis loop into Type C indicating open wedge-like pores, while in the case of G-PAN$_{800}$@Co the isotherms retained their Type B shape, and the reduction in the total volume of N$_2$ adsorbed was rather associated with decreasing microporosity (indicated by a dashed oval in the frame describing G-PAN$_{Temp}$@Co). Incidentally, decreasing microporosity with increasing

pyrolysis temperature might be the source of the close porosity that was implied by skeletal density considerations, as discussed above.

After treatment with aqua regia (right-hand side frames of Figure 8), the total volume of N_2 adsorbed was increased uniformly throughout all samples, but the shapes of the isotherms remained unchanged. As expected from the classification of the isotherm desorption loops as Type B, the pore size distributions calculated via the BJH method were broad (extending typically up to 100 nm); in the case of all Co-derived samples the pore size distribution was also bimodal. (The pore size distributions of all pyrolyzed samples before and after treatment with aqua regia are shown in Appendix V in Supporting Information.) Finally, except the two G-PAN$_{800}$_from_M (M: either Fe or Co) the BET surface areas of all the rest of the samples (i.e., those at Temp ≥ 1000 °C) were consistently higher than the surface areas of their immediate precursors (i.e., of G-PAN$_{Temp}$@M, M: Fe or Co). However, similarities of the two systems seem to end there: as shown in Figure 6E, the BET surface areas of G-PAN$_{Temp}$_from_Fe did not include any substantial portion that could be assigned to micropores, while in the case of G-PAN$_{Temp}$_from_Co, for Temp $\leq$ 1200 °C, up to 1/3 of the BET surface area was in fact assigned to micropores. Qualitatively, although the surface areas of the Co-system declined, the portion that seemed to go away first was the fraction allocated to micropores, so that at the end, the surface areas of G-PAN$_{1500}$_from_Co was 2.3× higher than the BET surface area of G-PAN$_{1500}$_from_Fe (98 m^2 g^{-1} versus 42 m^2 g^{-1}, respectively – see Tables S.1 and S.2 of Appendix II).

Closing the discussion of the N_2-sorption data, it should be noted that despite that the Type IV shape of all isotherms of samples obtained by pyrolysis at ≥ 800 °C suggests

mesoporous materials, referring back to Figure 6F, the total pore volume of pores with diameters >300 nm was always a multiple of times higher than the volume of pores sampled by N_2 (i.e., with pore sizes in the 1.7-to-300 nm range); that indicates that all G-PAN$_{Temp}$_*from*_M (and for this matter G-PAN$_{Temp}$@M as well – refer to Tables S.1 and S.2) were mostly macroporous materials, in agreement with SEM (Figure 7).

Overall, if we are to reach just a single conclusion about the Fe- versus the Co-catalyzed systems from their bulk material properties (Figure 6) and their microscopy (Figure 7), that conclusion would be that there is less variation in the density, porosity, external surface area, pore volume and microscopic appearance of the G-PAN$_{Temp}$_*from*_Co samples than in the corresponding properties of the G-PAN$_{Temp}$_*from*_Fe, (for 800 ºC ≤ Temp ≤ 1500 ºC). That can be put differently by stating that the properties of G-PAN$_{Temp}$_*from*_Co depart less from the properties of the lowest-temperature sample in the series, G-PAN$_{800}$_*from*_Co, than the properties of the corresponding samples in the G-PAN$_{Temp}$_*from*_Fe system. In turn, that can be attributed to Co being a less effective graphitization catalyst than Fe in the PAN@MOx systems. That conjecture finds support in the next section that describes the chemical evolution of the samples during processing along with characterization of the resulting graphites.

2.3. CHEMICAL CHARACTERIZATION ALONG PROCESSING

The liquid ^{13}C NMR spectrum of the bidentate, ABCVA-based, free-radical initiator supports quantitative reaction from both of its ends (Figure 1B): Upon reaction with EtOCOCl, the carbonyl (C=O) resonance of ABCVA moved upfield, from 171 ppm (f) to 165 ppm (f'); the carbonyl resonance of EtOCOCl moved also upfield, from 149.5

ppm (3) to 147.9 (3'); and, finally the methylene carbon of EtOCOCl, $CH_3\underline{C}H_2$-, moved also upfield, from 68.1 ppm (2) to 65.0 (2').

As mentioned above, the acrylonitrile suspensions of initiator@MOx remained liquid during the course of the free-radical polymerization process, pointing to the fact that no free radicals were formed in solution, thereby both radical fragments formed across –N=N– of the initiator remained surface-bound, as designed. The resulting PAN@MOx powders had uptaken large amounts of polymer. The identity of the polymer uptaken by the initiator@MOx suspensions was investigated with solid-state CPMAS ^{13}C NMR. Due to the paramagnetic properties of the metal-oxide frameworks of this study (FeOx and CoOx), and the intimate proximity of PAN and MOx at the nanoscopic level (the process was designed so that PAN would coat conformally the MOx nanoparticles), PAN@MOx and A-PAN@MOx, gave only very broad resonances in ^{13}C NMR.

However, treatment with dilute HCl removed the oxides, and the solid-state ^{13}C NMR spectra of the residues from PAN@FeOx and PAN@CoOX were identical to the spectrum of PAN@silica (included in Figure 9 for reference).[35] Similar treatment of A-PAN@FeOx and A-PAN@CoOx rendered solid-state ^{13}C NMR of those materials possible (included in Figure 9), and showed that the treatment at 300 ºC / O_2 oxidized aliphatic carbons completely, moving them in the aromatic region.

As in the case of PAN@silica, we noted the presence of additional oxidation products: pyridonic carbonyls (at around 170 ppm: 4′,4″, & 6′, see Equation 4), and sp^2 carbons on the terminal rings (at around 100 ppm: 5′ & 5″, see Equation 4).
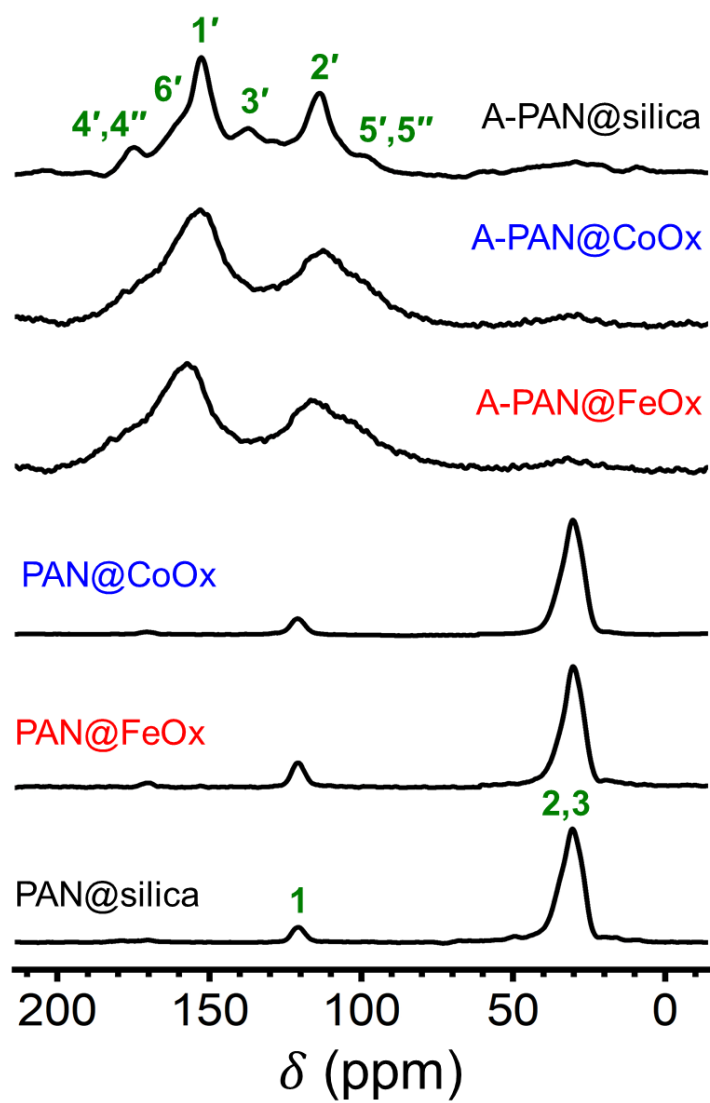
Figure 9. Solid-state CPMAS ^{13}C NMR spectra of PAN@silica (refer to the previous paper of this issue),[35] and of the residues after PAN@FeOx, PAN@CoOx, A-PAN@FeOx and A-PAN@CoOx were treated with dilute HCl. (For the assignments refer to Equations 3 and 4.)

By the same token, however, it is also pointed out that generally the ^{13}C resonances

in both A-PAN@FeOx and A-PAN@CoOx were broader than they were in the case of A-

PAN@silica, and therefore the signature-peaks of the oxidized end-groups in A-PAN@FeOx and A-PAN@CoOx were less pronounced.

Data confirming catalytic graphitization, and an evaluation of the quality of the resulting graphites were obtained with powder XRD, TEM, and Raman. Information about the chemical composition of the various carbons and the chemical identity of the residual functional groups was obtained with XPS.

CHN elemental analysis of the materials received at the highest pyrolysis temperature of this study (Temp = 1500 $^{\circ}$C), and subsequently treated with aqua regia, showed that G-PAN$_{1500}$_*from*_Fe consisted of more than 98% w/w of carbon, and G-PAN$_{1500}$_*from*_Co of more than 97% w/w (Table 1). X-ray photoelectron spectroscopy (XPS) confirmed that after aqua-regia treatment, samples contained no metals or metallic compounds. By the same token, however, XPS painted a different elemental picture for the surface of the corresponding samples: the percent weight of carbon dropped to about 95% w/w in G-PAN$_{1500}$_*from*_Fe and to about 88% w/w in G-PAN$_{1500}$_*from*_Co. In that regard, XPS also showed that in addition to C, the surfaces of all pyrolytic samples included N and O. Tables S.3 and S.4 of Appendix VI in Supporting Information present the evolution of the surface elemental composition by providing data from XPS surveys for samples pyrolyzed at a low (800 $^{\circ}$C), a medium (1100 $^{\circ}$C), and a high temperature (1500 $^{\circ}$C), before and after treatment with aqua regia. The amount of carbon generally increased with increasing pyrolysis temperature; the variation was occasionally non-monotonic, but at the end, the amount of carbon was always less than the amount found by CHN elemental analysis (Table 1). By the same token, the amounts of both O and N decreased with increasing pyrolysis temperature, but the reduction in N was more drastic.

Table 1. CHNO elemental analysis data for G-PAN$_{1500}$_*from*_Fe and G-PAN$_{1500}$_*from*_Co.

sample	C [% w/w]	H [% w/w]	N [% w/w]	O [% w/w]	O/N
G-PAN$_{1500}$_*from*_Fe	98.64	0.69	0.30	0.37	0.81
G-PAN$_{1500}$_*from*_Co	97.04	0.66	0.59	1.71	2.89

[a] The amount of oxygen was calculated as the difference from 100%.

Appendix VI in Supporting Information also includes a comparison of high-resolution XPS spectra of all samples obtained at all three temperatures above, both before and after aqua-regia treatment. A highlight of those data is presented in Figure 10 showing the high-resolution C 1s, N 1s and O 1s spectra of aqua-regia treated G-PAN$_{Temp}$_*from*_Fe obtained by pyrolysis at Temp = 800 ºC, and 1500 ºC (i.e., at the two extreme temperatures of this study). High-resolution XPS spectra elucidate the allocation of surface atoms into various types of bonding situations and functional groups (see Tables S.5 and S.6 in Appendix VI).[53,54] Thus, before treatment with aqua regia, G-PAN$_{800}$@Fe showed a strong Fe 2p signal and carbon bonded to Fe (see Figures S.32 and S.33 in Appendix VI), in agreement with XRD that shows formation of Fe$_3$C at Temp ≤ 1100 ºC (Figure 11). The absence of carbon bonded to metal in Figure 10 suggests that the carbide was removed by aqua regia quantitatively.

The high-resolution N 1s XPS spectra (Figures 10, S.34, S.38 and Tables S.5 and S.6) show that nitrogen on the surface of all samples exists as part of pyridinic, pyridonic and nitroxide groups. Similarly, from the O 1s XPS spectra (Figures 10, S.35, S.39, and Tables S.5 and S.6) oxygen on the surface of the samples exists as part of ester C–O, and

as part of carbonyl overlapping with phenoxide.[53] Before treatment with aqua regia, some metal-coordinated oxygen could be also detected (see Figures S.35, S.39 and Tables S.5 and S.6). Upon treatment with aqua regia, we noted a quantitative decrease in pyridinic nitrogen and a combined increase in pyridonic and pyridine oxide nitrogen, which could be attributed to surface-group oxidation by aqua regia.[54] The pyrolysis temperature also had a similar effect on the N 1s XPS spectra of some samples (see Figure 10, for example). Similarly, the distribution of oxygen between ester C–O and carbonyl/phenoxide groups was also a function of both the pyrolysis temperature and treatment with aqua regia, albeit the relationship appeared to be more complicated.

Powder XRD of the pyrolysis products before treatment with aqua regia, i.e., of G-PAN$_{Temp}$@M (Figure 11), showed the presence of Fe(0) from pyrolysis of A-PAN@FeOx (note the (110) diffraction at $2\theta = 44.8^\circ$ at all pyrolysis temperatures), and of Co(0) from pyrolysis of A-PAN@CoOx (note the (111) and (200) diffractions at $2\theta = 44.2^\circ$ and 51.5° also at all temperatures).

Fe(0) and Co(0) were formed carbothermally from the reduction of their corresponding metal oxides (MOx) by carbonized PAN, just as has been described previously with carbonizable phenolic and polyurea networks.[33,34,38–41]
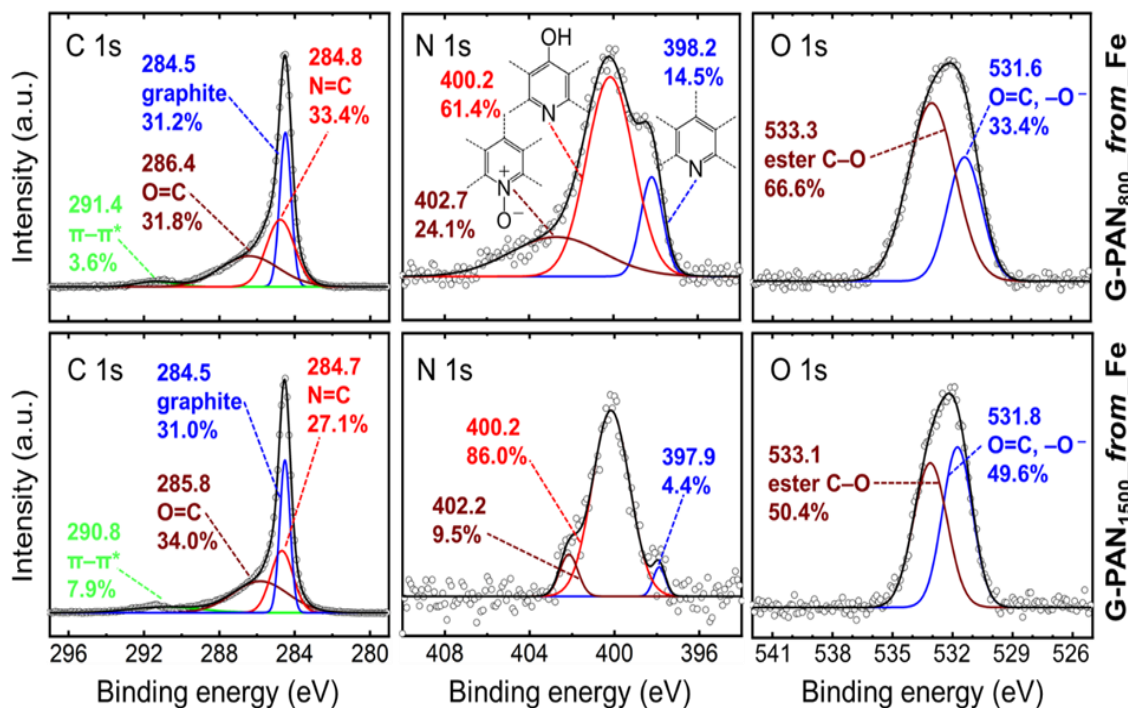
Figure 10. Representative high-resolution C 1s, N 1s, and O1s XPS spectra of aqua-regia treated samples obtained at two different pyrolysis temperatures, as shown: G-PAN$_{800}$_*from*_Fe (top row) and G-PAN$_{1500}$_*from*_Fe (bottom row). (The broad peak at ~286 eV in the C 1s spectra is assigned to both a straight carbonyl and C in keto/enol equilibrium,[54] consistent with the pyridonic groups in the N 1s spectra. Similarly, the peak at ~531.7 eV in the O 1s spectra is attributed to both a carbonyl and –O⁻,[53] the latter consistent with the nitroxide group in the N1s spectra.)

In the case of A-PAN@FeOx, we also noted formation of small amounts of Fe$_3$C from pyrolyses at ≤1100 °C; Fe$_3$C was absent at higher temperatures (≥1200 °C), in agreement with previous findings.[9,40,41]
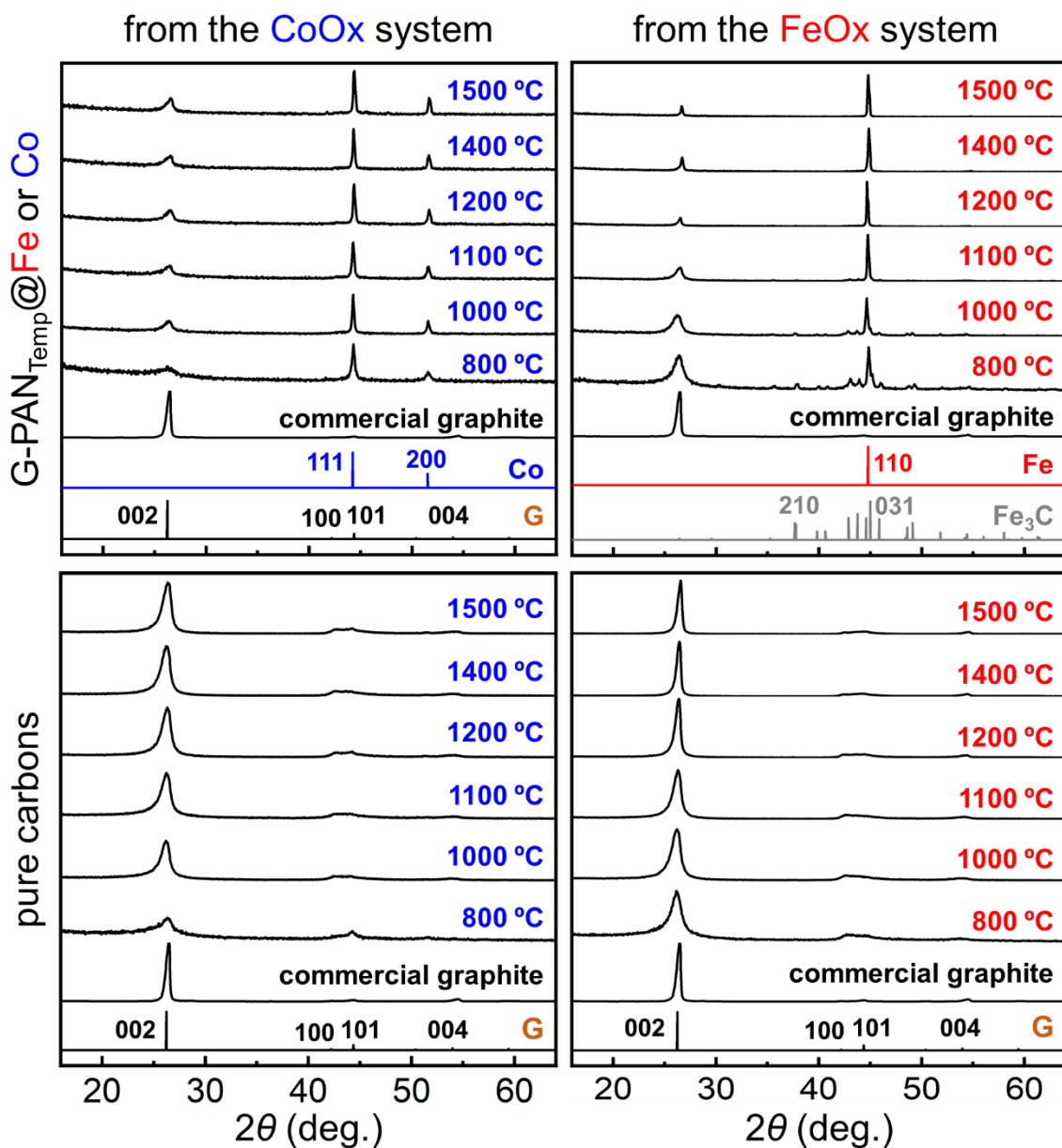
Figure 11. Powder XRD of pyrolytically derived graphitic carbon aerogel at different temperatures (denoted by subscripts "Temp" in the sample names). Top Row: As prepared (i.e., before treatment with aqua-regia) G-PAN$_{Temp}$@Co (left) and G-PAN$_{Temp}$@Fe (right); Bottom Row: pure, metal-free carbon samples after aqua-regia treatment (i.e., G-PAN$_{Temp}$_*from*_Co (left) and G-PAN$_{Temp}$_*from*_Fe (right)). (Commercial graphite controls, and standard line spectra are included at the bottom of each frame for reference. "G" stands for graphite.)

The *in situ*-formed Fe and Co metallic phases became clearly visible in TEM (Figure 12). Individual and clusters of the metal nanoparticles from about 30 nm to up to 100 nm in size were randomly distributed in a carbon matrix. Those nano Fe(0) and Co(0) domains were expected to be good low-temperature graphitization catalysts.[55–57] Indeed, concurrently with the metallic phases in XRD (Figure 11) we also noted peaks at 2θ equal to 26º, 42.5º and 54º that correspond to the (002), (101), and (004) diffractions, respectively, of hexagonal 2H graphite. After removal of Fe(0), Fe_3C and Co(0) with aqua regia, those graphite diffractions were the only remaining diffractions in the XRD data (Figure 11). The 2θ angles of the (002) reflections of all pure graphite G-PAN$_{Temp}$_*from*_Fe and G-PAN$_{Temp}$_*from*_Co samples are cited in Table S.7 of Appendix VII in Supporting Information. Those values were used to calculate the interlayer spacings, d_{002} (via $d = \lambda/(2 \sin\theta)$), which are also included in Table S.7. The interlayer spacings of the G-PAN$_{Temp}$_*from*_Fe samples decreased with increasing pyrolysis temperature, eventually converging at Temp = 1500 ºC to the graphite spacing (3.35 Å).[58] The d_{002} spacing of the G-PAN$_{Temp}$_*from*_Co samples was rather insensitive to the pyrolysis temperature, hovering around 3.38 Å even after pyrolysis at 1500 ºC.

Quantitative evaluation of the ratio of the graphitic versus amorphous carbon in the final, post-aqua-regia-treated samples was carried out by calculating the Degree of Crystallinity of all G-PAN$_{Temp}$_*from*_Fe or _*from*_Co aerogels from powder XRD data using Equation 5.[59,60] This method was validated with three controls prepared by mixing commercial graphite (graphitic carbon) and carbon black (amorphous carbon) at three predetermined ratios and analyzing the XRD data according to Equation 5 (see Figure S.40 and Table S.8 of Appendix VIII in Supporting Information).
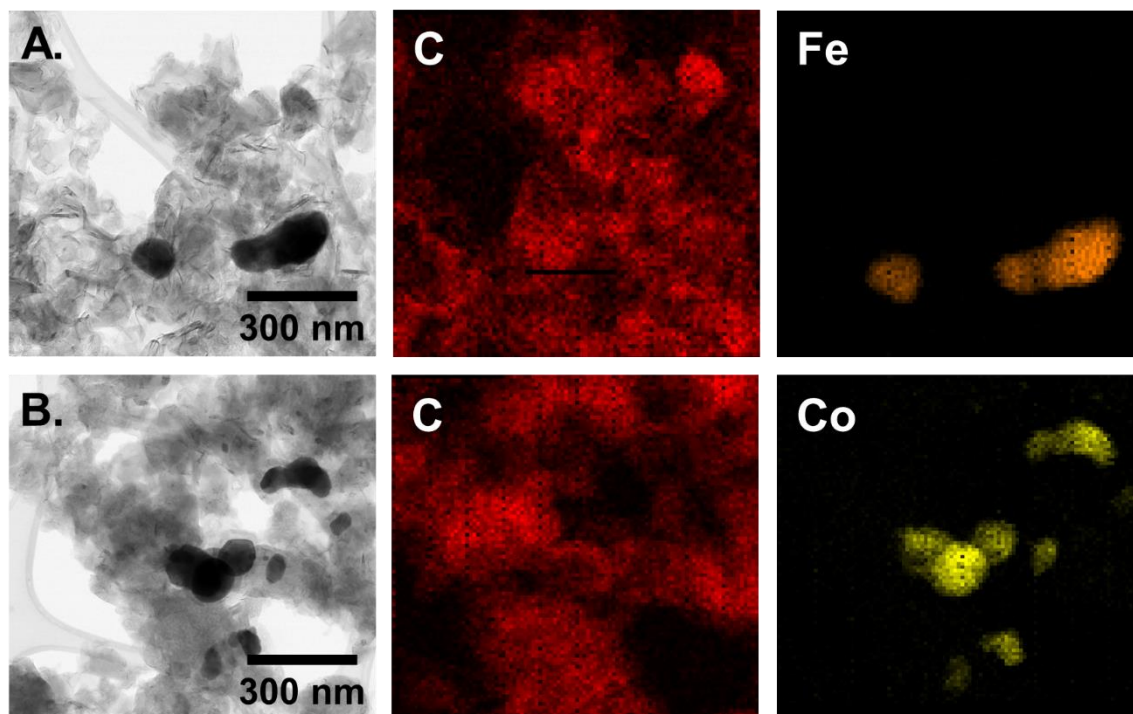
Figure 12. TEM image and EDX mapping of (A and <u>Top Row</u>) As-prepared G-PAN$_{1500}$@Fe i.e., of FeOx-derived samples pyrolyzed at 1500 ºC, before aqua-regia treatment. (B and <u>Bottom Row</u>) As-prepared G-PAN$_{1500}$@Co: i.e., CoOx-derived samples, pyrolyzed at 1500 ºC, before treatment with aqua-regia. Carbon shown in red, Fe in orange, and Co in green.

The weight percent values of graphitic carbon for all G-PAN$_{Temp}$_*from*_Fe and all G-PAN$_{Temp}$_*from*_Co are cited in Table S.7 and are plotted versus the pyrolysis temperature in Figure 13. The content in graphitic carbon increased continuously with the pyrolysis temperature. A maximum in the graphitic carbon content was observed in G-PAN$_{1500}$_*from*_Fe (99.8% w/w), which is within error from the graphitic content of commercial graphite (from Sigma-Aldrich, 99.2% w/w). The graphite content of G-PAN$_{1500}$_*from*_Co was 94.1% w/w.

$$Degree\_of\_Crystallinity = 100 \times \frac{\sum areas\_under\_the\_XRD\_peaks}{Total\_area\_under\_the\_XRD} \qquad (5)$$
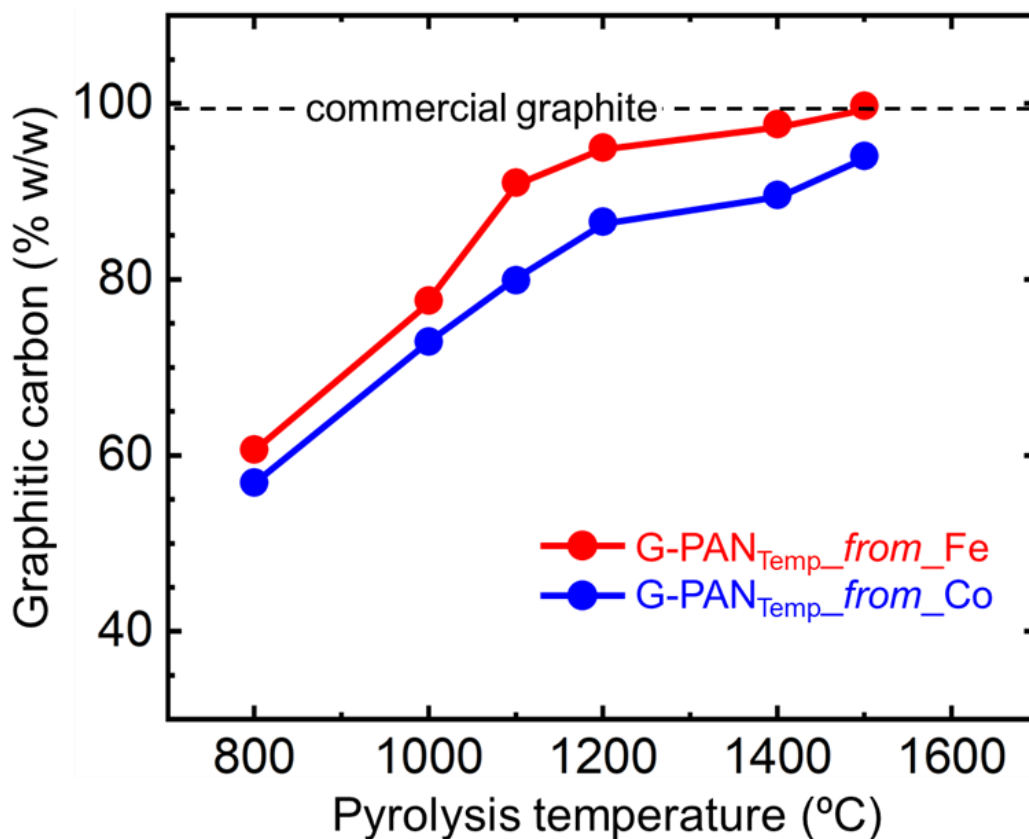
Figure 13. Percent of graphitic carbon as a function of the graphitization temperature for samples after treatment with aqua regia, as shown. (The percent of graphitic carbon was calculated from XRD data as demonstrated in Appendix XIII of the Supporting Information. Original data in Supporting Information: Table S.7). The dashed horizontal line marks the value for commercial graphite.

The crystallite dimensions within the graphitic carbons were evaluated from XRD and Raman data. The topology and growth of graphitic C was evaluated from TEM data.

$$L_c = \frac{K\lambda}{\beta \cos\theta} \qquad (6)$$

From XRD, the mean crystallite domain size, L_c (along the c-axis) was calculated from the line broadening, using the Scherrer's equation (Equation 6) along the (002) diffraction peak, where K is a dimensionless shape factor (0.9 in our case),[32,61] λ is the wavelength of our X-ray source (1.54056 Å for Cu Kα), β is the line broadening at half-maximum intensity after subtracting the instrumental line broadening (in radians), and θ is the Bragg's angle (in radians). L_c values increased continuously with increasing pyrolysis temperature, (see Figure 14). The maximum crystallite domain size of 168 Å was observed in G-PAN$_{1500}$_*from*_Fe, while the maximum crystalline domain in the G-PAN$_{1500}$_*from*_Co samples reached only 77.9 Å. For comparison, the crystallite domain size in the c-direction of commercial graphite was found equal to 187 Å.

The Raman spectra of all pyrolyzed samples after aqua-regia treatment (i.e., of G-PAN$_{Temp}$_*from*_Fe and G-PAN$_{Temp}$_*from*_Co) are shown in Figure 15. All samples show the three bands referred to as G, D and G′, associated with the honeycomb-like structure of fused aromatic sp^2 carbons:[61] the G band at around 1580 cm^{-1} is due to *cross-plane* vibrations that involve symmetric C–C bond stretching of E$_{2g}$ symmetry – necessarily the G band is present in graphite, but absent from graphene; the D peak around 1350 cm^{-1} is due to a propagating breathing mode of A$_{1g}$ symmetry of *individual* graphene sheets and is not Raman active in infinite sheets of perfect sp^2 carbons – however, in the presence of disorders (e.g., finite edges) that reflect back propagating breathing impulses, the oscillation effectively obtains a zero momentum and becomes Raman active; finally the overtone G′ (also referred to as 2D$_1$) at around 2700 cm^{-1} is a second-order two-phonon
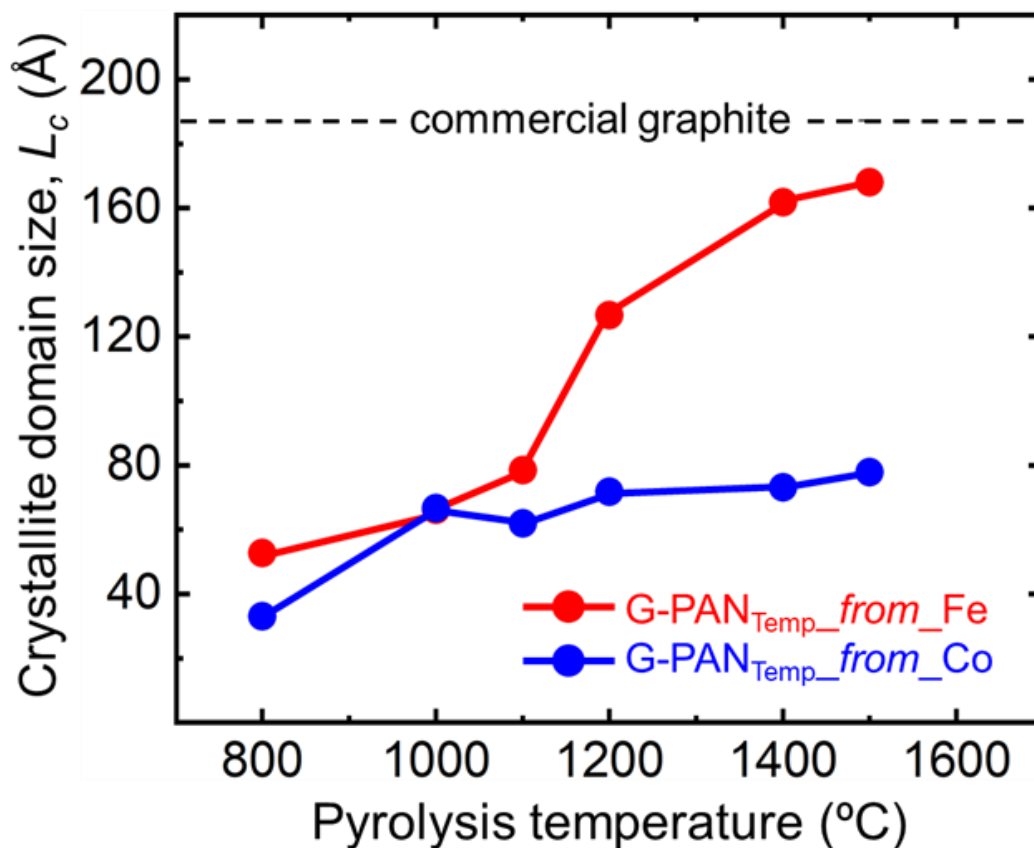
Figure 14. Crystallite domain size data, L_c, calculated via the Scherrer equation (Equation 6) from powder XRD data (Figure 11) as a function of the pyrolysis temperature for samples after treatment with aqua regia, as shown. The dashed horizontal line marks the value for commercial graphite.

process whereas one phonon goes to the right, the other one moves to the left, the total momentum is always zero, it is always Raman-allowed and no disorder is even needed for this band, which becomes the main band of graphene.[62] Interestingly, in our samples this band becomes a prominent one at intermediate pyrolysis temperatures (notice samples G-PAN$_{1100}$_*from*_Fe and G-PAN$_{1100\text{-}to\text{-}1400}$_*from*_Co), and then, say at 1500 °C, its intensity decreases again, suggesting formation of metastable graphene sheets at intermediate temperatures.

As the pyrolytic graphitization temperature increases, the D-band intensity decreases, while the G-band becomes narrower and its intensity increases. The shoulder of the G band at around 1620 cm^{-1} is labeled as D′, and is assigned to a lattice vibration, like the one responsible for the G band, but it involves the top and bottom graphene sheets in a stack; therefore, the D′ band is present in all graphites, and is absent from single graphene sheets. The D′ shoulder is present in all our samples, and curiously its intensity reaches a *minimum* (relative to G) when the intensity of G′ reaches its *maximum*; then the intensity of the D′ shoulder increases again, becoming comparable to the intensity of G in G-PAN$_{1500}$_*from*_Co, while in the case of G-PAN$_{Temp}$_*from*_Fe the intensity of D′ first increases from its minimum, and then decreases again: D′ reaches a new minimum in G-PAN$_{1500}$_*from*_Fe (always relative to G), comparable in size to that from commercial graphite (see Figure 15). If the variation of the intensity of D′ is considered together with the variation of G′, it corroborates toward accumulation of graphene in the intermediate temperature range (1100-1400 °C, the details depending on the specific catalyst).

Reasonably, the major disorder in our graphitic carbons should be attributed to grain boundaries. Therefore, the ratio of the integrated intensities of the Raman D- and G-band (I_D/I_G), which is related to the degree of disorder, is related to the grain (crystallite) size. As the pyrolysis temperature increased, the I_D/I_G ratio decreased, reaching the values of 0.55 (in C-PAN$_{1500}$_*from*_Fe) and 0.74 (in C-PAN$_{1500}$_*from*_Co – see Table S.7 in Supporting Information). For comparison, the I_D/I_G ratio of commercial graphite was 0.46.
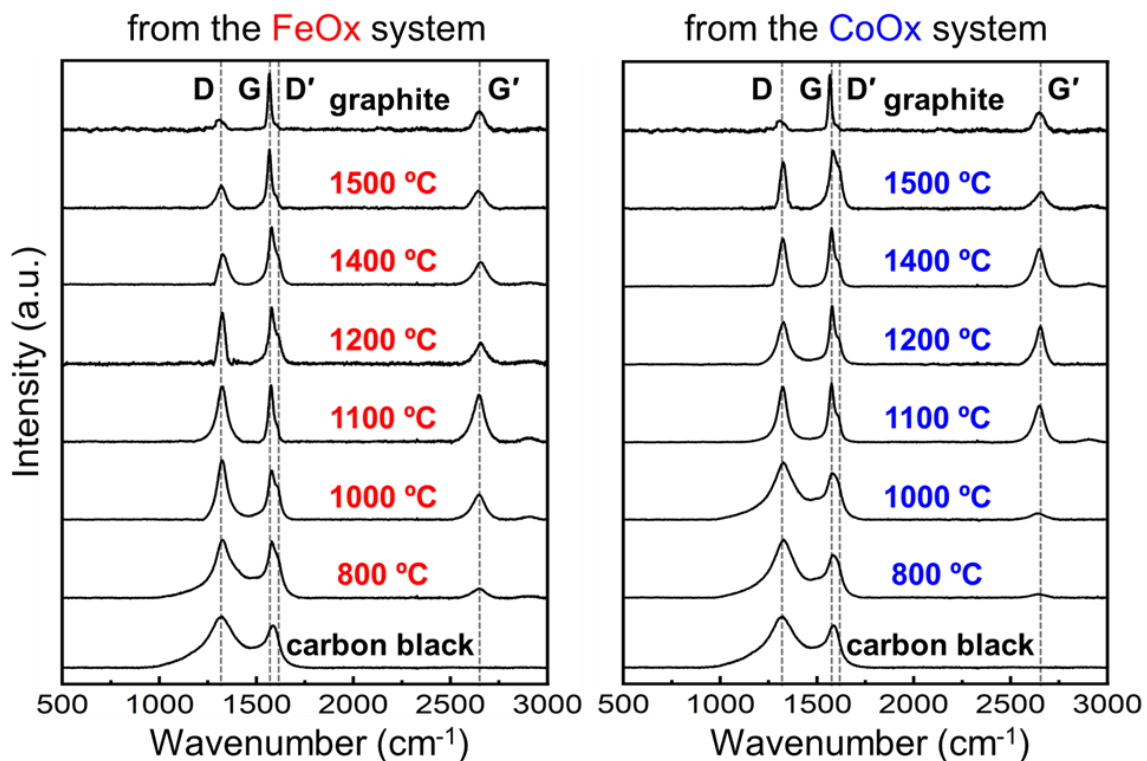
Figure 15. Raman spectra after aqua-regia treatment of graphitic carbon aerogel derived from different pyrolysis temperatures ("Temp") as shown: G-PAN$_{Temp}$_*from*_Fe (left column); and G-PAN$_{Temp}$_*from*_Co (right column).

Usually, the crystallite length, L_a (crystallite domain size along the a-axis), is calculated from the (100) diffraction peak in the XRD spectra via the Scherrer equation. Since the (100) diffraction peak is not prominent in the powder-XRD spectra of our samples, L_a was calculated from the Raman spectra using Knight's empirical formula (Equation 7), where λ_L is the laser wavelength in nm (632.8 nm for the He-Ne laser).

$$L_a = (2.4 \times 10^{-10})\, \lambda_L{}^4\, (I_D/I_G)^{-1} \qquad (7)$$

Irrespective of catalyst, L_a increased continuously with increasing pyrolysis temperature (Figure 16). A maximum crystallite length of 70 nm was reached in G-PAN$_{1500}$_*from*_Fe. In G-PAN$_{1500}$_*from*_Co, the length of the crystallites reached only 52

nm. By comparison, the L_a value in commercial graphite was 84 nm, and only 14 nm in carbon black (Table S.7 of Appendix VII in Supporting Information).

Overall, XRD and Raman data together suggest that longer (larger L_a), and thicker (larger L_c), crystallites were formed by pyrolysis at 1500 °C with either catalyst. However, only the properties of G-PAN$_{1500}$_*from*_Fe in terms of graphite content (via the degree of crystallinity), crystallite size (via L_a and L_c) and the overall quality of graphite (via the I_D/I_G ratio) approached those of commercial graphite.
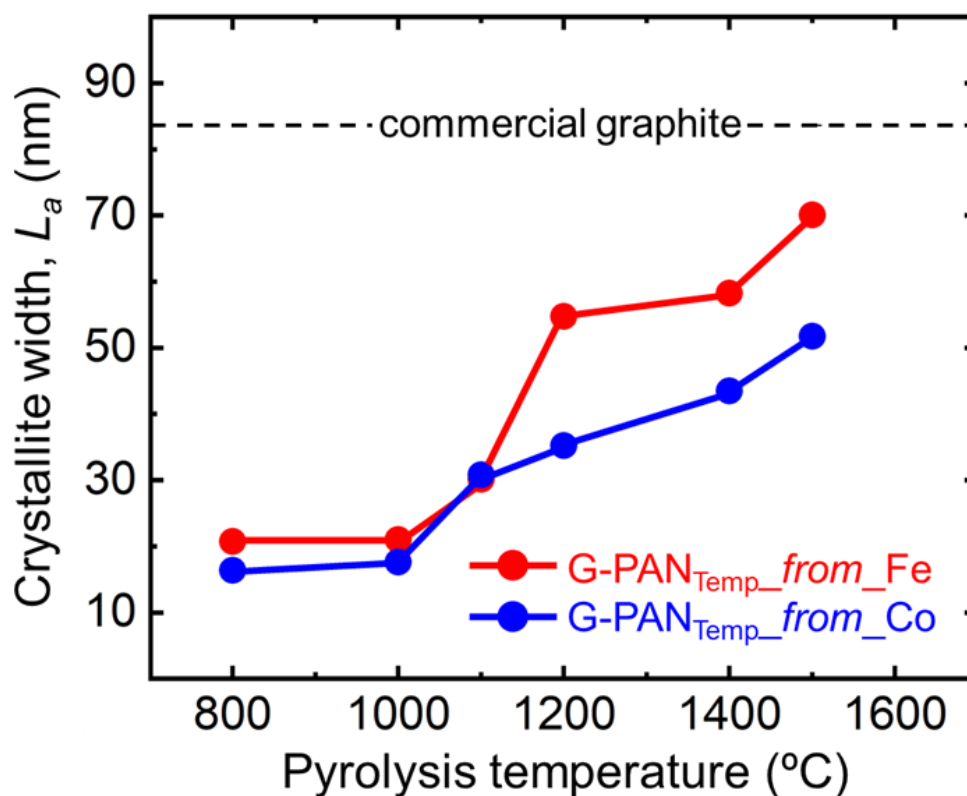
Figure 16. Crystallite width, L_a (nm), calculated from Raman data (Figure 15) using Knight's empirical formula (Equation 7) as a function of the pyrolysis temperature for terminal samples obtained after treatment with aqua regia, as shown. The dashed horizontal line marks the value for commercial graphite.

An insight into the evolution of the graphitization process as a function of the temperature and catalyst was obtained from TEM images before and after treatment with aqua regia (see Figures S.41 and S.42 of Appendix IX in Supporting Information). A representative image of samples derived at Temp = 800 °C is illustrated in Figure 17, using G-PAN$_{800}$_*from*_Co as an example. Representative images of all samples obtained at Temp = 1500 °C, i.e., G-PAN$_{1500}$@M and G-PAN$_{1500}$_*from*_M (M: Fe and Co) are shown in Figure 18. The common theme in all TEM is that the metallic particles are surounded by stacks of layers in a core-shell fashion. The shell thinckness around the Fe and Co particles of G-PAN$_{1500}$@Fe and G-PAN$_{1500}$@Co was estimated from low-magnification TEM images at about 157 nm and 122 nm, respectively.
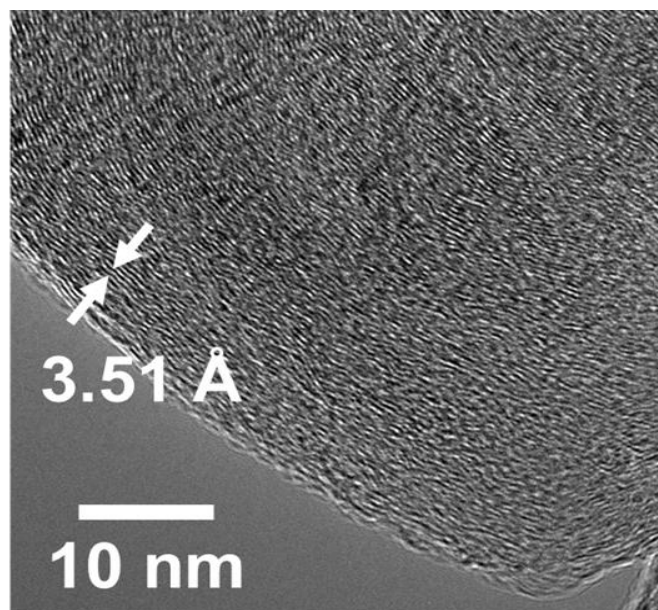
Figure 17. Typical high-resolution TEM of samples produced at Temp = 800 °C, demonstrated with G-PAN$_{800}$_*from*_Co (see also Figures S.41 and S.42 of Appendix IX in Supporting Information).

As shown in Figure 17, layered structures around the Fe and Co nanoparticles were already present at Temp = 800 ºC. However, it is also noted that despite the general orientation and stucking at that temperature, the individual layers within the stacks were interruped randomly and frequently. As the pyrolysis temperature was increased, the interruptions became less frequent (see Figures S.41 and S.42), the layered segments became longer, and by 1500 ºC those layers were practically continuous with few or no defects (Figures 18A and 18C).
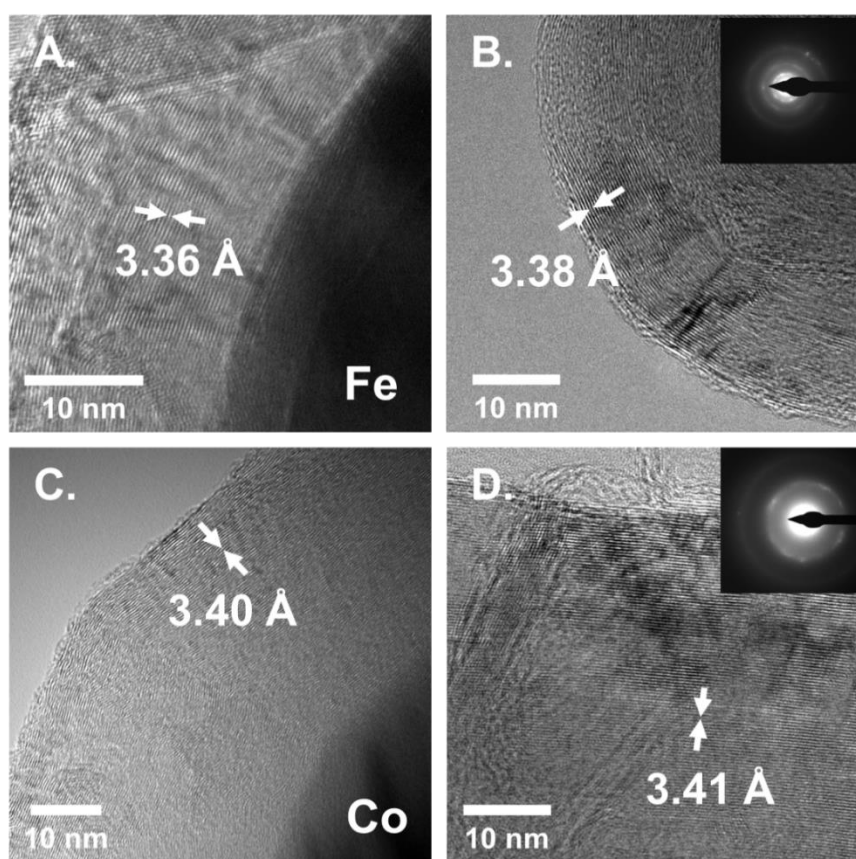
Figure 18. Representative high-resolution TEM images with graphite interlayer spacing data, of: (A) G-PAN$_{1500}$@Fe; (B) G-PAN$_{1500}$_from_Fe; (C) G-PAN$_{1500}$@Co; (D) G-PAN$_{1500}$_from_Co. Insets: Electron diffraction patterns (see also Figure S.44 of Appendix IX in Supporting Information).

The fact that treatment with aqua regia removed the metallic components completely from all samples was also confirmed with TEM-EDX (see Figure S.43 of Appendix IX in Supporting Information). The electron diffraction patterns of post-aqua regia G-PAN$_{1500}$_*from*_Fe and G-PAN$_{1500}$_*from*_Co showed only the (002), (100), (101), and (110) diffractions from graphite (see Insets in Figures 18B and 18D, and Figure S.44 of Appendix IX in Supporting Information). Post aqua regia treated samples consisted only of intertwined graphitic ribbons with pockets reminiscent of the metallic particles.

The interlayer spacing within the graphitic ribbons, d_{002}, decreased with increasing pyrolysis temperature, just as it was noted in XRD. For example, the d_{002} spacing in pure G-PAN$_{800}$_*from*_Fe was found equal to 3.40 Å and 3.50 Å with XRD and TEM, respectively; the same spacing in pure G-PAN$_{1500}$_*from*_Fe was found equal to 3.35 and 3.38 Å from XRD and TEM, respectively. The corresponding values for the Co system were 3.38 Å / 3.51 Å at Temp = 800 ºC, and 3.38 Å / 3.51 Å at Temp = 1500 ºC (Table S.7 of Appendix VII in Supporting Information). It seems that consistently TEM tended to slightly overestimate the interayer spacing, but the trends were the same as in XRD. Based on the corresponding d_{002} spacing values, and the thickness of the graphitic shells around the metallic particles, those graphitic carbon shells consisted of approximately 465 and 358 graphene layers, respectively.

Based on all the XRD, Raman and TEM data considered together, graphitization within our samples seems to proceed in stages.[63–66] The first stage, which actually sets the tone for the subsequent events, occurs at around 800 ºC to 1000 ºC, and comprises formation of small fused aromatic units that accumulate on the metallic particles and subsequently on themselves. Although those basic units are short and the resulting layers

on the metallic particles have many and frequent interruptions, it is still remarkable to note the orienting role of the metallic particles: as those layers became thicker, they remained conformal to the metal surface. The second stage of graphitization occurs at intermediate temperatures, say around 1000 ℃ to 1200 ℃, and comprises reduction of defects and distortions within the stacks on top of the particles. The individual layers within the stacks become more continuous, but the thickness of the stacks does not necessarily increase. At pyrolysis Temp = 1400 ℃ and higher is the stage of annealing with quantitative removal of defects and distortions, stacks become thicker and layers within stacks become continuous and more compact with practically no defects. Based on the high degree of graphitization above Temp = 1200 ℃ (refer to Figure 14), we are forced to assume that the microscopic features observed in SEM (see for example Figure 7) all consist of entangled graphitic ribbons like those we notice left behind all over the observable area when the metal was removed (Figures 18B and 18D, as well as Figure S.41 and Figure S.42 in Supporting Information).

2.4. EVALUATION OF THE GRAPHITIC CARBON AEROGELS AS ELECTRODES VIA THEIR LITHIUM-INTERCALATION PROPERTIES

One of the most successful electrochemical applications of graphite is as an electrode material in lithium-ion batteries.[67–69] Upon reduction of Li^+, Li atoms get intercalated between the graphene sheets of graphite. That process is reversible and results in storage of about 372 mAh of charge per g of graphite. The advantage of intercalation of Li^+ into graphite over straight Li^+ reduction and plating of lithium metal is that it halts dendritic growth of Li that may be detrimental to the performance of the electrochemical cell as a battery, e.g., by eventually shorting the two electrodes. Thus, the best-quality

graphitic aerogels of this study, G-PAN$_{1500}$_*from*_Fe, were evaluated as lithium-intercalation materials by using them as anodes in coin-cell batteries assembled with foils of lithium metal as common reference and counter electrodes (see Experimental section). The voltage across those coin cells was cycled 3 times between 1.8 V and 0.05 V versus Li$^+$/Li at a slow sweep rate (0.05 mV s^{-1}) – see Figure 19A.

It is observed that the first reduction sweep included a sizable cathodic wave at around 0.5 V versus Li$^+$/Li, which was attributed to irreversible formation of a solid-electrolyte interface (SEI). SEI is formed by reduction of the electrolyte; SEI is ionically conducting allowing Li$^+$ to diffuse/migrate through, but is also electronically insulating and therefore its growth stops at a thickness where electrons can no longer tunnel through.[70] The open-pore framework of graphitic carbon aerogels provides access by the electrolyte to plenty of internal surface area (42 m^2 g^{-1}) for SEI formation, hence the sizable reduction wave at around 0.5 V versus Li$^+$/Li. The lithiation and de-lithiation waves of graphitic carbon occur at around 0.05-0.15 V and 0.15-0.30 V, respectively.

The oxidation wave is resolved in two maxima (pointed at with arrows) which are attributed to LiC$_x$-type phase transformations during step-wise oxidative delithiation of G-PAN$_{1500}$_*from*_Fe.[71–73] The immediate result of consuming charge to form the SEI is a dramatically low coulombic efficiency of the first cycle (47%), which, however, kept on improving once the SEI was formed, i.e., in the subsequent charge/discharge cycles, reaching eventually 95-100%.

The durability of G-PAN$_{1500}$_*from*_Fe as an anode material was tested over 16 cycles at various discharge rates (C/20, C/10, and C/5); "C" was calculated based on the amount of G-PAN$_{1500}$_*from*_Fe and the theoretical capacity of graphite (372 mAh g^{-1}).

Figure 19B shows the voltage/capacity curves over the first 5 cycles. All charging processes were voltage-limited at 50 mV above the thermodynamic potential of Li^+ reduction on Li metal (0 V vs. Li^+/Li). Apart from the first charging cycle, the subsequent charging cycles coincided.

Similarly, after the first discharge process, the limiting discharge capacity increased slightly and all discharge curves of cycle No. 2 and beyond practically coincided. That behavior probably suggests settling of the SEI layer with increasing ionic conductivity.[74] As a consequence of the stability of the charge/discharge curves after the first cycle, their crossing remained stable at 0.3 V versus Li^+/Li throughout cycling, which is the electrochemical potential of graphite.[75] The charge capacity did decrease with increasing discharge rate, as expected (Figure 19C).[73]

However, the highest charge capacity at the slowest rate attempted here (about 100 mAh g^{-1}) was significantly lower than the theoretical capacity of lithium intercalation in graphite. It is quite possible that the extended internal surface area that is wetted by the electrolyte, and is coated with SEI, deactivates a significant portion of the graphite and takes it out of commission as far as lithium intercalation is concerned.
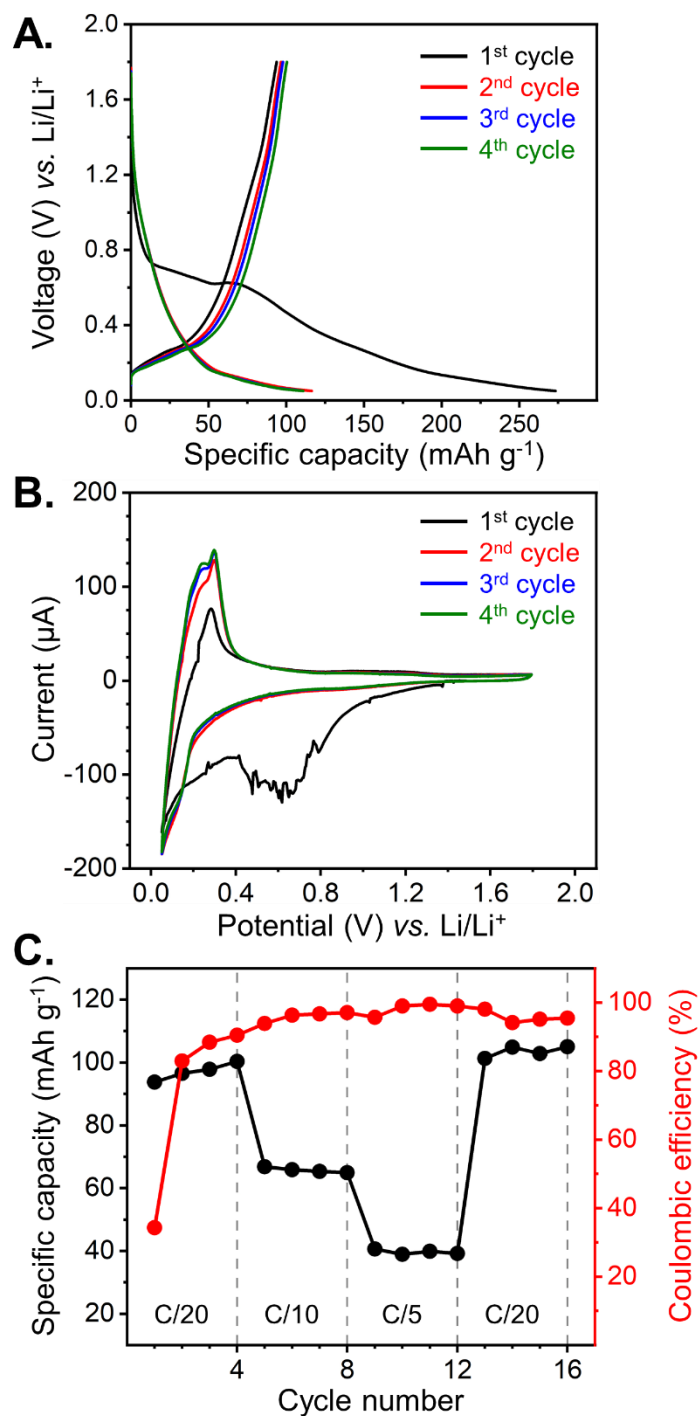
Figure 19. (A) Cyclic voltammogram of graphitic carbon (G-PAN$_{1500}$_*from*_Fe) cycled between 1.8 V and 0.05 V at 0.05 mV s^{-1} in a coin cell using a Li foil as a reference/counter electrode. (B) Charge/discharge curves of the coin cell at C/20. (C) Specific capacity and Coulombic efficiency of graphitic carbon at different discharge rates, as shown.

3. CONCLUSION

The aerogel-via-xerogel route has been applied successfully in the synthesis of monolithic graphite aerogels at low temperatures. For the creation of porosity, the aerogel-via-xerogel method relies on the mass loss by carbonizable polymers during pyrolysis, and thus bypasses aerogel precursors whose synthesis is lengthier, and requires more energy and materials (e.g., solvents). The innovative element here was that the inorganic scaffold for the accumulation of the carbonizable polymer was itself the precursor of known graphitization catalysts (Fe and Co). In terms of graphite quality (fewer defects, larger crystallites) certain graphite aerogels derived with Fe were at par with commercial graphite.

This report comprises a milestone along a long road that started with the application of the aerogel-via-xerogel concept in the facile synthesis of monolithic ceramic aerogels (SiC and Si_3N_4 – the latter for the first time),[33] and continued with the synthesis of metallic Co aerogels,[34] for which oxide aerogel precursors are difficult to make in monolithic form. Subsequently, the power of the method was applied in the synthesis of the most well-known, pyrolytically-derived aerogels, carbon aerogels (see previous paper of this issue),[35] and the road has reached the "holy grail" sort-of-speak in the carbon aerogel business with the low-temperature synthesis of graphitic aerogels. The new materials may find use in any application that requires porous / high surface area graphite.

4. EXPERIMENTAL

4.1. MATERIALS

All reagents and solvents were used as received, unless noted otherwise. Iron(III) chloride hexahydrate ($FeCl_3.6H_2O$, 97%, ACS reagent), cobalt(II) chloride hexahydrate ($CoCl_2.6H_2O$, 98%, ACS reagent), ethyl chloroformate (EtOCOCl, 99%, ACS reagent), sodium hydroxide pellets (NaOH), anhydrous sodium sulfate (Na_2SO_4, ACS certified), concentrated nitric acid (HNO_3, 70% solution in water, ACS reagent) and concentrated hydrochloric acid (HCl, 12 M in water, ACS reagent) were purchased from Fisher Scientific. Anhydrous triethylamine (Et_3N, ≥99.5%), anhydrous inhibitor-free tetrahydrofuran (THF, ≥99.9%), (±)-epichlorohydrin (EPH, ≥99%, GC-grade), 4,4'-azobis(4-cyanopentanoic acid) (ABCVA), anhydrous tetrahydrofuran (THF) and acrylonitrile (≥99%, containing 35-45 ppm monomethyl ether hydroquinone (MEHQ) as inhibitor) were purchased from Sigma-Aldrich Chemical Co. Reference graphitic carbon (graphite, CAS No. 7782-42-5) and amorphous carbon (carbon black, CAS No. 7440-44-0) were purchased from Sigma-Aldrich. Acrylonitrile was extracted three times with three portions of aqueous sodium hydroxide solution to remove the inhibitor, washed three times with distilled water, and dried using anhydrous sodium sulfate. This inhibitor-free acrylonitrile was stored at 0 °C and was used within a month. HPLC grade solvents including hexane, dimethylformamide (DMF), ethyl acetate (EtOAc) and toluene were purchased from Fisher Scientific. Technical grade acetone was purchased from Univar (St. Louis, MO). Ultra-high purity argon (grade 5), O_2, CO_2 and liquid N_2 were purchased from AirGas (Rolla, MO). For electrochemical experimentation, lithium ribbon (0.75 mm

thickness, 99.9% trace metal basis), 1-methyl-2-pyrrolidinone (NMP, 99.5% anhydrous), and a lithium hexafluorophosphate solution (1.0 M $LiPF_6$ in ethylene carbonate (EC) and dimethyl carbonate (DMC) 1:1 v/v, battery grade) were purchased from Sigma Aldrich. Poly(vinylidene fluoride) (PVDF, polymer binder for Li-ion battery electrodes) was purchased from Alfa Aesar. Carbon-black (super P conductive, 99+%) and Celgard 2325 film were purchased from MTI Corporation.

4.1.1. Preparation of Sol-Gel Iron Oxide Suspensions (FeOx – Scheme 1A). In a round-bottom flask, $FeCl_3 \cdot 6H_2O$ (17.8398 g, 0.0666 mol) was dissolved in DMF (100 mL) under vigorous stirring. Epichlorohydrin (EPH, 51.6 mL, 0.66 mol) was added, and the brown solution was heated at 80 ºC using a condenser fitted with a tube filled with Drierite^{TM}. A suspension (FeOx) started forming in about 10-15 min to which hexane (100 mL) was added and stirring was continued for 24 h at 80 ºC. The FeOx suspension was transferred to centrifuge tubes (50 mL, Fischer Scientific, Cat. no. 06-443-18), and the solvent was exchanged one time with DMF and three times with toluene. All centrifugations were carried out for 15-20 min at 2450 rpm. For each solvent exchange/washing step, the volume of the solvent that was brought in was twice the volume of the compacted paste at the bottom of the centrifuge tubes. Before every new centrifugation step, the compacted FeOx paste was resuspended by stirring with a glass rod. For characterization purposes, three washes with acetone rather than toluene were carried out, and the paste from the last wash was dried under reduced pressure at 80 ºC to give a dry, freely flowing FeOx powder.

4.1.2. Preparation of Sol-Gel Cobalt Oxide Suspensions (CoOx – Scheme 1B). In a round bottom flask, $CoCl_2 \cdot 6H_2O$ (15.756 g, 0.0662 mol) was dissolved in DMF (100

mL) under vigorous stirring. Epichlorohydrin (EPH, 55 mL, 0.632 mol) was added, and the resulting blue solution was heated at 80 ℃ for 2 h using a condenser fitted with a tube filled with Drierite^{TM}. A suspension (CoOx) started forming in about 15-20 min. After the heating period, the mixture was allowed to cool back down to room temperature and stirring was continued for another 24 h. The CoOx suspension was transferred to centrifuge tubes, and the solvent was exchanged one time with DMF and three times with toluene. All centrifugations were carried out for 15-20 min at 2450 rpm. For each solvent exchange/washing step, the volume of the solvent that was brought in was twice the volume of the compacted paste at the bottom of the centrifuge tubes. Before every new centrifugation step, the compacted CoOx paste was resuspended with a glass rod. For characterization purposes, three washes with acetone rather than toluene were carried out, and the paste from the last wash was dried under reduced pressure at 80 ℃ to give a dry, freely flowing CoOx powder.

4.1.3. Preparation of Initiator-Modified MOx Suspensions (initiator@MOx – Scheme 1C). The MOx paste from the last centrifugation was transferred to a round-bottom flask with the help of toluene (100 mL), and the suspension was refluxed at 160 ℃ for 24 h using a Dean-Stark between the round bottom flask and the condenser in order to collect and remove any residual water from the MOx suspensions. After 24 h, the reaction mixture was allowed to cool to room temperature while protected from light by wrapping the flask with aluminum foil. Subsequently the round bottom flask was placed in an ice-bath for 1 h. Anhydrous, inhibitor-free THF (60 mL) was placed in an amber-glass Erlenmeyer flask equipped with a seal stopper and was cooled to 0 ℃ using an ice-bath. To the cold THF, ABCVA (1.8499 g, 0.0066 mol), ethyl chloroformate (1.2747 mL, 0.0133

mol) and anhydrous triethylamine (1.8582 mL, 0.0133 mol) were dissolved sequentially, while the flask was kept at 0 ºC with the ice-bath (initiator:MOx = 1:10 mol/mol). After 25-30 min this initiator suspension in THF was transferred into centrifuge tubes that were wrapped with aluminum foil. The THF suspension was centrifuged for 2 min and the supernatant liquid (which contained the initiator in THF) was added to the wrapped with aluminum foil round-bottom flask containing the cold MOx suspension in toluene. This MOx suspension was stirred at 0 ºC for 24 h in the ice-bath. At the end of that period the suspension was transferred into centrifuge tubes wrapped with aluminum foil and was centrifuged for 5 min. The supernatant solvent was discarded. The resulting initiator@MOx paste was used to carry out surface-initiated free-radical polymerization of acrylonitrile.

4.1.4. Preparation of Crosslinked PAN@MOx Powders (Scheme 1C). The resulting initiator@MOx paste from the last centrifugation step above was added in a round bottom flask containing 45 mL inhibitor-free acrylonitrile (MOx:acrylonitrile = 1:10 mol/mol; initiator:MOx:acrylonitrile = 1:10:100 mol/mol/mol). The resulting suspension was kept at 55 ºC for 10 h for free-radical polymerization, while it was stirred magnetically at 400 rpm. At the end of that period, the suspension was allowed to cool to room temperature, and it was washed three times with toluene and three times with acetone. All washes were carried out with centrifugation for 15-20 min at 2450 rpm. For each wash, the volume of the new solvent that was brought in was twice the volume of the compacted paste at the bottom of the centrifuge tubes. Before every new centrifugation step, the compacted PAN@MOx paste was resuspended with vigorous agitation using a Vortex-Genie (Model no. K-550-G, Scientific Industries) and a glass rod. After the last acetone

wash, the paste was dried under reduced pressure at 65 ℃ and the dry powder was kept in vacuum oven at 80 ℃ for 24 h resulting into a dry, freely flowing PAN@MOx powder.

4.1.5. Preparation and Further Processing of PAN@MOx Compacts (Scheme 1C and Scheme 2). Dry PAN@MOx powder was compressed into cylindrical monoliths using stainless steel dies and a hydraulic press operated at 10,000 psi. Placing the powder in a die was carried out in small portions under continuous tapping. Compressed PAN@MOx compacts were then converted to aromatized A-PAN@MOx compacts pyrolytically at 300 ℃ for 24 h under flowing O_2. These aromatized A-PAN@MOx compacts were then carbonized and eventually graphitized to G-PAN@M compacts pyrolytically in the same tube furnace set at different temperatures (designated as Temp in the sample names) ranging from 800 ℃ to 1500 ℃ for 5 h under flowing ultrahigh purity Ar. These graphitized G-PAN$_{Temp}$@M compacts (M = Fe or Co) were then treated with aqua-regia to obtain pure graphitic carbon aerogels (G-PAN$_{Temp}$_*from*_Fe and G-PAN$_{Temp}$_*from*_Co).

4.1.6. Preparation of Coin-Cell Batteries. CR2032 type coin-cell batteries were assembled in an argon-filled glove box (O_2<0.1 ppm and H_2O<0.1 ppm). The working electrode composition was set equal to 75:15:10 % w/w of G-PAN$_{1500}$_*from*_Fe, carbon-black and PVDF. The three components were mixed with NMP (0.0444 g mL^{-1}). The slurry was ball-milled for 10 min, coated on the copper foil uniformly using a glass-rod and the film was dried in vacuum at 80 ℃ for 12 h. Disks (9.5 mm in diameter) were punched off the dry, coated electrodes using a hole puncher. The active-mass loading of the copper foils was ∼1-2 mg (that refers only to the mass of C-PAN$_{1500}$_*from*_Fe). The reference electrode was always a Li metal foil (0.75 mm thickness, cut into 12 mm in diameter circular disks),

1M LiPF$_6$ in EC/DMC was used as the electrolyte, and Celgards 2325 circular sheets (19 mm in diameter) as separators. All cells were sealed using a coin cell crimper. The newly prepared cells were aged for equilibration for about 12 h before electrochemical testing.

4.2. METHODS

4.2.1. Pyrolytic Aromatization and Graphitization of PAN@MOx Compacts.

Pyrolytic aromatization and graphitization of PAN@FeOx and PAN@CoOx compacts to A-PAN@FeOx and A-PAN@CoOx and further to G-PAN$_{Temp}$@Fe and G-PAN$_{Temp}$@Co graphitic carbon aerogels was carried out in a programmable MTI GSL1600X-80 tube furnace (outer and inner tubes both of 99.8% pure alumina; outer tube: 1022 mm × 82 mm × 70 mm; inner tube: 610 mm × 61.45 mm × 53.55 mm; length of the heating zone at the set temperature: 457 mm). The rate of heating and cooling was always maintained at 2.5 ℃ min^{-1}. All gas flow rates were set at 325 mL min^{-1}.

4.2.2. Aqua-Regia Acid Etching of G-PAN@M Compacts.
Aqua-regia acid (conc. HCl: conc. HNO$_3$ = 3:1 v/v) etching of graphitized G-PAN$_{Temp}$@Fe and G-PAN$_{Temp}$@Co compacts was carried out in high-density polyethylene (HDPE) vials (20 mL, Cat. no. 03-337-23, Fisher Scientific) capped with rubber septa (Cat. no. CG-3024-03, ChemGlass Life Sciences) under reduced pressure (using a water aspirator) until no more bubbles were observed coming out from these compacts. Subsequently, these compacts were washed three times with distilled water and three times with acetone in the HDPE vials, under reduced pressure for 15 min each time. Final washed compacts were dried in the vacuum oven at 80 ℃ for 24 h, resulting in pure G-PAN$_{Temp}$_*from*_Fe and pure G-PAN$_{Temp}$_*from*_Co graphitic carbon aerogels.

4.2.3. Physical Characterization. Bulk densities (ρ_b) were calculated from weight and physical dimensions of the samples. Skeletal densities (ρ_s) were measured using helium pycnometry on a Micromeritics AccuPyc II 1340 instrument. Samples for skeletal density measurements were outgassed for 24 h at 80 °C under vacuum before analysis. Percent porosities (Π) were determined from the ρ_b and the ρ_s values via $\Pi = 100 \times [(\rho_s - \rho_b) / \rho_s]$.

4.2.4. Chemical Characterization. Liquid ^{13}C NMR spectra were recorded with a 400 MHz Varian Unity Inova NMR instrument (100 MHz carbon frequency). The cross-linked polymer was identified as polyacrylonitrile with solid-state CPMAS ^{13}C NMR on a Bruker Avance III 400 MHz spectrometer with a carbon frequency 100 MHz, using 7 mm Bruker MAS probe at a magic angle spinning rate of 5 kHz with broadband proton suppression and CP total suppression of spinning side bands (TOSS) pulse sequence. The TOSS pulse sequence was applied by using a series of four properly timed 180° pulses on the carbon channel at different points of a cycle before the acquisition of the FID, after an initial excitation with a 90° pulse on the proton channel. The 90° excitation pulse on the proton and the 180° excitation pulse on the carbon were set to 4.2 and 10 μs, respectively. The cross-polarization contact time and the relaxation delay were set at 3000 μs and 5 s, respectively. The number of scans was set at 2048. Spectra were referenced externally to glycine (carbonyl carbon at 176.0300 ppm). Chemical shifts are reported versus tetramethylsilane (TMS, 0 ppm). Sample preparation was carried out as follows: dry PAN@MOx powder was treated for 30 min with conc. HCl (12 M). At the end of the period, the suspension was washed several times with distilled water and several times with acetone. The final paste was dried in vacuum oven at 80 °C for 24 h. PAN@MOx powders were attracted by magnets, while after removal of the MOx component with conc. HCl,

they were not. The NMR spectrum of the residue powder was compared with the NMR spectrum of PAN@silica.[35]

Powder X-ray diffraction (XRD) analysis was performed with dried powders using a PANalytical X'Pert Pro multipurpose diffractometer (MPD) with Cu Kα radiation (λ = 1.54 Å) and a proportional counter detector equipped with a flat graphite monochromator. Crystallite domain sizes (L_c) were calculated using the Scherrer equation, from the full-width-at-half-maxima of (002) reflection plane. A Gaussian correction was applied utilizing NIST SRM 660a LaB_6 to determine the instrumental broadening.

X-ray photoelectron spectroscopic analysis (XPS) was carried out with a ThermoFischer Scientific Nexsa X-ray Photoelectron Spectrometer System. Samples were mixed and ground together with Au powder (5% w/w) as an internal reference. Deconvolution of the spectra was performed with Gaussian function fitting using the OriginPro 9.7 software package.

Raman spectroscopy of graphitic carbons were conducted with a Horiba Jobin-Yvon LabRAM ARAMIS micro-Raman spectrometer with 17 mW He-Ne laser at 632.8 nm as the excitation source. A silicon wafer was used as calibration standard. A total of 20 scans, 10 s each, with a 1200 grating at 10× magnification were acquired for all samples.

CHN elemental analysis was conducted with an Exeter Analytical Model CE440 elemental analyzer, calibrated with acetanilide and glycine. The combustion furnace was operated at 925 ºC. The calibration standards and samples were run three times, and results are given as averages.

4.2.5. Thermal Characterization. Thermogravimetric Analysis (TGA) was conducted under O_2 up to 800 ºC with a TA Instruments Model Q50 instrument using a heating rate of 10 ºC min^{-1}.

Modulated Differential Scanning Calorimetry (MDSC) was conducted under O_2 and under N_2 from -30 ºC to 350 ºC, with a heating rate of 5 ºC min^{-1}, modulation amplitude/frequency at ±1 ºC min^{-1}, using a TA Instruments Differential Scanning Calorimeter Model Q2000.

4.2.6. Structural Characterization. Scanning electron microscopy (SEM) was conducted with Au/Pd (60/40) coated samples on a Hitachi Model S-4700 field-emission microscope. Samples were placed on the stub using a C-dot. Thin sticky copper strips were cut and placed on the edges and top of the sample, leaving space for the analysis.

Transmission Electron Microscopy (TEM) was conducted with a FEI Tecnai F20 instrument employing a Schottky field emission filament operating at a 200 kV accelerating voltage. Graphitic carbon aerogels were finely ground by hand in a mortar with a pestle and placed in 5 mL glass vials, isopropanol was added, and the vials were ultrasonicated for 20 min to disperse the small particles in the solvent. After removing from the ultrasonic bath and just before particle settling was complete, a single drop was taken and placed on a 200-mesh copper grid bearing a lacey Formvar/carbon film. Each grid was allowed to air-dry before been used for microscopy. At least 6 different areas/particles were examined on each sample to ensure that the results were uniform over the whole sample. Images were processed with Image J, a freely available software that allows measuring the distance between the graphitic carbon layers.

4.2.7. Pore Structure Analysis. N_2-sorption porosimetry at 77 K was conducted using Micromeritics TriStar II 3020 surface area and porosity analyzer. Before porosimetry, samples were outgassed for 24 h under vacuum at 120 ℃. Data were reduced to standard conditions of temperature and pressure (STP). Total surface areas were determined via the Brunauer-Emmett-Teller (BET) method from the N_2-sorption isotherms.

4.2.8. Mechanical Characterization. Quasi-static compression testing at low strain rates (2.5 mm/mm) was conducted on an Instron 4469 Universal Testing Machine using a 500 N load cell, following testing procedures and specimen length/diameter ratios as per ASTM D1621-04a (Standard Test Method for Compressive Properties of Rigid Cellular Plastics), as described before.[76] The specimens had a nominal diameter of 1.1 cm and a length/diameter ratio of 0.5. The recorded force as a function of displacement (machine-compliance corrected) was converted into stress as a function of strain.

4.2.9. Electrochemical Testing. Cyclic Voltammograms (CV) were obtained using a PAR EG&G Potentiostat/Galvanostat Model 273 in the potential range of 0.05-1.8 V (versus Li^+/Li) with a scan rate of 0.05 mV s^{-1}. All the galvanostatic measurements were carried out using a Neware Dual Range Battery tester (BTS-4008-5V6A-8) in the same potential limits as the CV. The current was applied in terms of C-rates calculated from the mass of the active component (C-PAN$_{1500}$_*from*_Fe) and the theoretical capacity of graphite (372 mAh g^{-1}). All electrochemical experiments were conducted at room temperature.

ACKNOWLEDGEMENTS
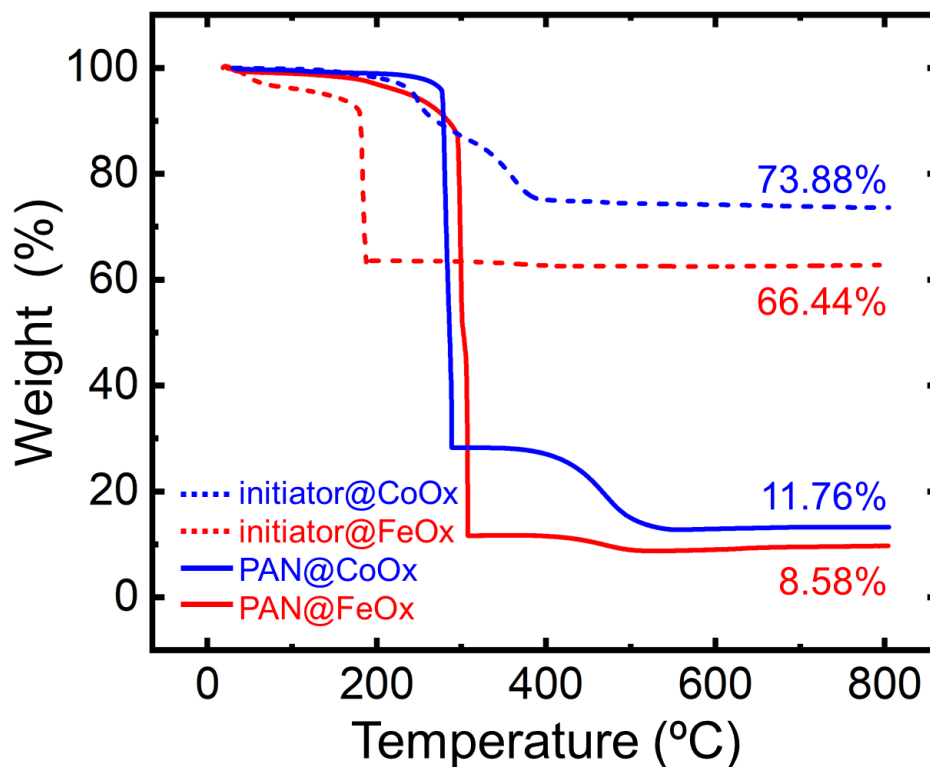
SUPPORTING INFORMATION

Figure S.1. Thermogravimetric analysis (TGA) under O_2 of initiator@FeOx (red dashed line), PAN@FeOx (red solid line), initiator@CoOx (blue dashed line), and PAN@CoOx (blue solid line) xerogel powders (heating rate: 20 $^{\circ}$C min^{-1}).

Table S.1. Materials characterization data along processing of PAN@FeOx xerogel compacts at different pyrolysis temperatures, before and after treatment with aqua regia.

sample	mass yield [% w/w][a,b]	linear shrinkage [%][a,c]	bulk density ρ_b [g cm^{-3}][a]	skeletal density ρ_s [g cm^{-3}][d]	porosity Π [% v/v][e]	specific pore volume [cm^3 g^{-1}]			BET surface area σ [m^2 g^{-1}][i]	average pore diameter [nm][j]
						V_{Total}[f]	$V_{1.7\text{-}300\_nm}$[g]	$V_{>300\ nm}$[h]		
PAN@FeOx	-	-	1.228 ± 0.004	1.304 ± 0.005	6	-	-	-	-	-
A-PAN@FeOx	67.61 ± 1.28	16.44 ± 1.68	1.107 ± 0.025	1.859 ± 0.010	40	0.37	0.00	0.37	13.03 (3.26)	112
Graphitic carbon compacts processed at different temperatures (Temp) BEFORE aqua regia treatment (i.e., before removal of iron): G-PAN$_{Temp}$@Fe										
Temp										
800 °C	48.27 ± 4.78	25.24 ± 2.80	0.801 ± 0.054	2.129 ± 0.006	62	0.78	0.23	0.55	190.9 (19.12)	16.3
1000 °C	44.11 ± 7.32	20.32 ± 5.09	0.949 ± 0.009	2.529 ± 0.004	63	0.66	0.28	0.38	119.0 (7.84)	22.2
1100 °C	30.44 ± 3.85	27.83 ± 4.15	0.717 ± 0.038	2.535 ± 0.035	72	1.00	0.26	0.74	105.3 (3.99)	38.7
1200 °C	30.98 ± 3.71	30.78 ± 2.72	0.763 ± 0.013	2.566 ± 0.005	70	0.92	0.18	0.74	61.07 (3.24)	60.9
1400 °C	32.05 ± 6.54	28.04 ± 3.81	0.762 ± 0.039	2.453 ± 0.006	69	0.90	0.09	0.81	25.66 (0.68)	150
1500 °C	34.45 ± 4.49	34.25 ± 2.27	0.748 ± 0.013	2.426 ± 0.008	69	0.93	0.09	0.84	23.60 (1.05)	183
Graphitic carbon compacts processed at different temperatures (Temp) AFTER aqua regia treatment (i.e., after removal of iron): G-PAN$_{Temp}$_from_Fe										
Temp										
800 °C	40.50 ± 6.46	25.37 ± 2.29	0.713 ± 0.089	1.937 ± 0.007	63	0.89	0.22	0.67	139.9 (3.36)	25.4
1000 °C	38.19 ± 7.29	20.35 ± 5.08	0.785 ± 0.073	2.143 ± 0.009	64	0.81	0.37	0.44	149.0 (4.23)	21.7
1100 °C	23.81 ± 5.46	27.88 ± 4.11	0.570 ± 0.050	2.145 ± 0.024	74	1.29	0.32	0.97	115.1 (1.06)	45.1
1200 °C	25.08 ± 4.88	30.51 ± 3.25	0.520 ± 0.056	2.099 ± 0.053	75	1.45	0.23	1.22	73.60 (0.21)	78.6
1400 °C	26.62 ± 6.85	28.62 ± 2.48	0.461 ± 0.022	2.020 ± 0.006	77	1.68	0.16	1.52	38.23 (0.72)	175
1500 °C	23.86 ± 4.70	35.64 ± 4.63	0.439 ± 0.007	2.021 ± 0.009	78	1.79	0.15	1.64	42.22 (1.28)	170

[a]Average of three samples; [b]Mass yields relative to the PAN@FeOx xerogel compacts; [c]Shrinkages relative to the PAN@FeOx xerogel compacts; [d]Single sample, average of 50 measurements; [e]Porosity, $\Pi = 100 \times (\rho_s - \rho_b)/ \rho_s$; [f]$V_{Total}$ was calculated via $V_{Total} = (1/\rho_b) - (1/\rho_s)$; [g]Cumulative pore volume $V_{1.7\text{-}300\_nm}$ was calculated via the Barrett-Joyner-Halenda (BJH) desorption method; [h]$V_{>300\ nm} = V_{Total} - V_{1.7\text{-}300\_nm}$; [i]Surface areas were calculated from N$_2$-sorption data via the Brunauer-Emmett-Teller (BET) equation; numbers in (parentheses): Micropore surface areas calculated via the t-plot method; [j]Average pore diameters were calculated via the $4 \times V/\sigma$ method by setting $V = V_{Total} = (1/\rho_b) - (1/\rho_s)$.

Table S.2. Materials characterization data along processing of PAN@CoOx xerogel compacts at different pyrolysis temperatures, before and after treatment with aqua regia.

sample	mass yield [% w/w][a,b]	linear shrinkage [%][a,c]	bulk density ρ_b [g cm^{-3}][a]	skeletal density ρ_s [g cm^{-3}][d]	porosity Π [% v/v][e]	specific pore volume [cm^3 g^{-1}]			BET surface area σ [m^2 g^{-1}][i]	average pore diameter [nm][j]
						V_{Total}[f]	$V_{\text{1.7-300 nm}}$[g]	$V_{>300\text{ nm}}$[h]		
PAN@CoOx	-	-	1.239 ± 0.028	1.412 ± 0.003	12	-	-	-	-	-
A-PAN@CoOx	71.70 ± 0.90	14.28 ± 0.52	1.228 ± 0.025	1.773 ± 0.004	31	0.25	0.00	0.25	0.93 (0.65)	1081
Graphitic carbon compacts processed at different temperatures (Temp) BEFORE aqua regia treatment (i.e., before removal of cobalt): G-PAN$_{\text{Temp}}$@Co										
Temp										
800 °C	51.05 ± 0.55	22.49 ± 0.29	0.953 ± 0.052	2.220 ± 0.004	57	0.60	0.17	0.43	291.8 (134.1)	8.21
1000 °C	47.23 ± 1.16	22.17 ± 2.86	0.913 ± 0.050	2.436 ± 0.005	63	0.68	0.24	0.44	197.1 (66.84)	13.9
1100 °C	44.19 ± 0.49	25.78 ± 2.39	0.847 ± 0.010	2.496 ± 0.009	66	0.78	0.23	0.55	184.8 (60.67)	16.9
1200 °C	43.25 ± 1.87	25.21 ± 1.32	0.917 ± 0.021	2.613 ± 0.005	65	0.71	0.27	0.44	136.9 (22.99)	20.7
1400 °C	42.79 ± 2.12	25.90 ± 1.91	0.914 ± 0.025	2.493 ± 0.007	63	0.69	0.24	0.45	109.6 (15.26)	25.3
1500 °C	31.40 ± 0.41	38.05 ± 1.52	0.740 ± 0.053	3.304 ± 0.017	66	1.04	0.01	1.03	1.96 (0.83)	2254
Graphitic carbon compacts processed at different temperatures (Temp) AFTER aqua regia treatment (i.e., after removal of cobalt): G-PAN$_{\text{Temp}}$_from_Co										
Temp										
800 °C	45.64 ± 2.16	22.61 ± 0.87	0.828 ± 0.062	2.030 ± 0.010	59	0.71	0.16	0.55	249.5 (89.18)	11.5
1000 °C	38.68 ± 1.16	23.29 ± 3.06	0.754 ± 0.050	2.073 ± 0.006	64	0.84	0.28	0.56	231.5 (75.76)	14.6
1100 °C	34.73 ± 1.72	25.96 ± 3.21	0.679 ± 0.023	2.060 ± 0.004	67	0.99	0.28	0.71	225.9 (70.84)	17.5
1200 °C	31.66 ± 2.08	26.23 ± 1.67	0.695 ± 0.034	2.061 ± 0.008	66	0.95	0.35	0.60	177.6 (26.61)	21.7
1400 °C	27.31 ± 0.98	26.12 ± 1.03	0.664 ± 0.036	2.068 ± 0.006	68	1.02	0.30	0.72	126.2 (7.70)	32.4
1500 °C	23.89 ± 1.42	38.69 ± 1.49	0.575 ± 0.022	2.009 ± 0.005	71	1.24	0.27	0.97	98.06 (2.32)	50.6

[a]Average of three samples; [b]Mass yields relative to the PAN@CoOx xerogel compacts; [c]Shrinkages relative to the PAN@CoOx xerogel compacts; [d]Single sample, average of 50 measurements; [e]Porosity, $\Pi = 100 \times (\rho_s - \rho_b)/\rho_s$; [f]$V_{\text{Total}}$ was calculated via $V_{\text{Total}} = (1/\rho_b) - (1/\rho_s)$; [g]Cumulative pore volume $V_{\text{1.7-300\_nm}}$ was calculated via the Barrett-Joyner-Halenda (BJH) desorption method; [h]$V_{>300\text{ nm}} = V_{\text{Total}} - V_{\text{1.7-300\_nm}}$; [i]Surface areas were calculated from N_2-sorption data via the Brunauer-Emmett-Teller (BET) equation; numbers in (parentheses): Micropore surface areas calculated via the t-plot method; [j]Average pore diameters were calculated via the $4 \times V/\sigma$ method by setting $V = V_{\text{Total}} = (1/\rho_b) - (1/\rho_s)$.
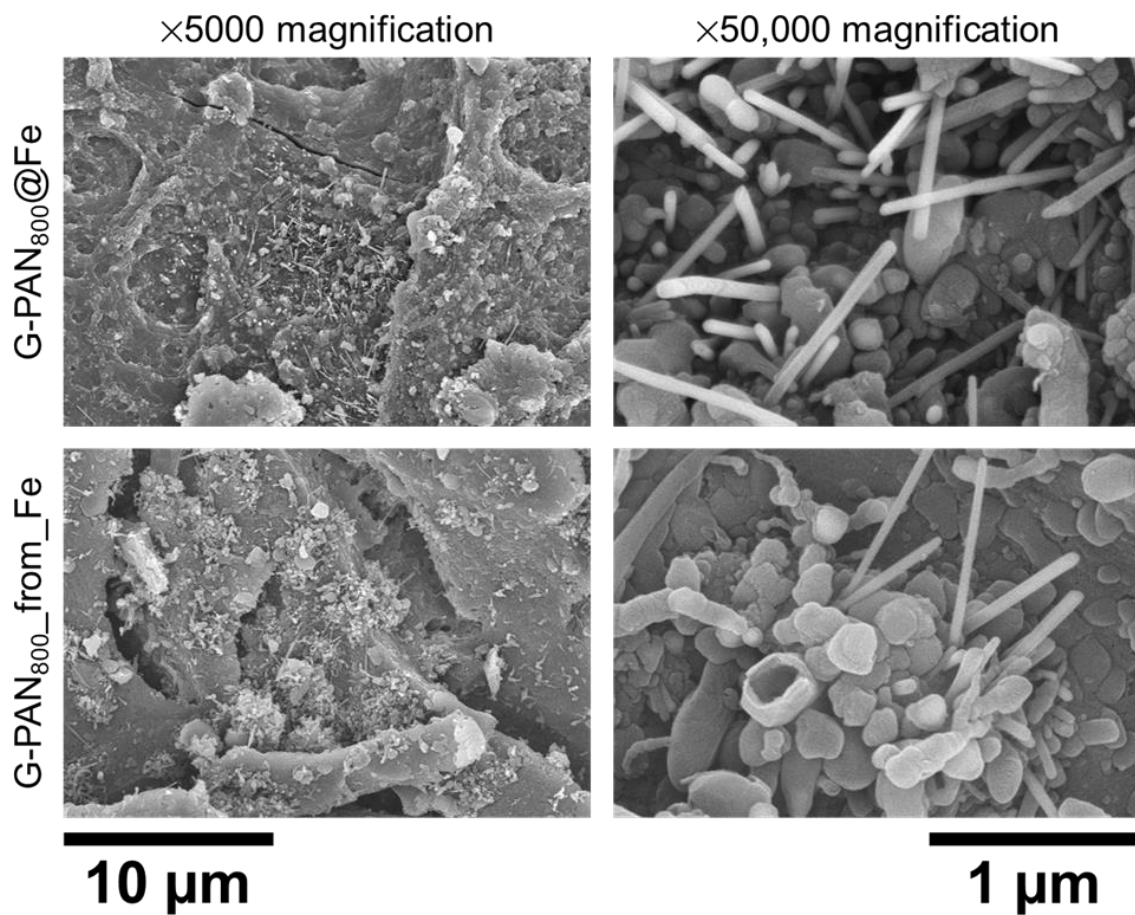
Fe-based systems

800 °C

Figure S.2. SEM images of G-PAN$_{800}$@Fe (top row) and G-PAN$_{800}$_*from*_Fe (bottom row), at low (left column) and high magnification (right column).
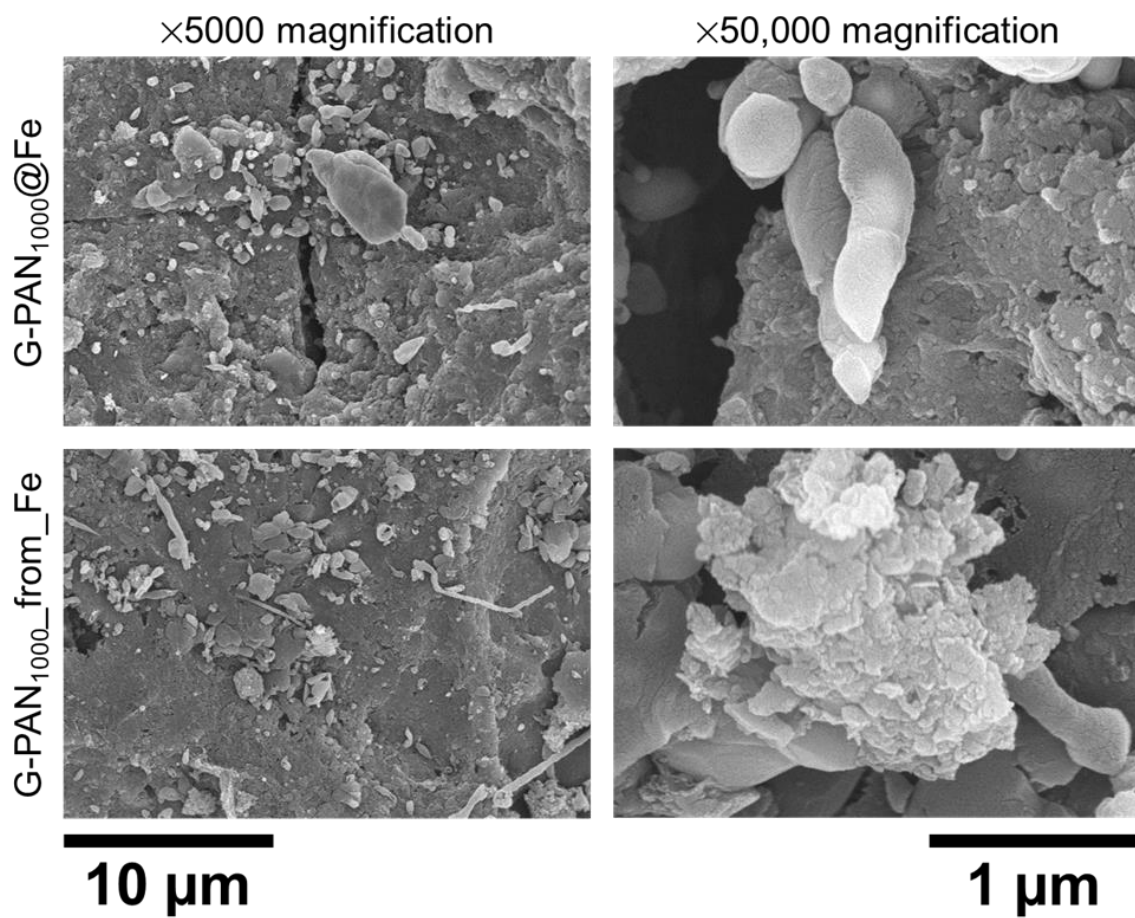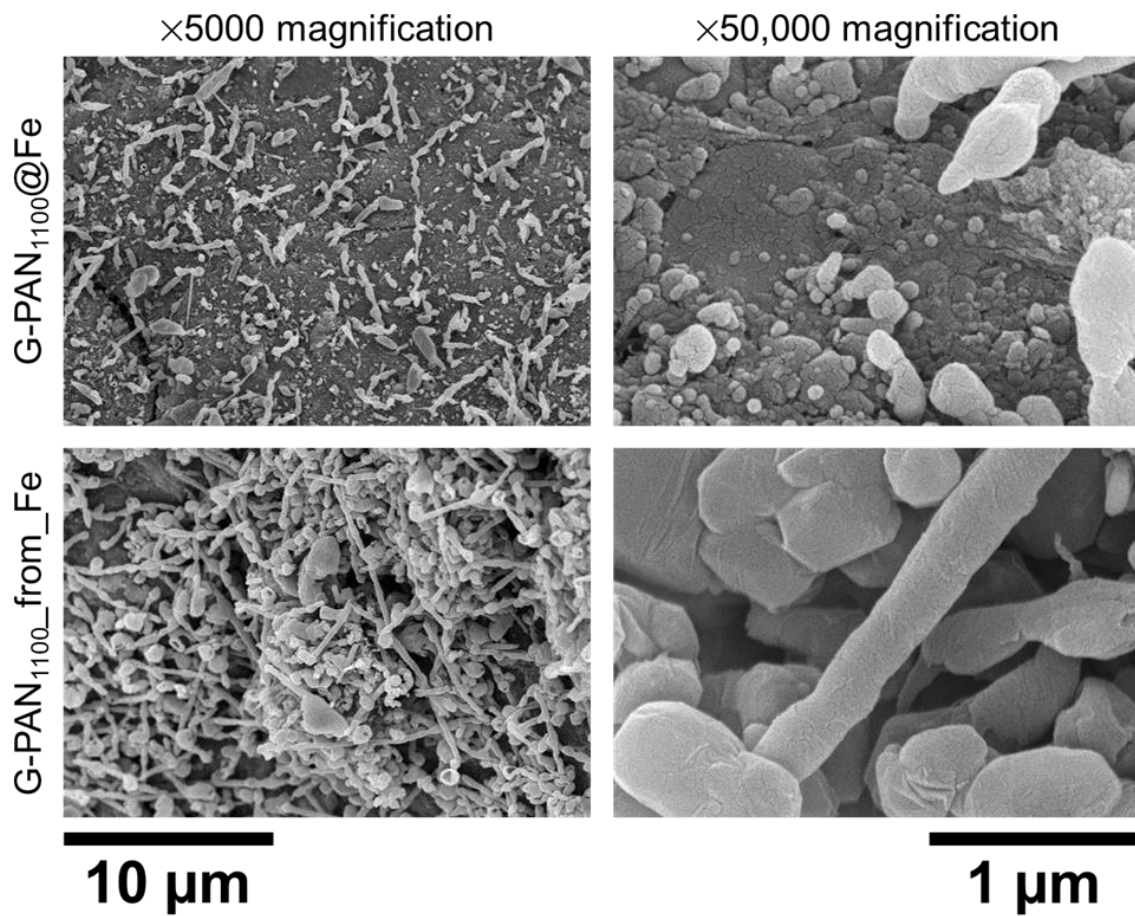
1000 ℃

Figure S.3. SEM images of G-PAN$_{1000}$@Fe (top row) and G-PAN$_{1000}$_*from*_Fe (bottom row), at low (left column) and high magnification (right column).

1100 ℃ (location one)

×5000 magnification ×50,000 magnification

G-PAN$_{1100}$@Fe

G-PAN$_{1100}$_from_Fe

10 µm 1 µm

Figure S.4. SEM images of G-PAN$_{1100}$@Fe (top row) and G-PAN$_{1100}$_*from*_Fe (bottom row), at low (left column) and high magnification (right column).

1100 ºC (location two)
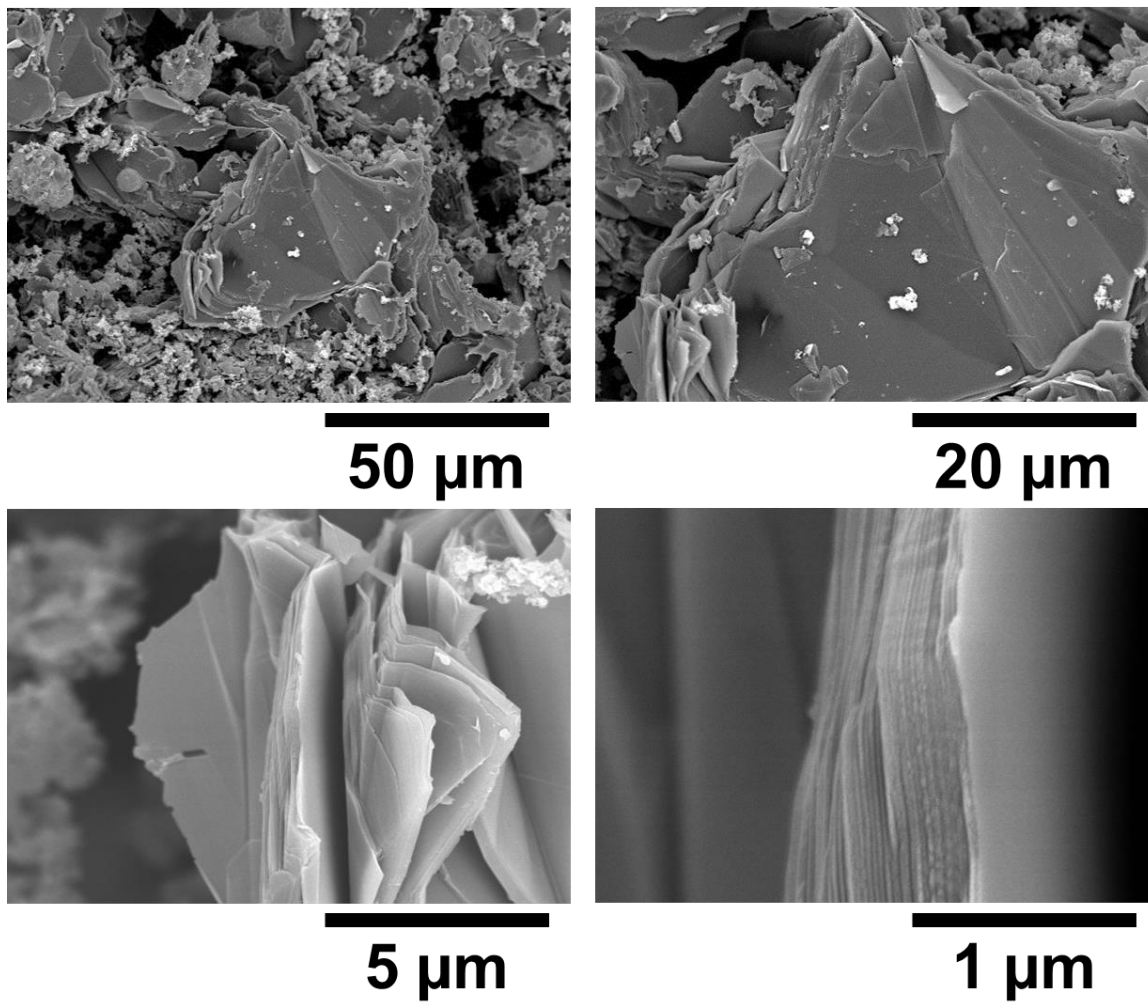
G-PAN$_{1100}$_from_Fe

Figure S.5. SEM images at various magnifications of G-PAN1100_*from*_Fe at a different location where stacks of probably graphene sheets are visible.
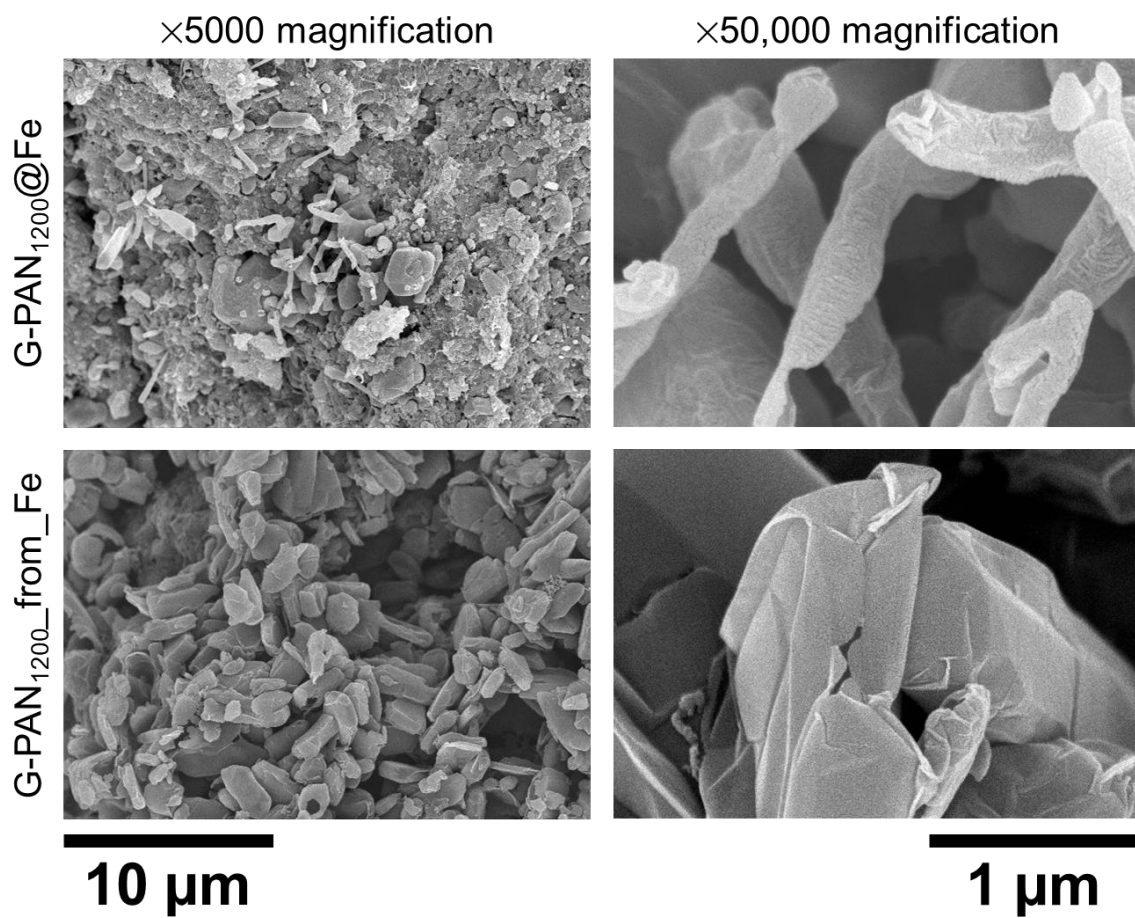
1200 °C

×5000 magnification   ×50,000 magnification

Figure S.6. SEM images of G-PAN$_{1200}$@Fe (top row) and G-PAN$_{1200}$_*from*_Fe (bottom row), at low (left column) and high magnification (right column).
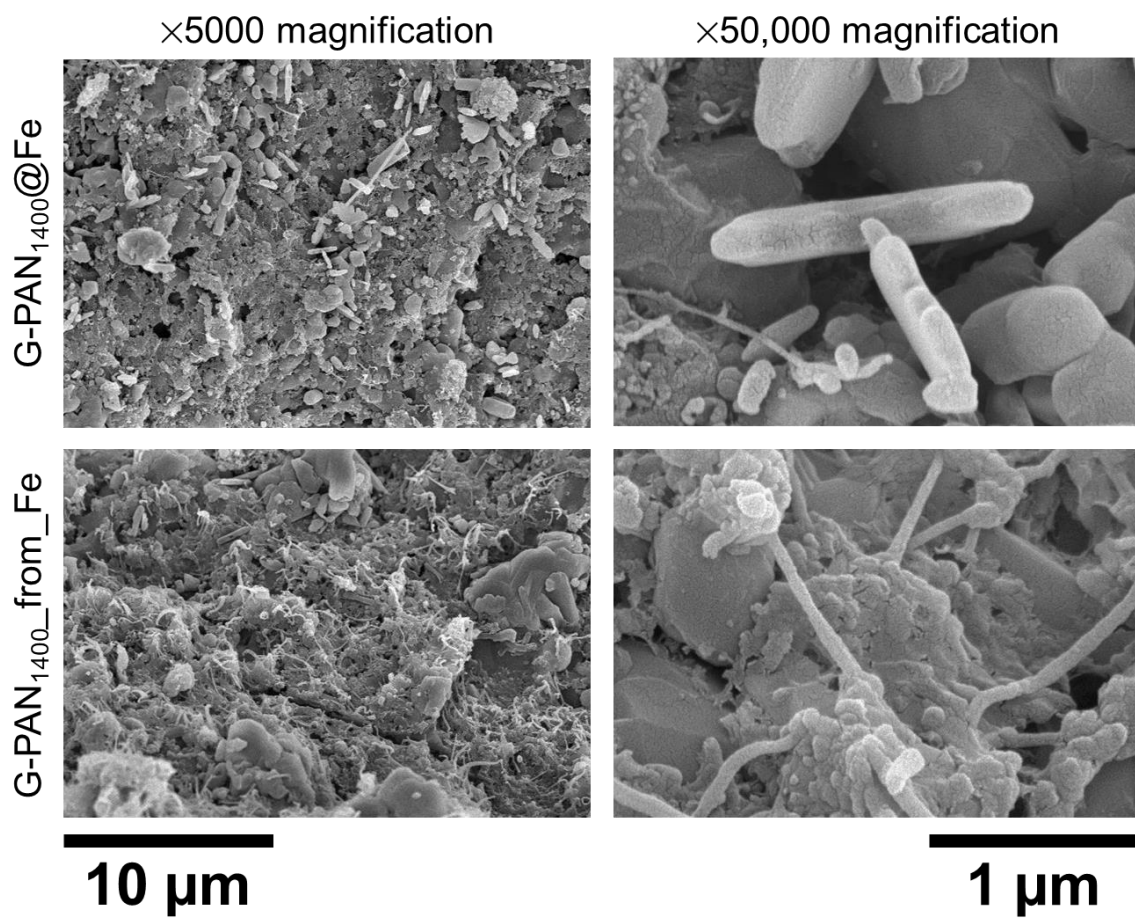
1400 ℃

Figure S.7. SEM images of G-PAN$_{1400}$@Fe (top row) and G-PAN$_{1400}$_*from*_Fe (bottom row), at low (left column) and high magnification (right column).

1500 ℃

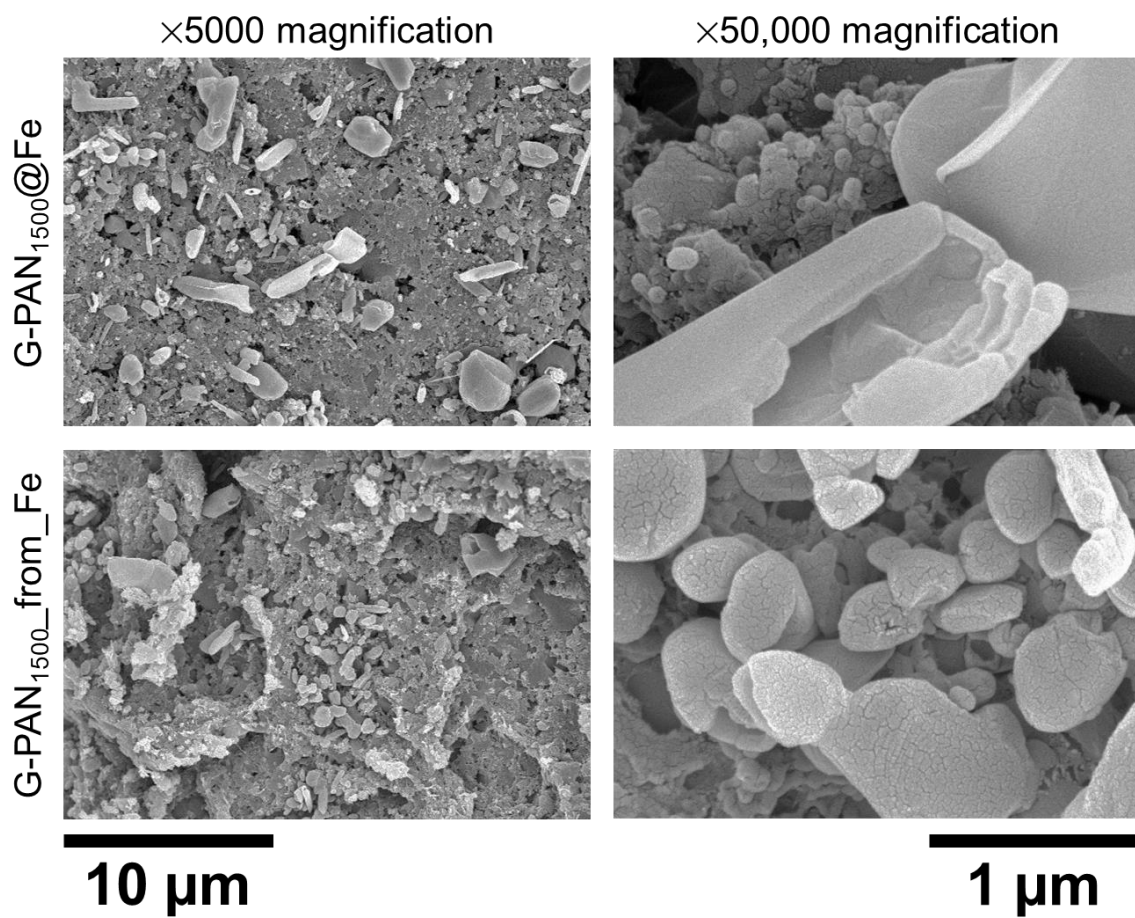×5000 magnification   ×50,000 magnification

10 µm   1 µm

Figure S.8. SEM images of G-PAN$_{1500}$@Fe (top row) and G-PAN$_{1500}$_*from*_Fe (bottom row), at low (left column) and high magnification (right column).
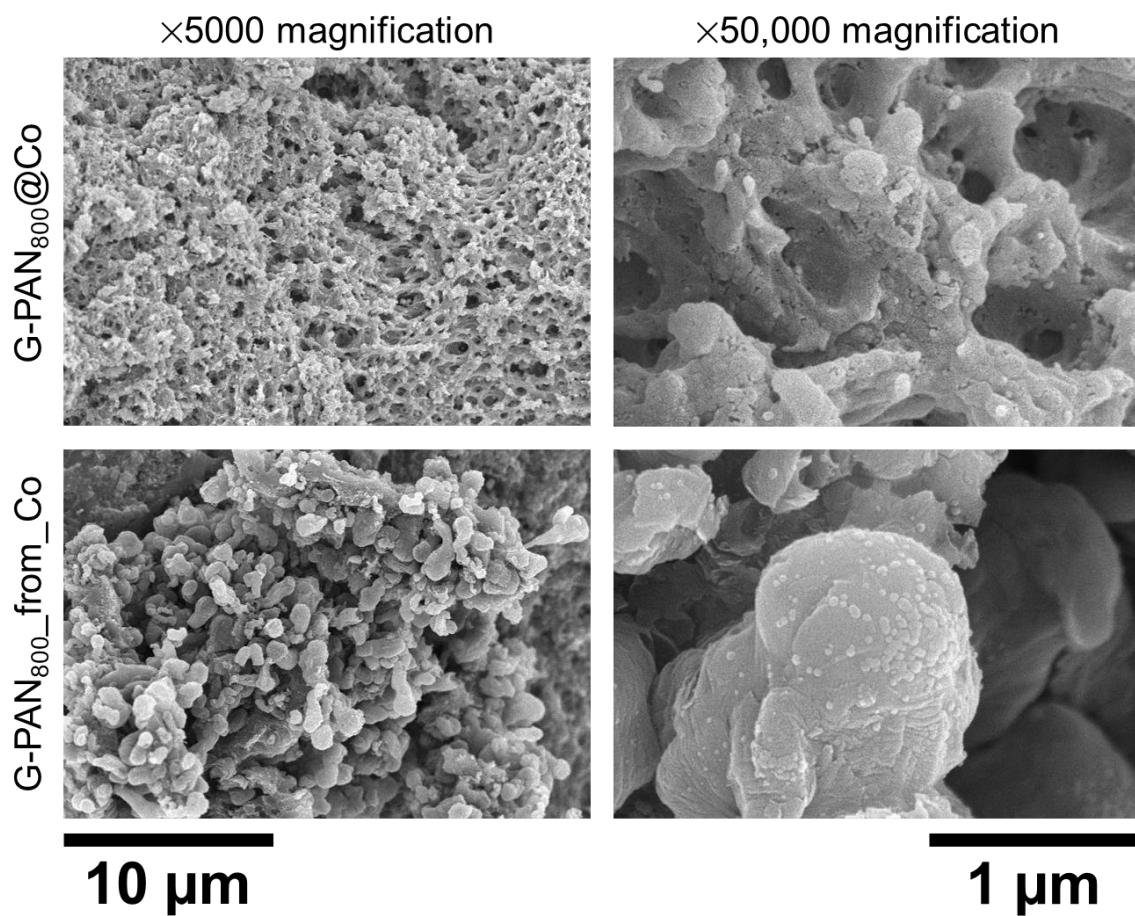
Co-based systems

800 ℃

Figure S.9. SEM images of G-PAN$_{800}$@Co (top row) and G-PAN$_{800}$_*from*_Co (bottom row), at low (left column) and high magnification (right column).

1000 ℃

Figure S.10. SEM images of G-PAN$_{1000}$@Co (top row) and G-PAN$_{1000}$_*from*_Co (bottom row), at low (left column) and high magnification (right column).

1100 ℃

×5000 magnification   ×50,000 magnification
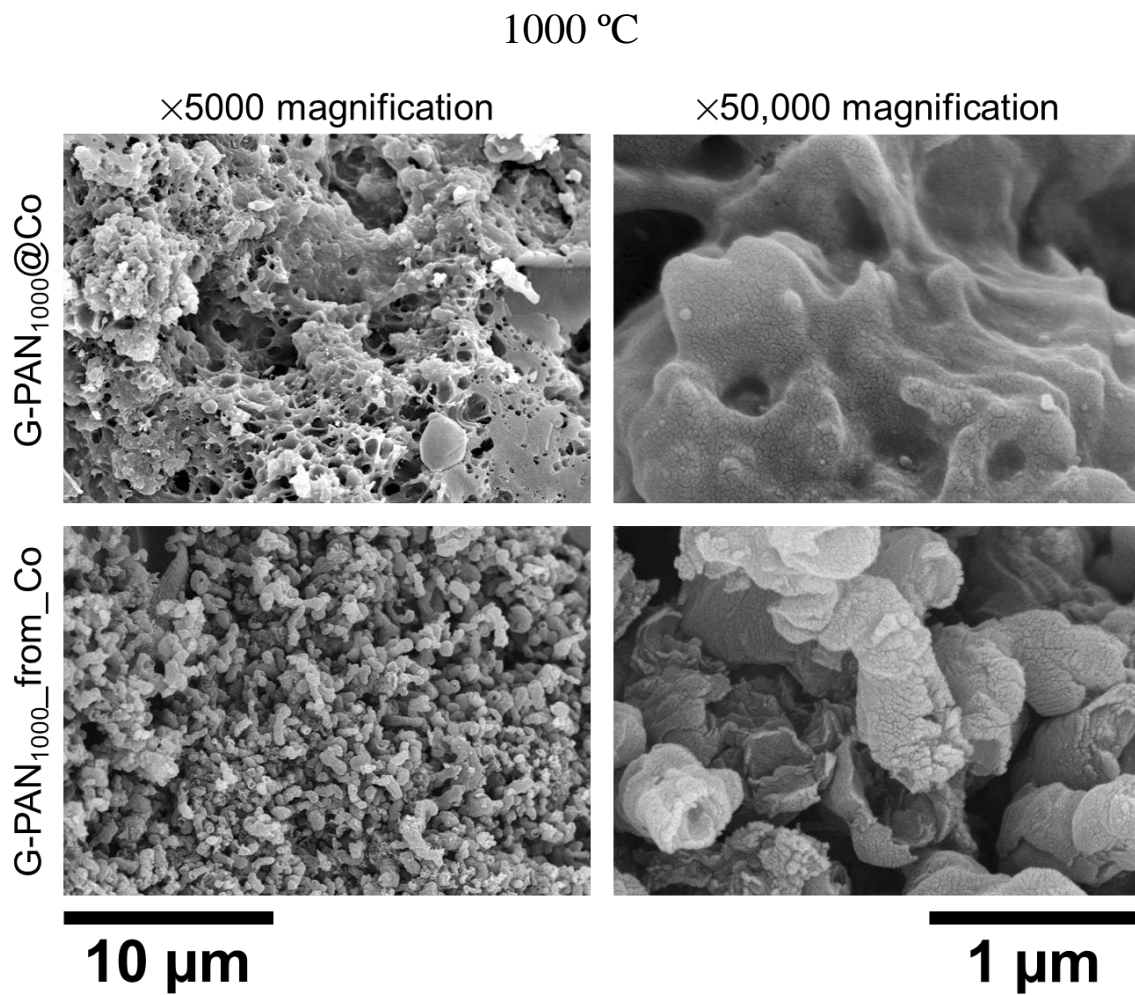

10 μm   1 μm

Figure S.11. SEM images of G-PAN$_{1100}$@Co (top row) and G-PAN$_{1100}$_*from*_Co (bottom row), at low (left column) and high magnification (right column).

1200 ℃

×5000 magnification   ×50,000 magnification

G-PAN$_{1200}$@Co

G-PAN$_{1200}$_from_Co

10 μm   1 μm
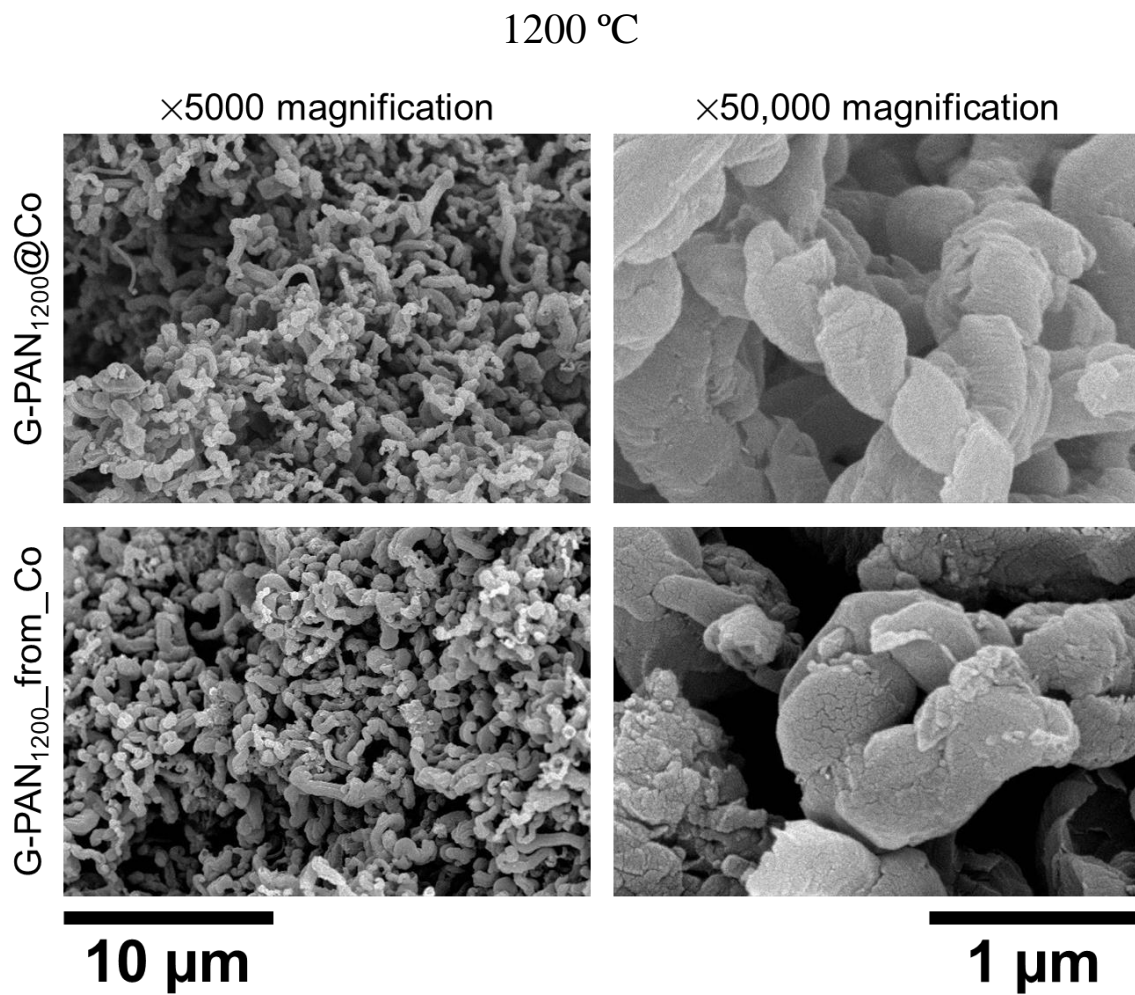
Figure S.12. SEM images of G-PAN$_{1200}$@Co (top row) and G-PAN$_{1200}$_*from*_Co (bottom row), at low (left column) and high magnification (right column).

1400 ℃

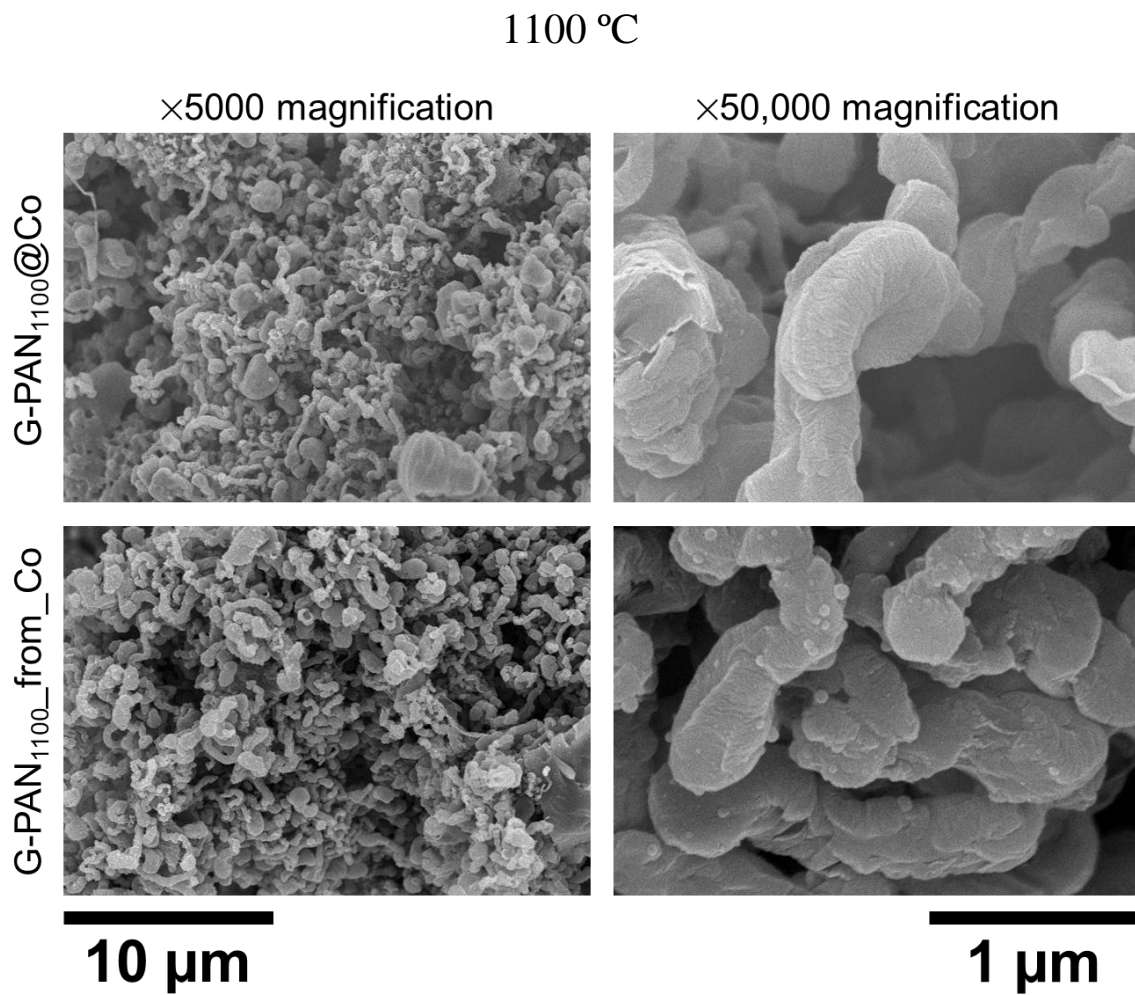×5000 magnification   ×50,000 magnification
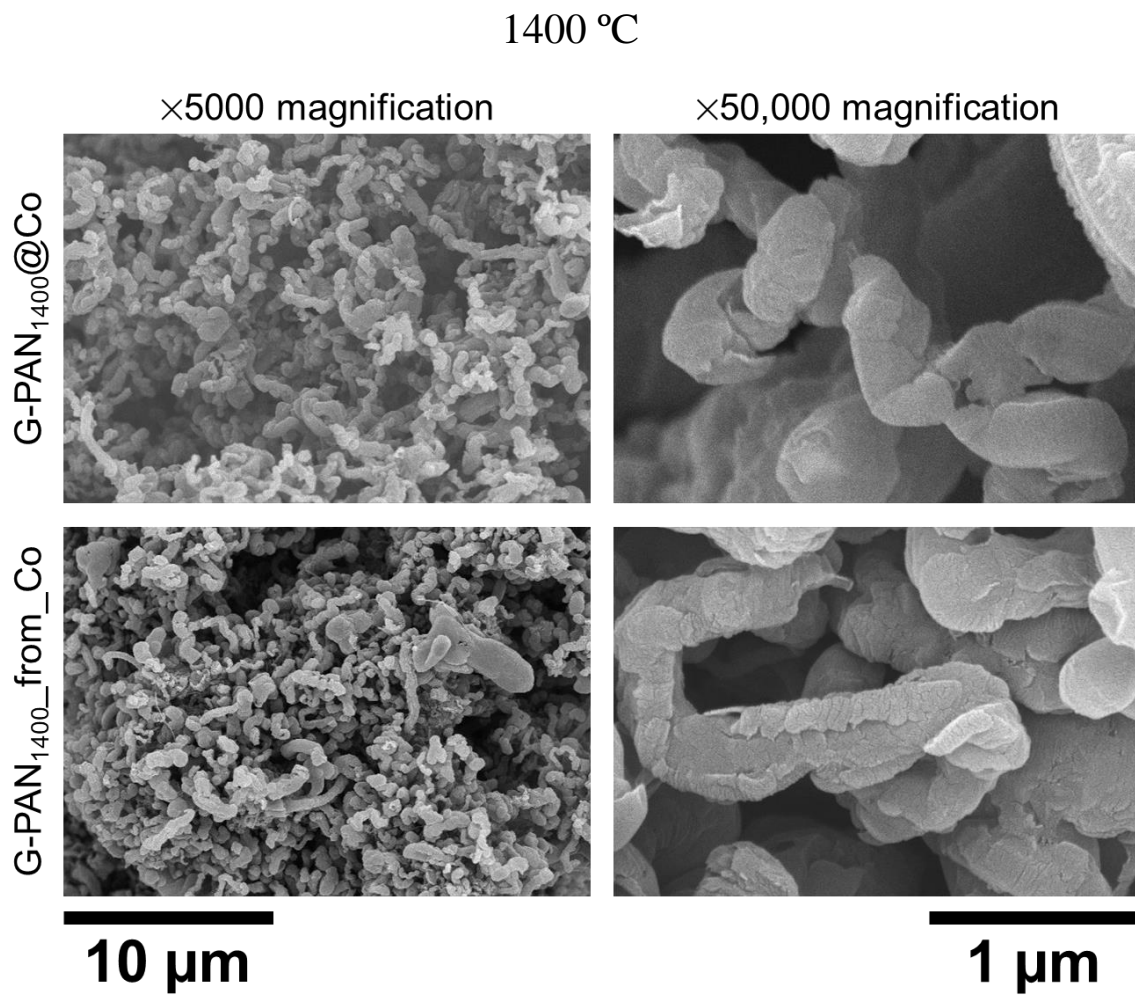
Figure S.13. SEM images of G-PAN$_{1400}$@Co (top row) and G-PAN$_{1400}$_*from*_Co (bottom row), at low (left column) and high magnification (right column).

1500 °C

×5000 magnification ×50,000 magnification

10 μm

1 μm
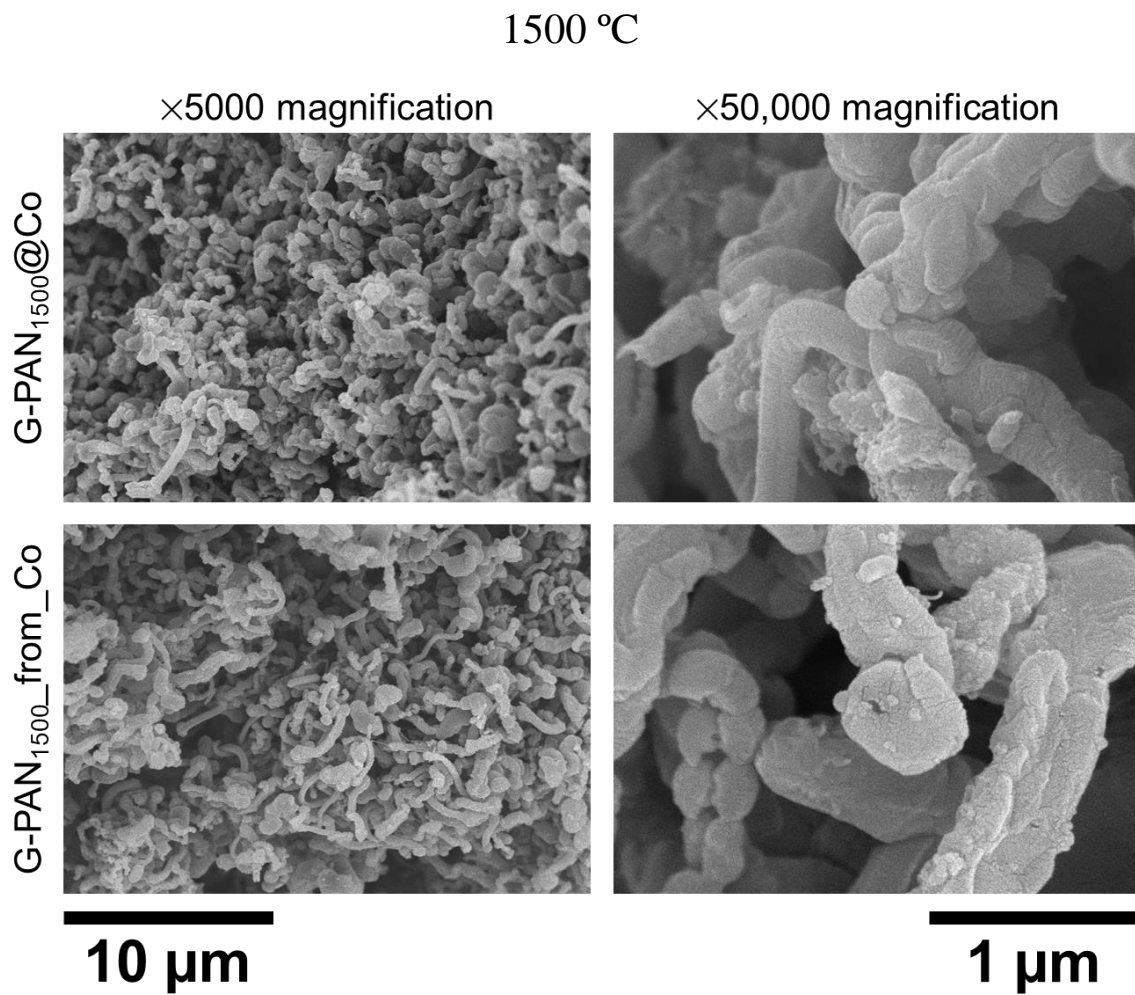
Figure S.14. SEM images of G-PAN$_{1500}$@Co (top row) and G-PAN$_{1500\_}$*from*$_\_$Co (bottom row), at low (left column) and high magnification (right column).

The mechanical properties of graphitic carbon aerogels obtained at 1500 °C, before and after aqua regia treatment were investigated under quasi-static compression, following ASTM D1621-04a using cylindrical monolithic specimens with thickness:diameter ratio of about 0.4 (see Experimental Section in the main article).[S.R.1] At low compressive strains (below 8-10%), the stress−strain curves showed typical elastomeric behavior,[S.R.2] and the materials eventually failed at around 13-18 % strain (Figure S.15). For G-PAN$_{1500}$@Fe and G-PAN$_{1500}$@Co with comparable bulk densities (0.748 g cm^{-3} versus 0.740 g cm^{-3}, respectively), the ultimate strengths were 53.24 MPa and 22.38 MPa, respectively (see Figure S.15). After treatment with aqua regia, the ultimate compressive strengths of G-PAN$_{1500}$_*from*_Fe and G-PAN$_{1500}$_*from*_Co (with bulk densities equal to 0.439 g cm^{-3} and 0.575 g cm^{-3}, respectively) were lower: 37.88 MPa and 12.77 MPa, respectively (see Figure S.15). The elastic moduli, E, of these materials were calculated from the early slopes of the stress−strain curves (at <3% strain) and were found equal to: 95.10 MPa, 70.73 MPa, 40.91 MPa, and 21.11 MPa for G-PAN$_{1500}$@Fe, G-PAN$_{1500}$_*from*_Fe, G-PAN$_{1500}$@Co, and G-PAN$_{1500}$_*from*_Co, respectively, following exactly the same trend as the ultimate compressive strength.

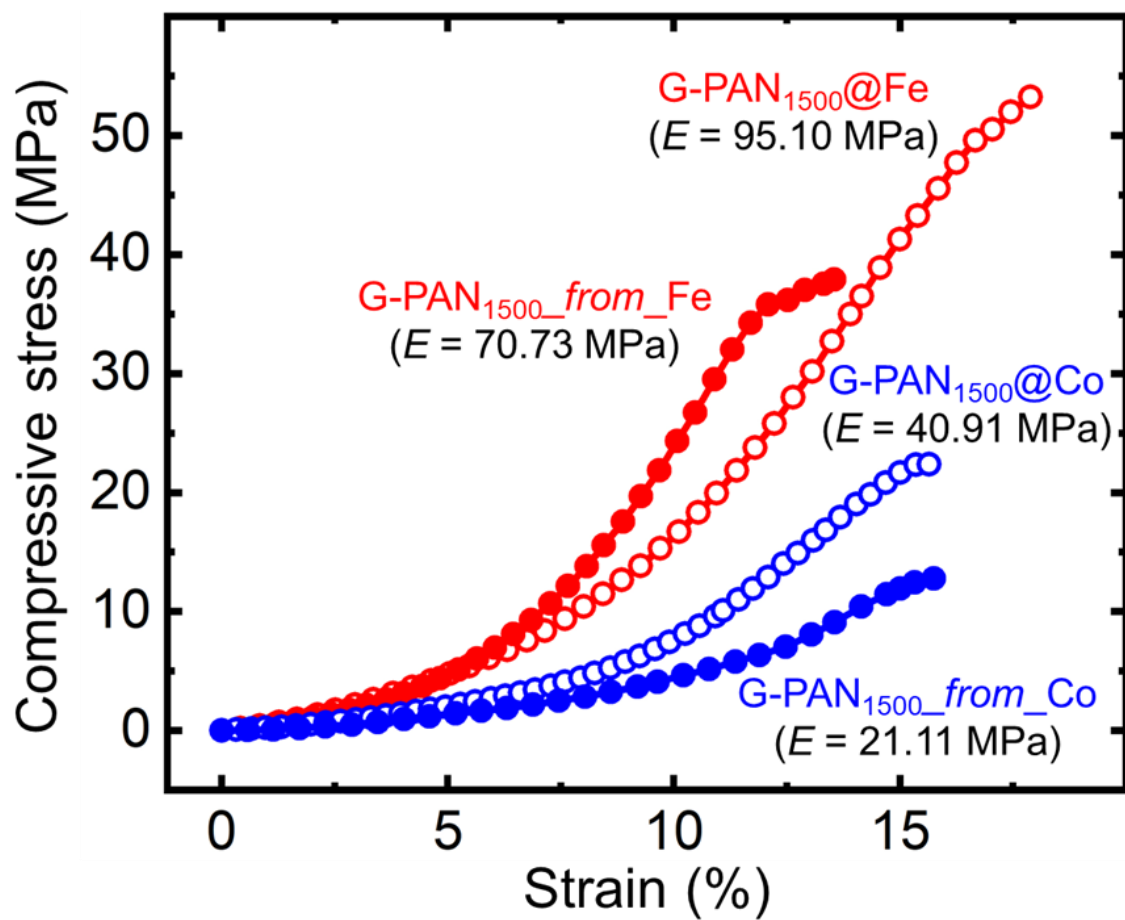Figure S.15. Compressive stress-strain data for: (A) G-PAN$_{1500}$@Fe (red, open circles); (B) G-PAN$_{1500}$_*from*_Fe (red, solid circles); (C) G-PAN$_{1500}$@Co (blue, open circles), and (D) G-PAN$_{1500}$_*from*_Co (blue, solid circles).

Materials from the PAN@FeOx system
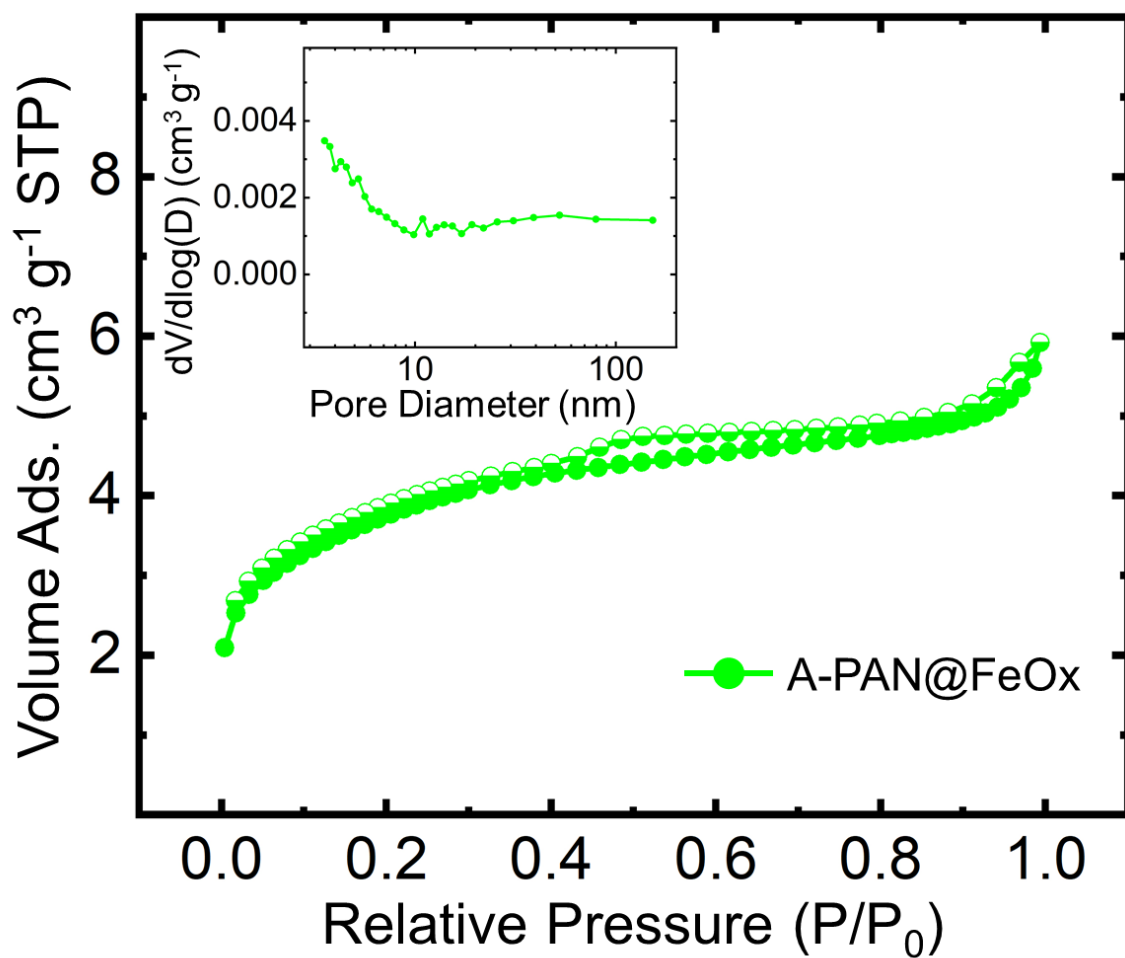
Figure S.16. N_2-sorption isotherms at 77 K of A-PAN@FeOx. <u>Inset:</u> Pore-size distribution by the BJH desorption method.

244

Figure S.17. N₂-sorption isotherms at 77 K of G-PAN$_{800}$@Fe and G-PAN$_{800}$_*from*_Fe.
Inset: Pore-size distribution by the BJH desorption method.
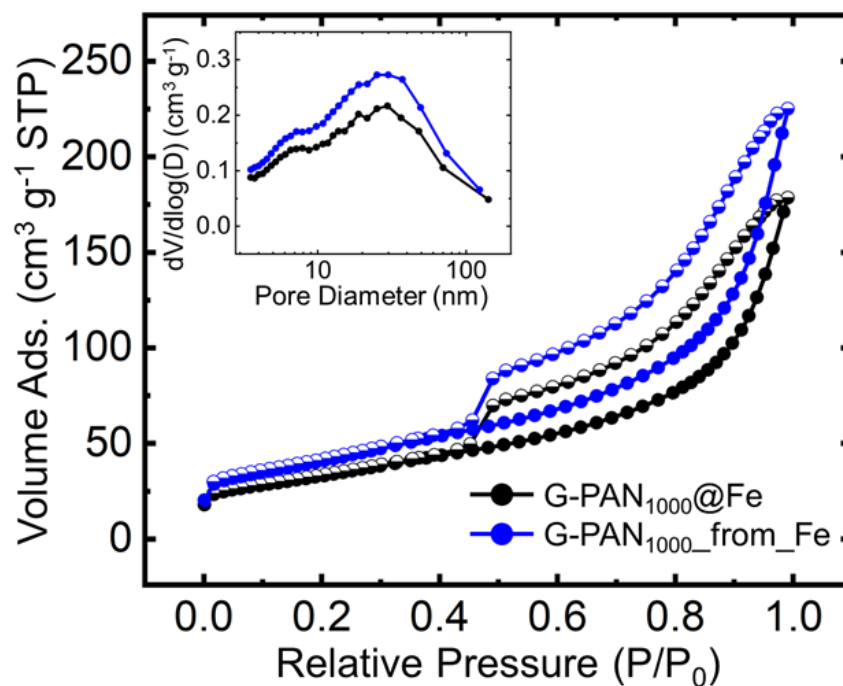
Figure S.18. N₂-sorption isotherms at 77 K of G-PAN$_{1000}$@Fe and G-PAN$_{1000}$_*from*_Fe.
Inset: Pore-size distribution by the BJH desorption method.
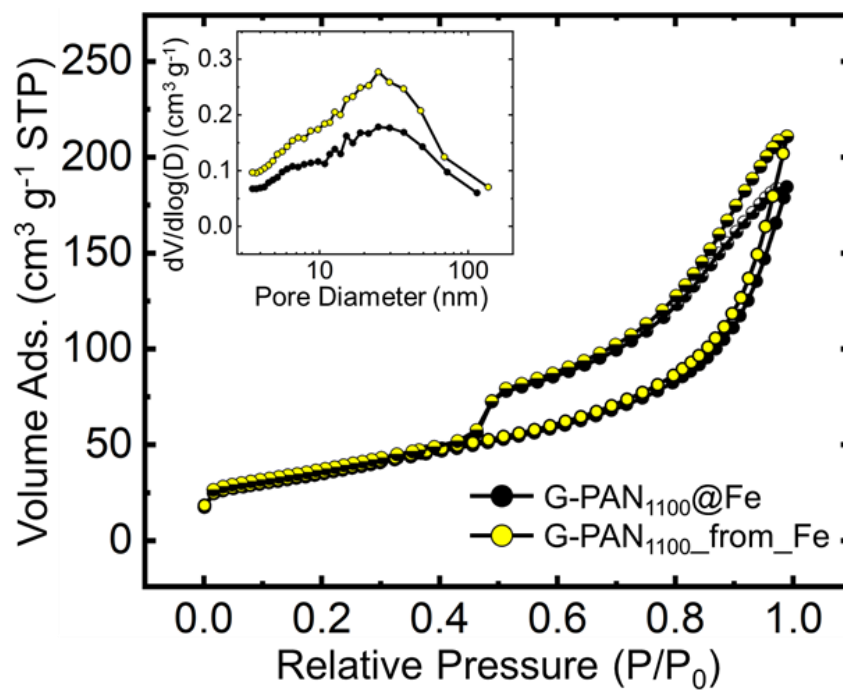
Figure S.19. N$_2$-sorption isotherms at 77 K of G-PAN$_{1100}$@Fe and G-PAN$_{1100}$_*from*_Fe. Inset: Pore-size distributions by the BJH desorption method.
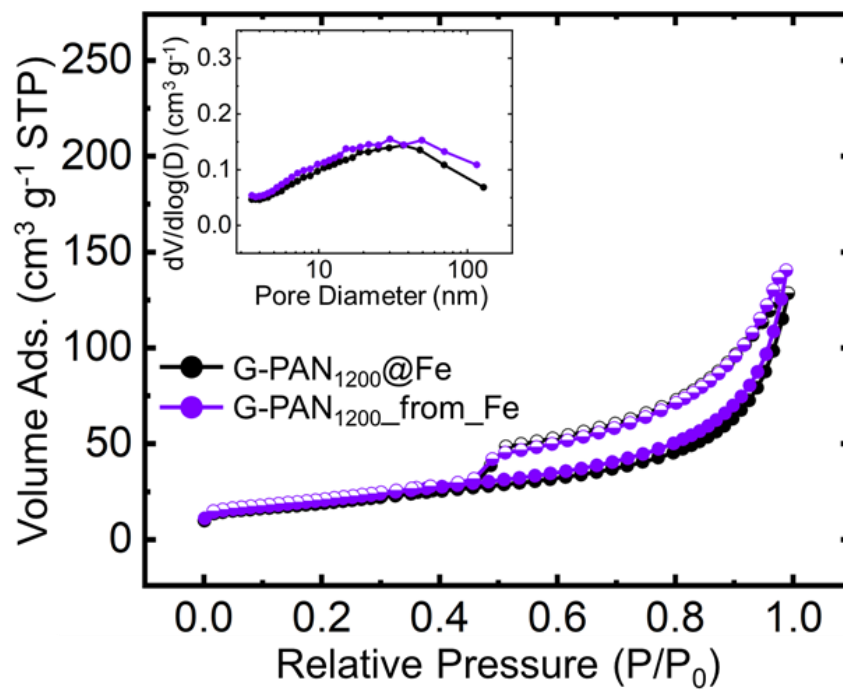
Figure S.20. N$_2$-sorption isotherms at 77 K of G-PAN$_{1200}$@Fe and G-PAN$_{1200}$_*from*_Fe. Inset: Pore-size distributions of by the BJH desorption method.
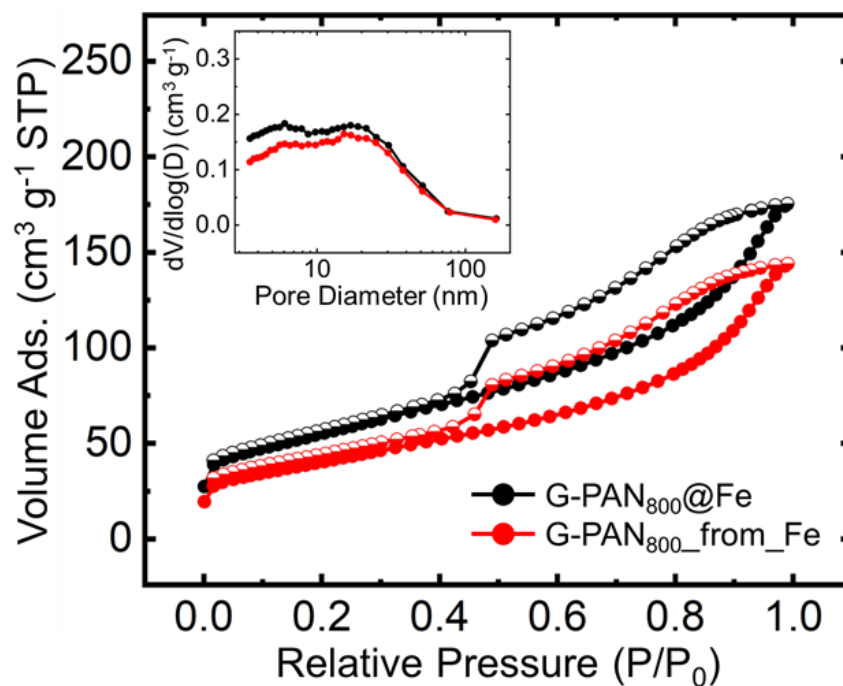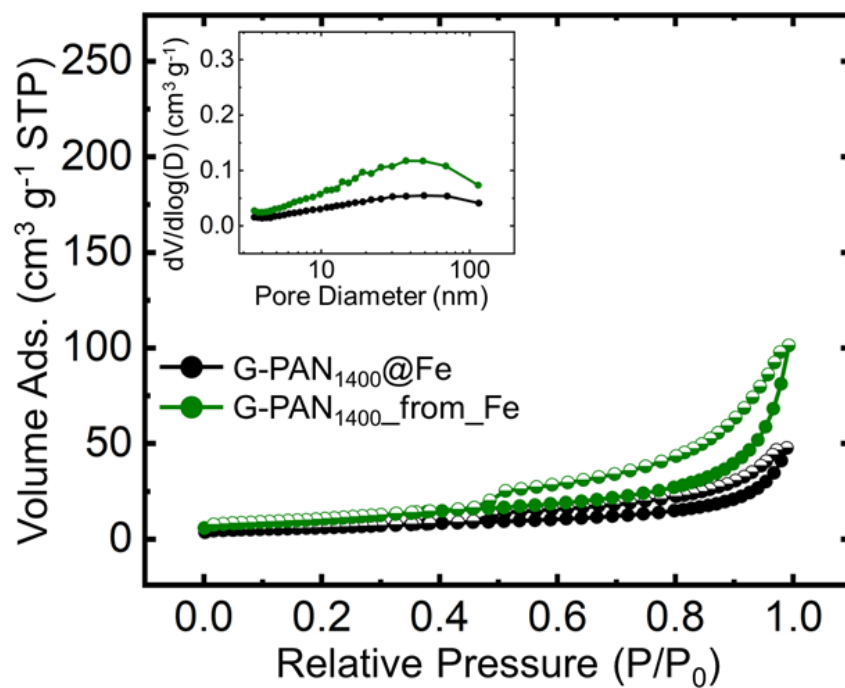
Figure S.21. N_2-sorption isotherms at 77 K of G-PAN$_{1400}$@Fe and G-PAN$_{1400}$_*from*_Fe.
<u>Inset</u>: Pore-size distributions by the BJH desorption method.
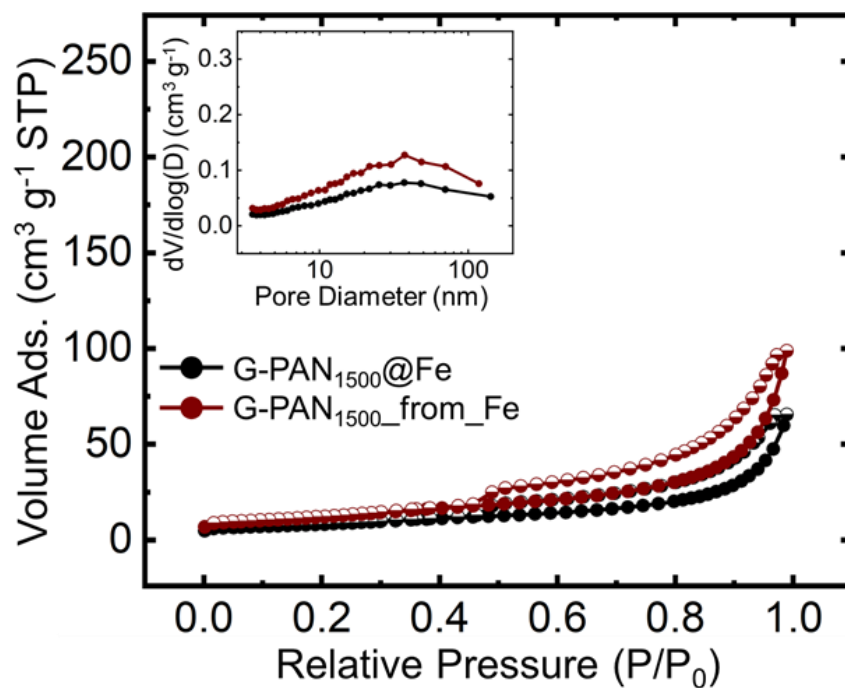
Figure S.22. N_2-sorption isotherms at 77 K of G-PAN$_{1500}$@Fe and G-PAN$_{1500}$_*from*_Fe.
<u>Inset</u>: Pore-size distributions by the BJH desorption method.

Materials from the PAN@CoOx system
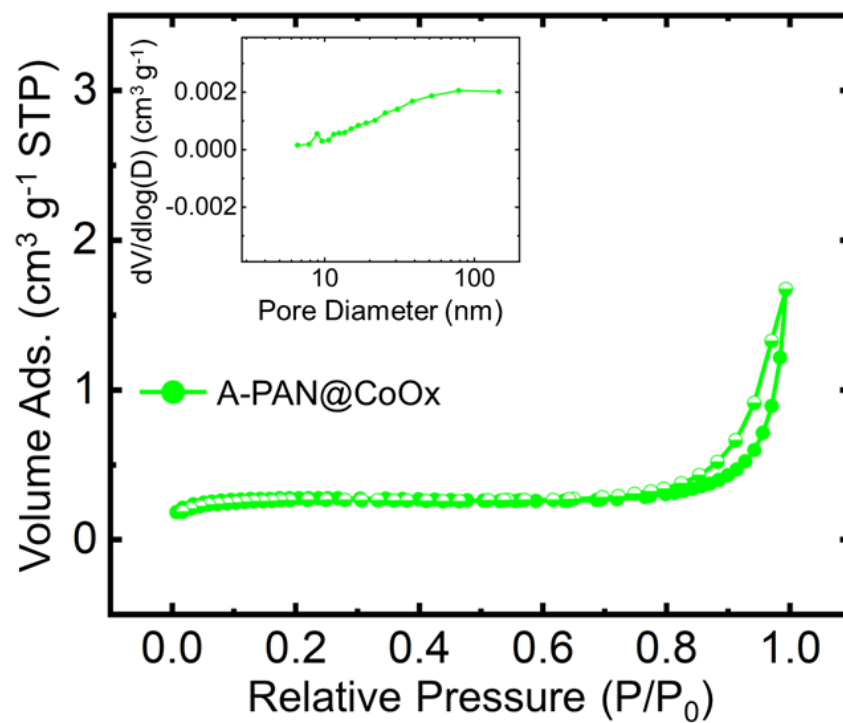
Figure S.23. N_2-sorption isotherms at 77 K of a A-PAN@CoOx compact. <u>Inset</u>: Pore-size distribution by the BJH desorption method.
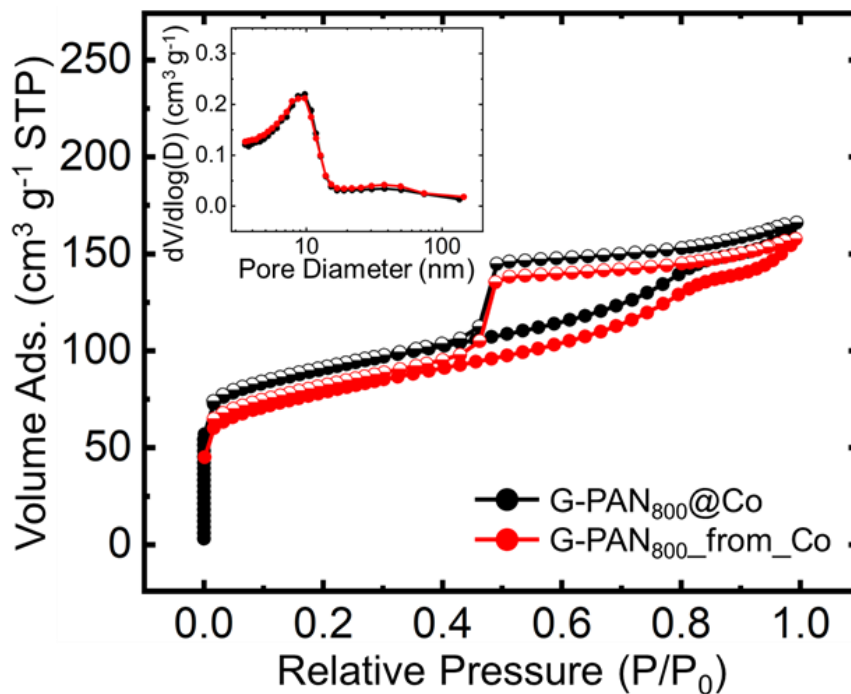
Figure S.24. N_2-sorption isotherms at 77 K of G-PAN$_{800}$@Co and G-PAN$_{800}$_*from*_Co. Inset: Pore-size distribution by the BJH desorption method.
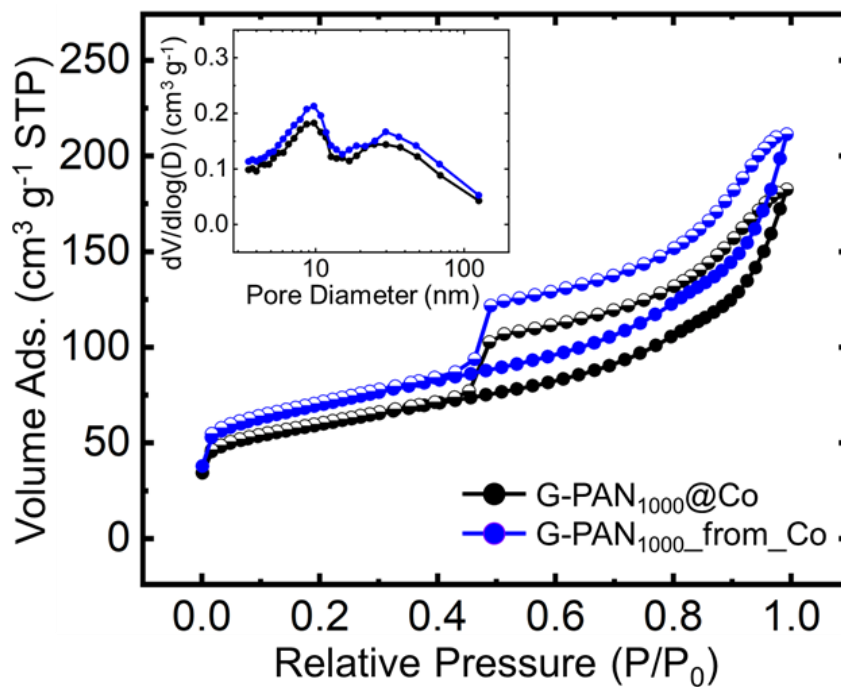
Figure S.25. N_2-sorption isotherms at 77 K of G-PAN$_{1000}$@Co and G-PAN$_{1000}$_*from*_Co. Inset: Pore-size distributions by the BJH desorption method.
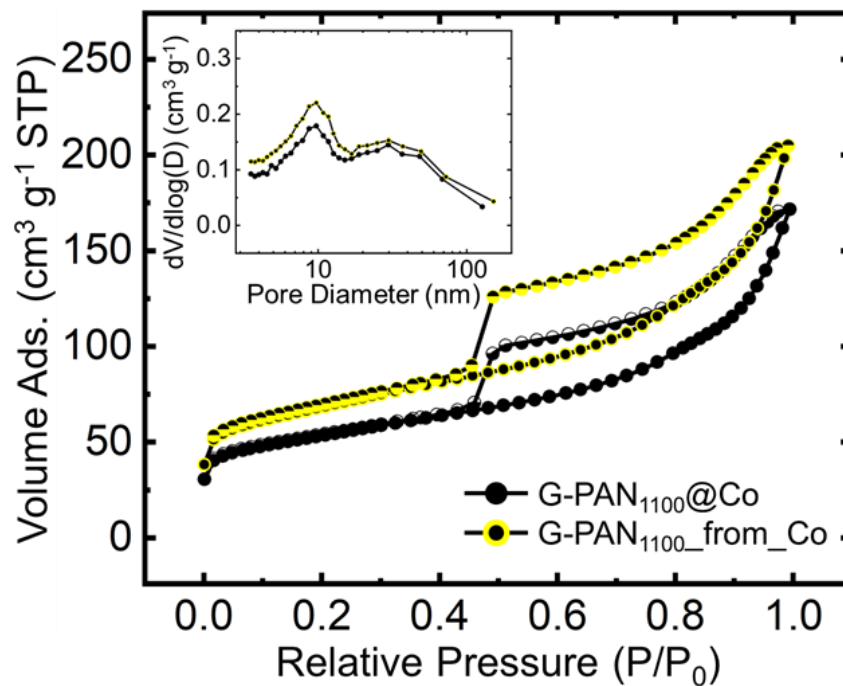
Figure S.26. N$_2$-sorption isotherms at 77 K of G-PAN$_{1100}$@Co and G-PAN$_{1100}$_*from*_Co. <u>Inset:</u> Pore-size distributions by the BJH desorption method.
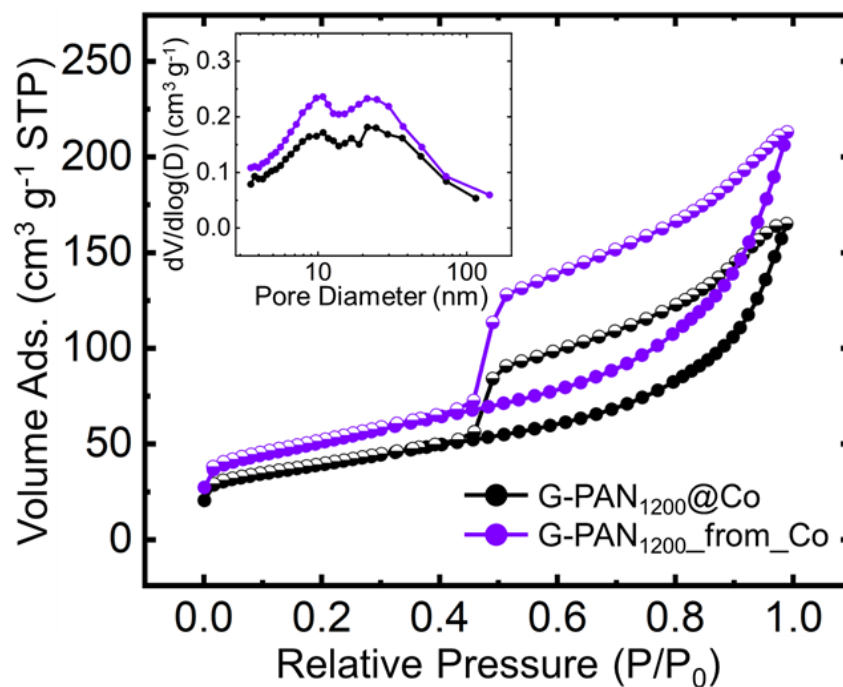
Figure S.27. N$_2$-sorption isotherms at 77 K of G-PAN$_{1200}$@Co and G-PAN$_{1200}$_*from*_Co. <u>Inset</u>: Pore-size distribution by the BJH desorption method.
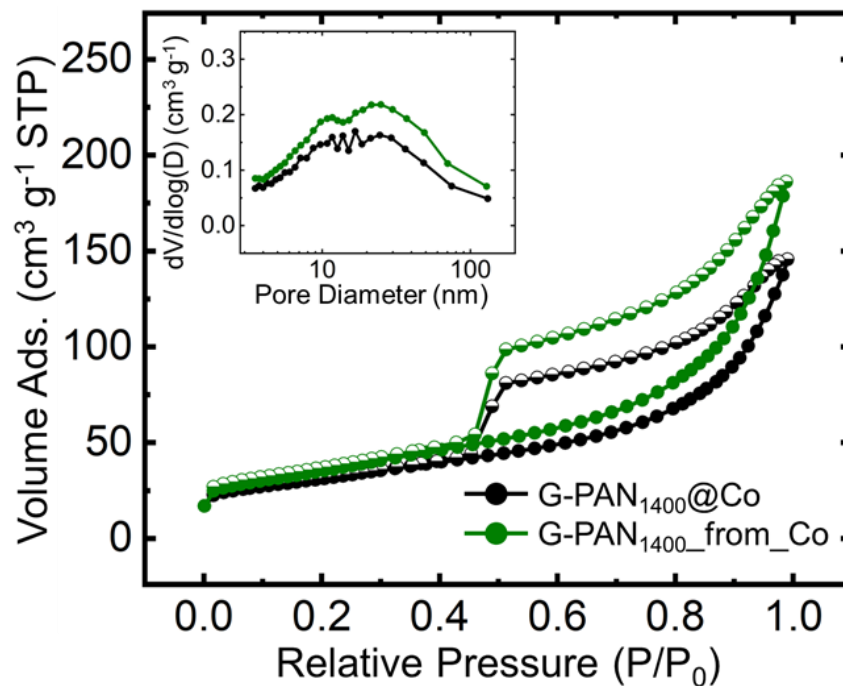
Figure S.28. N_2-sorption isotherms at 77 K of G-PAN$_{1400}$@Co and G-PAN$_{1400}$_*from*_Co.
Inset: Pore-size distributions by the BJH desorption method.
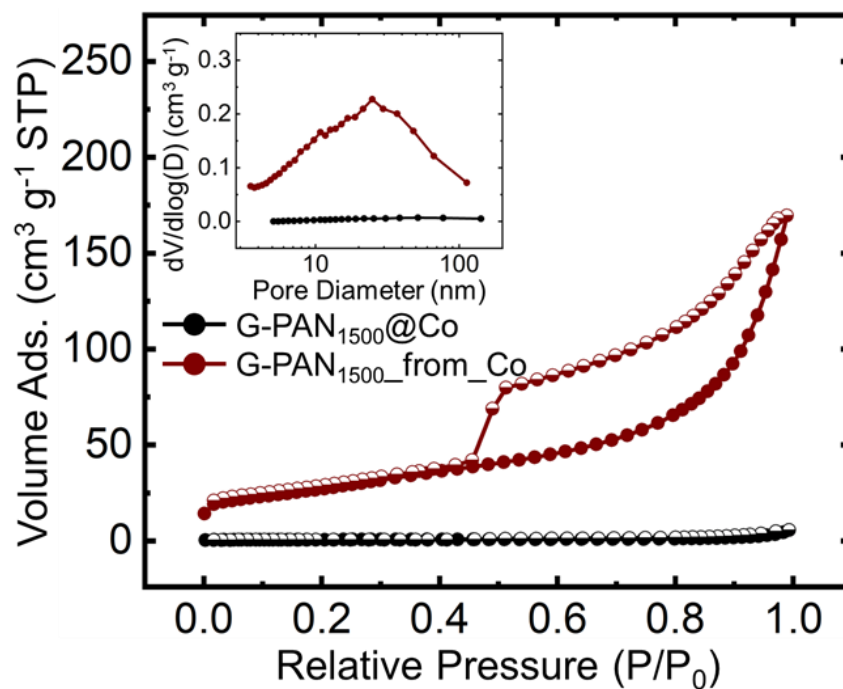
Figure S.29. N_2-sorption isotherms at 77 K of G-PAN$_{1500}$@Co and G-PAN$_{1500}$_*from*_Co.
Inset: Pore-size distributions by the BJH desorption method.
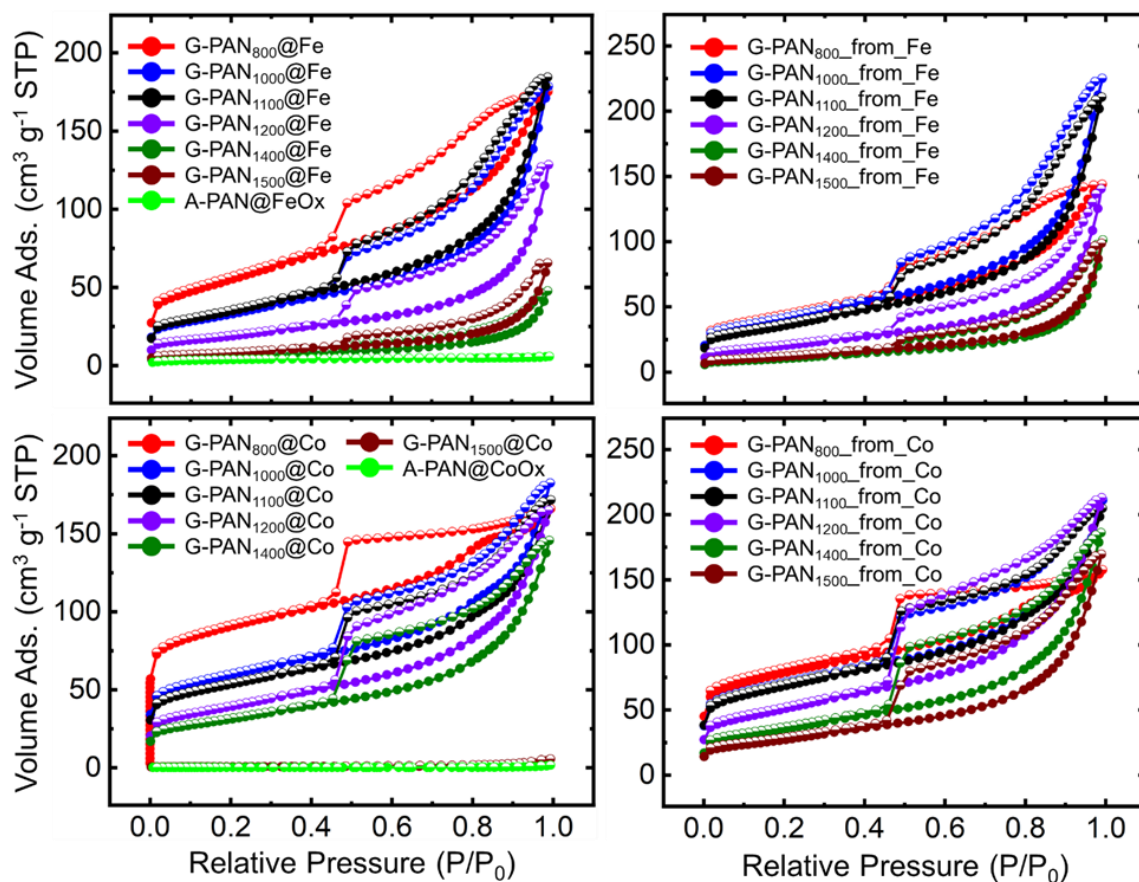
Figure S.30. Comparative N_2-sorption isotherms at 77 K of all PAN@FeOx-derived (top row) and PAN@CoOx-derived (bottom row) aerogel compacts from pyrolysis at different temperatures, before (left) and after (right) aqua-regia treatment.
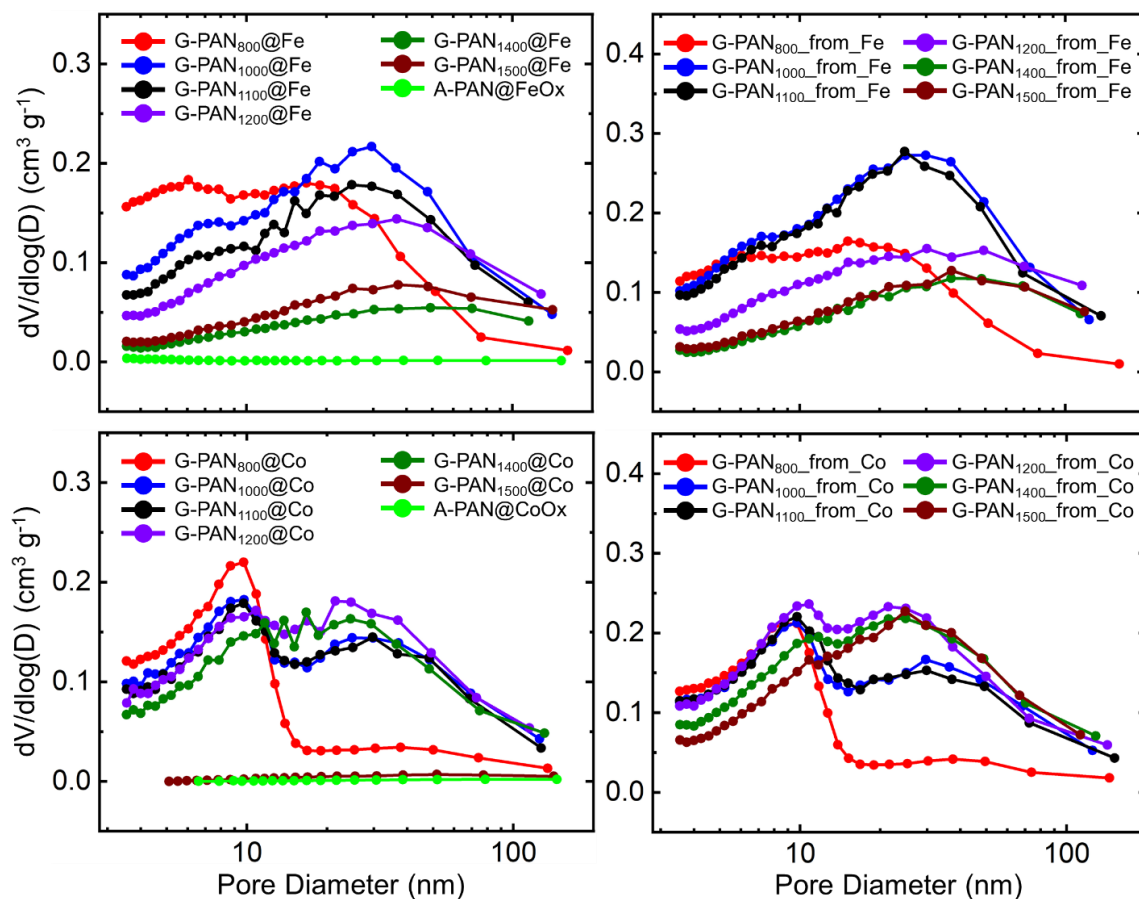
Figure S.31. Comparative pore-size distributions by the BJH desorption method of all PAN@FeOx-derived (top row) and PAN@CoOx-derived (bottom row) aerogel compacts from pyrolysis at different temperatures, before (left) and after (right) aqua-regia treatment.
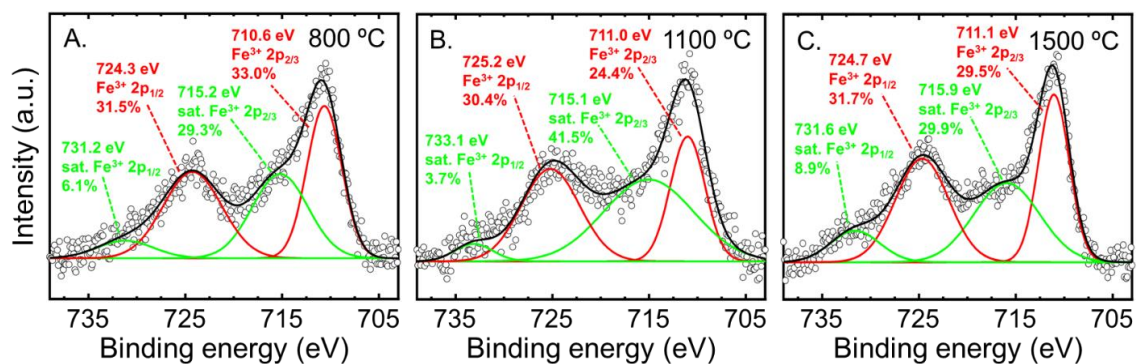
Figure S.32. High-resolution XPS spectra of Fe 2p from three samples prepared at three different temperatures (Temp) as shown: (A) G-PAN$_{800}$@Fe; (B) G-PAN$_{1100}$@Fe; (C) G-PAN$_{1500}$@Fe.
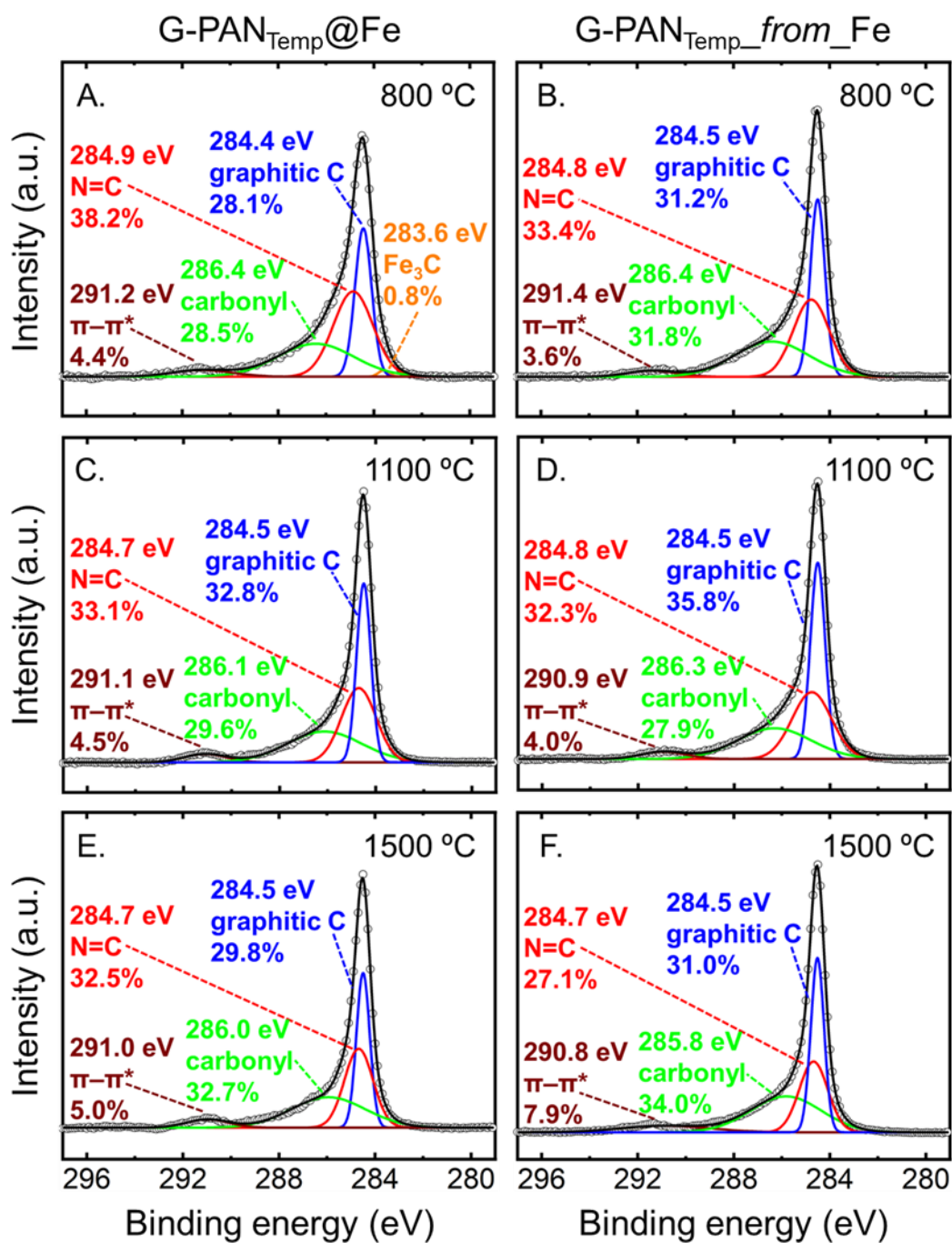
Figure S.33. High-resolution XPS spectra of C 1s of samples obtained at three pyrolysis temperatures (Temp), before and after treatment with aqua regia, as shown: (A) G-PAN$_{800}$@Fe; (B) G-PAN$_{800}$_*from*_Fe; (C) G-PAN$_{1100}$@Fe; (D) G-PAN$_{1100}$_*from*_Fe; (E) G-PAN$_{1500}$@Fe; (F) G-PAN$_{1500}$_*from*_Fe.

254
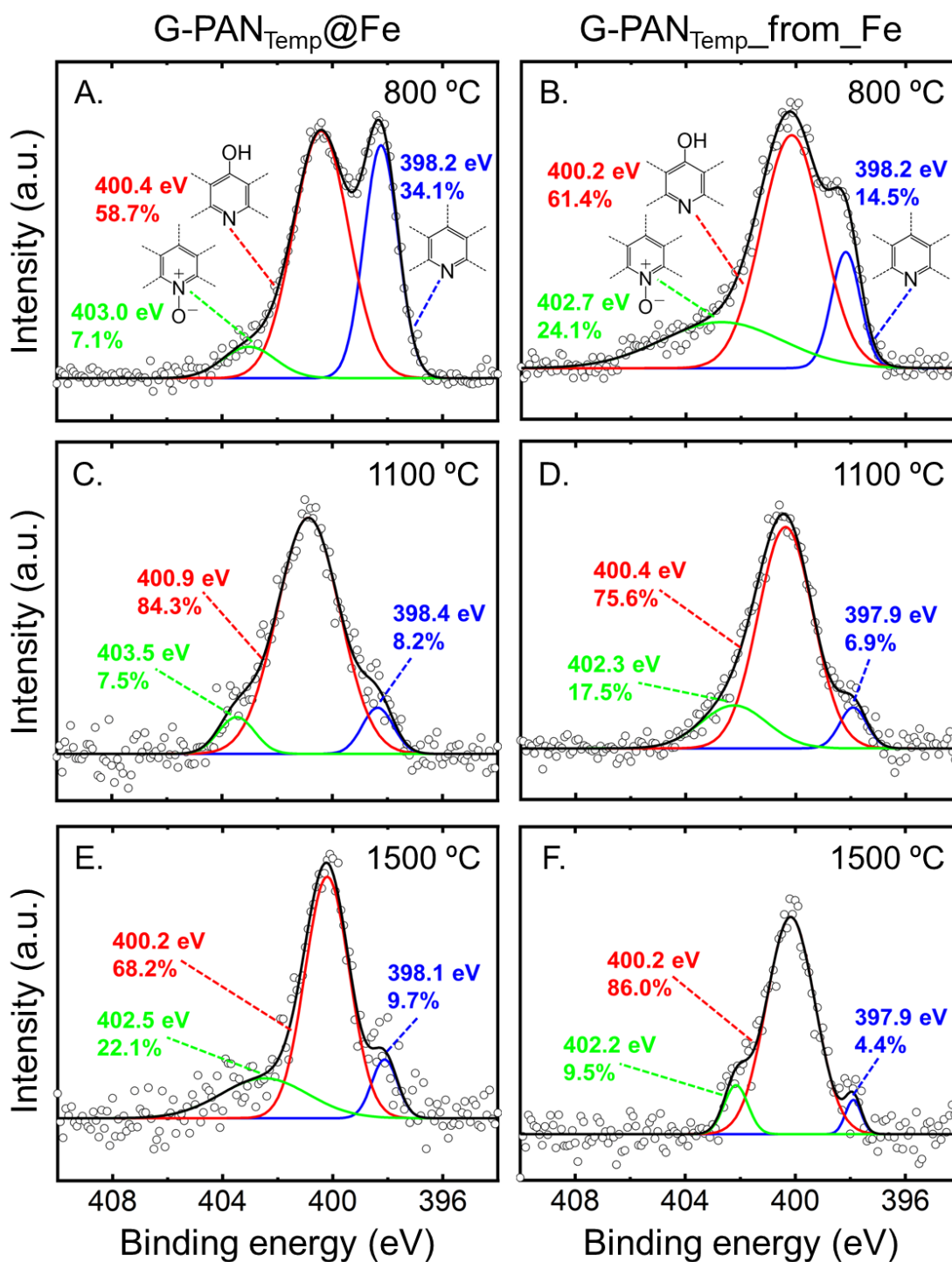
Figure S.34. High-resolution XPS spectra of N 1s of samples obtained at three pyrolysis temperatures (Temp), before and after treatment with aqua regia, as shown: (A) G-PAN$_{800}$@Fe; (B) G-PAN$_{800}$_*from*_Fe; (C) G-PAN$_{1100}$@Fe; (D) G-PAN$_{1100}$_*from*_Fe; (E) G-PAN$_{1500}$@Fe; (F) G-PAN$_{1500}$_*from*_Fe.
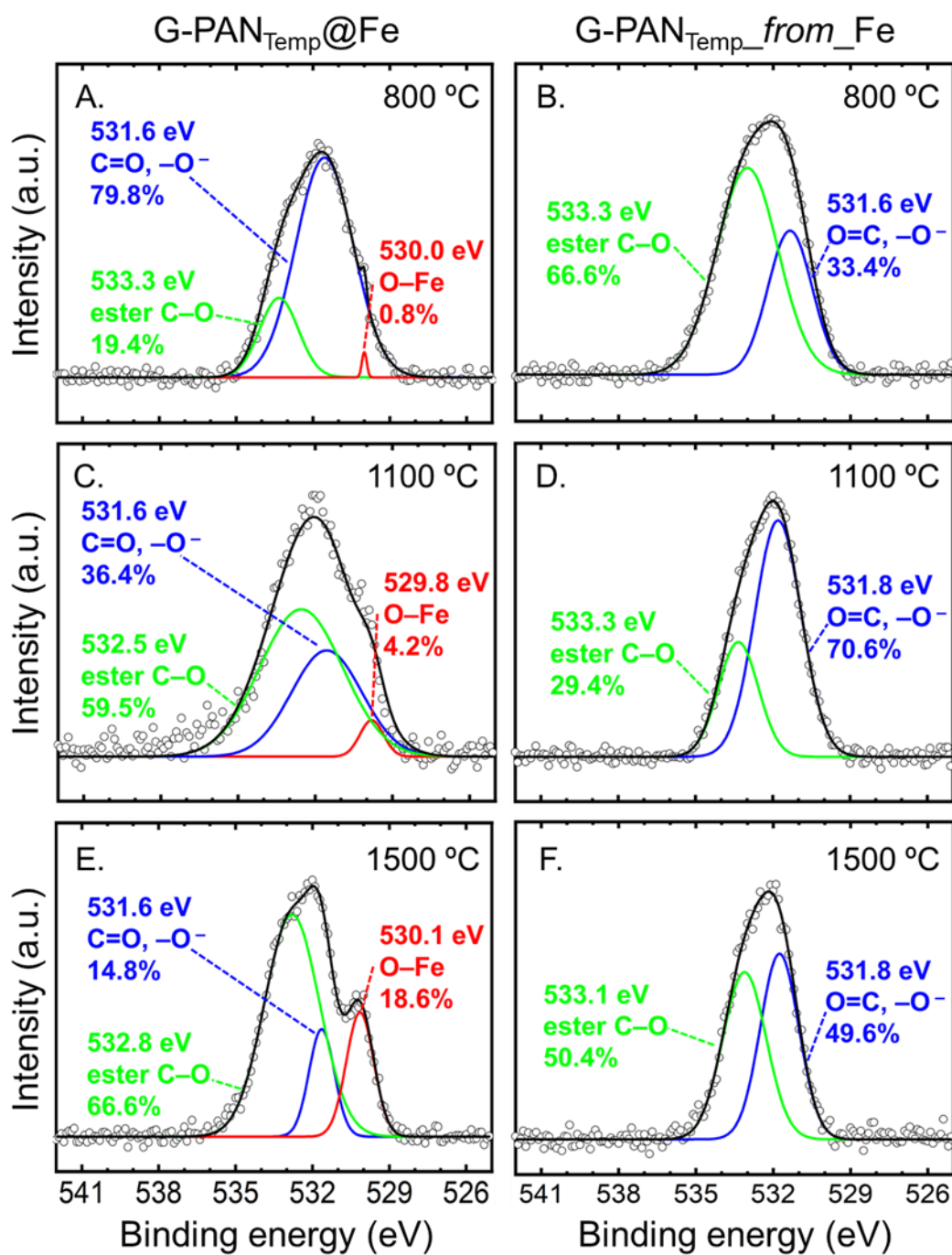
Figure S.35. High-resolution XPS spectra of O 1s of samples obtained at three pyrolysis temperatures (Temp), before and after treatment with aqua regia, as shown: (A) G-PAN$_{800}$@Fe; (B) G-PAN$_{800}$_*from*_Fe; (C) G-PAN$_{1100}$@Fe; (D) G-PAN$_{1100}$_*from*_Fe; (E) G-PAN$_{1500}$@Fe; (F) G-PAN$_{1500}$_*from*_Fe.
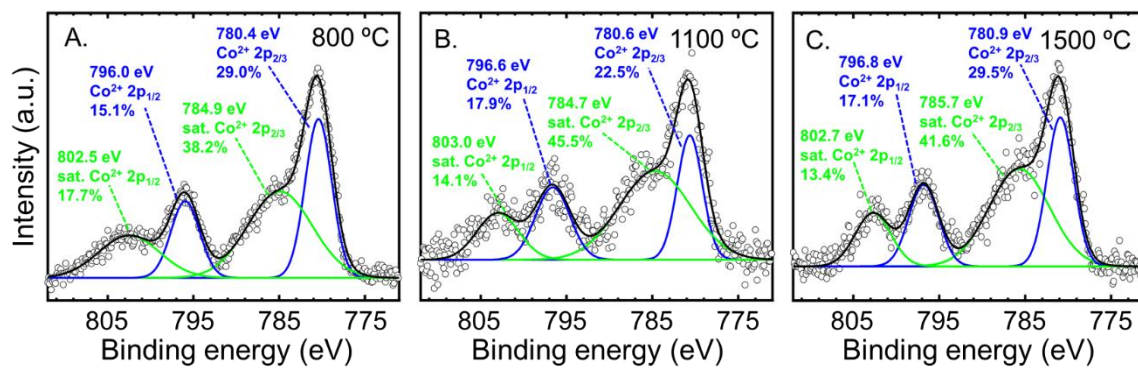
Figure S.36. High-resolution XPS spectra of Co 2p from three samples prepared at three different temperatures (Temp) as shown: (A) G-PAN$_{800}$@Co; (B) G-PAN$_{1100}$@Co; (C) G-PAN$_{1500}$@Co.
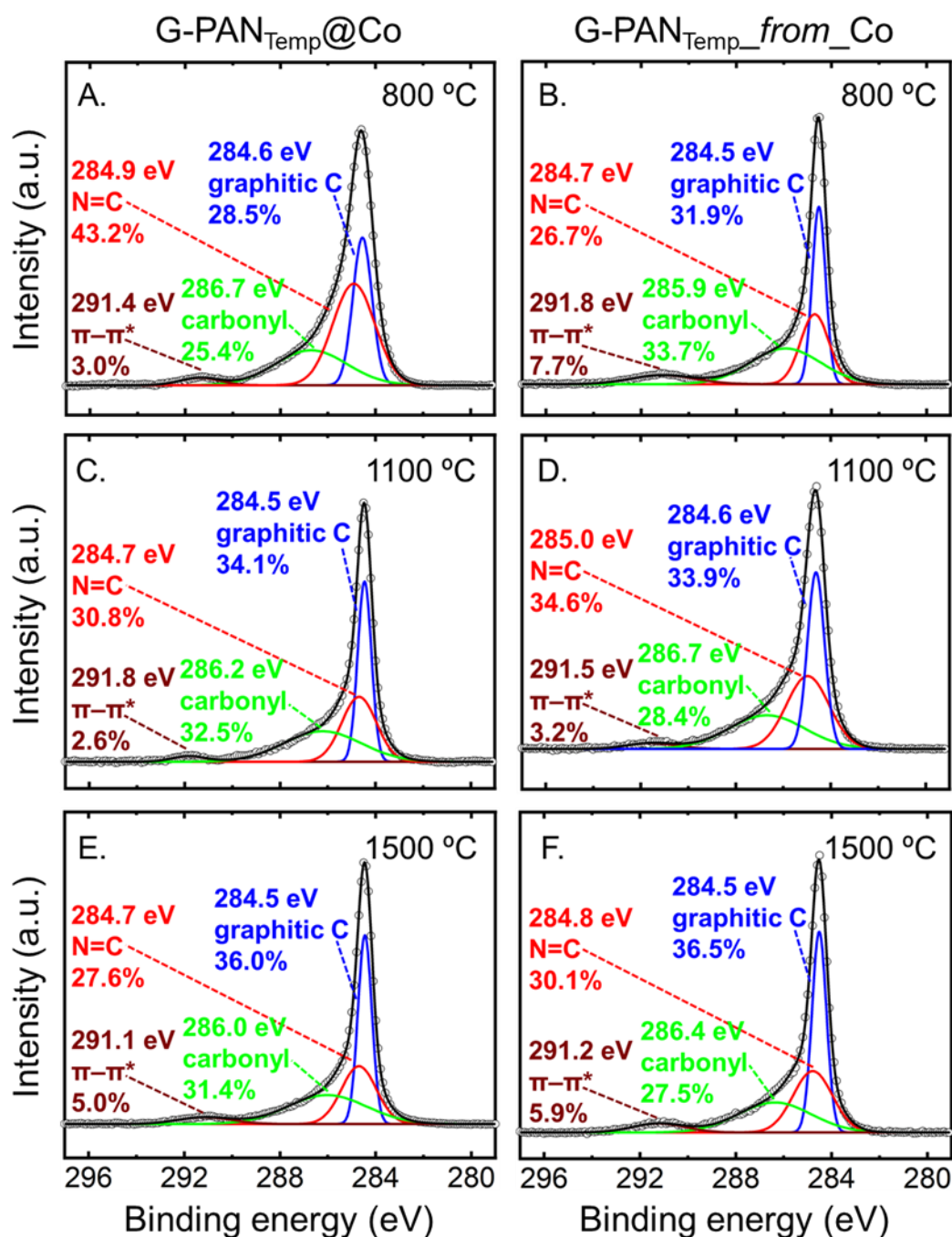
Figure S.37. High-resolution XPS spectra of C 1s of samples obtained at three pyrolysis temperatures (Temp), before and after treatment with aqua regia, as shown: (A) G-PAN$_{800}$@Co; (B) G-PAN$_{800}$_*from*_Co; (C) G-PAN$_{1100}$@Co; (D) G-PAN$_{1100}$_*from*_Co; (E) G-PAN$_{1500}$@Co; (F) G-PAN$_{1500}$_*from*_Co.
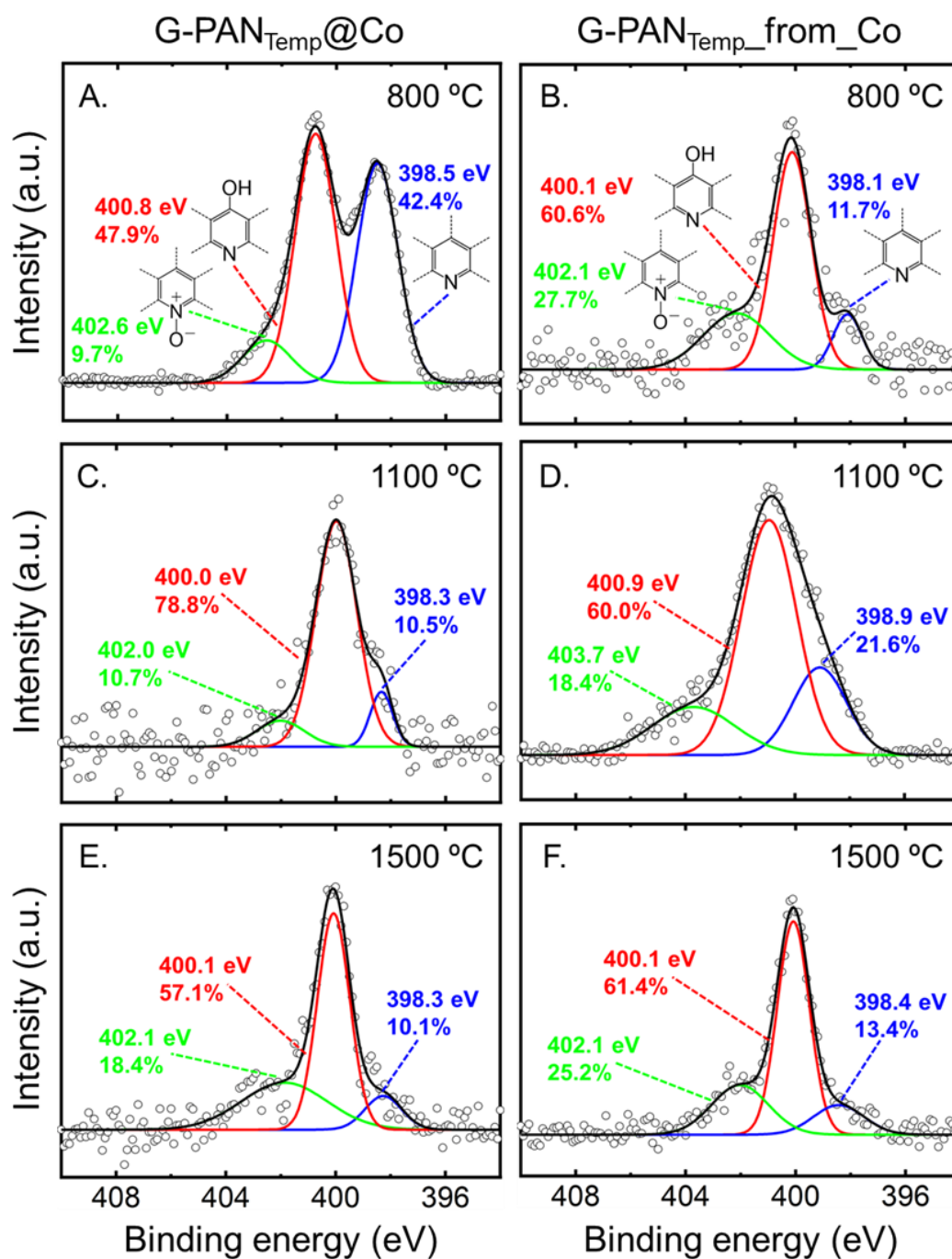
Figure S.38. High-resolution XPS spectra of N 1s of samples obtained at three pyrolysis temperatures (Temp), before and after treatment with aqua regia, as shown: (A) G-PAN$_{800}$@Co; (B) G-PAN$_{800}$_*from*_Co; (C) G-PAN$_{1100}$@Co; (D) G-PAN$_{1100}$_*from*_Co; (E) G-PAN$_{1500}$@Co; (F) G-PAN$_{1500}$_*from*_Co.
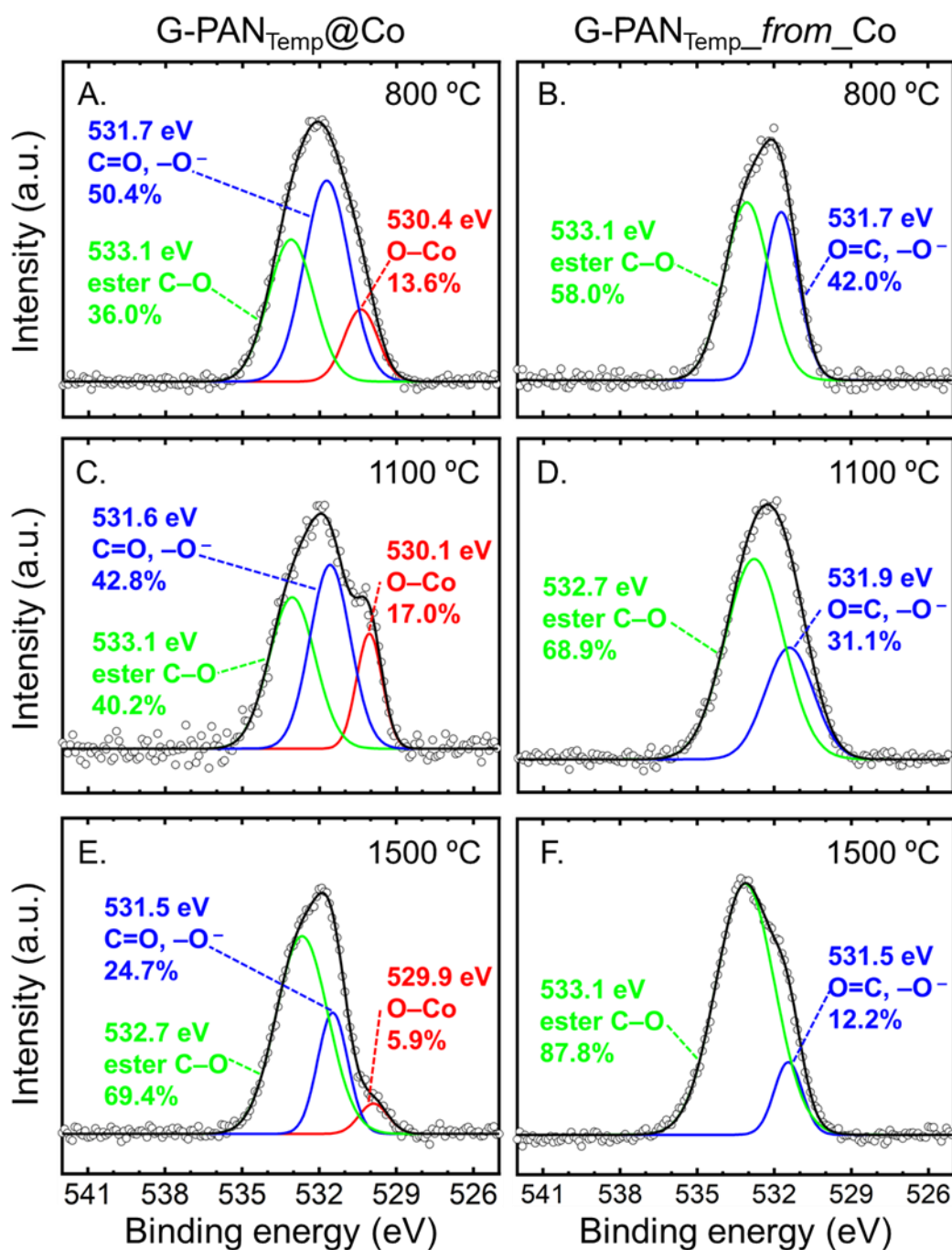
Figure S.39. High-resolution XPS spectra of O 1s of samples obtained at three pyrolysis temperatures (Temp), before and after treatment with aqua regia, as shown: (A) G-PAN$_{800}$@Co; (B) G-PAN$_{800}$_*from*_Co; (C) G-PAN$_{1100}$@Co; (D) G-PAN$_{1100}$_*from*_Co; (E) G-PAN$_{1500}$@Co; (F) G-PAN$_{1500}$_*from*_Co.

Table S.3. Atomic composition of G-PAN$_{Temp}$@Fe and G-PAN$_{Temp}$_*from*_Fe.

| sample	atomic % from XPS data				
	C	O	N	Fe	Au
before aqua-regia treatment					
G-PAN$_{800}$@Fe	85.64	5.67	7.10	0.72	0.87
G-PAN$_{1100}$@Fe	95.59	2.11	1.67	0.48	0.15
G-PAN$_{1500}$@Fe	91.25	4.48	2.15	1.46	0.66
after aqua-regia treatment					
G-PAN$_{800}$_*from*_Fe	90.10	4.83	4.21	-	0.86
G-PAN$_{1100}$_*from*_Fe	94.69	2.80	1.61	-	0.90
G-PAN$_{1500}$_*from*_Fe	94.98	2.55	1.57	-	0.90

Table S.4. Atomic composition of G-PAN$_{Temp}$@Co and G-PAN$_{Temp}$_*from*_Co.

sample	atomic % from XPS data				
	C	O	N	Co	Au
before aqua-regia treatment					
G-PAN$_{800}$@Co	89.03	4.12	5.74	0.96	0.15
G-PAN$_{1100}$@Co	92.69	3.88	1.98	0.59	0.86
G-PAN$_{1500}$@Co	93.68	3.12	1.53	0.34	1.33
after aqua-regia treatment					
G-PAN$_{800}$_*from*_Co	92.56	2.97	3.49	-	0.98
G-PAN$_{1100}$_*from*_Co	91.31	3.87	3.54	-	1.28
G-PAN$_{1500}$_*from*_Co	88.82	5.97	2.57	-	2.64

Table S.5. Deconvoluted binding energies and atomic compositions of G-PAN$_{Temp}$@Fe and G-PAN$_{Temp}$_*from*_Fe.

species	binding energy [eV]	atomic % of at G-PAN$_{Temp}$@Fe			atomic % of at G-PAN$_{Temp}$_*from*_Fe		
		800 ℃	1100 ℃	1500 ℃	800 ℃	1100 ℃	1500 ℃
C 1s							
Carbide (Fe-C)	283.6 ± 0.1	0.8	-	-	-	-	-
Graphitic C-C/C=C	284.5 ± 0.1	28.1	32.8	29.8	31.2	35.8	31.0
C=N	284.8 ± 0.1	38.2	33.1	32.5	33.4	32.3	27.1
C=O & C=O in keto/enol	286.3 ± 0.1	28.5	29.6	32.7	31.8	27.9	34.0
Plasmon loss (π-π*)	291.2 ± 0.1	4.4	4.5	5.0	3.6	4.0	7.9
N 1s							
Pyridinic N	398.3 ± 0.1	34.1	8.2	9.7	14.5	6.9	4.4
Pyridonic N	400.3 ± 0.1	58.7	84.3	68.2	61.4	75.6	86.0
Pyridine Oxide	402.5 ± 0.2	7.1	7.5	22.1	24.1	17.5	9.5
O 1s							
Metal oxide (Fe-O)	530.1 ± 0.2	0.8	4.2	18.6	-	-	-
C=O & Phenoxide (-O⁻)	531.6 ± 0.2	79.8	36.4	14.8	33.4	70.6	49.6
Ester C-O	533.0 ± 0.2	19.4	59.5	66.6	66.6	29.4	50.4
Fe 2p							
Fe^{3+} 2p$_{2/3}$	710.9 ± 0.2	33.0	24.4	29.5	-	-	-
satellite of Fe^{3+} 2p$_{2/3}$	715.4 ± 0.5	29.3	41.5	29.9	-	-	-
Fe^{3+} 2p$_{1/2}$	724.7 ± 0.5	31.5	30.4	31.7	-	-	-
satellite of Fe^{3+} 2p$_{1/2}$	732.0 ± 1.0	6.1	3.7	8.9	-	-	-

Table S.6. Deconvoluted binding energies and atomic compositions of G-PAN_{Temp}@Co and G-PAN_{Temp}_*from*_Co.

species	binding energy [eV]	atomic % of at G-PAN_{Temp}@Co			atomic % of at G-PAN_{Temp}_*from*_Co		
		800 ℃	1100 ℃	1500 ℃	800 ℃	1100 ℃	1500 ℃
C 1s							
Graphitic C-C/C=C	284.5 ± 0.1	28.5	34.1	36.0	31.9	33.9	36.5
C=N	284.8 ± 0.1	43.2	30.8	27.6	26.7	34.6	30.1
C=O & C=O in keto/enol	286.3 ± 0.1	25.4	32.5	31.4	33.7	28.4	27.5
Plasmon loss (π-π*)	291.2 ± 0.1	3.0	2.6	5.0	7.7	3.2	5.9
N 1s							
Pyridinic N	398.3 ± 0.1	42.4	10.5	10.1	11.7	21.6	13.4
Pyridonic N	400.3 ± 0.1	47.9	78.8	57.1	60.6	60.0	61.4
Pyridine Oxide	402.5 ± 0.2	9.7	10.7	18.4	27.7	18.4	25.2
O 1s							
Metal oxide (Co-O)	530.1 ± 0.2	13.6	17.0	5.9	-	-	-
C=O & Phenoxide (-O$^-$)	531.6 ± 0.2	50.4	42.8	24.7	42.0	31.1	12.2
Ester C-O	533.0 ± 0.2	36.0	40.2	69.4	58.0	68.9	87.8
Co 2p							
Co^{3+} 2p$_{2/3}$	780.7 ± 0.2	29.0	22.5	29.5	-	-	-
satellite of Co^{3+} 2p$_{2/3}$	785.1 ± 0.5	38.2	45.5	41.6	-	-	-
Co^{3+} 2p$_{1/2}$	796.5 ± 0.4	15.1	17.9	17.1	-	-	-
satellite of Co^{3+} 2p$_{1/2}$	802.7 ± 0.3	17.7	14.1	13.4	-	-	-

Table S.7. XRD, TEM and Raman data of samples as shown, including commercial graphite and carbon black.

sample	2θ for (002) [deg][c]	interlayer spacing from: [Å] XRD (d_{002})[d]	interlayer spacing from: [Å] TEM[e]	L_c from (002) [Å][f]	graphitic C from XRD [% w/w][g]	D peak [cm^{-1}]	G peak [cm^{-1}]	G' peak [cm^{-1}]	I_D/I_G[h]	$I_{G'}/I_G$[i]	L_a [nm][j]
commercial graphite[a]	26.40	3.37	3.34	187.1	99.21	1311	1567	2648	0.46	0.98	83.63
commercial carbon black[b]	25.20	3.53	-	12.2	-	1321	1579	-	2.85	-	13.49
Fe-derived pure graphitic carbon aerogels obtained at pyrolysis temperatures (Temp) after aqua-regia treatment: G-PAN$_{Temp}$_from_Fe											
Temp (ºC)											
800 ºC	26.18	3.40	3.50	52.7	60.68	1324	1584	2645	1.86	0.62	20.71
1000 ºC	26.20	3.40	3.48	66.1	77.58	1322	1576	2645	1.83	1.79	20.99
1100 ºC	26.33	3.38	3.43	78.5	91.01	1338	1582	2645	1.28	0.15	30.12
1200 ºC	26.40	3.37	3.44	126.7	94.96	1322	1585	2655	0.70	0.50	54.71
1400 ºC	26.45	3.37	3.39	161.7	97.65	1318	1567	2645	0.66	0.66	58.27
1500 ºC	26.58	3.35	3.38	168.0	99.82	1330	1584	2654	0.55	0.59	70.10
Co-derived pure graphitic carbon aerogels obtained at pyrolysis temperatures (Temp) after aqua-regia treatment: G-PAN$_{Temp}$_from_Co											
Temp (ºC)											
800 ºC	26.35	3.38	3.51	33.1	56.9	1327	1580	2642	2.35	0.07	16.39
1000 ºC	26.20	3.40	3.48	66.6	72.93	1330	1580	2640	2.19	0.13	17.60
1100 ºC	26.23	3.40	3.46	62.0	79.92	1325	1590	2655	1.25	0.32	30.81
1200 ºC	26.33	3.38	3.43	71.8	86.55	1321	1579	2646	1.09	0.87	35.19
1400 ºC	26.20	3.40	3.44	73.1	89.57	1322	1580	2646	0.89	0.97	43.46
1500 ºC	26.38	3.38	3.41	77.9	94.11	1325	1582	2650	0.74	0.75	51.73

[a] From Sigma Aldrich Item No. 808067. [b] From Sigma Aldrich Item No. 05105. [c] Obtained from powder XRD data. [d] Calculated using Bragg's law with Cu Kα wavelength of 1.54056 Å. [e] Calculated from HR-TEM images using the ImageJ software, average of 5 values at different areas. [f] Calculated using the Scherrer equation (see main article) with shape factor (k) of 0.9. [g] Calculated as described in Appendix VIII of this Supporting Information. [h,i] Calculated from Raman data using integral peak intensities (all peaks (average value): D (1323), G (1579), D' (1615), and G' (2647) were deconvoluted). [j] Calculated from Raman data via Knight's empirical formula (see main article).
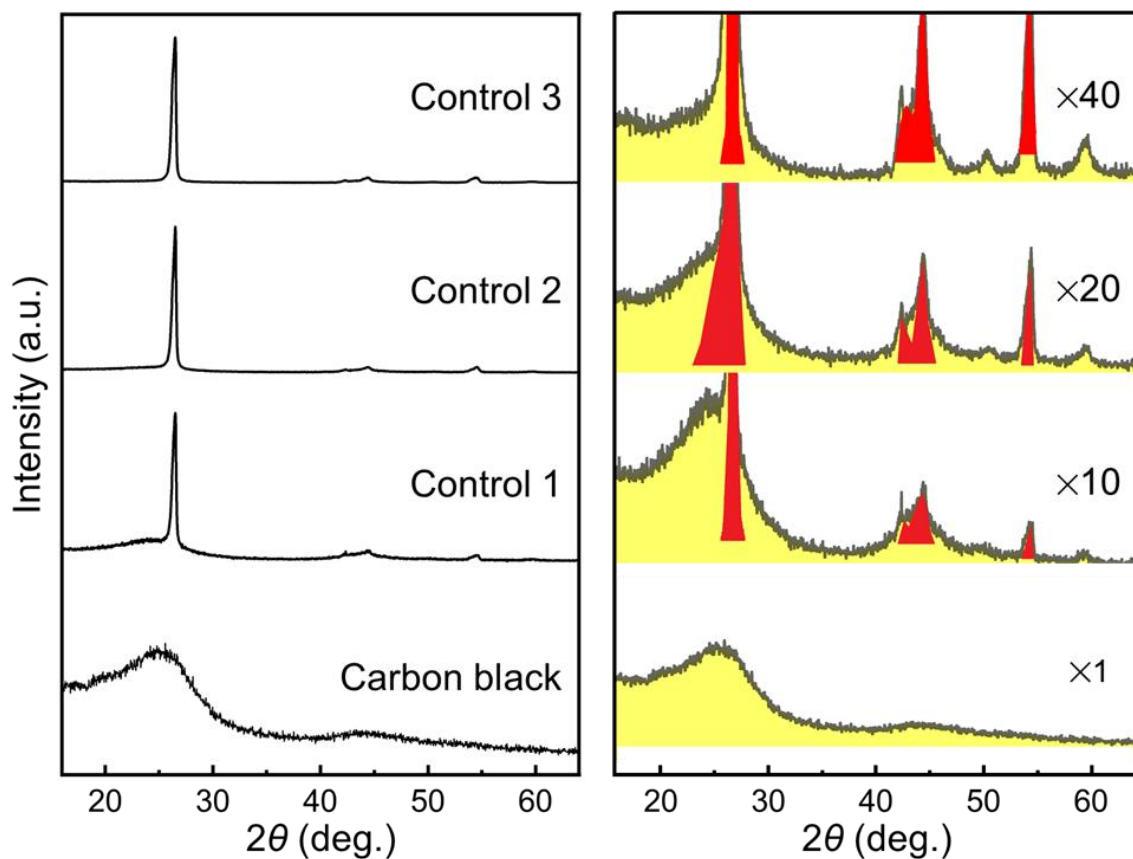
Figure S.40. Powder XRD of three control samples prepared by mixing (with a mortar and pestle) commercial graphite and carbon black, in the proportions shown in Table S.8 The expanded version shown on the right is intended to facilitate visualization of the relevant areas that are used in order to calculate the percent of crystalline carbon via:

$$Degree\_of\_Crystallinity = 100 \times \frac{\sum areas\_under\_the\_XRD\_peaks}{Total\_area\_under\_the\_XRD} = 100 \times \frac{Total\_red\_area}{Total\_red\_and\_yellow\_areas}$$

Table S.8. Graphitization yield (%) calculated from XRD data (see Figure S.40 above) via the degree of crystallinity formula (see legend of Figure S.40).

Control	Prepared at the following ratios		Calculated from XRD	
	Commercial graphite [% w/w]	Commercial carbon black [% w/w]	Graphitic C [% w/w]	Amorphous C [% w/w]
Control 1	20	80	20.18	79.82
Control 2	50	50	50.64	49.36
Control 3	80	20	78.01	21.99
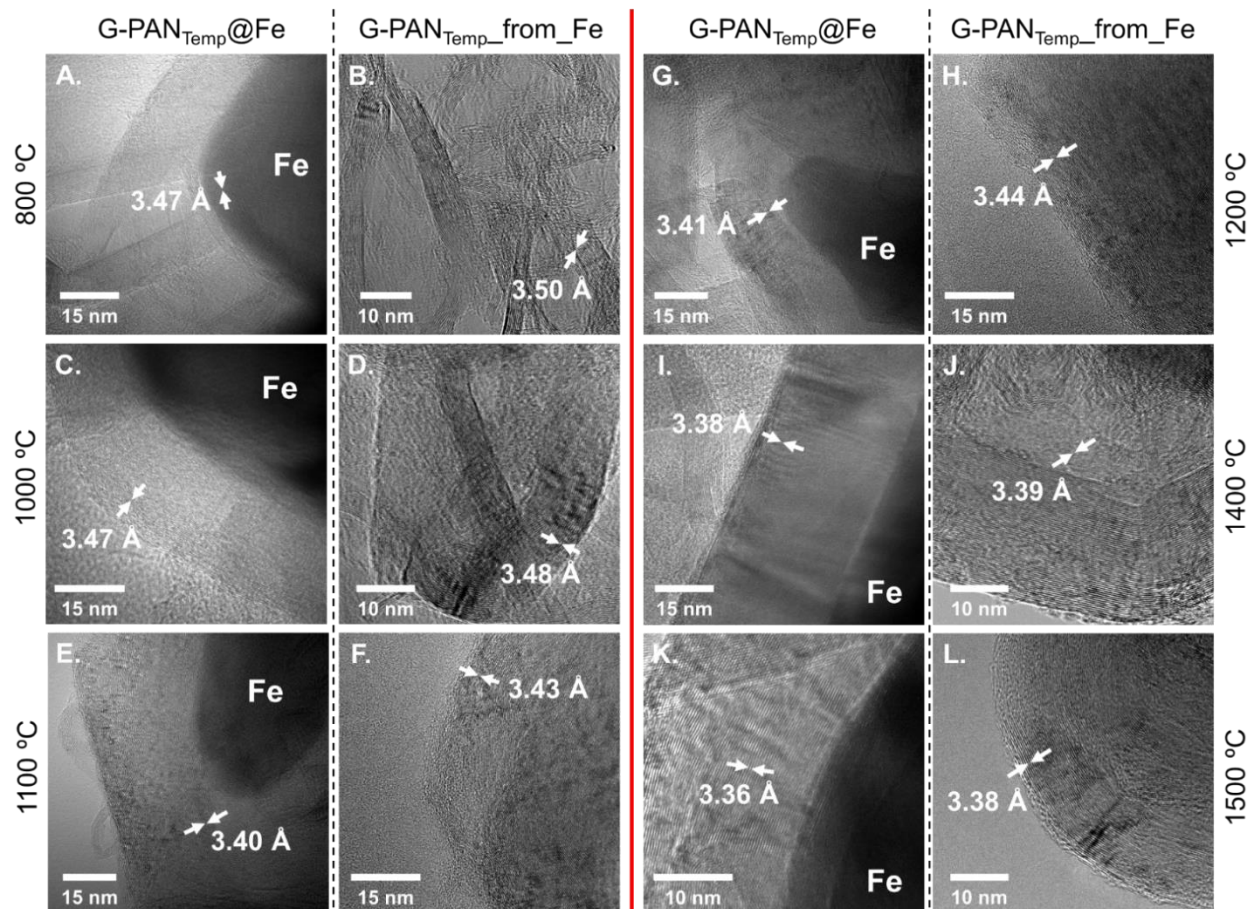
Figure S.41. Representative HR-TEM images of PAN@FeOx-derived graphitic carbon aerogels at different temperatures, before and after aqua-regia treatment: (A) G-PAN$_{800}$@Fe; (B) G-PAN$_{800}$_*from*_Fe; (C) G-PAN$_{1000}$@Fe; (D) G-PAN$_{1000}$_*from*_Fe; (E) G-PAN$_{1100}$@Fe; (F) G-PAN$_{1100}$_*from*_Fe; (G) G-PAN$_{1200}$@Fe; (H) G-PAN$_{1200}$_*from*_Fe; (I) G-PAN$_{1400}$@Fe; (J) G-PAN$_{1400}$_*from*_Fe; (K) G-PAN$_{1500}$@Fe; (L) G-PAN$_{1500}$_*from*_Fe. (The frames also include interlayer spacing data, which are tabulated and compared with data from XRD in Table S.7 of Appendix VII.)
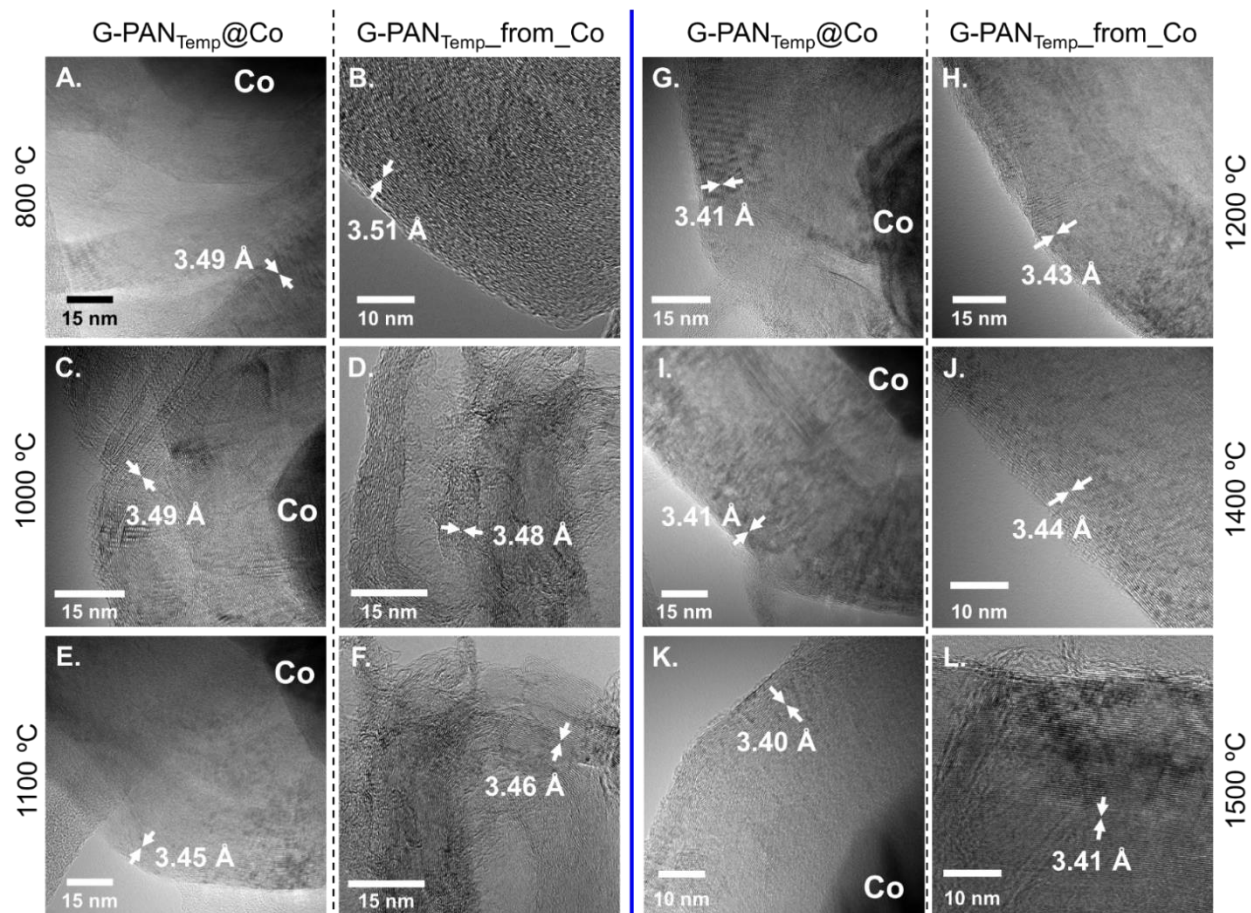
Figure S.42. Representative HR-TEM images of PAN@CoOx-derived graphitic carbon aerogels at different temperatures, before and after aqua-regia treatment: (A) G-PAN$_{800}$@Co; (B) G-PAN$_{800}$_*from*_Co; (C) G-PAN$_{1000}$@Co; (D) G-PAN$_{1000}$_*from*_Co; (E) G-PAN$_{1100}$@Co; (F) G-PAN$_{1100}$_*from*_Co; (G) G-PAN$_{1200}$@Co; (H) G-PAN$_{1200}$_*from*_Co; (I) G-PAN$_{1400}$@Co; (J) G-PAN$_{1400}$_*from*_Co; (K) G-PAN$_{1500}$@Co; (L) G-PAN$_{1500}$_*from*_Co. (The frames also include interlayer spacing data, which are tabulated and compared with data from XRD in Table S.7 of Appendix VII.)

Figure S.43. Representative TEM-EDX analysis at low-magnification of: (A) G-PAN$_{1500}$_*from*_Fe; and (B) G-PAN$_{1500}$_*from*_Co. (Cu from the TEM grid.)

Figure S.44. Representative electron diffraction patterns of: (A) G-PAN$_{1500}$_*from*_Fe; and (B) G-PAN$_{1500}$_*from*_Co.
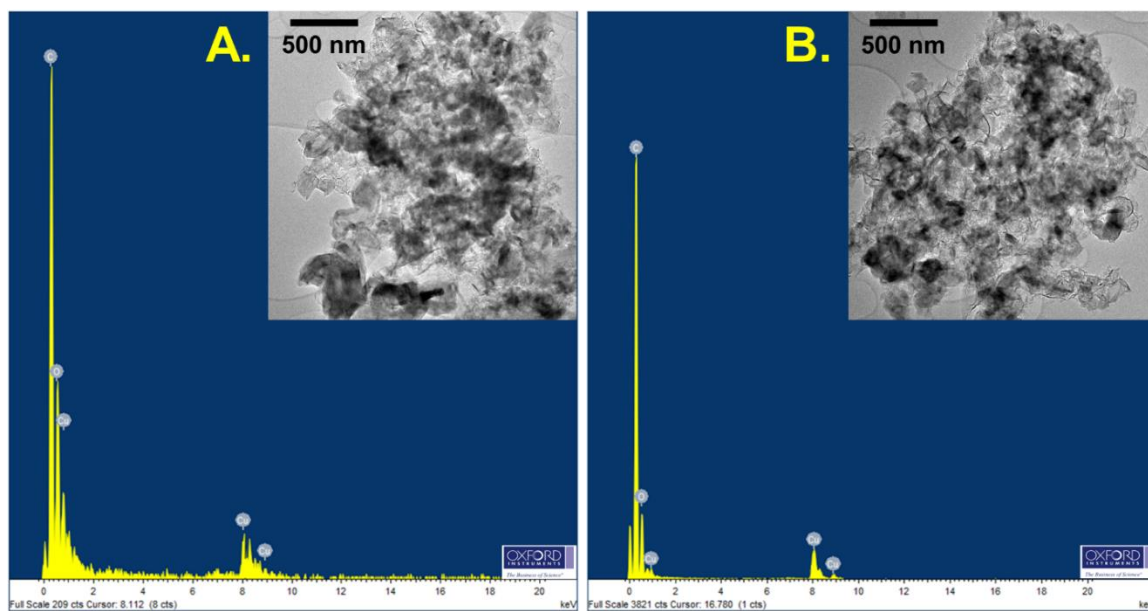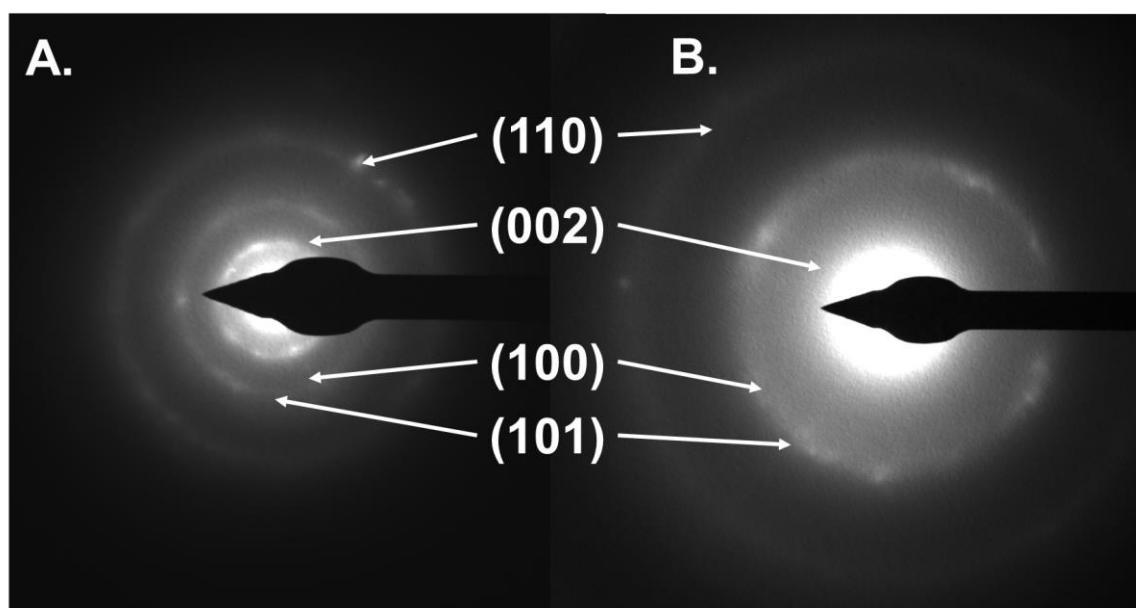
SUPPORTING REFERENCES

S.R.1   ASTM D1621-04a, Standard Test Method for Compressive Properties Of Rigid Cellular Plastics http://www.astm.org/cgi-bin/resolver.cgi?D1621 (Accessed 10-04-2021).

S.R.2   Yu, W.; Li, Y.; Zheng, Y. P.; Lim, N. Y.; Lu, M. H.; Fan, J. Softness Measurements for Open-Cell Foam Materials and Human Soft Tissue. *Meas. Sci. Technol.* **2006**, *17* (7), 1785–1791. https://doi.org/10.1088/0957-0233/17/7/017.

REFERENCES

(1)   Liang, C.; Chen, Y.; Wu, M.; Wang, K.; Zhang, W.; Gan, Y.; Huang, H.; Chen, J.; Xia, Y.; Zhang, J.; Zheng, S.; Pan, H. Green Synthesis of Graphite from CO_2 without Graphitization Process of Amorphous Carbon. *Nat. Commun.* **2021**, *12* (1), 1–9. https://doi.org/10.1038/s41467-020-20380-0.

(2)   Xiao, J.; Pan, X.; Guo, S.; Ren, P.; Bao, X. Toward Fundamentals of Confined Catalysis in Carbon Nanotubes. *J. Am. Chem. Soc.* **2015**, *137* (1), 477–482. https://doi.org/10.1021/ja511498s.

(3)   Yadavalli, T.; Ames, J.; Agelidis, A.; Suryawanshi, R.; Jaishankar, D.; Hopkins, J.; Thakkar, N.; Koujah, L.; Shukla, D. Drug-Encapsulated Carbon (DECON): A Novel Platform for Enhanced Drug Delivery. *Sci. Adv.* **2019**, *5* (8), 1–13. https://doi.org/10.1126/sciadv.aax0780.

(4)   Su, Y.-S.; Manthiram, A. A New Approach to Improve Cycle Performance of Rechargeable Lithium–Sulfur Batteries by Inserting a Free-Standing MWCNT Interlayer. *Chem. Commun.* **2012**, *48* (70), 8817–8819. https://doi.org/10.1039/C2CC33945E.

(5)   Zhang, S. S.; Xu, K.; Jow, T. R. Low Temperature Performance of Graphite Electrode in Li-Ion Cells. *Electrochim. Acta* **2002**, *48* (3), 241–246. https://doi.org/https://doi.org/10.1016/S0013-4686(02)00620-5.

(6)   Hsia, B.; Kim, M. S.; Luna, L. E.; Mair, N. R.; Kim, Y.; Carraro, C.; Maboudian, R. Templated 3D Ultrathin CVD Graphite Networks with Controllable Geometry: Synthesis and Application As Supercapacitor Electrodes. *ACS Appl. Mater. Interfaces* **2014**, *6* (21), 18413–18417. https://doi.org/10.1021/am504695t.

(7)   Iturrondobeitia, A.; Aguesse, F.; Genies, S.; Waldmann, T.; Kasper, M.; Ghanbari, N.; Wohlfahrt-Mehrens, M.; Bekaert, E. Post-Mortem Analysis of Calendar-Aged 16 Ah NMC/Graphite Pouch Cells for EV Application. *J. Phys. Chem. C* **2017**, *121* (40), 21865–21876. https://doi.org/10.1021/acs.jpcc.7b05416.

(8)   Bernat-Quesada, F.; Espinosa, J. C.; Barbera, V.; Álvaro, M.; Galimberti, M.; Navalón, S.; García, H. Catalytic Ozonation Using Edge-Hydroxylated Graphite-Based Materials. *ACS Sustain. Chem. Eng.* **2019**, *7* (20), 17443–17452. https://doi.org/10.1021/acssuschemeng.9b04646.

(9)   Saeed, A. M.; Wisner, C. A.; Donthula, S.; Majedi Far, H.; Sotiriou-Leventis, C.; Leventis, N. Reuseable Monolithic Nanoporous Graphite-Supported Nanocatalysts (Fe, Au, Pt, Pd, Ni, and Rh) from Pyrolysis and Galvanic Transmetalation of Ferrocene-Based Polyamide Aerogels. *Chem. Mater.* **2016**, *28* (13), 4867–4877. https://doi.org/10.1021/acs.chemmater.6b02364.

(10)   Li, J.; Li, J.; Luo, J. Superlubricity of Graphite Sliding against Graphene Nanoflake under Ultrahigh Contact Pressure. *Adv. Sci.* **2018**, *5* (11), 1800810. https://doi.org/https://doi.org/10.1002/advs.201800810.

(11)   Li, R.; Yang, X.; Wang, Y.; Zhang, J.; Li, J. Graphitic Encapsulation and Electronic Shielding of Metal Nanoparticles to Achieve Metal-Carbon Interfacial Superlubricity. *ACS Appl. Mater. Interfaces* **2021**, *13* (2), 3397–3407. https://doi.org/10.1021/acsami.0c18900.

(12)   Gao, W.; Majumder, M.; Alemany, L. B.; Narayanan, T. N.; Ibarra, M. A.; Pradhan, B. K.; Ajayan, P. M. Engineered Graphite Oxide Materials for Application in Water Purification. *ACS Appl. Mater. Interfaces* **2011**, *3* (6), 1821–1826. https://doi.org/10.1021/am200300u.

(13)   Gallego, N. C.; Klett, J. W. Carbon Foams for Thermal Management. *Carbon N. Y.* **2003**, *41* (7), 1461–1466. https://doi.org/https://doi.org/10.1016/S0008-6223(03)00091-5.

(14)   Chang, J.; Zhang, Q.; Lin, Y.; Zhou, C.; Yang, W.; Yan, L.; Wu, G. Carbon Nanotubes Grown on Graphite Films as Effective Interface Enhancement for an Aluminum Matrix Laminated Composite in Thermal Management Applications. *ACS Appl. Mater. Interfaces* **2018**, *10* (44), 38350–38358. https://doi.org/10.1021/acsami.8b12691.

(15)   Wu, Z.; Li, W.; Xia, Y.; Webley, P.; Zhao, D. Ordered Mesoporous Graphitized Pyrolytic Carbon Materials: Synthesis, Graphitization, and Electrochemical Properties. *J. Mater. Chem.* **2012**, *22* (18), 8835–8845. https://doi.org/10.1039/C2JM30192J.

(16)   Vázquez-Santos, M. B.; Geissler, E.; László, K.; Rouzaud, J.-N.; Martínez-Alonso, A.; Tascón, J. M. D. Graphitization of Highly Porous Carbons Derived from Poly(*p*-Phenylene Benzobisoxazole). *Carbon N. Y.* **2012**, *50* (8), 2929–2940. https://doi.org/https://doi.org/10.1016/j.carbon.2012.02.062.

(17) Patel, M. N.; Wang, X.; Slanac, D. A.; Ferrer, D. A.; Dai, S.; Johnston, K. P.; Stevenson, K. J. High Pseudocapacitance of MnO_2 Nanoparticles in Graphitic Disordered Mesoporous Carbon at High Scan Rates. *J. Mater. Chem.* **2012**, *22* (7), 3160–3169. https://doi.org/10.1039/C1JM14513D.

(18) Yoon, S. B.; Chai, G. S.; Kang, S. K.; Yu, J.-S.; Gierszal, K. P.; Jaroniec, M. Graphitized Pitch-Based Carbons with Ordered Nanopores Synthesized by Using Colloidal Crystals as Templates. *J. Am. Chem. Soc.* **2005**, *127* (12), 4188–4189. https://doi.org/10.1021/ja0423466.

(19) Su, P.; Jiang, L.; Zhao, J.; Yan, J.; Li, C.; Yang, Q. Mesoporous Graphitic Carbon Nanodisks Fabricated via Catalytic Carbonization of Coordination Polymers. *Chem. Commun.* **2012**, *48* (70), 8769–8771. https://doi.org/10.1039/C2CC34234K.

(20) Huang, C.-H.; Zhang, Q.; Chou, T.-C.; Chen, C.-M.; Su, D. S.; Doong, R.-A. Three-Dimensional Hierarchically Ordered Porous Carbons with Partially Graphitic Nanostructures for Electrochemical Capacitive Energy Storage. *ChemSusChem* **2012**, *5* (3), 563–571. https://doi.org/https://doi.org/10.1002/cssc.201100618.

(21) He, X.; Zhou, L.; Nesterenko, E. P.; Nesterenko, P. N.; Paull, B.; Omamogho, J. O.; Glennon, J. D.; Luong, J. H. T. Porous Graphitized Carbon Monolith as an Electrode Material for Probing Direct Bioelectrochemistry and Selective Detection of Hydrogen Peroxide. *Anal. Chem.* **2012**, *84* (5), 2351–2357. https://doi.org/10.1021/ac203061m.

(22) Wang, Y.; Li, B.; Zhang, C.; Song, X.; Tao, H.; Kang, S.; Li, X. A Simple Solid–Liquid Grinding/Templating Route for the Synthesis of Magnetic Iron/Graphitic Mesoporous Carbon Composites. *Carbon N. Y.* **2013**, *51*, 397–403. https://doi.org/https://doi.org/10.1016/j.carbon.2012.08.073.

(23) Yuan, D.; Yuan, X.; Zou, W.; Zeng, F.; Huang, X.; Zhou, S. Synthesis of Graphitic Mesoporous Carbon from Sucrose as a Catalyst Support for Ethanol Electro-Oxidation. *J. Mater. Chem.* **2012**, *22* (34), 17820–17826. https://doi.org/10.1039/C2JM33658H.

(24) Wickramaratne, N. P.; Perera, V. S.; Park, B.-W.; Gao, M.; McGimpsey, G. W.; Huang, S. D.; Jaroniec, M. Graphitic Mesoporous Carbons with Embedded Prussian Blue-Derived Iron Oxide Nanoparticles Synthesized by Soft Templating and Low-Temperature Graphitization. *Chem. Mater.* **2013**, *25* (14), 2803–2811. https://doi.org/10.1021/cm401124d.

(25) Chuenchom, L.; Kraehnert, R.; Smarsly, B. M. Recent Progress in Soft-Templating of Porous Carbon Materials. *Soft Matter* **2012**, *8* (42), 10801–10812. https://doi.org/10.1039/C2SM07448F.

(26) Oya, A.; Yamashita, R.; Otani, S. Catalytic Graphitization of Carbons by Borons. *Fuel* **1979**, *58* (7), 495–500. https://doi.org/10.1016/0016-2361(79)90167-4.

(27) Chen, Z.; Weng, D.; Sohn, H.; Cai, M.; Lu, Y. High-Performance Aqueous Supercapacitors Based on Hierarchically Porous Graphitized Carbon. *RSC Adv.* **2012**, *2* (5), 1755–1758. https://doi.org/10.1039/C2RA00887D.

(28) Lu, A.-H.; Li, W.-C.; Salabas, E.-L.; Spliethoff, B.; Schüth, F. Low Temperature Catalytic Pyrolysis for the Synthesis of High Surface Area, Nanostructured Graphitic Carbon. *Chem. Mater.* **2006**, *18* (8), 2086–2094. https://doi.org/10.1021/cm060135p.

(29) Majedi Far, H.; Rewatkar, P. M.; Donthula, S.; Taghvaee, T.; Saeed, A. M.; Sotiriou-Leventis, C.; Leventis, N. Exceptionally High CO_2 Adsorption at 273 K by Microporous Carbons from Phenolic Aerogels: The Role of Heteroatoms in Comparison with Carbons from Polybenzoxazine and Other Organic Aerogels. *Macromol. Chem. Phys.* **2019**, *220* (1), 1–16. https://doi.org/10.1002/macp.201800333.

(30) Pekala, R. W.; Mayer, S. T.; Kaschmitter, J. L.; Kong, F. M. Carbon Aerogels: An Update on Structure, Properties, and Applications BT - Sol-Gel Processing and Applications; Attia, Y. A., Ed.; Springer US: Boston, MA, 1994; pp 369–377. https://doi.org/10.1007/978-1-4615-2570-7_32.

(31) Pekala, R. W.; Farmer, J. C.; Alviso, C. T.; Tran, T. D.; Mayer, S. T.; Miller, J. M.; Dunn, B. Carbon Aerogels for Electrochemical Applications. *J. Non. Cryst. Solids* **1998**, *225*, 74–80. https://doi.org/https://doi.org/10.1016/S0022-3093(98)00011-8.

(32) Sadekar, A. G.; Mahadik, S. S.; Bang, A. N.; Larimore, Z. J.; Wisner, C. A.; Bertino, M. F.; Kalkan, A. K.; Mang, J. T.; Sotiriou-Leventis, C.; Leventis, N. From "Green" Aerogels to Porous Graphite by Emulsion Gelation of Acrylonitrile. *Chem. Mater.* **2012**, *24* (1), 26–47. https://doi.org/10.1021/cm202975p.

(33) Rewatkar, P. M.; Taghvaee, T.; Saeed, A. M.; Donthula, S.; Mandal, C.; Chandrasekaran, N.; Leventis, T.; Shruthi, T. K.; Sotiriou-Leventis, C.; Leventis, N. Sturdy, Monolithic SiC and Si_3N_4 Aerogels from Compressed Polymer-Cross-Linked Silica Xerogel Powders. *Chem. Mater.* **2018**, *30* (5), 1635–1647. https://doi.org/10.1021/acs.chemmater.7b04981.

(34) Rewatkar, P. M.; Soni, R. U.; Sotiriou-Leventis, C.; Leventis, N. A Cobalt Sunrise: Thermites Based on $LiClO_4$-Filled Co(0) Aerogels Prepared from Polymer-Cross-Linked Cobaltia Xerogel Powders. *ACS Applied Materials and Interfaces*. 2019. https://doi.org/10.1021/acsami.9b04734.

(35) Soni, R. U.; Edlabadkar, V. A.; Greenan, D.; Rewatkar, P. M.; Leventis, N.; Sotiriou-Leventis, C. Preparation of Carbon Aerogels from Polymer-Crosslinked Xerogel Powders without Supercritical Fluid Drying and Their Application in Highly-Selective CO_2 Adsorption. *Chem. Mater.* **2021**, *xx* (xx), xx.

(36) L'vov, B. V. Mechanism of Carbothermal Reduction of Iron, Cobalt, Nickel and Copper Oxides. *Thermochim. Acta* **2000**, *360* (2), 109–120. https://doi.org/https://doi.org/10.1016/S0040-6031(00)00540-2.

(37) Anderson, R. N.; Parlee, N. A. D. Carbothermic Reduction of Refractory Metals. *J. Vac. Sci. Technol.* **1976**, *13* (1), 526–529. https://doi.org/10.1116/1.568917.

(38) Gash, A. E.; Tillotson, T. M.; Satcher, J. H.; Poco, J. F.; Hrubesh, L. W.; Simpson, R. L. Use of Epoxides in the Sol-Gel Synthesis of Porous Iron(III) Oxide Monoliths from Fe(III) Salts. *Chem. Mater.* **2001**, *13* (3), 999–1007. https://doi.org/10.1021/cm0007611.

(39) Leventis, N.; Donthula, S.; Mandal, C.; Ding, M. S.; Sotiriou-Leventis, C. Explosive versus Thermite Behavior in Iron(0) Aerogels Infiltrated with Perchlorates. *Chem. Mater.* **2015**, *27* (23), 8126–8137. https://doi.org/10.1021/acs.chemmater.5b03898.

(40) Mahadik-Khanolkar, S.; Donthula, S.; Bang, A.; Wisner, C.; Sotiriou-Leventis, C.; Leventis, N. Polybenzoxazine Aerogels. 2. Interpenetrating Networks with Iron Oxide and the Carbothermal Synthesis of Highly Porous Monolithic Pure Iron(0) Aerogels as Energetic Materials. *Chem. Mater.* **2014**, *26* (3), 1318–1331. https://doi.org/10.1021/cm403484e.

(41) Leventis, N.; Chandrasekaran, N.; Sotiriou-Leventis, C.; Mumtaz, A. Smelting in the Age of Nano: Iron Aerogels. *J. Mater. Chem.* **2009**, *19* (1), 63–65. https://doi.org/10.1039/B815985H.

(42) Mulik, S.; Sotiriou-Leventis, C.; Churu, G.; Lu, H.; Leventis, N. Cross-Linking 3D Assemblies of Nanoparticles into Mechanically Strong Aerogels by Surface-Initiated Free-Radical Polymerization. *Chem. Mater.* **2008**, *20* (15), 5035–5046. https://doi.org/10.1021/cm800963h.

(43) Usami, T.; Itoh, T.; Ohtani, H.; Tsuge, S. Structural Study of Polyacrylonitrile Fibers during Oxidative Thermal Degradation by Pyrolysis-Gas Chromatography, Solid-State Carbon-13 NMR, and Fourier-Transform Infrared Spectroscopy. *Macromolecules* **1990**, *23* (9), 2460–2465. https://doi.org/10.1021/ma00211a009.

(44) McKenzie, D. R.; Muller, D.; Pailthorpe, B. A. Compressive-Stress-Induced Formation of Thin-Film Tetrahedral Amorphous Carbon. *Phys. Rev. Lett.* **1991**, *67* (6), 773–776. https://doi.org/10.1103/PhysRevLett.67.773.

(45) Salamone, J. C. *Concise Polymeric Materials Encyclopedia*; CRC Press: Boca Raton, FL, U.S.A, **1999**, pp 570.

(46) Pierson, H. O. *Handbook of Carbon, Graphite, Diamond and Fullerenes*; Noyes Publications: Park Ridge, NJ, U.S.A., **1993**, pp 131.

(47) Onodera, A.; Irie, Y.; Higashi, K.; Umemura, J.; Takenaka, T. Graphitization of Amorphous Carbon at High Pressures to 15 GPa. *J. Appl. Phys.* **1991**, *69* (4), 2611–2617. https://doi.org/10.1063/1.348652.

(48) Samoilov, V. M.; Verbets, D. B.; Bubnenkov, I. A.; Steparyova, N. N.; Nikolaeva, A. V; Danilov, E. A.; Ponomareva, D. V; Timoshchuk, E. I. Influence of Graphitization Conditions at 3000°C on Structural and Mechanical Properties of High-Modulus Polyacrylonitrile-Based Carbon Fibers. *Inorg. Mater. Appl. Res.* **2018**, *9* (5), 890–899. https://doi.org/10.1134/S2075113318050258.

(49) Labani, M. M.; Rezaee, R.; Saeedi, A.; Hinai, A. Al. Evaluation of Pore Size Spectrum of Gas Shale Reservoirs Using Low Pressure Nitrogen Adsorption, Gas Expansion and Mercury Porosimetry: A Case Study from the Perth and Canning Basins, Western Australia. *J. Pet. Sci. Eng.* **2013**, *112*, 7–16. https://doi.org/https://doi.org/10.1016/j.petrol.2013.11.022.

(50) Rastegar, H.; Bavand-vandchali, M.; Nemati, A.; Golestani-Fard, F. Catalytic Graphitization Behavior of Phenolic Resins by Addition of in Situ Formed Nano-Fe Particles. *Phys. E Low-dimensional Syst. Nanostructures* **2018**, *101*, 50–61. https://doi.org/https://doi.org/10.1016/j.physe.2018.03.013.

(51) Goldie, S. J.; Jiang, S.; Coleman, K. S. Cobalt Nanoparticle Catalysed Graphitization and the Effect of Metal Precursor Decomposition Temperature. *Mater. Adv.* **2021**, *2* (10), 3353–3361. https://doi.org/10.1039/D1MA00125F.

(52) Thambiliyagodage, C. J.; Ulrich, S.; Araujo, P. T.; Bakker, M. G. Catalytic Graphitization in Nanocast Carbon Monoliths by Iron, Cobalt and Nickel Nanoparticles. *Carbon N. Y.* **2018**, *134*, 452–463. https://doi.org/https://doi.org/10.1016/j.carbon.2018.04.002.

(53) Morgan, P. *Carbon Fibers and Their Composites*, 1st ed.; CRC Press: Boca Raton, FL, U.S.A, 2005. https://doi.org/https://doi.org/10.1201/9781420028744.

(54) Kern, A.; Madsen, I. C.; Scarlett, N. V. Y. Uniting Electron Crystallography and Powder Diffraction. In *Quantifying amorphous phases*; Kolb, U., Shankland, K., Meshi, L., Avilov, A., David, W., Eds.; **2012**; pp 434–445.

(55) Kern, A.; Madsen, I. C.; Scarlett, N. V. Y. Quantifying Amorphous Phases https://www.icdd.com/assets/ppxrd/presentations/12/P30-Arnt-Kern-ppxrd-12.pdf (Accessed Apr 10, 2021).

(56) Madsen, I. C.; Scarlett, N. V. Y.; Kern, A. Description and Survey of Methodologies for the Determination of Amorphous Content via X-Ray Powder Diffraction. *Zeitschrift für Krist.* **2011**, *226* (12), 944–955. https://doi.org/doi:10.1524/zkri.2011.1437.

(57) Jensen, H.; Pedersen, J. H.; Jorgensen, J. E.; Pedersen, J. S.; Joensen, K. D.; Iversen, S. B.; Sogaard, E. G. Determination of Size Distributions in Nanosized Powders by TEM, XRD, and SAXS. *J. Exp. Nanosci.* **2006**, *1* (3), 355–373. https://doi.org/10.1080/17458080600752482.

(58) Blyth, R. I. R.; Buqa, H.; Netzer, F. P.; Ramsey, M. G.; Besenhard, J. O.; Golob, P.; Winter, M. XPS Studies of Graphite Electrode Materials for Lithium Ion Batteries. *Appl. Surf. Sci.* **2000**, *167* (1), 99–106. https://doi.org/10.1016/S0169-4332(00)00525-0.

(59) Mezzi, A.; Kaciulis, S. Surface Investigation of Carbon Films: From Diamond to Graphite. *Surf. Interface Anal.* **2010**, *42* (6–7), 1082–1084. https://doi.org/10.1002/sia.3348.

(60) Figueiredo, J. L.; Pereira, M. F. R. The Role of Surface Chemistry in Catalysis with Carbons. *Catal. Today* **2010**, *150* (1–2), 2–7. https://doi.org/10.1016/j.cattod.2009.04.010.

(61) Figueiredo, J. L.; Pereira, M. F. R.; Freitas, M. M. A.; Órfão, J. J. M. Modification of the Surface Chemistry of Activated Carbons. *Carbon N. Y.* **1999**, *37* (9), 1379–1389. https://doi.org/10.1016/S0008-6223(98)00333-9.

(62) Li, P.; Jiang, E. Y.; Bai, H. L. Fabrication of Ultrathin Epitaxial γ-Fe_2O_3 Films by Reactive Sputtering. *J. Phys. D: Appl. Phys.* **2011**, *44*, 75003–75007. https://doi.org/10.1088/0022-3727/44/7/075003.

(63) Biesinger, M. C.; Payne, B. P.; Grosvenor, A. P.; Lau, L. W. M.; Gerson, A. R.; Smart, R. S. C. Resolving Surface Chemical States in XPS Analysis of First Row Transition Metals, Oxides and Hydroxides: Cr, Mn, Fe, Co and Ni. *Appl. Surf. Sci.* **2011**, *257* (7), 2717–2730. https://doi.org/10.1016/j.apsusc.2010.10.051.

(64) Xie, S.; Liu, Y.; Deng, J.; Yang, J.; Zhao, X.; Han, Z.; Zhang, K.; Dai, H. Insights into the Active Sites of Ordered Mesoporous Cobalt Oxide Catalysts for the Total Oxidation of O-Xylene. *J. Catal.* **2017**, *352*, 282–292. https://doi.org/https://doi.org/10.1016/j.jcat.2017.05.016.

(65) Lan, Y.; Zondode, M.; Deng, H.; Yan, J.-A.; Ndaw, M.; Lisfi, A.; Wang, C.; Pan, Y.-L. Basic Concepts and Recent Advances of Crystallographic Orientation Determination of Graphene by Raman Spectroscopy. *Crystals* **2018**, *8* (10), 375–402. https://doi.org/10.3390/cryst8100375.

(66) Liu, Y.; Liu, Z.; Lew, W. S.; Wang, Q. J. Temperature Dependence of the Electrical Transport Properties in Few-Layer Graphene Interconnects. *Nanoscale Res. Lett.* **2013**, *8* (1), 335–341. https://doi.org/10.1186/1556-276X-8-335.

(67) [a] Mochida, I.; Yoon, S.-H.; Qiao, W. Catalysts in Syntheses of Carbon and Carbon Precursors. *J. Braz. Chem. Soc.* **2006**, *17* (6), 1059–1073. https://doi.org/https://doi.org/10.1590/S0103-50532006000600002. [b] Oberlin, A. Carbonization and Graphitization. *Carbon* **1984**, *22* (6), 521–541. https://doi.org/https://doi.org/10.1016/0008-6223(84)90086-1. [c] Rouzaud, J. N.; Oberlin, A. Structure, Microtexture, and Optical Properties of Anthracene and Saccharose-Based Carbons. *Carbon* **1989**, *27* (4), 517–529. https://doi.org/10.1016/0008-6223(89)90002-X. [d] Goma, J.; Oberlin, M. Graphitization of Thin Carbon Films. *Thin Solid Films* **1980**, *65* (2), 221–232. https://doi.org/https://doi.org/10.1016/0040-6090(80)90256-4.

(68) Xie, J.; Lu, Y.-C. A Retrospective on Lithium-Ion Batteries. *Nat. Commun.* **2020**, *11* (1), 2499–2502. https://doi.org/10.1038/s41467-020-16259-9.

(69) Asenbauer, J.; Eisenmann, T.; Kuenzel, M.; Kazzazi, A.; Chen, Z.; Bresser, D. The Success Story of Graphite as a Lithium-Ion Anode Material – Fundamentals, Remaining Challenges, and Recent Developments Including Silicon (Oxide) Composites. *Sustain. Energy Fuels* **2020**, *4* (11), 5387–5416. https://doi.org/10.1039/D0SE00175A.

(70) Cheng, Q.; Okamoto, Y.; Tamura, N.; Tsuji, M.; Maruyama, S.; Matsuo, Y. Graphene-Like-Graphite as Fast-Chargeable and High-Capacity Anode Materials for Lithium Ion Batteries. *Sci. Rep.* **2017**, *7* (1), 14782-14795. https://doi.org/10.1038/s41598-017-14504-8.

(71) An, S. J.; Li, J.; Daniel, C.; Mohanty, D.; Nagpure, S.; Wood, D. L. The State of Understanding of the Lithium-Ion-Battery Graphite Solid Electrolyte Interphase (SEI) and Its Relationship to Formation Cycling. *Carbon N. Y.* **2016**, *105*, 52–76. https://doi.org/https://doi.org/10.1016/j.carbon.2016.04.008.

(72) Levi, M. D.; Aurbach, D. The Mechanism of Lithium Intercalation in Graphite Film Electrodes in Aprotic Media. Part 1. High Resolution Slow Scan Rate Cyclic Voltammetric Studies and Modeling. *J. Electroanal. Chem.* **1997**, *421* (1), 79–88. https://doi.org/https://doi.org/10.1016/S0022-0728(96)04832-2.

(73) Zhang, S.; Ding, M. S.; Xu, K.; Allen, J.; Jow, T. R. Understanding Solid Electrolyte Interface Film Formation on Graphite Electrodes. *Electrochem. Solid-State Lett.* **2001**, *4* (12), A206–A208. https://doi.org/10.1149/1.1414946.

(74) Ding, F.; Xu, W.; Choi, D.; Wang, W.; Li, X.; Engelhard, M. H.; Chen, X.; Yang, Z.; Zhang, J.-G. Enhanced Performance of Graphite Anode Materials by AlF_3 Coating for Lithium-Ion Batteries. *J. Mater. Chem.* **2012**, *22* (25), 12745–12751. https://doi.org/10.1039/C2JM31015E.

(75) Hu, Y.-S.; Adelhelm, P.; Smarsly, B. M.; Hore, S.; Antonietti, M.; Maier, J. Synthesis of Hierarchically Porous Carbon Monoliths with Highly Ordered Microstructure and Their Application in Rechargeable Lithium Batteries with High-Rate Capability. *Adv. Funct. Mater.* **2007**, *17* (12), 1873–1878. https://doi.org/https://doi.org/10.1002/adfm.200601152.

(76) Franco Gonzalez, A.; Yang, N.-H.; Liu, R.-S. Silicon Anode Design for Lithium-Ion Batteries: Progress and Perspectives. *J. Phys. Chem. C* **2017**, *121* (50), 27775–27787. https://doi.org/10.1021/acs.jpcc.7b07793.

(77) Leventis, N.; Vassilaras, P.; Fabrizio, E. F.; Dass, A. Polymer Nanoencapsulated Rare Earth Aerogels: Chemically Complex but Stoichiometrically Similar Core–Shell Superstructures with Skeletal Properties of Pure Compounds. *J. Mater. Chem.* **2007**, *17* (15), 1502–1508. https://doi.org/10.1039/B612625A.

SECTION

2. CONCLUSION

Novel synthetic methods for different porous materials were reported along with their applications. These aerogel materials where not synthesized via traditional supercritical fluid drying methods, instead a xerogel processing route was explored and further developed. This method of making *aerogels-via-xerogels* bypasses the most common and energy consuming step of supercritical fluid drying, thus making the overall process cost-efficient. Also, the processing via *xerogels* (both monolithic and powders) allows easy handling and faster solvent exchanges instead of handling extremely fragile, traditional wet-monolithic gels, which results in a time- and material-efficient process. Also, these xerogel powders can be easily molded into different sizes and shapes to obtain desired aerogels. Importantly, we showed that this process of making carbon aerogels-via-xerogel route can be extended and generalized for any sol-gel system.

In Paper-I, polymeric aerogels with foam-like porosity and structural characteristics of the corresponding aerogels were prepared using a pressurized sol-gel approach. These polyurethane aerogel foams were synthesized without any chemical foaming agents or templates, resulting in less expensive, more efficient, readily adaptable, and environmentally friendly process. Aerogel foams exhibited significantly lower bulk density (by 25%), higher porosity (by 10%), lower thermal conductivity (by 25%), and higher oil retention (by 36%) compared to their regular aerogel counterparts. As this technique does not alter the chemical composition of the resulting aerogel foams, it is anticipated that it can be used for a variety of different types of aerogels and formulations in order to lower

their bulk density and improve desired physical properties such as thermal conductivity for different targeted applications.

In Paper-II, synthesis of pure metallic cobalt aerogels is shown. Since the cobalt sol-gel system resists or takes long time to gel, was diverted to polyurea-crosslinked cobaltia to obtain Co(0) aerogels via carbothermal reduction. These pure metallic aerogels were around 70% v/v porous and further filled with $LiClO_4$ to make monolithic thermites. They were ignited using a hot nichrome wire at ~1100 °C. The highest temperatures reached was 1515 °C and the heat released was ~ -55 kcal mol^{-1}. It was found that the pore structure plays an important role in keeping the perchlorate intact within the Co(0) network during ignition. Co(0) made by pyrolysis at 800 °C had larger pores compared to the one made at 900 °C, due to sintering at higher temperatures. The advantage of nanostructured thermites based on Co(0) aerogels is the 100% efficiency by which the metal is consumed during its reaction with $LiClO_4$ filling the pores.

In Paper-III, the process of making *aerogels-via-xerogels* route was further generalized from Paper-II by extending the idea to synthesize amorphous carbon aerogels from two different precursors (polyurea- and polyacrylonitrile-crosslinked silica xerogel powders) following two different chemistries (polycondensation and free-radical surface-initiated polymerization) with similar processing conditions. Using silica as a removable template, we proposed an etching model to achieve desired BET surface area and control the micro- and meso-porosities in the final aerogels. These porous carbon aerogels were further analyzed for gas adsorption. We investigated CO_2 adsorption of these porous carbon aerogels and selectivity towards other gases (CH_4, H_2, and N_2). High CO_2 adsorption (up to 9.15 mmol g^{-1}) and excellent selectivities were attributed towards the microporosities in

the final porous carbon aerogels. Easy regeneration of these porous carbon aerogels can be achieved as the isosteric heat of adsorption is low (~32 kJ mol^{-1}) due to physical adsorption of CO_2 on the surface.

In Paper-IV, the process of making *aerogels-via-xerogels* route was further generalized from Paper-II and Paper-III by extending the idea, to have Fe- or Co-catalyzed synthesis of porous graphitic carbon aerogels. This process of synthesizing porous graphitic carbon aerogels bypasses the traditional supercritical fluid drying and the pyrolytic graphitization takes place at lower temperatures (800-1500 ℃) compared to conventional graphitization (>2400 ℃). Polyacrylonitrile-crosslinked metal oxide (FeOx or CoOx) xerogel powders were synthesized via free-radical surface-initiated polymerization of acrylonitrile. Pyrolysis of aromatized compacts of these xerogel powders reduced the metal oxides to pure metal (Fe(0) or Co(0)) in the presence of carbonizable carbon, and induced in-situ pyrolytic graphitization of the aromatized polyacrylonitrile. Final aerogels with high porosities (63-78% v/v) were obtained due to (a) the pyrolytic graphitization of polyacrylonitrile, and (b) the removal of the metal using aqua-regia etching. Excellent quality of graphitic carbon aerogels were obtained and analyzed with powder-XRD, Raman, TEM, SEM, N_2-sorption, and XPS. These graphitic carbon aerogels showed different nanomorphologies ranging from nanorods, nano-worms, nanofibers, and platelets (by SEM). These graphitic carbon aerogels were demonstrated as anodes for Li-ion batteries with good charge capacity (100 mAh g-1), low working voltage (0.3 V), and excellent coulombic efficiency.

APPENDIX

CCC
RightsLink®

Home | Help ∨ | Live Chat | Sign in | Create Account

Synthesis of aerogel foams through a pressurized sol-gel method

Author:
Sadeq Malakooti,Ethan Zhao,Nicholas Tsao,Ning Bian,Rushi U. Soni,ABM Shaheen ud Doulah,Chariklia Sotiriou-Leventis,Nicholas Leventis,Hongbing Lu

Publication: Polymer

Publisher: Elsevier

Date: 3 November 2020

© 2020 Published by Elsevier Ltd.

Journal Author Rights

Please note that, as the author of this Elsevier article, you retain the right to include it in a thesis or dissertation, provided it is not published commercially. Permission is not required, but please ensure that you reference the journal as the original source. For more information on this and on your other retained rights, please visit: https://www.elsevier.com/about/our-business/policies/copyright#Author-rights

BACK | CLOSE WINDOW

Copyrights for Paper-I

CCC
RightsLink®

Home   Help ∨   Live Chat   Sign in   Create Account

A Cobalt Sunrise: Thermites Based on LiClO4-Filled Co(0) Aerogels Prepared from Polymer-Cross-Linked Cobaltia Xerogel Powders

ACS Publications
Most Trusted. Most Cited. Most Read.

Author: Parwani M. Rewatkar, Rushi U. Soni, Chariklia Sotiriou-Leventis, et al

Publication: Applied Materials

Publisher: American Chemical Society

Date: Jun 1, 2019

Copyright © 2019, American Chemical Society

BACK

CLOSE WINDOW

Copyrights for Paper-II

BIBLIOGRAPHY

(1)   Rechberger, F.; Niederberger, M. Synthesis of Aerogels: From Molecular Routes to 3-Dimensional Nanoparticle Assembly. *Nanoscale Horiz.* **2017**, *2* (1), 6–30. https://doi.org/10.1039/C6NH00077K.

(2)   Gesser, H. D.; Goswami, P. C. Aerogels and Related Porous Materials. *Chem. Rev.* **1989**, *89* (4), 765–788. https://doi.org/10.1021/cr00094a003.

(3)   Fricke, J.; Emmerling, A. Aerogels—Recent Progress in Production Techniques and Novel Applications. *J. Sol-Gel Sci. Technol.* **1998**, *13* (1), 299–303. https://doi.org/10.1023/A:1008663908431.

(4)   Fricke, J.; Emmerling, A. Aerogels. *J. Am. Ceram. Soc.* **1992**, *75* (8), 2027–2035. https://doi.org/https://doi.org/10.1111/j.1151-2916.1992.tb04461.x.

(5)   Armori, J. N.; Carlson, E. J.; Carrasquillo, G. Metallic Aerogels: A Novel Synthesis of Very Fine Copper Powder. *Mater. Lett.* **1989**, *4*, 373–376.

(6)   Wei, G.; Liu, Y.; Zhang, X.; Yu, F.; Du, X. Thermal Conductivities Study on Silica Aerogel and Its Composite Insulation Materials. *Int. J. Heat Mass Transf.* **2011**, *54* (11), 2355–2366. https://doi.org/https://doi.org/10.1016/j.ijheatmasstransfer.2011.02.026.

(7)   Yoda, S.; Takeshita, S.; Ono, T.; Tada, R.; Ota, H. Development of a New Silica Aerogel-Polypropylene Foam Composite as a Highly Flexible Thermal Insulation Material. *Front. Mater.* **2021**, *8*, 178. https://doi.org/10.3389/fmats.2021.674846.

(8)   Detcheverry, F.; Kierlik, E.; Rosinberg, M. L.; Tarjus, G. Mechanisms for Gas Adsorption and Desorption in Silica Aerogels: The Effect of Temperature. *Langmuir* **2004**, *20* (19), 8006–8014. https://doi.org/10.1021/la0488506.

(9)   Majedi Far, H.; Rewatkar, P. M.; Donthula, S.; Taghvaee, T.; Saeed, A. M.; Sotiriou-Leventis, C.; Leventis, N. Exceptionally High CO_2 Adsorption at 273 K by Microporous Carbons from Phenolic Aerogels: The Role of Heteroatoms in Comparison with Carbons from Polybenzoxazine and Other Organic Aerogels. *Macromol. Chem. Phys.* **2019**, *220* (1), 1–16. https://doi.org/10.1002/macp.201800333.

(10)   Gu, H.; Zhou, X.; Lyu, S.; Pan, D.; Dong, M.; Wu, S.; Ding, T.; Wei, X.; Seok, I.; Wei, S.; Guo, Z. Magnetic Nanocellulose-Magnetite Aerogel for Easy Oil Adsorption. *J. Colloid Interface Sci.* **2020**, *560*, 849–856. https://doi.org/https://doi.org/10.1016/j.jcis.2019.10.084.

(11)   Zhang, X.; Wang, H.; Cai, Z.; Yan, N.; Liu, M.; Yu, Y. Highly Compressible and Hydrophobic Anisotropic Aerogels for Selective Oil/Organic Solvent Absorption. *ACS Sustain. Chem. Eng.* **2019**, *7* (1), 332–340. https://doi.org/10.1021/acssuschemeng.8b03554.

(12)   Diao, S.; Liu, H.; Chen, S.; Xu, W.; Yu, A. Oil Adsorption Performance of Graphene Aerogels. *J. Mater. Sci.* **2020**, *55* (11), 4578–4591. https://doi.org/10.1007/s10853-019-04292-z.

(13)   Alhwaige, A. A.; Ishida, H.; Qutubuddin, S. Carbon Aerogels with Excellent CO_2 Adsorption Capacity Synthesized from Clay-Reinforced Biobased Chitosan-Polybenzoxazine Nanocomposites. *ACS Sustain. Chem. Eng.* **2016**, *4* (3), 1286–1295. https://doi.org/10.1021/acssuschemeng.5b01323.

(14)   Salazar, J. M.; Hohn, K. L. Partial Oxidation of N-Butane over a Sol-Gel Prepared Vanadium Phosphorous Oxide. *Catalysts* **2013**, *3* (1), 11–26. https://doi.org/10.3390/catal3010011.

(15)   Sousa, J. P. S.; Pereira, M. F. R.; Figueiredo, J. L. Carbon Xerogel Catalyst for NO Oxidation. *Catalysts* **2012**, *2* (4), 447–465. https://doi.org/10.3390/catal2040447.

(16)   Domínguez, M.; Taboada, E.; Molins, E.; Llorca, J. Co-Fe-Si Aerogel Catalytic Honeycombs for Low Temperature Ethanol Steam Reforming. *Catalysts* **2012**, *2* (3), 386–399. https://doi.org/10.3390/catal2030386.

(17)   Mahadik-Khanolkar, S.; Donthula, S.; Bang, A.; Wisner, C.; Sotiriou-Leventis, C.; Leventis, N. Polybenzoxazine Aerogels. 2. Interpenetrating Networks with Iron Oxide and the Carbothermal Synthesis of Highly Porous Monolithic Pure Iron(0) Aerogels as Energetic Materials. *Chem. Mater.* **2014**, *26* (3), 1318–1331. https://doi.org/10.1021/cm403484e.

(18)   Leventis, N.; Donthula, S.; Mandal, C.; Ding, M. S.; Sotiriou-Leventis, C. Explosive versus Thermite Behavior in Iron(0) Aerogels Infiltrated with Perchlorates. *Chem. Mater.* **2015**, *27* (23), 8126–8137. https://doi.org/10.1021/acs.chemmater.5b03898.

(19)   Mao, J.; Iocozzia, J.; Huang, J.; Meng, K.; Lai, Y.; Lin, Z. Graphene Aerogels for Efficient Energy Storage and Conversion. *Energy Environ. Sci.* **2018**, *11* (4), 772–799. https://doi.org/10.1039/C7EE03031B.

(20)   Rewatkar, P. M.; Soni, R. U.; Sotiriou-Leventis, C.; Leventis, N. A Cobalt Sunrise: Thermites Based on $LiClO_4$-Filled Co(0) Aerogels Prepared from Polymer-Cross-Linked Cobaltia Xerogel Powders. *ACS Appl. Mater. Interfaces.* **2019**, *11* (25), 22668-22676. https://doi.org/10.1021/acsami.9b04734.

(21)   Rewatkar, P. M.; Taghvaee, T.; Saeed, A. M.; Donthula, S.; Mandal, C.; Chandrasekaran, N.; Leventis, T.; Shruthi, T. K.; Sotiriou-Leventis, C.; Leventis, N. Sturdy, Monolithic SiC and Si_3N_4 Aerogels from Compressed Polymer-Cross-Linked Silica Xerogel Powders. *Chem. Mater.* **2018**, *30* (5), 1635–1647. https://doi.org/10.1021/acs.chemmater.7b04981.

(22)   Leventis, N.; Sadekar, A.; Chandrasekaran, N.; Sotiriou-Leventis, C. Click Synthesis of Monolithic Silicon Carbide Aerogels from Polyacrylonitrile-Coated 3D Silica Networks. *Chem. Mater.* **2010**, *22* (9), 2790–2803. https://doi.org/10.1021/cm903662a.

(23) Cheng, F.; Kelly, S. M.; Lefebvre, F.; Clark, S.; Supplit, R.; Bradley, J. S. Preparation of a Mesoporous Silicon Aluminium Nitride via a Non-Aqueous Sol–Gel Route. *J. Mater. Chem.* **2005**, *15* (7), 772–777. https://doi.org/10.1039/B414627A.

(24) Dardel, G.; Hennings, S. A.; Svensson, L. C. Silica Aerogel. U.S. Patent No. 4,402,927, 1981.

(25) Lagamba, L.; others. Silica Aerogel Threshold Cherenkov Counters for the JLab Hall A Spectrometers: Improvements and Proposed Modifications. *Nucl. Instrum. Meth. A* **2001**, *471*, 325–332. https://doi.org/10.1016/S0168-9002(01)00808-7.

(26) Cantin, M.; Casse, M.; Koch, L.; Jouan, R.; Mestreau, P.; Roussel, D.; Saclay, C.; Bonnin, F.; Moutel, J.; Teichner, S. J. Silica Aerogels Used as Cherenkov Radiators. *Nucl. Instrum. Meth.* **1974**, *118*, 177–182. https://doi.org/10.1016/0029-554X(74)90700-9.

(27) Jung, S. M.; Kim, D. W.; Jung, H. Y. Which Is the Most Effective Pristine Graphene Electrode for Energy Storage Devices: Aerogel or Xerogel? *Nanoscale* **2019**, *11* (38), 17563–17570. https://doi.org/10.1039/c9nr06898h.

(28) Chen, Z.; Li, H.; Tian, R.; Duan, H.; Guo, Y.; Chen, Y.; Zhou, J.; Zhang, C.; DUGNANI, R.; Liu, H. Three Dimensional Graphene Aerogels as Binder-Less, Freestanding, Elastic and High-Performance Electrodes for Lithium-Ion Batteries. *Sci. Rep.* **2016**, *6* (1), 27365. https://doi.org/10.1038/srep27365.

(29) Phadatare, M.; Patil, R.; Blomquist, N.; Forsberg, S.; Örtegren, J.; Hummelgård, M.; Meshram, J.; Hernández, G.; Brandell, D.; Leifer, K.; Sathyanath, S. K. M.; Olin, H. Silicon-Nanographite Aerogel-Based Anodes for High Performance Lithium Ion Batteries. *Sci. Rep.* **2019**, *9* (1), 14621. https://doi.org/10.1038/s41598-019-51087-y.

(30) Yang, J.; Li, Y.; Zheng, Y.; Xu, Y.; Zheng, Z.; Chen, X.; Liu, W. Versatile Aerogels for Sensors. *Small* **2019**, *15* (41), 1902826. https://doi.org/https://doi.org/10.1002/smll.201902826.

(31) Kai, P.; Xian, S.; Zhen, X.; Xiaoting, L.; Yingjun, L.; Liang, Z.; Yuxin, P.; Jianxiang, W.; Jingzhi, Z.; Fanxu, M.; Jian, W.; Chao, G. Hydroplastic Foaming of Graphene Aerogels and Artificially Intelligent Tactile Sensors. *Sci. Adv.* **2021**, *6* (46), 4045. https://doi.org/10.1126/sciadv.abd4045.

(32) Zhuo, H.; Hu, Y.; Chen, Z.; Peng, X.; Liu, L.; Luo, Q.; Yi, J.; Liu, C.; Zhong, L. A Carbon Aerogel with Super Mechanical and Sensing Performances for Wearable Piezoresistive Sensors. *J. Mater. Chem. A* **2019**, *7* (14), 8092–8100. https://doi.org/10.1039/C9TA00596J.

(33) Fischer, U.; Saliger, R.; Bock, V.; Petricevic, R.; Fricke, J. Carbon Aerogels as Electrode Material in Supercapacitors. *J. Porous Mater.* **1997**, *4* (4), 281–285. https://doi.org/10.1023/A:1009629423578.

(34) Pottathara, Y. B.; Tiyyagura, H. R.; Ahmad, Z.; Sadasivuni, K. K. Graphene Based Aerogels: Fundamentals and Applications as Supercapacitors. *J. Energy Storage* **2020**, *30*, 101549. https://doi.org/https://doi.org/10.1016/j.est.2020.101549.

(35) *IUPAC, Compendium of Chemical Terminology (the "Gold Book"), Second Ed.*; Blackwell Scientific Publications, Oxford, 1997.

(36) Brinker, C. J.; Scherer, G. W. The Physics and Chemistry of Sol-Gel Processing. In *Sol-Gel Science*; Academic Press: New York, 1990; p 461.

(37) Kistler, S. S. Coherent Expanded-Aerogels. *J. Phys. Chem.* **1932**, *36* (1), 52–64. https://doi.org/10.1021/j150331a003.

(38) Aegerter, M. A.; Leventis, N.; Koebel, M. M. *Aerogels Handbook*; Springer US: New York, 2011.

(39) Mandal, C.; Donthula, S.; Soni, R.; Bertino, M.; Sotiriou-Leventis, C.; Leventis, N. Light Scattering and Haze in TMOS-Co-APTES Silica Aerogels. *J. Sol-Gel Sci. Technol.* **2019**, *90* (1), 127–139. https://doi.org/10.1007/s10971-018-4801-0.

(40) Aspen Aerogels Thermal Insulation https://www.aerogel.com/pyrogel-product-family/.

(41) Lucas, E. M.; Doescher, M. S.; Ebenstein, D. M.; Wahl, K. J.; Rolison, D. R. Silica Aerogels with Enhanced Durability, 30-Nm Mean Pore-Size, and Improved Immersibility in Liquids. *J. Non. Cryst. Solids* **2004**, *350*, 244–252. https://doi.org/https://doi.org/10.1016/j.jnoncrysol.2004.07.074.

(42) Hæreid, S.; Anderson, J.; Einarsrud, M. A.; Hua, D. W.; Smith, D. M. Thermal and Temporal Aging of TMOS-Based Aerogel Precursors in Water. *J. Non. Cryst. Solids* **1995**, *185* (3), 221–226. https://doi.org/https://doi.org/10.1016/0022-3093(95)00016-X.

(43) Katti, A.; Shimpi, N.; Roy, S.; Lu, H.; Fabrizio, E. F.; Dass, A.; Capadona, L. A.; Leventis, N. Chemical, Physical, and Mechanical Characterization of Isocyanate Cross-Linked Amine-Modified Silica Aerogels. *Chem. Mater.* **2006**, *18* (2), 285–296. https://doi.org/10.1021/cm0513841.

(44) Mulik, S.; Sotiriou-Leventis, C.; Churu, G.; Lu, H.; Leventis, N. Cross-Linking 3D Assemblies of Nanoparticles into Mechanically Strong Aerogels by Surface-Initiated Free-Radical Polymerization. *Chem. Mater.* **2008**, *20* (15), 5035–5046. https://doi.org/10.1021/cm800963h.

(45) Ilhan, F.; Fabrizio, E. F.; McCorkle, L.; Scheiman, D. A.; Dass, A.; Palczer, A.; Meador, M. B.; Johnston, J. C.; Leventis, N. Hydrophobic Monolithic Aerogels by Nanocasting Polystyrene on Amine-Modified Silica. *J. Mater. Chem.* **2006**, *16* (29), 3046–3054. https://doi.org/10.1039/B604323B.

(46) Rewatkar, P. M.; Saeed, A. M.; Majedi Far, H.; Donthula, S.; Sotiriou-Leventis, C.; Leventis, N. Polyurethane Aerogels Based on Cyclodextrins: High-Capacity Desiccants Regenerated at Room Temperature by Reducing the Relative Humidity of the Environment. *ACS Appl. Mater. Interfaces* **2019**, *11* (37), 34292–34304. https://doi.org/10.1021/acsami.9b10755.

(47) Donthula, S.; Mandal, C.; Leventis, T.; Schisler, J.; Saeed, A. M.; Sotiriou-Leventis, C.; Leventis, N. Shape Memory Superelastic Poly(Isocyanurate-Urethane) Aerogels (PIR-PUR) for Deployable Panels and Biomimetic Applications. *Chem. Mater.* **2017**, *29* (10), 4461–4477. https://doi.org/10.1021/acs.chemmater.7b01020.

(48) Meador, M. A. B.; Fabrizio, E. F.; Ilhan, F.; Dass, A.; Zhang, G.; Vassilaras, P.; Johnston, J. C.; Leventis, N. Cross-Linking Amine-Modified Silica Aerogels with Epoxies: Mechanically Strong Lightweight Porous Materials. *Chem. Mater.* **2005**, *17* (5), 1085–1098. https://doi.org/10.1021/cm048063u.

(49) Leventis, N.; Sotiriou-Leventis, C.; Chandrasekaran, N.; Mulik, S.; Larimore, Z. J.; Lu, H.; Churu, G.; Mang, J. T. Multifunctional Polyurea Aerogels from Isocyanates and Water. A Structure−Property Case Study. *Chem. Mater.* **2010**, *22* (24), 6692–6710. https://doi.org/10.1021/cm102891d.

(50) Saunders, J. H.; Frisch, K. C. In Polyurethane Chemistry and Technology I. In *Chemistry*; Interscience Publishers: New York, 1963; pp 63–118.

(51) Malakooti, S.; Zhao, E.; Tsao, N.; Bian, N.; Soni, R. U.; Doulah, A. S. ud; Sotiriou-Leventis, C.; Leventis, N.; Lu, H. Synthesis of Aerogel Foams through a Pressurized Sol-Gel Method. *Polymer.* **2020**, *208*, 122925. https://doi.org/10.1016/j.polymer.2020.122925.

(52) Scherer, G. W. *Xerogels Encyclopedia of Materials: Science and Technology*; Buschow, K. H. J., Cahn, R. W., Flemings, M. C., Ilschner, B., Kramer, E. J., Mahajan, S., Veyssière, P., Eds.; Elsevier: New Jersey, 2001.

(53) Alemán, J. V; Chadwick, A. V; He, J.; Hess, M.; Horie, K.; Jones, R. G.; Kratochvíl, P.; Meisel, I.; Mita, I.; Moad, G.; Penczek, S.; Stepto, R. F. T. Definitions of Terms Relating to the Structure and Processing of Sols, Gels, Networks, and Inorganic-Organic Hybrid Materials (IUPAC Recommendations 2007). *Pure Appl. Chem.* **2007**, *79* (10), 1801–1829. https://doi.org/doi:10.1351/pac200779101801.

(54) Freundlich, H. *Colloid and Capillary Chemistry*, Duttom Ed.; New York, 1923.

(55) Iannibello, A.; Mitchell, P. C. H. Preparative Chemistry of Cobalt-Molybdenum/Alumina Catalysts. In *Preparation of Catalysts II*; Delmon, B., Grange, P., Jacobs, P., Poncelet, G. B. T.-S. in S. S. and C., Eds.; Elsevier, 1979; Vol. 3, pp 469–478. https://doi.org/https://doi.org/10.1016/S0167-2991(09)60230-5.

(56)   Leventis, N.; Vassilaras, P.; Fabrizio, E. F.; Dass, A. Polymer Nanoencapsulated Rare Earth Aerogels: Chemically Complex but Stoichiometrically Similar Core–Shell Superstructures with Skeletal Properties of Pure Compounds. *J. Mater. Chem.* **2007**, *17* (15), 1502–1508. https://doi.org/10.1039/B612625A.

(57)   Bayer, O. Das Di-Isocyanat-Polyadditionsverfahren (Polyurethane). *Angew. Chemie - Int. Ed.* **1947**, *59*, 257–272.

(58)   Wilkes, G. L.; Dziemianowicz, T. S.; Ophir, Z. H.; Artz, E.; Wildnauer, R. Thermally Induced Time Dependence of Mechanical Properties in Biomedical Grade Polyurethanes. *J. Biomed. Mater. Res.* **1979**, *13* (2), 189–206. https://doi.org/https://doi.org/10.1002/jbm.820130204.

(59)   Kim, H.-D.; Lee, T.-J.; Huh, J.-H.; Lee, D.-J. Preparation and Properties of Segmented Thermoplastic Polyurethane Elastomers with Two Different Soft Segments. *J. Appl. Polym. Sci.* **1999**, *73* (3), 345–352. https://doi.org/https://doi.org/10.1002/(SICI)1097-4628(19990718)73:3<345::AID-APP5>3.0.CO;2-T.

(60)   Nazaré, S.; Davis, R. D. 17 - Flame Retardancy Testing and Regulation of Soft Furnishings. In *Woodhead Publishing Series in Textiles*; Kilinc, F. S. B. T.-H. of F. R. T., Ed.; Woodhead Publishing, 2013; pp 456–498. https://doi.org/https://doi.org/10.1533/9780857098931.3.456.

(61)   Mills, N. J. Chapter 9 - Seating Case Study; Mills, N. J. B. T.-P. F. H., Ed.; Butterworth-Heinemann: Oxford, 2007; pp 205–233. https://doi.org/https://doi.org/10.1016/B978-075068069-1/50010-6.

(62)   Burchardt, B. 3 - Advances in Polyurethane Structural Adhesives. In *Woodhead Publishing in Materials*; Dillard, D. A. B. T.-A. in S. A. B., Ed.; Woodhead Publishing, 2010; pp 35–65. https://doi.org/https://doi.org/10.1533/9781845698058.1.35.

(63)   Islam, M. R.; Beg, M. D. H.; Jamari, S. S. Development of Vegetable-Oil-Based Polymers. *J. Appl. Polym. Sci.* **2014**, *131* (18), 40787. https://doi.org/https://doi.org/10.1002/app.40787.

(64)   Delebecq, E.; Pascault, J.-P.; Boutevin, B.; Ganachaud, F. On the Versatility of Urethane/Urea Bonds: Reversibility, Blocked Isocyanate, and Non-Isocyanate Polyurethane. *Chem. Rev.* **2013**, *113* (1), 80–118. https://doi.org/10.1021/cr300195n.

(65)   Engels, H.-W.; Pirkl, H.-G.; Albers, R.; Albach, R. W.; Krause, J.; Hoffmann, A.; Casselmann, H.; Dormish, J. Polyurethanes: Versatile Materials and Sustainable Problem Solvers for Today's Challenges. *Angew. Chemie Int. Ed.* **2013**, *52* (36), 9422–9441. https://doi.org/https://doi.org/10.1002/anie.201302766.

(66)   Nozaki, S.; Masuda, S.; Kamitani, K.; Kojio, K.; Takahara, A.; Kuwamura, G.; Hasegawa, D.; Moorthi, K.; Mita, K.; Yamasaki, S. Superior Properties of Polyurethane Elastomers Synthesized with Aliphatic Diisocyanate Bearing a Symmetric Structure. *Macromolecules* **2017**, *50* (3), 1008–1015. https://doi.org/10.1021/acs.macromol.6b02044.

(67)   Wang, R.; Zhou, B.; Zhu, Y.; Wang, Z. Preparation and Characterization of Rigid Polyurethane Foams with Different Loadings of Lignin-Derived Polycarboxylic Acids. *Int. J. Polym. Sci.* **2019**, *2019*, 3710545. https://doi.org/10.1155/2019/3710545.

(68)   Ugarte, L.; Saralegi, A.; Fernández, R.; Martín, L.; Corcuera, M. A.; Eceiza, A. Flexible Polyurethane Foams Based on 100% Renewably Sourced Polyols. *Ind. Crops Prod.* **2014**, *62*, 545–551. https://doi.org/https://doi.org/10.1016/j.indcrop.2014.09.028.

(69)   Chowdhury, R. A.; Clarkson, C. M.; Shrestha, S.; El Awad Azrak, S. M.; Mavlan, M.; Youngblood, J. P. High-Performance Waterborne Polyurethane Coating Based on a Blocked Isocyanate with Cellulose Nanocrystals (CNC) as the Polyol. *ACS Appl. Polym. Mater.* **2020**, *2* (2), 385–393. https://doi.org/10.1021/acsapm.9b00849.

(70)   Chidambareswarapattar, C.; McCarver, P. M.; Luo, H.; Lu, H.; Sotiriou-Leventis, C.; Leventis, N. Fractal Multiscale Nanoporous Polyurethanes: Flexible to Extremely Rigid Aerogels from Multifunctional Small Molecules. *Chem. Mater.* **2013**, *25* (15), 3205–3224. https://doi.org/10.1021/cm401623h.

(71)   March, J. *Advanced Organic Chemistry: Reactions, Mechanisms, and Structure*, 3rd ed.; Wiley New York: New York, 1985.

(72)   Smith, M. B.; March, J. *Advanced Organic Chemistry: Reactions, Mechanisms, and Structure*, 6th ed.; Wiley-Interscience: New York, 2007.

(73)   Sadekar, A. G.; Mahadik, S. S.; Bang, A. N.; Larimore, Z. J.; Wisner, C. A.; Bertino, M. F.; Kalkan, A. K.; Mang, J. T.; Sotiriou-Leventis, C.; Leventis, N. From "Green" Aerogels to Porous Graphite by Emulsion Gelation of Acrylonitrile. *Chem. Mater.* **2012**, *24* (1), 26–47. https://doi.org/10.1021/cm202975p.

(74)   Hyun, J.; Chilkoti, A. Surface-Initiated Free Radical Polymerization of Polystyrene Micropatterns on a Self-Assembled Monolayer on Gold. *Macromolecules* **2001**, *34* (16), 5644–5652. https://doi.org/10.1021/ma002125u.

(75)   Zoppe, J. O.; Ataman, N. C.; Mocny, P.; Wang, J.; Moraes, J.; Klok, H.-A. Surface-Initiated Controlled Radical Polymerization: State-of-the-Art, Opportunities, and Challenges in Surface and Interface Engineering with Polymer Brushes. *Chem. Rev.* **2017**, *117* (3), 1105–1318. https://doi.org/10.1021/acs.chemrev.6b00314.

(76)   Lee, J.; Kim, J.; Hyeon, T. Recent Progress in the Synthesis of Porous Carbon Materials. *Adv. Mater.* **2006**, *18* (16), 2073–2094. https://doi.org/https://doi.org/10.1002/adma.200501576.

(77)   Lee, J.-H.; Park, S.-J. Recent Advances in Preparations and Applications of Carbon Aerogels: A Review. *Carbon N. Y.* **2020**, *163*, 1–18. https://doi.org/https://doi.org/10.1016/j.carbon.2020.02.073.

(78)   Far, H. M.; Donthula, S.; Taghvaee, T.; Saeed, A. M.; Garr, Z.; Sotiriou-Leventis, C.; Leventis, N. Air-Oxidation of Phenolic Resin Aerogels: Backbone Reorganization, Formation of Ring-Fused Pyrylium Cations, and the Effect on Microporous Carbons with Enhanced Surface Areas. *RSC Adv.* **2017**, *7* (81), 51104–51120. https://doi.org/10.1039/c7ra10958j.

(79)   Pekala, R. W.; Alviso, C. T.; Kong, F. M.; Hulsey, S. S. Aerogels Derived from Multifunctional Organic Monomers. *J. Non. Cryst. Solids* **1992**, *145*, 90–98. https://doi.org/https://doi.org/10.1016/S0022-3093(05)80436-3.

(80)   Zheng, H.; Qu, Q.; Zhang, L.; Liu, G.; Battaglia, V. S. Hard Carbon: A Promising Lithium-Ion Battery Anode for High Temperature Applications with Ionic Electrolyte. *RSC Adv.* **2012**, *2* (11), 4904–4912. https://doi.org/10.1039/C2RA20536J.

(81)   Kamiyama, A.; Kubota, K.; Nakano, T.; Fujimura, S.; Shiraishi, S.; Tsukada, H.; Komaba, S. High-Capacity Hard Carbon Synthesized from Macroporous Phenolic Resin for Sodium-Ion and Potassium-Ion Battery. *ACS Appl. Energy Mater.* **2020**, *3* (1), 135–140. https://doi.org/10.1021/acsaem.9b01972.

(82)   Khosravi, M.; Bashirpour, N.; Nematpour, F. Synthesis of Hard Carbon as Anode Material for Lithium Ion Battery. *Adv. Mater. Res.* **2014**, *829*, 922–926. https://doi.org/10.4028/www.scientific.net/AMR.829.922.

(83)   Franklin, R. E. The Structure of Graphitic Carbons. *Acta Crystallogr.* **1951**, *4* (3), 253–261. https://doi.org/10.1107/s0365110x51000842.

(84)   Geng, S.; Wei, J.; Jonasson, S.; Hedlund, J.; Oksman, K. Multifunctional Carbon Aerogels with Hierarchical Anisotropic Structure Derived from Lignin and Cellulose Nanofibers for CO_2 Capture and Energy Storage. *ACS Appl. Mater. Interfaces* **2020**, *12* (6), 7432–7441. https://doi.org/10.1021/acsami.9b19955.

(85)   Li, Z.; Xu, J.; Sun, D.; Lin, T.; Huang, F. Nanoporous Carbon Foam for Water and Air Purification. *ACS Appl. Nano Mater.* **2020**, *3* (2), 1564–1570. https://doi.org/10.1021/acsanm.9b02347.

(86)   Park, J.; Jung, M.; Jang, H.; Lee, K.; Attia, N. F.; Oh, H. A Facile Synthesis Tool of Nanoporous Carbon for Promising H_2, CO_2, and CH_4 Sorption Capacity and Selective Gas Separation. *J. Mater. Chem. A* **2018**, *6* (45), 23087–23100. https://doi.org/10.1039/c8ta08603f.

(87)   Germain, J.; Fréchet, J. M. J.; Svec, F. Nanoporous Polymers for Hydrogen Storage. *Small* **2009**, *5* (10), 1098–1111. https://doi.org/10.1002/smll.200801762.

(88)   Lam, E.; Luong, J. H. T. Carbon Materials as Catalyst Supports and Catalysts in the Transformation of Biomass to Fuels and Chemicals. *ACS Catal.* **2014**, *4* (10), 3393–3410. https://doi.org/10.1021/cs5008393.

(89)   Job, N.; Marie, J.; Lambert, S.; Berthon-Fabry, S.; Achard, P. Carbon Xerogels as Catalyst Supports for PEM Fuel Cell Cathode. *Energy Convers. Manag.* **2008**, *49* (9), 2461–2470. https://doi.org/10.1016/j.enconman.2008.03.025.

(90)   Eshetu, G. G.; Elia, G. A.; Armand, M.; Forsyth, M.; Komaba, S.; Rojo, T.; Passerini, S. Electrolytes and Interphases in Sodium-Based Rechargeable Batteries: Recent Advances and Perspectives. *Adv. Energy Mater.* **2020**, *10* (20). https://doi.org/10.1002/aenm.202000093.

(91)   Qi, Y.; Harris, S. J. In Situ Observation of Strains during Lithiation of a Graphite Electrode. *J. Electrochem. Soc.* **2010**, *157* (6), A741. https://doi.org/10.1149/1.3377130.

(92)   Saeed, A. M.; Rewatkar, P. M.; Majedi Far, H.; Taghvaee, T.; Donthula, S.; Mandal, C.; Sotiriou-Leventis, C.; Leventis, N. Selective CO_2 Sequestration with Monolithic Bimodal Micro/Macroporous Carbon Aerogels Derived from Stepwise Pyrolytic Decomposition of Polyamide-Polyimide-Polyurea Random Copolymers. *ACS Appl. Mater. Interfaces* **2017**, *9* (15), 13520–13536. https://doi.org/10.1021/acsami.7b01910.

(93)   Liang, C.; Chen, Y.; Wu, M.; Wang, K.; Zhang, W.; Gan, Y.; Huang, H.; Chen, J.; Xia, Y.; Zhang, J.; Zheng, S.; Pan, H. Green Synthesis of Graphite from CO_2 without Graphitization Process of Amorphous Carbon. *Nat. Commun.* **2021**, *12* (1), 1–9. https://doi.org/10.1038/s41467-020-20380-0.

(94)   Xiao, J.; Pan, X.; Guo, S.; Ren, P.; Bao, X. Toward Fundamentals of Confined Catalysis in Carbon Nanotubes. *J. Am. Chem. Soc.* **2015**, *137* (1), 477–482. https://doi.org/10.1021/ja511498s.

(95)   Yadavalli, T.; Ames, J.; Agelidis, A.; Suryawanshi, R.; Jaishankar, D.; Hopkins, J.; Thakkar, N.; Koujah, L.; Shukla, D. Drug-Encapsulated Carbon (DECON): A Novel Platform for Enhanced Drug Delivery. *Sci. Adv.* **2019**, *5* (8), 1–13. https://doi.org/10.1126/sciadv.aax0780.

(96)   Manthiram, A.; Tsang, C. Electrode Materials for Rechargeable Lithium Batteries. *An. des la Asoc. Quim. Argentina* **1996**, *84* (3), 265–270.

(97)   Zhang, S. S.; Xu, K.; Jow, T. R. Low Temperature Performance of Graphite Electrode in Li-Ion Cells. *Electrochim. Acta* **2002**, *48* (3), 241–246. https://doi.org/10.1016/S0013-4686(02)00620-5.

(98)   Iturrondobeitia, A.; Aguesse, F.; Genies, S.; Waldmann, T.; Kasper, M.; Ghanbari, N.; Wohlfahrt-Mehrens, M.; Bekaert, E. Post-Mortem Analysis of Calendar-Aged 16 Ah NMC/Graphite Pouch Cells for EV Application. *J. Phys. Chem. C* **2017**, *121* (40), 21865–21876. https://doi.org/10.1021/acs.jpcc.7b05416.

(99) Bernat-Quesada, F.; Espinosa, J. C.; Barbera, V.; Álvaro, M.; Galimberti, M.; Navalón, S.; García, H. Catalytic Ozonation Using Edge-Hydroxylated Graphite-Based Materials. *ACS Sustain. Chem. Eng.* **2019**, *7* (20), 17443–17452. https://doi.org/10.1021/acssuschemeng.9b04646.

(100) Saeed, A. M.; Wisner, C. A.; Donthula, S.; Majedi Far, H.; Sotiriou-Leventis, C.; Leventis, N. Reuseable Monolithic Nanoporous Graphite-Supported Nanocatalysts (Fe, Au, Pt, Pd, Ni, and Rh) from Pyrolysis and Galvanic Transmetalation of Ferrocene-Based Polyamide Aerogels. *Chem. Mater.* **2016**, *28* (13), 4867–4877. https://doi.org/10.1021/acs.chemmater.6b02364.

(101) Li, J.; Li, J.; Luo, J. Superlubricity of Graphite Sliding against Graphene Nanoflake under Ultrahigh Contact Pressure. *Adv. Sci.* **2018**, *5* (11), 1800810. https://doi.org/https://doi.org/10.1002/advs.201800810.

(102) Li, R.; Yang, X.; Wang, Y.; Zhang, J.; Li, J. Graphitic Encapsulation and Electronic Shielding of Metal Nanoparticles to Achieve Metal-Carbon Interfacial Superlubricity. *ACS Appl. Mater. Interfaces* **2021**, *13* (2), 3397–3407. https://doi.org/10.1021/acsami.0c18900.

(103) Gao, W.; Majumder, M.; Alemany, L. B.; Narayanan, T. N.; Ibarra, M. A.; Pradhan, B. K.; Ajayan, P. M. Engineered Graphite Oxide Materials for Application in Water Purification. *ACS Appl. Mater. Interfaces* **2011**, *3* (6), 1821–1826. https://doi.org/10.1021/am200300u.

(104) Gallego, N. C.; Klett, J. W. Carbon Foams for Thermal Management. *Carbon N. Y.* **2003**, *41* (7), 1461–1466. https://doi.org/https://doi.org/10.1016/S0008-6223(03)00091-5.

(105) Chang, J.; Zhang, Q.; Lin, Y.; Zhou, C.; Yang, W.; Yan, L.; Wu, G. Carbon Nanotubes Grown on Graphite Films as Effective Interface Enhancement for an Aluminum Matrix Laminated Composite in Thermal Management Applications. *ACS Appl. Mater. Interfaces* **2018**, *10* (44), 38350–38358. https://doi.org/10.1021/acsami.8b12691.

(106) Whoriskey, P. In your phone, In their air https://www.washingtonpost.com/graphics/business/batteries/graphite-mining-pollution-in-china/.

(107) Wu, Z.; Li, W.; Xia, Y.; Webley, P.; Zhao, D. Ordered Mesoporous Graphitized Pyrolytic Carbon Materials: Synthesis, Graphitization, and Electrochemical Properties. *J. Mater. Chem.* **2012**, *22* (18), 8835–8845. https://doi.org/10.1039/C2JM30192J.

(108) Yoon, S. B.; Chai, G. S.; Kang, S. K.; Yu, J.-S.; Gierszal, K. P.; Jaroniec, M. Graphitized Pitch-Based Carbons with Ordered Nanopores Synthesized by Using Colloidal Crystals as Templates. *J. Am. Chem. Soc.* **2005**, *127* (12), 4188–4189. https://doi.org/10.1021/ja0423466.

(109) Vázquez-Santos, M. B.; Geissler, E.; László, K.; Rouzaud, J.-N.; Martínez-Alonso, A.; Tascón, J. M. D. Graphitization of Highly Porous Carbons Derived from Poly(*p*-Phenylene Benzobisoxazole). *Carbon N. Y.* **2012**, *50* (8), 2929–2940. https://doi.org/https://doi.org/10.1016/j.carbon.2012.02.062.

(110) Patel, M. N.; Wang, X.; Slanac, D. A.; Ferrer, D. A.; Dai, S.; Johnston, K. P.; Stevenson, K. J. High Pseudocapacitance of MnO_2 Nanoparticles in Graphitic Disordered Mesoporous Carbon at High Scan Rates. *J. Mater. Chem.* **2012**, *22* (7), 3160–3169. https://doi.org/10.1039/C1JM14513D.

(111) Su, P.; Jiang, L.; Zhao, J.; Yan, J.; Li, C.; Yang, Q. Mesoporous Graphitic Carbon Nanodisks Fabricated via Catalytic Carbonization of Coordination Polymers. *Chem. Commun.* **2012**, *48* (70), 8769–8771. https://doi.org/10.1039/C2CC34234K.

(112) Wisner, C. A. Graphite Aerogels and the Formation Mechanism of Unusual Micron-Sized Rod and Helical Structures. **2014**, Thesis Missouri S&T.

(113) Dawson, R.; Cooper, A. I.; Adams, D. J. Chemical Functionalization Strategies for Carbon Dioxide Capture in Microporous Organic Polymers. *Polym. Int.* **2013**, *62* (3), 345–352. https://doi.org/https://doi.org/10.1002/pi.4407.

(114) Rahman, F. A.; Aziz, M. M. A.; Saidur, R.; Bakar, W. A. W. A.; Hainin, M. R.; Putrajaya, R.; Hassan, N. A. Pollution to Solution: Capture and Sequestration of Carbon Dioxide (CO2) and Its Utilization as a Renewable Energy Source for a Sustainable Future. *Renew. Sustain. Energy Rev.* **2017**, *71*, 112–126. https://doi.org/https://doi.org/10.1016/j.rser.2017.01.011.

(115) Aminu, M. D.; Nabavi, S. A.; Rochelle, C. A.; Manovic, V. A Review of Developments in Carbon Dioxide Storage. *Appl. Energy* **2017**, *208*, 1389–1419. https://doi.org/https://doi.org/10.1016/j.apenergy.2017.09.015.

(116) *Compendium of Open and Unresolved Recommendations*; 2021.

(117) CO_2 earth https://www.co2.earth/daily-CO2.

(118) Wennersten, R.; Sun, Q.; Li, H. The Future Potential for Carbon Capture and Storage in Climate Change Mitigation – an Overview from Perspectives of Technology, Economy and Risk. *J. Clean. Prod.* **2015**, *103*, 724–736. https://doi.org/https://doi.org/10.1016/j.jclepro.2014.09.023.

(119) Wang, J.; Huang, L.; Yang, R.; Zhang, Z.; Wu, J.; Gao, Y.; Wang, Q.; O'Hare, D.; Zhong, Z. Recent Advances in Solid Sorbents for CO2 Capture and New Development Trends. *Energy Environ. Sci.* **2014**, *7* (11), 3478–3518. https://doi.org/10.1039/C4EE01647E.

(120) Stuart, H. R. Carbon Capture and Storage: How Green Can Black Be? *Science* **2009**, *325* (5948), 1647–1652. https://doi.org/10.1126/science.1172246.

(121) Kanniche, M.; Gros-Bonnivard, R.; Jaud, P.; Valle-Marcos, J.; Amann, J.-M.; Bouallou, C. Pre-Combustion, Post-Combustion and Oxy-Combustion in Thermal Power Plant for CO2 Capture. *Appl. Therm. Eng.* **2010**, *30* (1), 53–62. https://doi.org/https://doi.org/10.1016/j.applthermaleng.2009.05.005.

(122) Wypych, G. 1 - INTRODUCTION; Wypych, G. B. T.-H. of F. and B. A., Ed.; ChemTec Publishing, 2017; pp 1–2. https://doi.org/https://doi.org/10.1016/B978-1-895198-99-7.50003-9.

(123) Teo, N.; Jana, S. C. Open Cell Aerogel Foams via Emulsion Templating. *Langmuir* **2017**, *33* (44), 12729–12738. https://doi.org/10.1021/acs.langmuir.7b03139.

(124) Leventis, N.; Mulik, S.; Wang, X.; Dass, A.; Patil, V. U.; Sotiriou-Leventis, C.; Lu, H.; Churu, G.; Capecelatro, A. Polymer Nano-Encapsulation of Templated Mesoporous Silica Monoliths with Improved Mechanical Properties. *J. Non. Cryst. Solids* **2008**, *354* (2), 632–644. https://doi.org/https://doi.org/10.1016/j.jnoncrysol.2007.06.094.

(125) Teo, N.; Gu, Z.; Jana, S. C. Polyimide-Based Aerogel Foams, via Emulsion-Templating. *Polymer (Guildf).* **2018**, *157*, 95–102. https://doi.org/https://doi.org/10.1016/j.polymer.2018.10.030.

(126) Burpo, F. J.; Nagelli, E. A.; Morris, L. A.; Woronowicz, K.; Mitropoulos, A. N. Salt-Mediated Au-Cu Nanofoam and Au-Cu-Pd Porous Macrobeam Synthesis. *Molecules* . 2018. https://doi.org/10.3390/molecules23071701.

VITA

Rushi Umeshkumar Soni is from Gujarat, India and received his Bachelor of Technology degree in Surface Coating Technology in 2016 from the Institute of Chemical Technology (ICT, formerly U.D.C.T.), Mumbai, Maharashtra, India. He came to Rolla, Missouri, USA in the Fall of 2016 to pursue his Ph.D. degree in Chemistry at Missouri University of Science and Technology (Missouri S&T) with Prof. Chariklia Sotiriou-Leventis as his advisor. Rushi was involved in synthesis and analysis of different light-weight porous materials (aerogels) for various targeted applications. During the course of his Ph.D., Rushi has published five papers and submitted three more articles for publishing. He is the primary inventor of a U.S. Provisional Patent entitled "Amorphous and Graphitic Carbon Aerogels from Compressed Xerogel Powders" (Application No. 63/170,827) and a co-inventor of a second U.S. Provisional Patent entitled "Poly(tetrahydroquinazoline) and Derived Carbons" (Application No. 63/170,614), both filed in 2021. He has also presented his research in five national ACS meetings. Rushi received the Missouri S&T Council of Graduate Students Scholarship Award in 2020, the Chemistry Department's Outstanding Graduate Researcher Assistant Award in 2021, and the Missouri S&T Council of Graduate Student's Distinguished Research and Innovation Excellence Award in 2021. He received his Doctor of Philosophy in Chemistry from Missouri S&T in December of 2021.